Studies of Young, Star-forming Circumstellar Disks

by

Jaehan Bae

A dissertation submitted in partial fulfillment
of the requirements for the degree of
Doctor of Philosophy
(Astronomy and Astrophysics)
in The University of Michigan
2017

Doctoral Committee:

Professor Lee William Hartmann, Chair
Professor Fred C. Adams
Professor Edwin Anthony Bergin
Professor Nuria Pilar Calvet
Professor Richard P. Nelson, Queen Mary University of London

Jaehan Bae

jaehbae@umich.edu

ORCID iD: 0000-0001-7258-770X

For my family.

ACKNOWLEDGMENTS

This thesis would not have been possible without supports from many people. First and foremost, I would like to thank Lee Hartmann for being an insightful and supportive advisor. There were moments that I had hard time to figure out why things were going wrong in my simulations (although it eventually turned out that nothing was wrong with the simulations) and I remember you really tried to cheer me up. Thank you, Lee.

I would like to thank Richard Nelson for many insightful and invaluable discussion, without which the second half of my thesis would not have been possible. Nothing was of your duty, but I know you put a lot of time and effort to teach me. Thank you. Richard.

I am grateful to my dissertation committee, Lee Hartmann, Fred Adams, Edwin Bergin, Nuria Calvet, and Richard Nelson, for asking me challenging questions and providing helpful feedback for my work. I am thankful to Zhaohuan Zhu for sharing many of his codes with me and for being such a great collaborator. I also thank former and current Stars, Planets, and Formation group members for inspiring me with new stuffs every Tuesday.

I would also like to thank people in Korea. I did not recognize at that time, but now that I am looking back my years in undergrad and master in Seoul National University, I see that I have learned a great deal about Astronomy during the years. In particular, I would like to thank my undergrad and master degrees advisor Woong-Tae Kim and the group members. Also, I would like to thank Do-Young Byun and Kee-Tae Kim, who helped me write my first two journal papers while I worked at KASI.

Finally, I would like to thank my family. Mom and Dad, nothing would have been possible without your immense love and support. Thank you for believing in me. Jaejin, thank you for your support and for being my awesome brother. Hyehwan, this thesis was only possible with your great support and patience. Thank you for staying with me during the rough time. Ian, everyday is full of surprises and enjoy with you. Thank you for being healthy and happy all the time.

TABLE OF CONTENTS

LIST OF FIGURES

FIGURE

LIST OF TABLES

TABLE

LIST OF ABBREVIATION

ALMA Atacama Large Millimeter/submillimeter Array

AU Astronomical unit

CV Cataclysmic variable

DZRV Dead zone residual viscosity

EUV Extreme Ultraviolet

FUV Far Ultraviolet

GI Gravitational instability

GPI Gemini Planet Imager

ILR Inner Lindblad resonance

IR Infrared

ISM Interstellar medium

MHD Magnetohydrodynamic

MMSN Minimum mass solar nebular

MRI Magnetorotational instability

RWI Rossby wave instability

SWI Spiral wave instability

TI Thermal instability

UV Ultraviolet

VLT Very Large Telescope

ABSTRACT

Disks of gas and dust around forming stars – circumstellar disks – last only a few million years. This is a very small fraction of the entire lifetime of Sun-like stars, several billion years. Nevertheless, by the time circumstellar disks dissipate stars complete building up their masses, giant planets finish accreting gas, and terrestrial bodies are nearly fully grown and ready for their final assembly to become planets. Understanding the evolution of circumstellar disks are thus crucial in many contexts.

Using numerical simulations as the primary tool, my thesis has focused on the studies of various physical processes that can occur throughout the lifetime of circumstellar disks, from their formation to dispersal. Chapters 2, 3, and 4 emphasize the importance of early evolution, during which time a forming star-disk system obtains mass from its natal cloud: the infall phase. In Chapter 2 and 3, I have modeled episodic outbursts of accretion in protostellar systems resulting from disk instabilities – gravitational instability and magnetorotational instability. I showed that outbursts occur preferentially during the infall phase, because the mass addition provides more favorable conditions for gravitational instability to initiate the outburst cycle, and that forming stars build up a significant fraction of their masses through repeated short-lived, episodic outbursts. The infall phase can also be important for the formation of planets. Recent ALMA observations revealed sets of bright and dark rings in circumstellar disks of young, forming stars, potentially indicating early formation of planets. In Chapter 4, I showed that infall streams can create radial pressure bumps near the outer edge of the mass landing on the disk, from which vortices can form, collecting solid particles very efficiently to make initial seeds of planets. The next three chapters highlight the role of planets in setting the observational appearance and the evolution of circumstellar disks. When a planet forms in a disk, the gravitational interaction between the planet and disk can create structures, such as spiral arms and gaps. In Chapter 5, I compared the disk structures formed by planetary companions in numerical simulations with the observed structures in

the disk surrounding an 8 Myr-old Herbig Ae star SAO 206462. Based on the experiments, I made predictions for the mass and position of a currently unrevealed planet, which can help guide future observations to search for more conclusive evidence for the existence of a planetary companion in the system. In Chapter 6, I showed for the first time in global simulation domains that spiral waves, driven for instance by planets or gravitational instability, can be unstable due to resonant interactions with inertial modes, breaking into turbulence. In Chapter 7, I showed that the spiral wave instability operates on the waves launched by planets and that the resulting turbulence can significantly stir up solid particles from the disk midplane. The stirring of solid particles can have influences on the observation appearance of the parent disk and on the subsequent assembly of planetary bodies in the disk. Finally, in Chapter 8, I investigated the dispersal of circumstellar disks via photoevaporative winds, finding that the photoevaporative loss alone, coupled with a range of initial angular momenta of protostellar clouds, can explain the observed decline of the disk frequency with increasing age. The findings and future possibilities are summarized in Chapter 9.

CHAPTER I

Introduction

1.1 Formation of Circumstellar Disks

Stars form in cold, dense cores of molecular clouds. These cores are supported by internal thermal/magnetic pressure and/or turbulence, but once the self-gravity of a core overcomes the outward support it starts to collapse. Since the star-forming core collapse involves many orders of magnitude decrease in size – from $\sim 10^{13}$ km for cores to $\sim 10^{6}$ km for (proto)stars – non-negligible amount of rotation in natal cloud cores results in the formation of disks around forming protostars, in order to conserve angular momentum: the material orbiting close to the rotation axis of a core carries small amount of angular momentum and so falls close to the center of the system, whereas the material orbiting far from the rotation axis carries large amount of angular momentum and thus falls far out onto a rotating disk.

Theoretical models predict that the collapse of molecular clouds takes place over roughly a free-fall time (e.g., Shu, 1977). For solar-mass cores with typical molecule number densities of 10^{3}–10^{5} cm^{-3} (Myers et al. 1983; Benson & Myers 1989; Lee & Myers 1999; see also Evans 1999 and Williams et al. 2000 for reviews), the collapse thus lasts for about 0.1–1 million years. This phase during which time the forming protostar is deeply embedded in the collapsing envelope cloud is called "protostellar" or "Class 0/I" phase[1]. Correspondingly, the disk surrounding the protostar during this phase is called a "protostellar" or "Class 0/I" disk. The disk after the gravitational collapse is completed, on the other hand, is called a

[1]An initial attempt to classify young stellar objects was made by Lada (1987), who used the shapes of objects' spectral energy distributions. Class 0 phase is proposed later by André et al. (1993). See review by André et al. (2000)

"protoplanetary", "Class II", or "Classical T-Tauri" disk. Throughout this thesis, I use the term circumstellar disks to refer to the disks in both protostellar and protoplanetary phases.

In recent years, radio interferometers, including the Plateau de Bure Interferometer, Submillimeter Array, and Atacama Large Millimeter/submillimeter Array (ALMA), have allowed astronomers to spatially resolve circumstellar disks and to characterize their properties (e.g., size and mass). Unfortunately, even with the great advances in available instruments, observing disks in Class 0/I phases is still challenging mainly because of the confusion with the gas and dust in the envelope. We are thus left with only a handful of well-observed, confirmed Class 0/I disks (e.g., L1489 IRS, Yen et al. 2014; L1527 IRS, Tobin et al. 2012; TMC1, TMC1A, Harsono et al. 2014; VLA1623A, Murillo et al. 2013). We have better statistics for the disks in the later evolutionary phases. Sub-millimeter and millimeter observations of T-Tauri disks around low-mass – solar-mass and lower – stars suggest that the disks typically have sizes of tens to hundreds AU and masses of a fraction of a per cent to a few per cent of the central stellar mass (Andrews et al. 2009, 2010, 2013; see also review by Williams & Cieza 2011 and references therein). It is generally believed that Class 0/I disks contain more mass than T-Tauri disks (e.g., Eisner, 2012), but conclusive observational evidence for this is lacking.

One potentially important ingredient in the formation of star-disk systems is magnetic fields. Magnetic fields can extract angular momentum from infalling material, resulting in the formation of smaller disks or no disk at all (Allen et al., 2003; Galli et al., 2006; Hennebelle & Fromang, 2008; Mellon & Li, 2008; Hennebelle & Ciardi, 2009). However, the prevalence of premature, gaseous circumstellar disks as well as mature, planetary systems discovered around main-sequence stars implies that such "catastrophe" should not happen universally. There are possible solutions to circumvent this magnetic braking catastrophe including the non-ideal magnetohydrodynamic (MHD) effects, and the degree to which magnetic fields play a role in the formation of star-disk systems is being actively investigated by many researchers (see review by Li et al. 2014 and references therein).

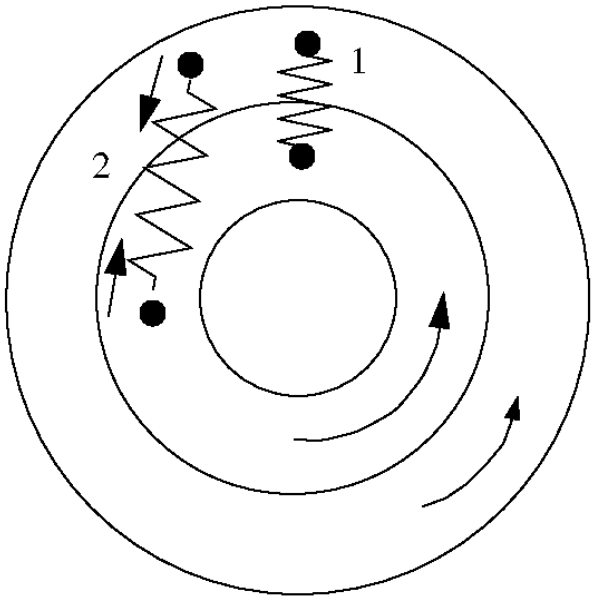

Figure 1.1. A schematic diagram showing how angular momentum can be transferred between two gas blobs in two adjacent annuli. If there exists some restoring force, illustrated with strings in this figure, differential rotation of a disk will stretch the springs. The pulling force between the two gas blobs will try to spin up the gas blob in the outer annulus and spin down the gas blob in the inner annulus. This results in an exchange of angular momentum between the two gas blobs and the consequent redistribution of the two gas blobs in the disk. Figure adapted from Hartmann (2009).

1.2 Accretion Processes in Circumstellar Disks

1.2.1 What Enables Accretion?

The main driver of disk evolution is accretion. Accretion process can be understood as an exchange of angular momentum among disk material and the consequent redistribution of mass. For a Keplerian disk, the specific angular momentum l is an increasing function of radius R: $l = Rv_\phi = \sqrt{GM_* R}$. Therefore, in order for a gas blob to be accreted inward, it needs to lose its angular momentum.

In order to see how angular momentum can be transferred within a disk, let us imagine two gas blobs in two adjacent disk annuli as illustrated in the schematic diagram of Figure 1.1. In a Keplerian disk, the gas blob in the inner annulus rotates faster than the one in the outer annulus. Therefore, if there exists some restoring force that pulls each other as they rotate differentially, the restoring force will spin down the inner gas blob and spin up the

outer gas blob. This interaction is what enables an exchange of angular momentum between the two gas blobs: the inner one slows down so loses angular momentum, whereas the outer one spins up so gains angular momentum. This in turn results in a redistribution of mass: as the inner gas blob loses angular momentum it will direct inward, whereas the outer one will direct outward as it obtains angular momentum.

It has long been thought that the gravitational instability (GI) and magnetorotational instability (MRI) are the most likely mechanisms for driving accretion in many astrophysical disks. In circumstellar disks, however, it is unclear whether the two mechanisms are the dominant processes in producing accretion, as discussed below.

In order for the GI to operate, a disk has to be massive enough so that its self-gravity is important. The Toomre Q parameter is often used to quantify the importance of disk self-gravity, where Q is defined as (Toomre, 1964)

$$Q \equiv \frac{c_s \kappa}{\pi G \Sigma}. \tag{1.1}$$

In the above form, c_s is the sound speed, κ is the epicyclic frequency, G is the gravitational constant, and Σ is the disk surface density. In general, self-gravity becomes important as Q approaches to unity. Using $M_d \simeq \pi R^2 \Sigma$, $\kappa \simeq \Omega_K$, and $c_s/v_K = H/R$, where M_d is the disk mass, Ω_K and v_K are Keplerian angular frequency and velocity, and H is the disk scale height at radius R, one may express the condition for GI to operate in a more intuitive way:

$$Q \simeq \frac{M_*}{M_d}\frac{H}{R} \lesssim 1 \quad \text{or} \quad \frac{M_d}{M_*} \gtrsim \frac{H}{R}. \tag{1.2}$$

Figure 1.2 presents the cumulative distribution of M_d/M_* for statistically complete Class II disks in the $\sim$ 2 Myr-old Taurus star-forming region. Note that most of the Class II disks have masses less than a few per cent of their host stars' masses. Since the disk aspect ratio H/R generally ranges 0.05–0.2, GI is unlikely to operate in the T-Tauri phase and is rather limited to the early stages (i.e., Class 0/I) when mass loading from their natal clouds continues and thus circumstellar disks are massive.

In order for the MRI to operate, a disk has to have a sufficiently high ionization level to couple disk gas with magnetic fields. However, such an ionization level can be achieved only in

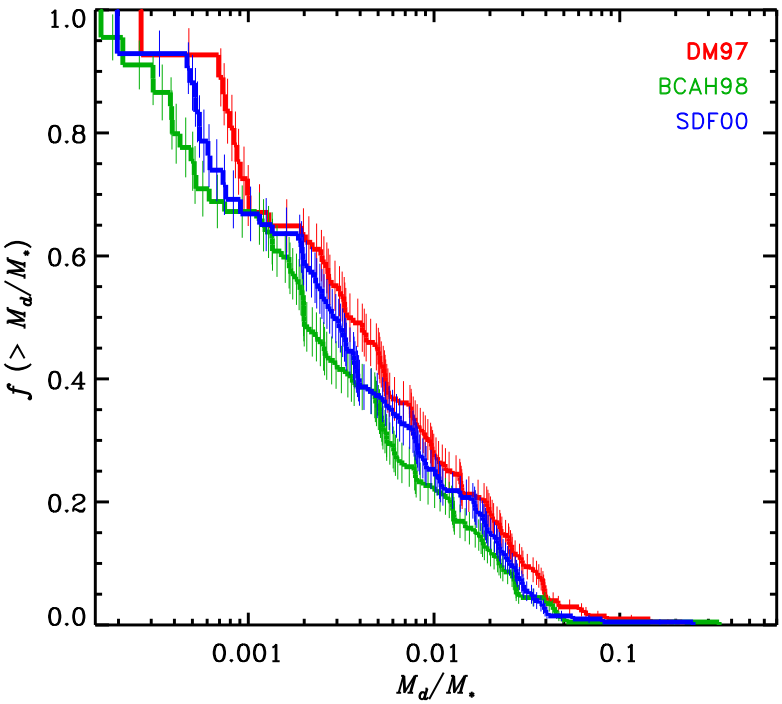

Figure 1.2. The cumulative distribution of the disk-to-star mass ratios M_d/M_* of Class II disks in the Taurus star-forming region. Different colors in the figure indicate results with different methods in obtaining stellar masses. Note that the majority of the sample has $M_d/M_* \leq 0.05$ for which ratios GI is very unlikely to operate. Figure adapted from Andrews et al. (2013).

limited regions of circumstellar disks: (1) the innermost region ($\ll 1$ AU) where temperature is high enough ($\gtrsim 1000$ K) to thermally ionize alkali metals; and (2) the optically thin outer disk region (typically $\gg 10$ AU) where energetic photons (e.g., stellar X-rays, cosmic rays) can maintain non-thermal ionization. Regions in between are too cold and/or too optically thick, so that disks do not have high enough ionization levels to couple disk gas with magnetic fields. Due to the inability to sufficiently ionize the disk gas, Gammie (1996) suggested that circumstellar disks might have a thin magnetically active layer near the surface, where non-thermal ionization can occur, leaving a magnetically inert main body around the midplane sandwiched in between active layers – the so-called "dead-zone".

More recently, numerical simulations including non-ideal MHD effects suggest that the disk midplane remains laminar – little or no turbulence – similar to Gammie's picture. Bai & Stone (2013b) and Gressel et al. (2015) have shown that the MRI is suppressed with the inclusion of ambipolar diffusion and the disk midplane remains laminar. In addition, non-

ideal MHD calculations with ambipolar diffusion show the development of strong disk winds from the surface layer (Bai & Stone, 2013b; Gressel et al., 2015), which might be sufficient to explain the observed accretion rates in T-Tauri stars (Gressel et al., 2015). Including the Hall effect can also result in laminar disk structure in the midplane (Bai, 2014; Lesur et al., 2014; Simon et al., 2015). It is also worth noting that in the Hall-dominated regime the accretion efficiency could differ by orders of magnitude depending upon the alignment between the net magnetic field and the disk rotation axis (Bai, 2014; Lesur et al., 2014; Simon et al., 2015). Including all non-ideal MHD effects with proper disk ionization and thermodynamic models in a global simulation domain is numerically very expensive, but some progress has been made (e.g., Béthune et al., 2016) and a more complete picture of magnetically-driven accretion processes is hopeful to emerge in the future.

There are some other alternatives as well. It is possible that purely hydrodynamic instabilities can produce turbulence and drive accretion, depending on the disk conditions. This includes the vertical shear instability (Urpin & Brandenburg, 1998; Nelson et al., 2013) which arises from a non-zero shear in rotational velocity along the vertical direction, and the subcritical baroclinic instability (Petersen et al., 2007; Lesur & Papaloizou, 2010) which arises from a radial entropy gradient.

1.2.2 α Disk Model

As alluded above, the mechanism(s) through which circumstellar disks transport mass and angular momentum is still not fully understood at the time of writing this thesis. Nevertheless, it seems clear that circumstellar disks maintain accretion throughout their lifetime. Observational estimates show that the accretion rate onto the central star is of order of $10^{-9} - 10^{-7}\ M_{\odot}\ \mathrm{yr}^{-1}$, generally decreasing as a function of age (see review by Hartmann et al. 2016 and references therein). One may thus desire to parameterize the efficiency of disk accretion regardless of its origin. The most widely used form is the one introduced by Shakura & Sunyaev (1973), in which a dimensionless parameter α characterizes the accretion efficiency of a disk and relates the efficiency to the viscosity as $\nu = \alpha c_s^2/\Omega$. In terms of this α notation, the observed accretion rates in circumstellar disks are well explained with $\alpha \sim 10^{-3} - 10^{-2}$ (e.g., Hartmann et al., 1998). The various accretion processes described in

the previous section yield a broadly consistent accretion efficiency of $\alpha \sim 10^{-4} - 10^{-2}$.

1.2.3 Accretion Outbursts

The gravitational core collapse model of Shu (1977) suggests a mass infall rate of $\dot{M}_{\rm infall} \sim c_s^3/G \sim 3 \times 10^{-6}\ M_\odot\ {\rm yr}^{-1}$ for a core temperature of 10 K, which explains well the estimated duration of the infall phase to form a solar-mass star (i.e., a few $\times 10^5$ yr; see Section 1.1 and also Dunham et al. 2014 and references therein). Other core collapse models with improved treatments also suggest similar, or even larger infall rates (e.g., Lin & Pringle, 1990; Galli & Shu, 1993; Basu, 1997). This implies that, *if* the accretion process in a disk is smooth and steady, such that the accretion rate within the disk and the accretion rate from the disk on to the central star are comparable in magnitude ($\dot{M}_{\rm infall} \simeq \dot{M}_{\rm disk} \simeq \dot{M}_*$), one would expect an accretion luminosity of

$$L_{\rm acc} = \frac{GM_*\dot{M}_*}{2R_*} \simeq 24\ L_\odot, \tag{1.3}$$

assuming $M_* = 0.5 M_\odot$, $\dot{M}_* = 3 \times 10^{-6}\ M_\odot\ {\rm yr}^{-1}$, and $R_* = 2R_\odot$. However, it turned out that this number far exceeds the observed luminosities of embedded, Class 0/I protostars, which have been shown to peak near 1 $L_\odot$ with a significant fraction of objects at sub-solar luminosities (Wilking et al., 1989; Kenyon et al., 1990; Enoch et al., 2009; Evans et al., 2009; Kryukova et al., 2012; Dunham et al., 2013; Stutz et al., 2013, see also Dunham et al. 2014 for review). This was recognized as a problem – the so-called luminosity problem (Kenyon et al., 1990).

One potential solution to the luminosity problem is outbursts of accretion. The idea is that the accretion in protostellar disks is low ($\dot{M}_* \sim 10^{-9}$–$10^{-7}\ M_\odot\ {\rm yr}^{-1}$) for the most of the time, in agreement with observations, with occasional short-lived periods of high accretion (Kenyon et al., 1990). In Chapters 2 and 3, we develop one- and two-dimensional numerical models which make use of disk instabilities – GI and MRI – to trigger outbursts of accretion. As discussed in Section 1.2, the GI and MRI are not always operational in circumstellar disks. When a disk manages to have the instabilities become operational, however, the efficiency of disk accretion can be significantly enhanced, resulting in an outburst with $\dot{M}_* \sim 10^{-6}$–$10^{-4}\ M_\odot\ {\rm yr}^{-1}$.

1.3 Planet Formation

Thanks to the dedicated search for exoplanets by the *Kepler* mission, which alone has discovered more than 2,300 exoplanets[2], we now know that planets are common in our galaxy. Statistical studies based on exoplanet searches with various methods suggest that $\gtrsim 50$ % of Sun-like stars – stars with spectral type of F, G, or K – host at least one planet around them (Fressin et al. 2013; Petigura et al. 2013; see also review by Winn & Fabrycky 2015 and references therein).

Capturing signatures of on-going planet formation in circumstellar disks, on the other hand, has not been possible until very recently, mainly because of high spatial resolution and sensitivity required. The situation has changed in the last few years with the advent of state-of-the-art instruments, including ALMA, Very Large Telescope (VLT), and Gemini Planet Imager (GPI). High spatial resolution observations of protoplanetary disks at infrared and (sub-)millimeter with these instruments have imaged disk structures, such as rings and gaps, inner cavity, and spiral arms, that are likely to be created by forming planets. Figure 1.3 shows two examples. In the left panel is a scattered-light image of an 8 Myr-old Herbig Ae star SAO 206462 in the J band (Stolker et al., 2016). The two-armed spirals shown in the image is a very suggestive feature of the existence of a companion body in the disk (e.g., Dong et al., 2015; Dong & Fung, 2017). On the right panel, the continuum emission of an 1 Myr old solar-mass star HL Tau at 1.3 millimeter is presented (ALMA Partnership et al., 2015). The multiple rings and gaps can be reproduced with multiple sub-Jupiter-mass planets (Jin et al., 2016). The existence of such a perturbing body has yet to be confirmed, while the planet explanation is tempting. Future observations will shed light on the origin(s) of these structures.

Formation of planets itself is an important process, but it is also an important step in the evolution of circumstellar disks. This is because planets interact with their host disks and can provide feedback. As we will show in Chapters 5 and 7, the feedback from forming planets can affect the observational appearance and subsequent evolution of circumstellar disks.

[2]This is the number of confirmed planets by the mission as of March 2017; find an up-to-date number at https://kepler.nasa.gov.

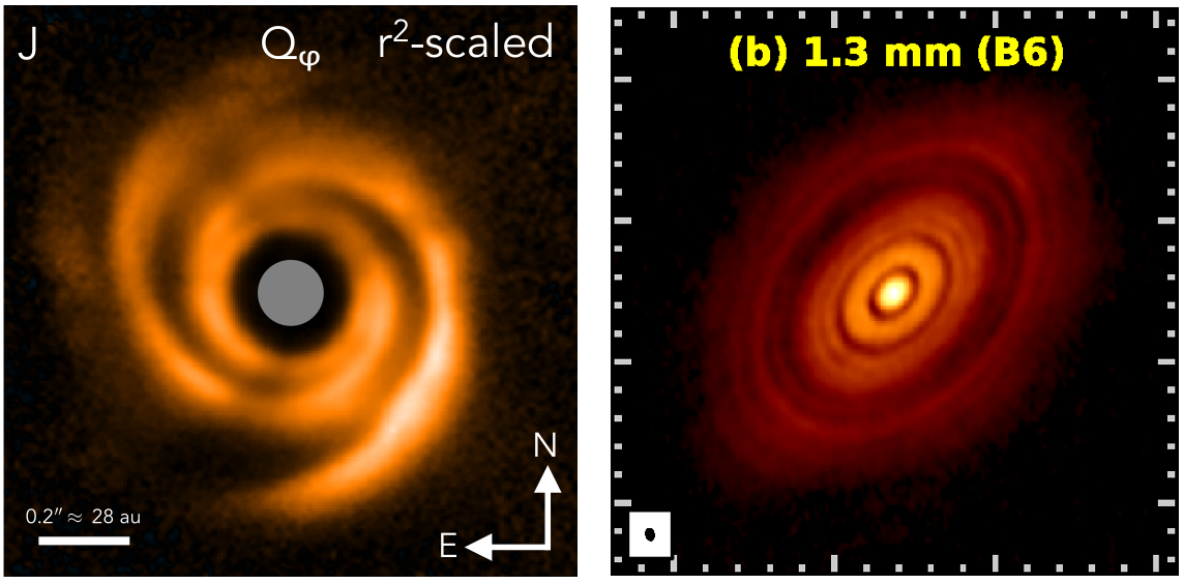

Figure 1.3. (Left) A scattered-light image of SAO 206462 (HD 135344B) in the J band observed with VLT SPHERE. Figure adapted from Stolker et al. (2016). (Right) Continuum emission of HL Tau at 1.3 millimeter with ALMA. Figure adapted from ALMA Partnership et al. (2015). While the origin is yet to be confirmed, the structures seen in the disks – spiral arms, rings, and gaps – could be potential signatures of planets.

Keeping in mind the importance of the formation of planet, in this Chapter, I summarize the leading theories of terrestrial and giant planet formation.

1.3.1 Terrestrial Planet Formation

In order to make rocky, terrestrial planets, it is necessary to collect and grow solid material. In general, this can be done by growing sub-μm-sized ISM grains[3]. The very initial stage of the growth is relatively well understood. Small μm-sized particles can grow up to about a millimeter by sticking to each other, as the van der Waals force is strong enough to bind them (Dominik & Tielens, 1997; Ormel et al., 2007). As particles grow, however, they face barriers to overcome. When particles are grown to about a millimeter in size, collisions between particles start to bounce off each other (Güttler et al., 2010; Zsom et al., 2010). This is called the bouncing barrier. Another difficulty is that particles start to suffer from rapid radial drift because aerodynamic drag becomes severe (Weidenschilling, 1977). This

[3]However, there are models explaining that terrestrial planets can form via tidal stripping of giant planets that are originally formed through disk instabilities. See Nayakshin (2010, 2011).

is called the radial drift barrier. The exact sizes of particles facing the radial drift barrier depend on the disk mass, but in general it is about a centimeter to a meter.

There are ways to circumvent these barriers, and they commonly require the concentration of millimeter- to meter-sized particles in a trap, followed by gravitationally collapse to form objects of $\sim$10–100 km in size, planetesimals. One way to concentrate particles is via the streaming instability (Youdin & Goodman, 2005). The instability occurs when the local particle density is comparable to the gas density. Under such a condition, marginally coupled solid particles can be concentrated in clumps which in turn collapse by self-gravity, forming planetesimals. Vortices provide another possible channel to collect solid particles and form planetesimals (e.g., Adams & Watkins, 1995; Barge & Sommeria, 1995; Tanga et al., 1996). Previously, it was known that vortices can form at the edge of the disk dead-zone (Inaba & Barge, 2006; Varnière & Tagger, 2006; Lyra et al., 2008, 2009; Lyra & Mac Low, 2012; Regály et al., 2012) or at the edge of gaps carved by a planet (de Val-Borro et al., 2007; Lin, 2014). In Chapter 4, we suggest a new way to create vortices in circumstellar disks – infall streams – and show that the vortices can efficiently trap solid particles.

Once planetesimals form in the sea of pebbles – particles that are millimeters to decimeters in size – gas-drag aided pebble accretion (Johansen & Lacerda, 2010; Ormel & Klahr, 2010; Lambrechts & Johansen, 2012; Morbidelli & Nesvorny, 2012) can expedite the growth of planetesimals to planetary embryos. The idea of pebble accretion is that planetesimals take advantage of the large accretion cross section produced by aerodynamic drag as they are embedded in a gaseous disk. The accretion cross section can be orders of magnitude larger than the geometric cross section of planetesimals, helping to form planetary embryos before all the gas dissipates. The idea of pebble accretion helps resolve the excessive timescales for accumulating material onto solid cores that planet formation theories have long been struggling with. On the other hand, it is worth pointing out that the pebble accretion process is very sensitive to the level of background turbulence (Lambrechts & Johansen, 2012; Johansen et al., 2015). In order for this mechanism to work efficiently, it is necessary to concentrate pebbles into a thin layer at the midplane, about the size of the Hill radius of planetesimals (Lambrechts & Johansen, 2012). Under typical conditions, this can only be satisfied with a very low turbulence level of $\alpha \lesssim 10^{-4}$. In Chapter 7, we show that the spiral

waves launched by gas giants can dissipate through an instability introduced in Chapter 6 and enhance the level of turbulence in their host disks. After a gas giant forms in a disk, it is hence possible that terrestrial body formation through pebble accretion can be slowed down.

Finally, planetary embryos complete their growth and form terrestrial planets during the gas-free debris phase through collisions with planetesimals and/or other embryos, which typically takes several tens to hundreds million years after gas has removed (see review by Morbidelli et al. 2012 and references therein).

1.3.2 Giant Planet Formation

The growth of solid bodies described in the previous section can be more efficient beyond the snowline (e.g., Morbidelli et al., 2015). It has been suggested that 10 $M_\oplus$ mass cores can form within about one million year through pebble accretion (Bitsch et al., 2015; Levison et al., 2015a; Morbidelli et al., 2015). When the core mass successfully reaches about 10–15 $M_\oplus$ before all disk gas dissipates, runaway accretion of gas onto the core can initiate. Given that circumstellar disks typically live a few million years (Haisch et al., 2001; Hernández et al., 2007; Mamajek, 2009), such cores are then allowed sufficient time to accrete gas and evolve into gas giants, assuming that about another million year is required for the runaway accretion process to form a Jupiter-mass planet (e.g., Pollack et al., 1996; Movshovitz et al., 2010).

A completely different picture from the above core accretion scenario is available when the disk is massive enough so gravitationally unstable. When the cooling of a disk is rapid so that it efficiently takes away the heat GI provides, the disk can fragment and create self-gravitating clumps that can evolve into giant planets (e.g., Boss, 1997, 1998). As fragmentation requires rapid cooling, the underlying disk thermodynamics is important. Exactly how fast the cooling should be to trigger fragmentation seems to be dependent upon numerical settings (e.g., numerical resolution and grid-based code vs. smoothed particle code; Meru & Bate 2011a,b, 2012), but analytical/numerical investigations typically show that the cooling timescale should be shorter than a few dynamical timescales (e.g., Gammie, 2001; Rice et al., 2003; Rafikov, 2005). It is also possible that a disk can fragment if the mass addition

rate to a local region exceeds the maximum mass transport rate allowed by the GI (Kratter et al., 2008), which, if at all, is most likely to happen during the infall phase.

On the other hand, it is still under debate whether GI-driven fragments will end up within the planetary mass range or keep growing to brown dwarf or stellar masses (Kratter et al. 2010, see also review by Kratter et al. 2016 and references therein). Also, whether or not GI-driven fragments can survive against tidal stripping and/or migration is some other challenges to be overcome (Nayakshin, 2010, 2011; Cha & Nayakshin, 2011; Zhu et al., 2012a).

1.4 Dispersal of Circumstellar Disks

Gaseous disks around protostars do not live forever as one can infer from the present-day solar system. Some fraction of disk material accretes onto the forming central star (§1.2) and some other fraction is used up to make planetary bodies (§1.3) when allowed. Yet some other fraction can be removed from the system, as described in this section.

It is known that circumstellar disks typically disperse within several million years, although the exact timescale of disk clearing should differ system by system. One way to estimate the disk lifetime is to study the excess infrared continuum emission, which originates from μm-sized dust particles. Figure 1.4 presents the fraction of stars with near-infrared disk emission as a function of the age of the stellar group, compiled by Hernández et al. (2007). Despite the caveats using dust particles as a probe, the drop in the observed disk frequency as a function of the age strongly suggests that circumstellar disks experience a significant evolution over a few Myr timescales.

The currently most popular theory for disk dispersal is photoevaporative winds (see review by Alexander et al., 2014). Protostars are known to emit strong high-energy radiation in the ultraviolet (UV) and X-rays (e.g., Feigelson et al., 2003; Güdel et al., 2007). Since this high-energy radiation can heat the disk surface to high temperatures, the heated layers can be unbound from the potential well of the star-disk system and escaping mass flows can be launched from the surface. While the underlying physics is much more complicated, in order to have a simplistic view of the mechanism one may assume a situation that the

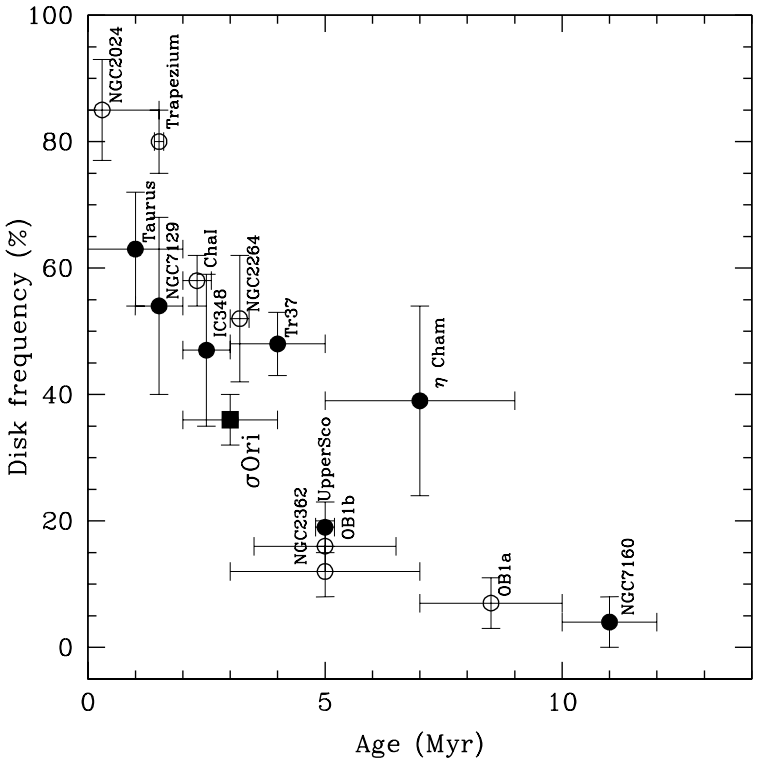

Figure 1.4. The fraction of stars with near-infrared disk emission as a function of the age of the stellar group. Open symbols used J, H, K, and L-band observations to derive the disk frequencies, whereas filled symbols used IRAC 3.6, 4.5, 5.8, and 8.0 μm data to derive the disk frequencies. Figure adapted from Hernández et al. (2007). References for individual data point (from left to right): NGC 2024 (Haisch et al., 2001), Taurus (Hartmann et al., 2005), Trapezium (Haisch et al., 2001), NGC 7129 (Gutermuth et al., 2004), Chamaeleon I (Gómez & Kenyon, 2001), IC 348 (Lada et al., 2006), andσ Ori (Hernández et al., 2007), NGC 2264 (Haisch et al., 2001), Tr 37 (Sicilia-Aguilar et al., 2006), Upper Scorpius (Carpenter et al., 2006), NGC 2362 (Haisch et al., 2001), OB 1b (Hernández et al., 2005), η Chameleontis (Megeath et al., 2005), OB 1a (Hernández et al., 2005), and NGC 7160 (Sicilia-Aguilar et al., 2006).

sound speed of the heated gas becomes comparable to the Keplerian speed: $c_s \simeq \sqrt{GM_*/R}$. Considering photons that have large enough energy to ionize hydrogen atoms and heat the surface layer, which is applicable to Extreme-UV (EUV) with 13.6 eV $< h\nu <$ 100 eV and X-rays with $h\nu >$ 100 eV, the ionized surface layer reaches a nearly isothermal temperature of $T \sim 10^4$ K (e.g. Hollenbach et al., 1994; Owen et al., 2010, 2012). Around a solar-mass star, the corresponding sound speed of $c_s \simeq 9$ km s^{-1} provides a characteristic radius $R_g \simeq 10$ AU beyond which the sound speed of heated gas exceeds the local Keplerian speed. The disk beyond R_g can thus lose mass if the region does not keep replenished by the accretion from

the outer disk.

Hydrodynamic and radiation-hydrodynamic models of photoevaporation show that the mass loss rate from the photoevaporative winds ranges $\sim 10^{-11}$–10^{-7} $M_\odot$ yr^{-1} (Hollenbach et al., 1994; Clarke et al., 2001; Alexander et al., 2006; Ercolano et al., 2009; Gorti & Hollenbach, 2009; Gorti et al., 2009; Owen et al., 2010, 2011, 2012). The detailed outcome of photoevaporation, such as the radial profile of the mass loss and the total mass loss rate, is dependent upon many factors including the strength and spectrum of the incident radiation field, but note that the mass loss rate can be comparable to or exceed the typical mass accretion rate of T-Tauri stars – $\sim 10^{-9}$–10^{-7} $M_\odot$ yr^{-1} (see review by Hartmann et al. 2016 and references therein). As the star reaches to its final mass, the disk accretion declines and the photoevaporative winds eventually dominate the disk surface density evolution, opening a gap around R_g. Without a resupply of gas from the outer disk, the inner disk ($R \leq R_g$) will be cleared in a viscous timescale – this can be as fast as $\sim 10^5$ years when $\alpha = 0.01$. After the inner disk is cleared the inner edge of the outer disk is directly exposed to the stellar irradiation so it is possible that the photoevaporation can rapidly enlarge the cavity. In Chapter 8, we investigate opening of gaps/cavities and dispersal of protoplanetary disks through photoevaporative winds, by implementing a photoevaporation prescription to a time-dependent disk evolution model developed in Chapter 2, and show that the photoevaporative loss, coupled with a range of initial angular momenta of the protostellar cloud, can indeed explain the observed decline of the disk frequency with increasing age (e.g., Hernández et al., 2007).

1.5 Overview of the Thesis

In Chapter 2, we present one-dimensional models of accretion outbursts. The models use the α parameterization of Shakura & Sunyaev (1973) to realize disk accretion. More specifically, we consider accretion through the GI ($\alpha_{\rm GI}$), MRI ($\alpha_{\rm MRI}$), and residual viscosity in the dead-zone ($\alpha_{\rm rd}$) that can originate from the hydrodynamic turbulence propagated from the MRI-active surface layers: $\alpha = \alpha_{\rm GI} + \alpha_{\rm MRI} + \alpha_{\rm rd}$. We find that the presence of a small but finite residual viscosity in the dead-zone can significantly alter the outburst properties,

including the triggering of outbursts, peak accretion rate, outburst duration, and period between outbursts. In particular, the addition of non-zero $\alpha_{\rm rd}$ can trigger inside-out bursts of accretion, starting at or near the inner edge of the disk, instead of the previously-found outside-in bursts with zero dead-zone viscosity, which originate at a few AU in radius.

In Chapter 3, we extend the one-dimensional outburst model presented in Chapter 2 into two dimensions. This extension allowed us to discard the α parameterization for the GI and to explicitly solve disk self-gravity. We find that GI-driven spiral waves propagate well inside of the gravitationally unstable region ($\sim$5–10 AU) and can heat the inner regions ($\lesssim$ 1 AU) via compressional heating. This heating can thermally trigger the MRI in the otherwise magnetically inert "dead-zone" in the inner disk, which in turn results in a sudden increase in mass accretion rate. We also find that protostellar systems stay in the outbursting phase for less than 15 % of the infall phase, which might explain the small number of known outbursting objects and resolve the luminosity problem introduced in §1.2.3.

Recent ALMA observations revealed sets of bright and dark rings in the circumstellar disk of HL Tau (ALMA Partnership et al., 2015). This is particularly interesting because HL Tau is believed to be still undergoing infall from its natal cloud (e.g., Beckwith et al., 1989), and thus a very young system ($\lesssim$ 1 Myr). If those observed rings are formed due to planets (e.g., Jin et al., 2016), it suggests a surprisingly early formation of planets. In Chapter 4, we propose a new vortex formation mechanism in protoplanetary disks: streams of material infalling from the protostellar envelope. Infall streams generate a steep radial gas pressure gradient near the outer edge of the mass landing on the disk (i.e., centrifugal radius). If the pressure gradient becomes significant enough as infall proceeds, a strong azimuthal velocity shear develops around the centrifugal radius in order to maintain the radial force balance, which then is capable of making the disk unstable against the Rossby wave instability, creating vortices. Using two-fluid calculations which simultaneously simulate gas and dust, we showed that the vortices can efficiently trap dust particles, locally enhancing the dust to gas ratio by a factor of $\gtrsim$ 10 for particles with stopping times of order of orbital time. The results imply that protoplanetary disks can have favorable conditions for vortex formation as early as while they are obtaining mass from their natal clouds. This potentially enhances early formation of planetary cores/planets.

The disk surrounding SAO 206462, an 8 Myr old Herbig Ae star, has recently been reported to reveal two-armed spirals in near-IR scattered light observations (Garufi et al., 2013; Stolker et al., 2016, see the left panel in Figure 1.3), one of which exhibits an abrupt change in its brightness, and a vortex-like asymmetry in sub-mm dust continuum observations (Pérez et al., 2014). In Chapter 5, we carry out two-dimensional, two-fluid gas + dust calculations and suggest that a planetary-mass companion can generate the observed structures. In this model, the planet excites two spiral arms, carves a gap, and creates a vortex at the gap edge. Based on synthetic ALMA observations, we propose that the vortex at the gap edge is responsible for the asymmetry in sub-mm dust continuum. In addition, the scattered light can be boosted when one of the spiral arms passes through the high density vortex region, possibly explaining the abrupt brightness change in the observations.

In Chapter 6, we show that spiral waves in accretion disks, such as the ones driven by gravitational instability or companion bodies, can become unstable to the growth of a parametric instability. This spiral wave instability (SWI) arises as inertial modes, natural oscillations in rotating systems, amplify as they resonantly couple with and extract energy from the propagating background spiral waves. During the non-linear phase of the instability, the growing unstable inertial modes lead to break down of the spiral waves into turbulence.

In Chapter 7, motivated by the SWI in Chapter 6, we examine whether the instability operates on the spiral waves launched by a planetary companion in a circumstellar disk. One of the most important consequence of the instability, in the context of planet formation, is that the SWI-driven turbulence can significantly stir up solid particles. Interior to the orbit of a Jupiter-mass planet, we estimate that the vertical particle stirring associated with the SWI-driven turbulence is $\alpha \sim 10^{-3} - 10^{-2}$, with which particles with sizes up to several centimeters can be vertically dispersed to one gas pressure scale height. This significant particle stirring implies that, if accretion of pebbles introduced in §1.3.1 dominates the growth of terrestrial bodies, the formation of a giant planet in the outer disk can affect the subsequent formation of terrestrial planets and/or their precursor embryos in the disk, as initial conditions for the late-stage gas-free evolution.

In Chapter 8, we examine whether the photoevaporative winds can explain the observed lifetime of circumstellar disks, assuming that protostaller systems form from molecular clouds

that have a range of initial angular momenta. In order to do this, we implement photoevaporation prescriptions of Owen et al. (2012) to the evolutionary model developed in Chapter 2. We show that photoevaporative winds can open gaps/cavities in circumstellar disks, as observed in some circumstellar disks, and can eventually disperse the disks. In addition, we show that the observed decline of the disk frequency with increasing age can be reproduced with this evolutionary model, when the initial angular momenta distribution of the protostellar cloud is skewed toward a slow rotation (the median rotation rate to be ~ 3 % of the breakup angular frequency).

Finally, in Chapter 9, we provide a summary of findings and propose directions for future work.

CHAPTER II

Variable Accretion Outbursts in Protostellar Evolution

2.1 Abstract

We extend the one-dimensional, two-zone models of long-term protostellar disk evolution with infall of Zhu et al. to consider the potential effects of a finite viscosity in regions where the ionization is too low for the magnetorotational instability (MRI) to operate (the "dead zone"). We find that the presence of a small but finite dead zone viscosity, as suggested by simulations of stratified disks with MRI-active outer layers, can trigger inside-out bursts of accretion, starting at or near the inner edge of the disk, instead of the previously-found outside-in bursts with zero dead zone viscosity, which originate at a few AU in radius. These inside-out bursts of accretion bear a qualitative resemblance to the outburst behavior of one FU Ori object, V1515 Cyg, in contrast to the outside-in burst models which more closely resemble the accretion events in FU Ori and V1057 Cyg. Our results suggest that the type and frequency of outbursts are potentially a probe of transport efficiency in the dead zone. Simulations must treat the inner disk regions, $R \lesssim 0.5$ AU, to show the detailed time evolution of accretion outbursts in general and to observe the inside-out bursts in particular. This chapter has been published in the Astrophysical Journal, Volume 764, 141 (2013), in collaboration with Lee Hartmann, Zhaohuan Zhu, and Charles Gammie.

2.2 Introduction

The (re)discovery of the magnetorotational instability (MRI; e.g., Balbus & Hawley, 1998, and references therein), appears to resolve the long-standing problem of the anomalous

viscosity in sufficiently ionized accretion disks. To a crude approximation, this validates the use of Shakura & Sunyaev (1973) "α viscosity" disks, though there are differences in detail (e.g., Balbus & Papaloizou, 1999; Gammie, 1996). Constant α disks have been employed in many situations, including the evolution of pre-main-sequence disks (e.g., Hartmann et al., 1998). However, as pointed out by Gammie (1996), thermal ionization levels in protostellar and protoplanetary disks generally are so low that it is unlikely that the MRI operates everywhere. Gammie suggested that transport in these regions might be limited to surface "active" layers, in which non-thermal ionization (cosmic rays, stellar X-rays) could allow the MRI to operate, while in the central regions of the disk there could be a non-viscous "dead zone". A rich variety of phenomena are thus enabled beyond simple (quasi-steady) viscous disks (Vorobyov & Basu, 2005, 2006, 2007, 2009; Zhu et al., 2010a,b; Martin & Lubow, 2011; Martin et al., 2012a,b).

Gammie (1996) noted that if the MRI-active layer has a roughly constant surface density, the result is a pileup of material in the inner disk which eventually could become gravitationally unstable and result in a rapid burst of accretion, perhaps producing an FU Ori outburst (Hartmann & Kenyon, 1996). While early models of FU Ori accretion events relied on traditional thermal instability (TI) theory (Clarke et al., 1990; Bell & Lin, 1994), Zhu et al. (2007) showed that the rapidly accreting region of FU Ori extends much further in radius from the central star than can be achieved with this theory. The very large amount of mass accreted in one of FU Ori's outbursts ($\sim 10^{-2}\ M_\odot$) over such short timescales ($\sim 10^2$ yr) requires a large amount of material to be present in the disk at relatively small radii. This is a natural result of models in which gravitational instability (GI) triggers the outbursts (Armitage et al., 2001; Vorobyov & Basu, 2006, 2007, 2009; Zhu et al., 2009c, 2010a,b; Martin & Lubow, 2011; Martin et al., 2012a,b).

Zhu et al. (2010b) presented one-dimensional, two-layer evolutionary disk models including infall from a rotating protostellar cloud, and showed that they could qualitatively reproduce the main features of the outbursts of FU Ori and V1057 Cyg, with rapid rise times and slowly-decaying accretion. The simulations included irradiation from the central star, but did not take into account the accretion luminosity, which during outbursts can be far larger than the stellar photospheric radiation. While the geometry of disk accretion may

not favor self-irradiation (Bell, 1999), during infall the dusty opaque envelope will act as a blanket, reradiating a significant portion of the accretion luminosity toward the disk. In addition the Zhu et al. (2010b) calculations assumed that the central layer – the dead zone – had no viscosity unless it became gravitationally unstable. However, detailed shearing box simulations of the MRI in disks with a stratified structure and a resistivity that increases toward the midplane indicate that MHD turbulence generated in the upper MRI-active layers produces some hydrodynamic turbulence in the inactive layers (Fleming & Stone, 2003; Okuzumi & Hirose, 2011; Gressel et al., 2012). Furthermore, these investigations suggest that this turbulence creates Maxwell stresses, which result in a small but non-zero viscosity that can transport angular momentum outward and thus mass inward.

These considerations motivate further investigations of protostellar accretion using the two-layer one-dimensional model. We find that the position and properties of the inner boundary, the inclusion of irradiation by the accretion luminosity generated in the inner disk, and any non-zero dead zone viscosity have significant effects on the resulting bursts of mass accretion. Our treatment is sufficiently limited to preclude detailed predictions, but the qualitative behavior is suggestive, given that continuing observations of protostars and pre-main-sequence stars are increasingly found to exhibit a wide variety of accretion events, beyond the large FU Ori outbursts (Hartmann & Kenyon, 1996; Herbig, 2008; Muzerolle et al., 2005; Reipurth & Aspin, 2010; Aspin et al., 2010; Covey et al., 2011; Lorenzetti et al., 2012).

2.3 Methods

We use a modified version of the one-dimensional, two-zone disk model previously introduced in Zhu et al. (2010a,b), including changes to the infall model, enhanced disk heating, and viscosity in the dead zone. Here we review our scheme.

2.3.1 Surface Density Evolution

The surface density of a disk is evolved based on the mass and angular momentum conservation equations in cylindrical coordinates,

$$2\pi R\frac{\partial \Sigma_i}{\partial t} - \frac{\partial \dot{M}_i}{\partial R} = 2\pi g_i(R,t) \tag{2.1}$$

and

$$2\pi R\frac{\partial}{\partial t}(\Sigma_i R^2\Omega) - \frac{\partial}{\partial R}(\dot{M}_i R^2\Omega) = 2\pi\frac{\partial}{\partial R}(R^2 W_{R\phi,i}) + 2\pi\Lambda_i(R,t), \tag{2.2}$$

where Σ_i is the surface density, Ω is the angular frequency, $\dot{M}_i$ is the radial mass flux, $W_{R\phi,i} = R\Sigma_i\nu_i d\Omega/dR$, and ν_i is the viscosity. The subscript i denotes either the active layer ("a") or dead zone ("d"). The terms $2\pi g_i(R,t)$ and $2\pi\Lambda_i(R,t)$ are the mass and angular momentum flux per unit distance of infall material from an envelope cloud (Cassen & Moosman, 1981). Then, assuming instantaneous centrifugal balance (see Zhu et al. 2010b), Equations (2.1) and (2.2) can be simplified to

$$\dot{M}_i = 6\pi R^{1/2}\frac{\partial}{\partial R}(R^{1/2}\Sigma_i\nu_i) + \frac{2\pi R^2\Sigma_i}{M_R}\frac{\partial M_R}{\partial t} - 4\pi\left(\frac{R}{GM_R}\right)^{1/2}(\Lambda_i(R,t) - g_i(R,t)R^2\Omega(R)), \tag{2.3}$$

where M_R is the sum of the mass of the central star and the disk mass within R. We then sequentially solve Equations (2.3) and (2.1) to evolve the disk.

In Zhu et al. (2010b), mass and angular momentum were added to the disk using the infall model of Cassen & Moosman (1981),

$$g(R,t) = \frac{\dot{M}_{\rm in}}{4\pi R_c}\left(1 - \frac{R}{R_c}\right)^{-1/2} \text{ if } R \le R_c, \tag{2.4}$$

$$g(R,t) = 0 \text{ if } R > R_c, \tag{2.5}$$

and

$$\Lambda(R,t) = g(R,t)R\left(\frac{GM_c}{R_c}\right)^{1/2} \text{ if } R \le R_c, \tag{2.6}$$

$$\Lambda(R,t) = 0 \text{ if } R > R_c. \tag{2.7}$$

Here R_c is the centrifugal radius, that is, the outer radius at which mass is added to the disk at time t, and $\dot{M}_{\rm in} = 0.975 c_s^3/G$ is a constant total infall mass rate at a given cloud temperature (Shu, 1977; Terebey et al., 1984). However, this model has a singularity at $R = R_c$; with finite grids this potentially causes non-convergent behavior at different grid resolutions. To avoid this we modified the infall model to eliminate the singularity by using a constant mass flux per unit distance.

Another problem occurs at the inner boundary, which is difficult to make very small because for numerical reasons (short time steps, dust evaporation, etc.) as well as fundamental uncertainties; for example, is the disk truncated by a stellar magnetosphere, and if so where, and is there an outflow from the inner disk edge. In addition, mass infall right at the inner boundary produces different results depending on on precisely which inner boundary radius we choose. To minimize these problems we take inner boundary radii which are relatively small but still comfortably outside the expected point of magnetospheric truncation. We further assume that envelope material does not fall onto the disk inside $0.2R_c$, justified on the basis that the well-known emergence of jets and outflows seen in even the earliest protostellar phases should prevent the lowest-angular momentum material from reaching the disk or star (Reipurth & Bally, 2001). By tying the inner radius of infall to R_c we effectively assume that the same streamline denotes the boundary between outflow and inflow, such that the outflow cone retains the same opening angle, in this case, a half-angle of 26.°6. This particular choice of opening angle is arbitrary and adopted mainly for numerical convenience.

The mass infall rate of the modified model is

$$g(R,t) = \frac{\dot{M}_{\rm in}}{2\pi R_c} \text{ if } 0.2R_c \le R \le R_c \tag{2.8}$$

and

$$g(R,t) = 0 \text{ if } R < 0.2R_c \text{ or } R > R_c. \tag{2.9}$$

The corresponding angular momentum added to the disk per unit distance is

$$\Lambda(R,t) = g(R,t) R \left(\frac{GM_c}{R_c}\right)^{1/2} \text{ if } 0.2R_c \le R \le R_c \tag{2.10}$$

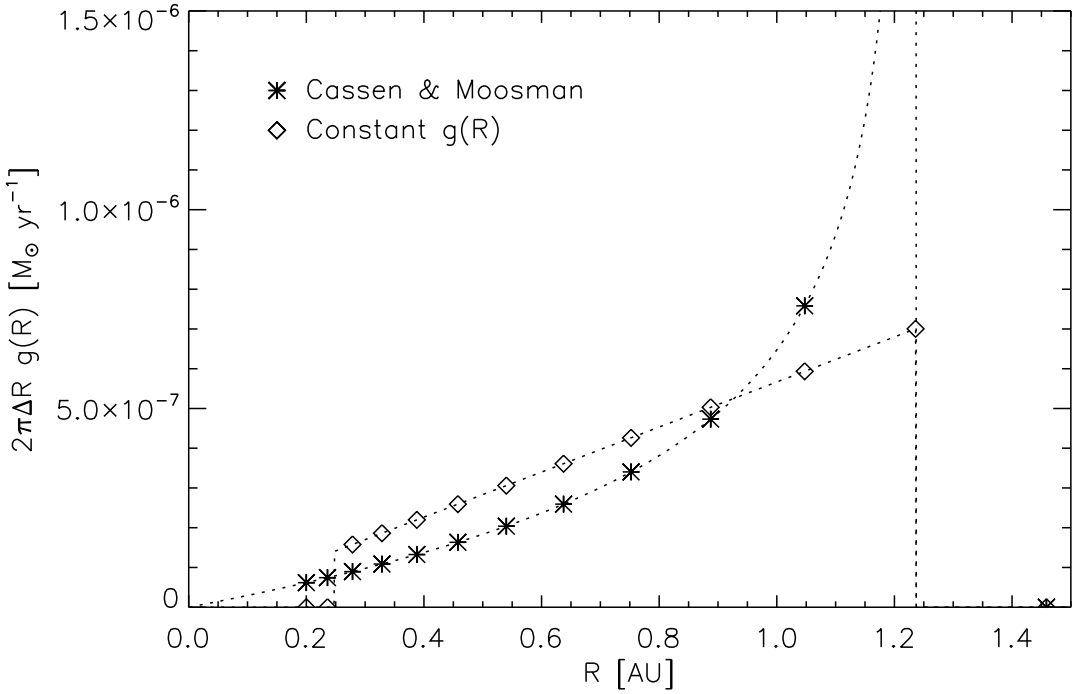

Figure 2.1. The mass infall rate at $t = 0.05$ Myr of Cassen & Moosman (1981) model (asterisks) and our constant $g(R)$ model (diamonds). The centrifugal radius at the time is $R_c \sim 1.24$ AU. Cassen & Moosman (1981) model gives $\sim 1.3 \times 10^{-5}\ M_\odot\ \mathrm{yr}^{-1}$ of mass infall rate at the nearest grid to R_c, which is about an order of magnitude large to be fitted in the figure. The mass infall rate inside 0.2 R_c is set to zero in our model to imitate protostellar outflows (see the text). Dotted curves show analytic estimates of the mass infall rate of each model.

and

$$\Lambda(R,t) = 0 \text{ if } R < 0.2R_c \text{ or } R > R_c. \tag{2.11}$$

A comparison of the radial mass infall profile of our model to that of the Cassen & Moosman (1981) model is presented in Figure 2.1. In total, our model adds 11 % less angular momentum to the disk per unit mass infall than the Cassen & Moosman (1981) model. These modifications result in better convergence with increasing grid resolution.

2.3.2 Temperature Evolution

The disk layer temperatures are determined by the balance between heating and radiative cooling. For the active layer, the energy equation is

$$\begin{aligned} C_{\Sigma,a}\partial_t T_a &= Q_{\mathrm{heat},a} - Q_{\mathrm{cool},a} \\ &= Q_{\mathrm{vis},a} + Q_{\mathrm{infall},a} + Q_{\mathrm{grav},a} + \frac{16}{3}\sigma\left(T_{\mathrm{ext}}^4 \frac{\tau_a}{1+\tau_a^2} + T_d^4 \frac{\tau_d}{1+\tau_d^2}\right) \\ &- \frac{16}{3}\sigma T_a^4 \left(\frac{\tau_a}{1+\tau_a^2} + \frac{\tau_d}{1+\tau_d^2}\right), \end{aligned} \tag{2.12}$$

where $C_{\Sigma,a} = \Sigma_a c_{s,a}^2/T_a$ is the heat capacity of the active layer. Here T_{ext} characterizes the heating flux due to the irradiation of the disk by the stellar and (inner disk) accretion luminosity, and τ_a and τ_d are the optical depths of the active layer and the dead zone, respectively,

$$\tau_a = \frac{1}{2}\Sigma_a \kappa(\rho_a, T_a) \tag{2.13}$$

and

$$\tau_d = \frac{1}{2}\Sigma_d \kappa(\rho_d, T_d) \tag{2.14}$$

using the Rosseland mean opacity κ taken from Zhu et al. (2009a). In Equation (2.12), the first three terms are local heating of the active layer due to the viscosity, the infall, and the gravitational potential energy change, respectively. The fourth term consists of the external heating (see below) and the radiative heating from the underlying dead zone. The last term includes the radiative cooling toward each side of the active layer.

The energy equation of the dead zone is similar to that of the active layer,

$$C_{\Sigma,d}\partial_t T_d = Q_{\mathrm{heat},d} - Q_{\mathrm{cool},d}, \tag{2.15}$$

where $C_{\Sigma,d} = \Sigma_d c_{s,d}^2/T_d$ is the heat capacity of the dead zone. If the active layer is optically thick, the energy equation is

$$C_{\Sigma,d}\partial_t T_d = Q_{\mathrm{vis},d} + Q_{\mathrm{infall},d} + Q_{\mathrm{grav},d} + \frac{16}{3}\sigma T_a^4 \frac{\tau_d}{1+\tau_d^2} - \frac{16}{3}\sigma T_d^4 \frac{\tau_d}{1+\tau_d^2}. \tag{2.16}$$

On the other hand, if the active layer is optically thin, the incident flux from the outside of the dead zone would be $\sigma(\tau_a T_a^4 + T_{\rm ext}^4)$ so that the energy equation is

$$C_{\Sigma,d}\partial_t T_d = Q_{{\rm vis},d} + Q_{{\rm infall},d} + Q_{{\rm grav},d} + \frac{16}{3}\sigma(\tau_a T_a^4 + T_{\rm ext}^4)\frac{\tau_d}{1+\tau_d^2} - \frac{16}{3}\sigma T_d^4 \frac{\tau_d}{1+\tau_d^2}. \quad (2.17)$$

Again, the first three terms in Equations (2.16) and (2.17) represent local heating, while the last two terms account for radiative heating from the outside of the dead zone and the radiative cooling.

In the energy equations, the viscous heating is

$$Q_{{\rm vis},i} = \frac{3}{2} W_{R\phi,i}\Omega, \quad (2.18)$$

where $W_{R\phi,i} = (3/2)\Sigma_i \nu_i \Omega$ and $\nu_i = \alpha_i c_{s,i}^2/\Omega$. The viscosity parameter α_i is explained in detail in the next section.

During infall the added material has smaller specific angular momentum than the disk material at the same radius. This results in a readjustment of the disk such a way that material moves inward. As we are assuming effectively instantaneous centrifugal balance, the increase in the gravitational potential energy driven by the readjustment process must be accompanied by the corresponding energy release. Here we assume that this heats the active layer only ($Q_{{\rm infall},d} = 0$), as this is the material directly impacted by the infalling matter. The heating by infalling material is then

$$Q_{{\rm infall},a} = \frac{GM_*\dot{M}_{\rm in}}{4\pi R_c^3}\frac{3 - 2\sqrt{(R/R_c)}}{(R/R_c)^2} \text{ if } 0.2R_c \le R \le R_c \quad (2.19)$$

and

$$Q_{{\rm infall},a} = 0 \text{ if } R < 0.2R_c \text{ or } R > R_c. \quad (2.20)$$

As accretion proceeds, the central stellar mass increases and the disk gravitational potential energy will become more negative. In response, even in the absence of viscosity disk material will move inward, implying additional accretion luminosity. The heating by this

effect is

$$Q_{\mathrm{grav},i} = \frac{G\dot{M}_*\Sigma_i}{2R}, \tag{2.21}$$

where $\dot{M}_*$ is change in the mass of the central star.

The irradiation flux can be written as

$$\sigma T_{\mathrm{ext}}^4 = \frac{f_* L_*}{4\pi R^2} + \frac{f_{\mathrm{acc}} L_{\mathrm{acc}}}{4\pi R^2} + \sigma T_{\mathrm{env}}^4, \tag{2.22}$$

where L_* and L_{acc} are the stellar luminosity and the accretion luminosity, respectively, and T_{env} is the envelope cloud temperature. The coefficients f_* and f_{acc} account for the non-normal irradiation of the disk surface. For the stellar irradiation we use $f_* = 0.1$ as in Zhu et al. (2010a) and assume that the stellar luminosity follows the mass–luminosity relation

$$\log\left(\frac{L_*}{L_\odot}\right) = 0.20 + 1.74\log\left(\frac{M_*}{M_\odot}\right) \tag{2.23}$$

which is an approximate power-law fit to pre-main-sequence stars in the Taurus molecular cloud, using the luminosities and effective temperatures from Kenyon & Hartmann (1995), and adopting the Siess et al. (2000) evolutionary tracks to obtain the masses. The mass–luminosity relation is slightly modified from Zhu et al. (2010b).

The inclusion of external heating by inner disk accretion is another new feature of our calculations. The accretion luminosity is calculated as

$$L_{\mathrm{acc}} = \frac{GM_*\dot{M}}{2R_\odot}, \tag{2.24}$$

where we assume a typical T Tauri stellar radius. In this case the appropriate value of f_{acc} is quite uncertain. At low to moderate accretion rates, magnetospheric accretion onto the star can occur at high latitudes, so that adoption of $f_{\mathrm{acc}} = 0.1$, similar to that used for the stellar photospheric irradiation, seems reasonable. On the other hand, at high accretion rates, the spectra of FU Ori objects provide no indication of magnetospheric accretion (Hartmann & Kenyon, 1996), and irradiation of the outer disk by a relatively flat inner disk should be much less effective (Bell, 1999). However, if a substantial infalling envelope surrounds the

disk, it can capture much of the accretion luminosity and reradiate a significant part toward the disk (Natta, 1993; D'Alessio et al., 1997). We therefore use both $f_{\rm acc} = 0.1$ and 0.01 to examine the importance of this heating.

The last term in Equation (2.22) is the flux from the envelope cloud whose temperature is assumed to 20 K. Thus, the stellar luminosity irradiation Q_* and the accretion luminosity irradiation $Q_{\rm acc}$ on the active layer become

$$Q_* = \frac{16}{3}\frac{f_* L_*}{4\pi R^2}\frac{\tau_a}{1+\tau_a^2} \tag{2.25}$$

and

$$Q_{\rm acc} = \frac{16}{3}\frac{f_{\rm acc} L_{\rm acc}}{4\pi R^2}\frac{\tau_a}{1+\tau_a^2}. \tag{2.26}$$

We note that the accretion luminosity irradiation $Q_{\rm acc}$ should be distinguished from the local viscous accretion heating $Q_{\rm vis}$. The relative importance of the individual heating terms, and their effects, during disk evolution will be discussed in §2.4.

2.3.3 Disk Viscosity

The viscosity parameter α_i is the sum of the MRI viscosity parameter $\alpha_{M,i}$ and the GI viscosity parameter $\alpha_{Q,i}$. The MRI viscosity parameter is assumed to have a fixed value of $\alpha_{\rm MRI}$ only if a region can sustain the MRI. Thus, the active layer viscosity parameter is always set to $\alpha_{M,a} = \alpha_{\rm MRI}$ while the dead zone has MRI viscosity only if the midplane temperature is higher than a critical temperature $T_{\rm MRI}$ to produce sufficient ionization levels. For the dead zone, we consider a residual viscosity as well as MRI viscosity and GI viscosity, $\alpha_d = \alpha_{M,d} + \alpha_{Q,d} + \alpha_{\rm rd}$.

The idea of the dead zone residual viscosity (DZRV) $\alpha_{\rm rd}$ is based on recent numerical magnetohydrodynamic simulations suggesting that magnetic turbulence in the active layers can drive hydrodynamic turbulence in the dead zone, implying a non-zero residual viscosity parameter $\sim 10^{-3}$ to 10^{-5} (Bai & Stone 2011; Okuzumi & Hirose 2011; Gressel et al. 2012). Thus, for non-zero DZRV model we set

$$\alpha_{\rm rd} = \min\left(10^{-4},\ f_{\rm rd}\alpha_{\rm MRI}\frac{\Sigma_a}{\Sigma_d}\right), \tag{2.27}$$

where $f_{\rm rd}$ is the efficiency of accretion in the dead zone whose value is chosen to be ≤ 1; this is intended to limit the effect of the active-layer induced turbulence such that the mass accretion rate of the dead zone (approximately) does not exceed that of the active layer ($\dot{M}_d \leq \dot{M}_a$). This seems intuitively reasonable. We consider the upper limit $f_{\rm rd} = 1$ and consider a case with $f_{\rm rd} = 0.1$ as it is unlikely that the active layer can be that effective in driving accretion.

Finally, the GI viscosity parameter is the same as in Zhu et al. (2010a),

$$\alpha_{Q,i} = e^{-Q^2}, \tag{2.28}$$

where Q is the Toomre parameter.

2.4 Results

2.4.1 Initial Conditions

We start with a 0.1 $M_\odot$ central protostar surrounded by an $M_c = 1$ $M_\odot$ cloud. We parameterize the cloud rotation in terms of $\omega = \Omega_c/\Omega_{\rm b}$, where Ω_c is the (constant) angular frequency of the initial cloud, and $\Omega_{\rm b} = 2^{3/2}c_s^3/GM_{\rm c}$ is the breakup angular frequency at the outer cloud edge, and c_s is the (uniform) cloud sound speed. Our fiducial models assume $\omega = 0.03$, which results in ~ 15 % larger cloud angular frequency than that used in the fiducial model of Zhu et al. (2010b) ($\Omega_c \sim 1.15 \times 10^{-14}$ rad s^{-1} in our model). We set the maximum non-thermally ionized surface density Σ_A to 100 g cm^{-2} for our fiducial choice and assume that it is constant. We assume $T_{\rm MRI} = 1500$ K and $\alpha_{\rm MRI} = 0.01$ for all calculations. We adopt a cloud envelope temperature of $T_{\rm env} = 20$ K, which yields a constant infall rate of $\sim 3.4 \times 10^{-6}$ $M_\odot\,{\rm yr}^{-1}$. This is 20 % smaller than the infall rate for conventional singular isothermal collapse model (Shu, 1977) because of our modified infall model (see §2.3.1). The infall lasts for ~ 0.24 Myr, adding 0.8 $M_\odot$ to the central star + disk in total.

2.4.2 Zero Dead Zone Viscosity Model

Zhu et al. (2010a) found that GI moves matter from the outer disk to the inner disk, leading to a pileup at $R \sim 2$ AU because GI is increasingly ineffective at small radii. Eventually enough material piles up to trap thermal energy that makes $T_d > T_{\rm MRI}$, turns on the MRI thermally in the dead zone, and thus produces an outburst of accretion. Zhu et al. (2010b) investigated the long-term evolution of such disks and found that the evolution can be divided into three stages. The evolution starts with a quasi-steady disk accretion since the infall is to small radii where the inner disk can become hot enough to sustain the MRI thermally. Then, it turns into the outburst stage as the infall occurs at radii > 1 AU. After infall stops, the disk enters the T Tauri phase, having only a few GI-driven outside-in outbursts with a low mass accretion rate in between bursts.

Figure 2.2 shows the mass accretion rate and the mass of the central star, the disk, and the central star + disk as a function of time. The modified infall model and additional heating sources discussed in §2 produce no qualitative difference in the overall evolution

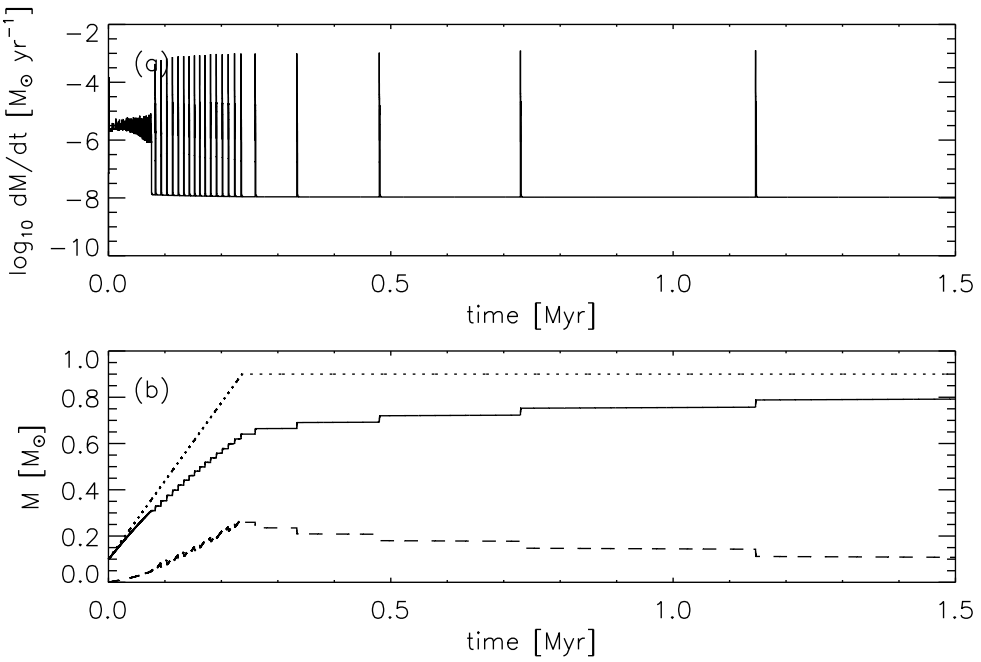

Figure 2.2. (a) Mass accretion rate and (b) mass of the central star + disk (dotted curve), mass of the central star (solid curve), and mass of the disk (dashed curve) with time for the standard zero DZRV model.

from Zhu et al. (2010b).

The new heating sources for the first 0.3 Myr of the evolution at $R = 1$ and 10 AU are presented in Figures 2.3 and 2.4, together with the previously considered sources. In these figures, newly added terms in this Chapter are plotted in color while other terms have considered in Zhu et al. (2010a) and drawn in black. As one can see, heating by the change in gravitational energy is usually several orders of magnitude smaller than other terms so that it makes no change in the evolution. Infall heating provides comparable amount of heat to the active layer but is only limited to the region material falls onto, increasing the local disk temperature slightly. However, the large increase in the accretion luminosity during outburst produces enough irradiation to make the outer disk temperature increase dramatically. This is shown in Figure 2.5, where we show the mass accretion rate during a single outburst and the radial profiles of the disk surface density and the midplane temperature before outburst, at the maximum accretion rate, and at the end of the outburst. The temperature increase at the outer disk during outbursts does not affect the long-term evolution, because the viscous time of the outer regions ($\sim 10^5$ yr) is much longer than the outburst timescale of $\sim 10^3$ yr.

We also call attention to the jump in temperature at radii < 0.5 AU, which is due to TI (Zhu et al., 2010a). This increase in temperature, which affects the behavior of the outburst of accreting material onto the central star, would not have been found if we had taken an inner radius of $\gtrsim 1$ AU (see discussion in §4).

The GI-driven outside-in bursts accrete $\sim 0.027\ M_\odot$ of material onto the central star and last for ~ 1340 years on average. Although the duration obtained in our calculation is longer than the typical outburst timescale seen in FU Ori, the timescale of an outburst can be scaled with a choice of $\alpha_{\rm MRI}$ since $\Delta t_{\rm burst} \sim R^2/\nu \propto \ {\alpha_{\rm MRI}}^{-1}$ (see Zhu et al. 2010a). The outside-in bursts are rare, because the disk needs a lot of material to trigger MRI through GI while it is difficult to do so with zero DZRV. The duty cycle of this model is thus pretty small, ~ 0.06 during outburst stage and ~ 0.005 during T Tauri phase. The details of disk properties at 0.24 and 1 Myr and of outside-in bursts are summarized in Table 2.1. All the outburst quantities in the table are time-averaged values after the initial quasi-accretion phase while those vary with time.

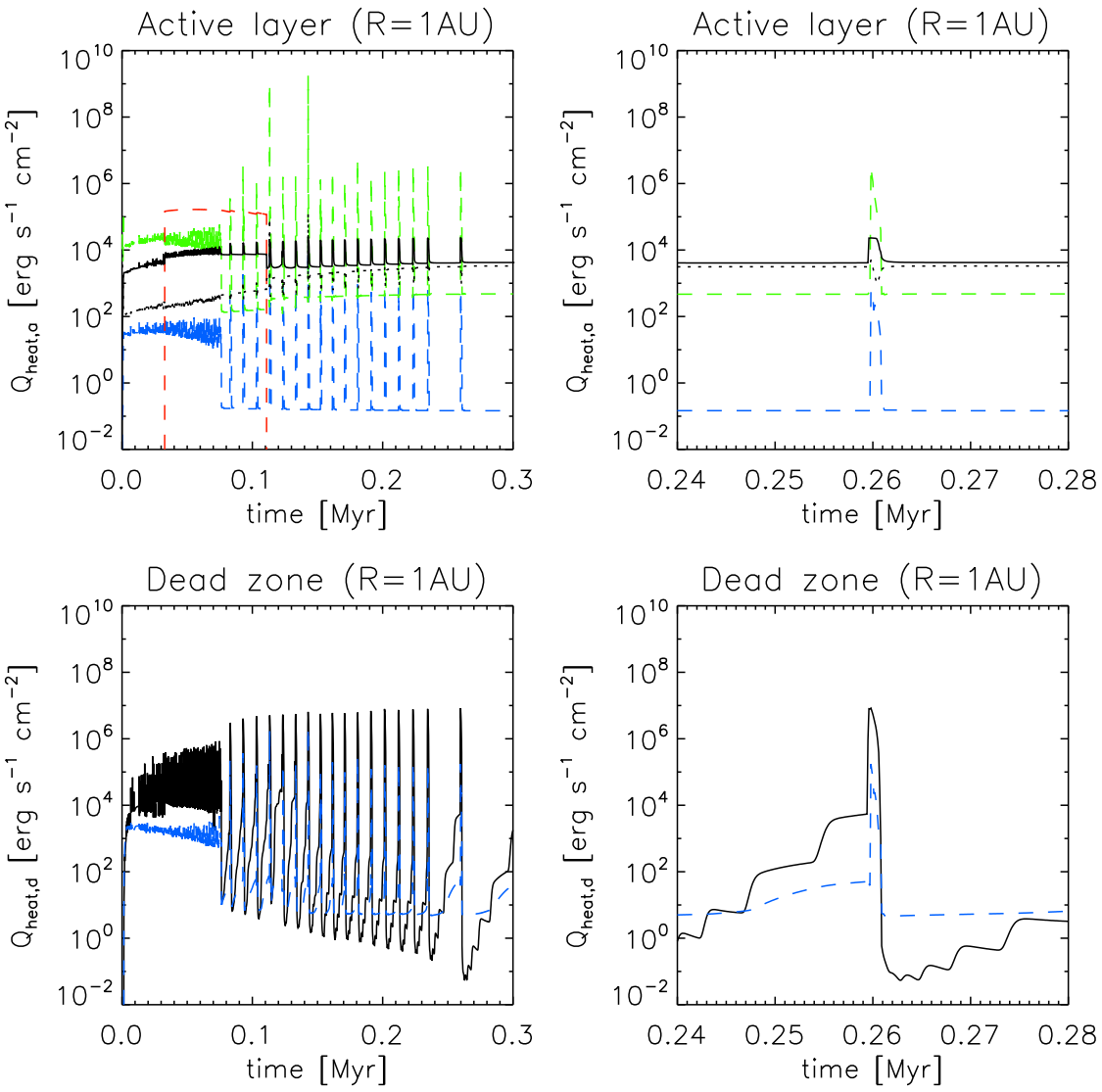

Figure 2.3. Various heating sources of the active layer (upper panels) and the dead zone (lower panels) at $R = 1$ AU for the first 0.3 Myr (left panels) and during a single outburst (right panels) with zero DZRV. Newly added heating sources in this Chapter are plotted in color while the heating sources considered in (Zhu et al., 2010a,b) are presented with black curves. Upper panels: $Q_{\rm vis,a}$ (black solid), Q_* (black dotted), $Q_{\rm infall}$ (red dashed), $Q_{\rm acc}$(green dashed), and $Q_{\rm grav,a}$ (blue dashed) are presented. Lower panels: $Q_{\rm vis,d}$ (black solid) and $Q_{\rm grav,d}$ (blue dashed) are presented.

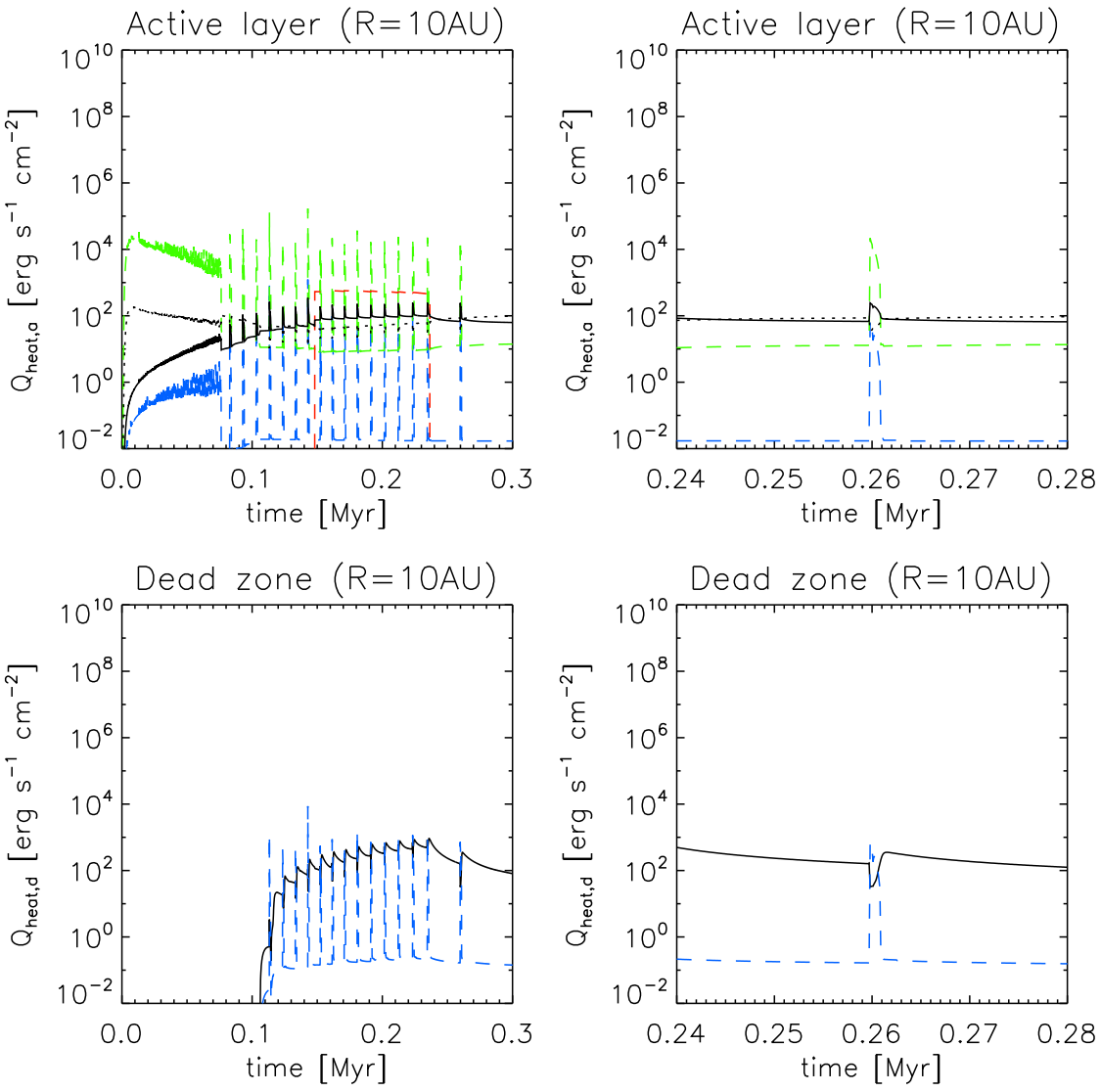

Figure 2.4. Same as Figure 2.3 but at $R = 10$ AU.

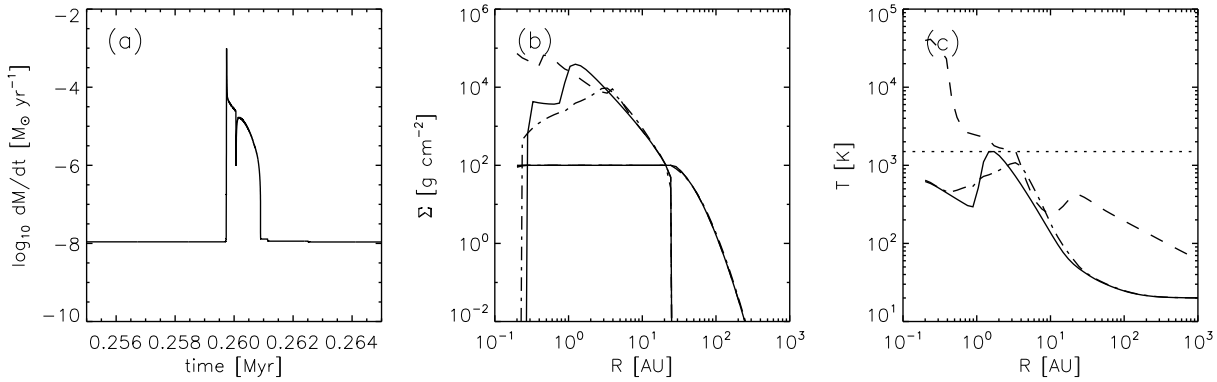

Figure 2.5. (a) Mass accretion rate of a single outburst of the standard zero DZRV model. The "drop out" in accretion during the middle of the outburst is an artifact of the one-dimensional treatment (Zhu et al., 2010a). Radial profiles of (b) the surface densities and (c) the midplane temperatures before the outburst (solid curves), at the maximum accretion rate (dashed curves), and at the end (dash-dotted curves) of the burst are plotted. In panel (b), the curves with higher surface densities at the inner disk represent the dead zone surface density, while the lower ones extend further out represent the active layer. In panel (c), the dotted horizontal line represents the MRI activation temperature $T_{\rm MRI} = 1500$ K.

Table 2.1. Model Parameters and Results for One-dimensional Outburst Calculations

$\alpha_{\rm rd}$	$\alpha_{\rm MRI}$	Σ_A (g cm^{-2})	$R_{\rm dead}$[a] (AU)	M_*[a] ($M_\odot$)	$M_{\rm disk}$[a] ($M_\odot$)	$M_{\rm in}$[a] ($M_\odot$)	$M_{\rm out}$[a] ($M_\odot$)	$M_{\rm burst}$[b] ($M_\odot$)	$\dot{M}_{\rm max}$[b] ($M_\odot$ yr^{-1})	$\Delta t_{\rm burst}$[b] (yr)	D_O[c]	D_T[d]
Zero	0.01	100	29/5.5	0.64/0.76	0.26/0.14	0.21/0.08	0.05/0.06	0.027	1.11×10^{-3}	1340	0.06	0.005
Non-zero	0.01	100	24/6.5	0.65/0.80	0.25/0.10	0.20/0.04	0.05/0.06	1.5×10^{-3}	3.17×10^{-6}	450	0.16	0.06
Zero	0.05	20	33.9/7.6	0.65/0.80	0.25/0.10	0.22/0.08	0.03/0.02	0.028	4.34×10^{-3}	310	0.016	0.002
Non-zero	0.05	20	33.9/7.6	0.65/0.82	0.25/0.08	0.22/0.05	0.04/0.03	4.6×10^{-3}	4.26×10^{-5}	200	0.08	0.015

[a]Quantities are taken at 0.24 and 1 Myr.

[b]Outburst quantities are averaged over time after infall ends.

[c]Duty cycle during outburst stage.

[d]Duty cycle during T Tauri phase.

2.4.3 Non-zero Dead Zone Residual Viscosity Model

While the modified infall model and additional heating sources with zero DZRV make no qualitative change in the overall evolution, a finite DZRV makes a lot of difference in the long-term evolution and in the single outburst behavior as well. Figure 2.6 shows the mass accretion rate and the mass of the central star, the disk, and the central star + disk as a function of time. During infall the disk has a quasi-steady accretion phase at the beginning ($t \lesssim 0.08$ Myr) and the outburst stage follows, as in the zero DZRV case. However, the evolution after the accretion phase is different in that the non-zero DZRV model shows a lot of smaller outbursts instead of a few large outbursts.

Figures 2.7 and 2.8 show the heating sources of active layer and dead zone of the non-zero DZRV model at $R = 1$ and 10 AU, respectively. The major difference between this model and the zero DZRV model is that dead zone viscous heating provides a significant amount of heat at the inner disk even after infall ends. We have run calculations with different $T_{\rm MRI}$

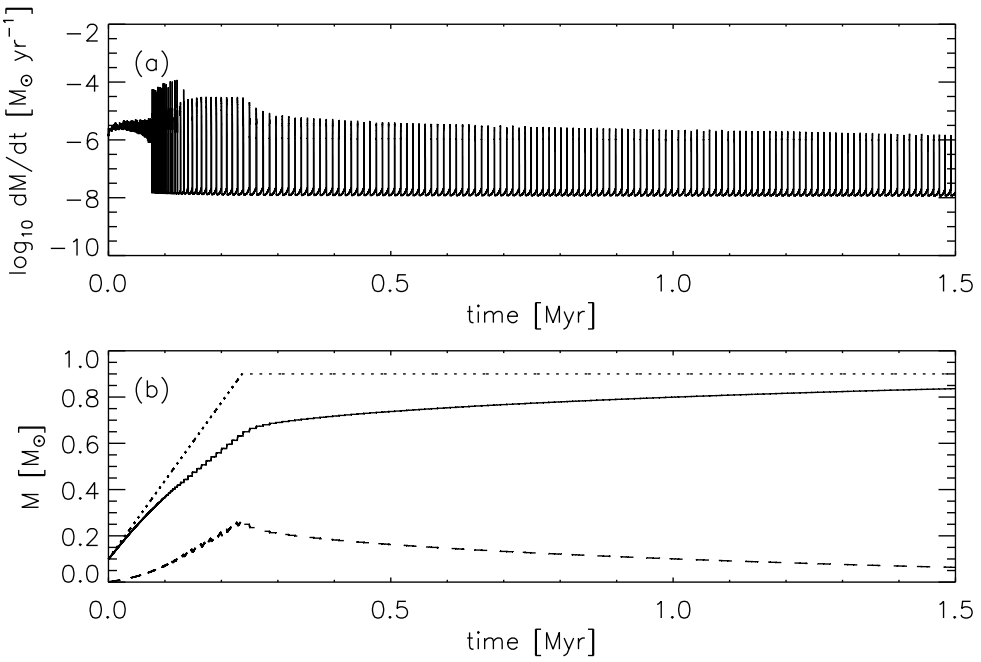

Figure 2.6. (a) Mass accretion rate and (b) mass of the central star + disk (dotted curve), mass of the central star (solid curve), and mass of the disk (dashed curve) with time for the standard non-zero DZRV model.

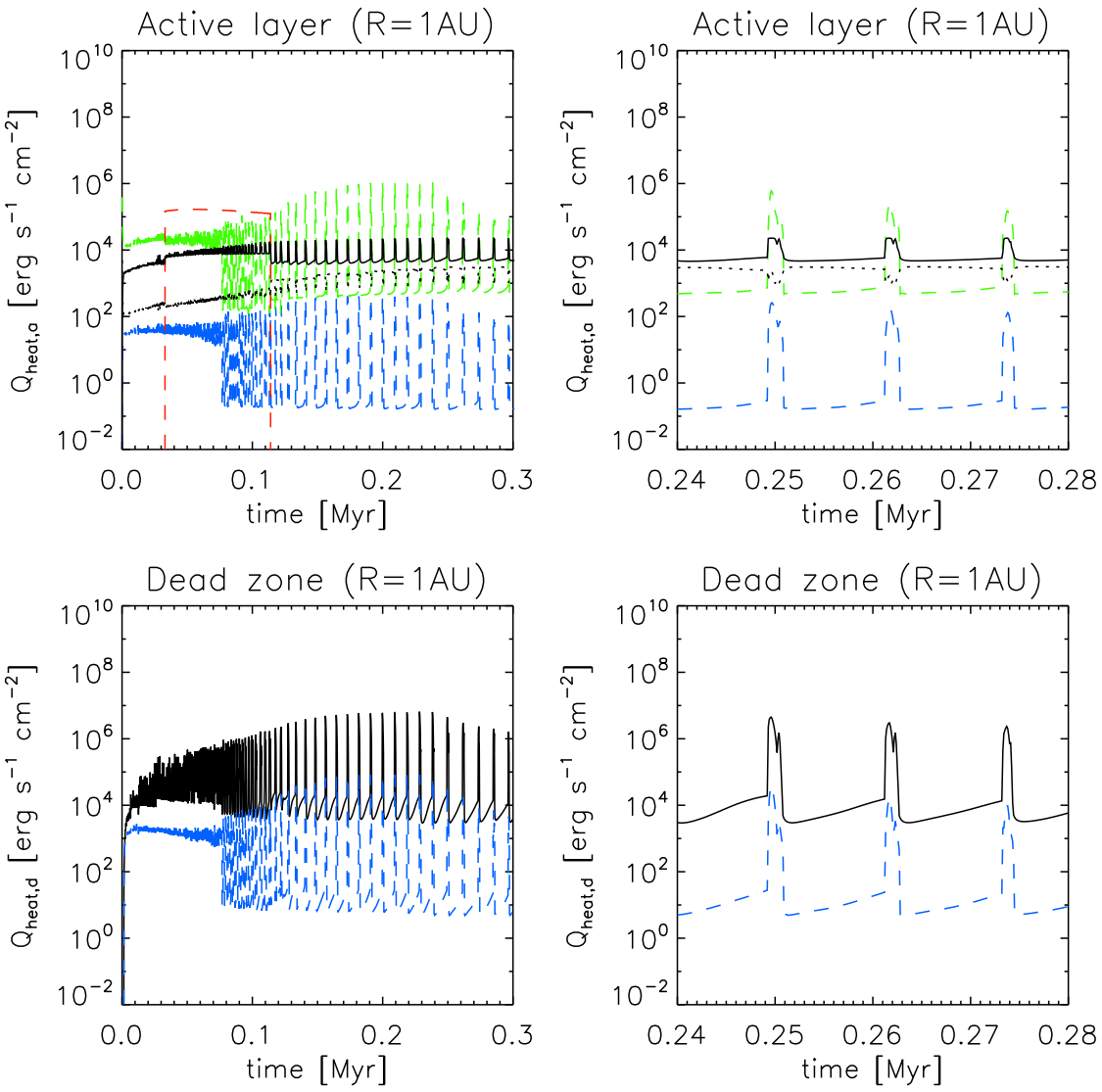

Figure 2.7. Various heating sources of the active layer (upper panels) and the dead zone (lower panels) at $R = 1$ AU for the first 0.3 Myr (left panels) and during a single outburst (right panels) with non-zero DZRV. Newly added heating sources in this Chapter are plotted in color while the heating sources considered in (Zhu et al., 2010a,b) are presented with black curves. Upper panels: $Q_{\rm vis,a}$ (black solid), Q_* (black dotted), $Q_{\rm infall}$ (red dashed), $Q_{\rm acc}$(green dashed), and $Q_{\rm grav,a}$ (blue dashed) are presented. Lower panels: $Q_{\rm vis,d}$ (black solid) and $Q_{\rm grav,d}$ (blue dashed) are presented.

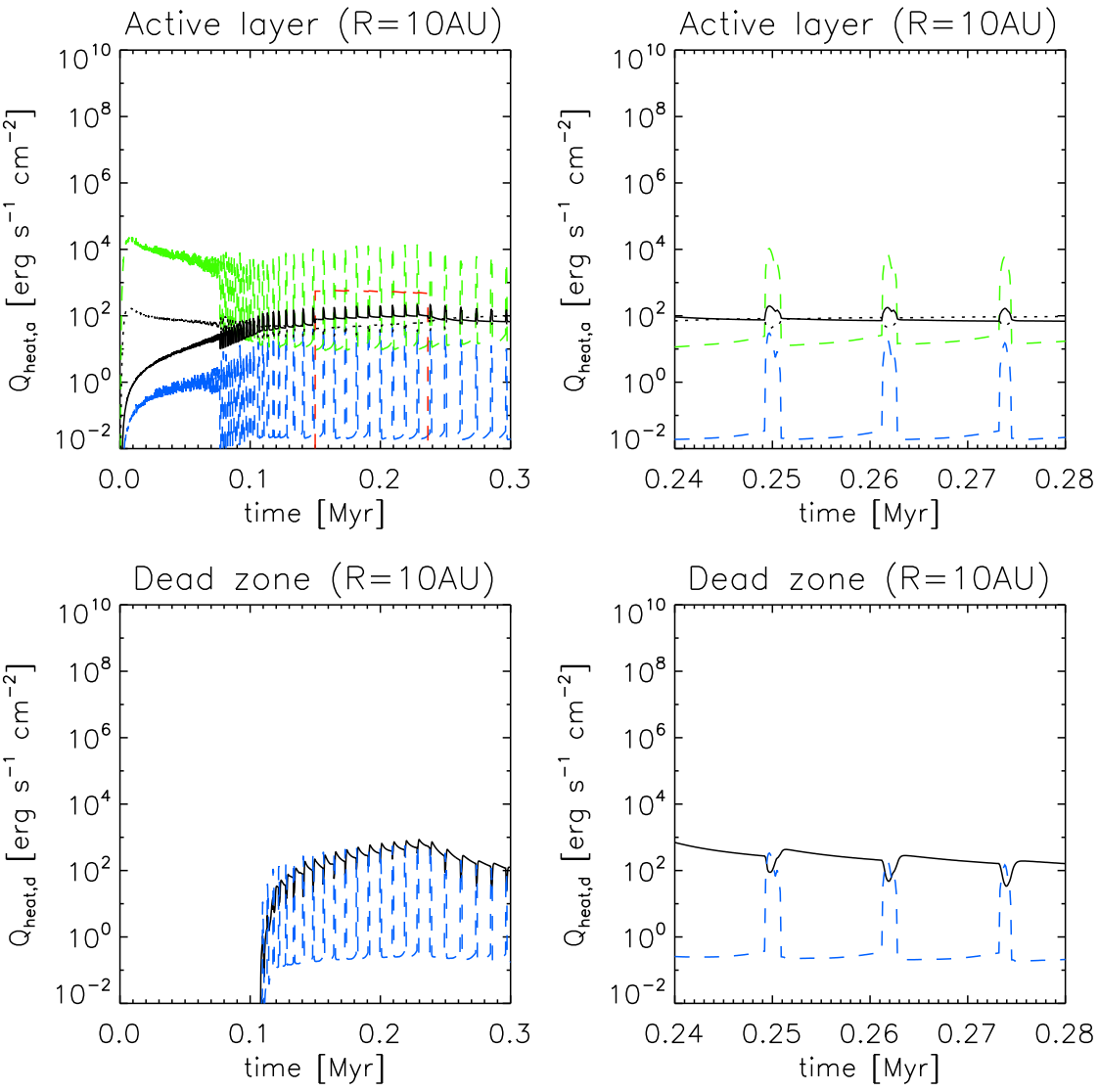

Figure 2.8. Same as Figure 2.7 but at $R = 10$ AU.

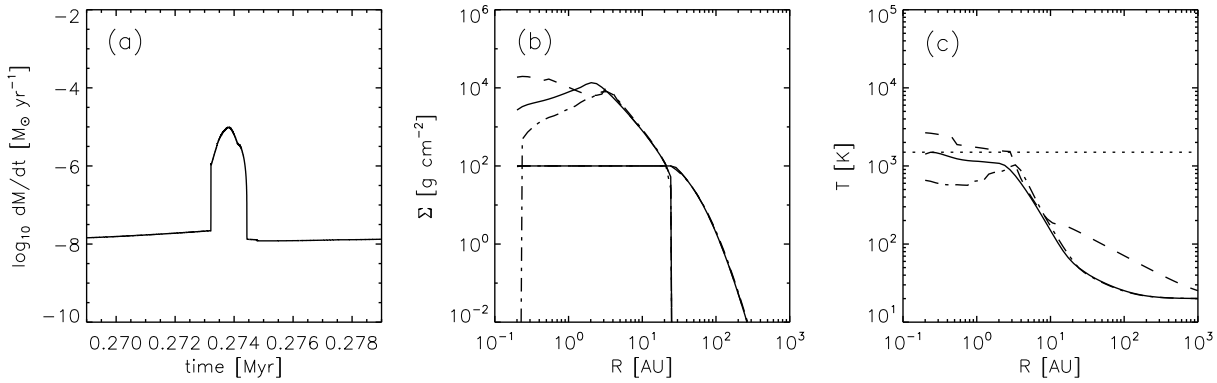

Figure 2.9. (a) Mass accretion rate of a single outburst of the standard non-zero DZRV model. Radial profiles of (b) the surface densities and (c) the midplane temperatures at the beginning (solid curves), at the maximum accretion rate (dashed curves), and at the end (dash-dotted curves) of the burst. In panel (b), the curves with higher surface densities at the inner disk represent the dead zone surface density while the lower ones extend further out represent the active layer. In panel (c), the dotted horizontal line represents the MRI activation temperature $T_{\rm MRI} = 1500$ K.

(1300 K and 1800 K) and found that the overall features are not sensitive to the choice of $T_{\rm MRI}$. At the outer disk, the accretion luminosity irradiation is still important during bursts while the temperature increase is not as dramatic as in the zero DZRV model due to lower accretion peak. Infall and gravitational heating are less important than others.

Figure 2.9(a) shows the mass accretion rate during a single outburst with non-zero DZRV. Radial surface density and midplane temperature profiles at the beginning, at the maximum accretion rate, and at the end of the burst are presented in Figures 2.9(b) and (c). The accretion behavior during a single outburst is remarkably different from that of the zero DZRV model. The outburst has a peak of $\dot{M}_{\rm max} \sim 10^{-5}\ M_\odot\,{\rm yr}^{-1}$, which is about two orders of magnitude smaller than that of the outside-in bursts. In addition, the accretion rate initially shows a rapid increase but has a slow rise time to its peak and a slow decrease after the peak as well. In this model, the dead zone is able to transport material with the help of the non-zero DZRV. Thus, the inner disk can be heated viscously and outbursts are initiated at the inner boundary of the disk before the GI piles up enough material at the middle of the disk ($R \sim 2$ AU) to initiate the MRI, which is the case for outside-in bursts. The ionization front propagates out to several AU from the inner boundary. Since the inside-out bursts have

an MRI active inner boundary from their initiation, the disk continues to dump material from its innermost part during the whole bursts. Therefore, the system is not able to show a huge accretion rate as seen in outside-in bursts, but only generates moderate accretion rate. Note again that the outburst triggers first at small radii, inside of ~ 0.5 AU (§2.5).

On average, the mass accreted onto the central star during a single inside-out burst is $\sim 1.5 \times 10^{-3}\ M_\odot$ and it lasts ~ 450 years. The inside-out bursts occur frequently enough to get a duty cycle of ~ 0.16 during outburst stage and ~ 0.06 during T Tauri phase. The disk properties and outburst details of the non-zero DZRV model are summarized in Table 2.1.

2.4.4 Efficiency of Accretion Luminosity Irradiation

As shown in the previous sections, irradiation by the inner disk plays an important role during outburst on the temperature profile at the outer disk. However, the efficiency of the accretion luminosity irradiation is uncertain as far as the non-normal irradiation of the disk is considered. We thus test the effect of changing $f_{\rm acc}$ to 0.01, which is 10 times smaller than the fiducial value.

We found essentially no change in the overall evolution of both zero and non-zero DZRV cases, since the accretion luminosity irradiation is several orders of magnitude smaller than main heating sources – active layer viscous heating and stellar irradiation – during the quiescent phase. During outbursts, however, the accretion luminosity irradiation still dominates the heating even with a 10 times smaller efficiency, making a significant difference to the outer disk temperature. Not surprisingly, the increase in outer disk temperature during bursts is smaller than the standard cases by a factor of ~ 2.

2.4.5 Accretion Efficiency in Dead Zone

Intuitively, it seems unlikely that the turbulence generated by the active layers within the dead zone can transport as much mass as the active layer (e.g., Hartmann et al., 2006). In our models this happens when $\alpha_{\rm rd} \gtrsim 10^{-4}$, where $\Sigma_d \gtrsim 10^5$ g cm^{-2}. This could be an overestimate of the efficiency with which the MRI turbulence in the active layers drives accretion in the dead zone. We therefore adjust the dead zone accretion efficiency $f_{\rm rd}$ to 0.1 so that dead zone only has an accretion rate of ~ 10 % of the active layer at most.

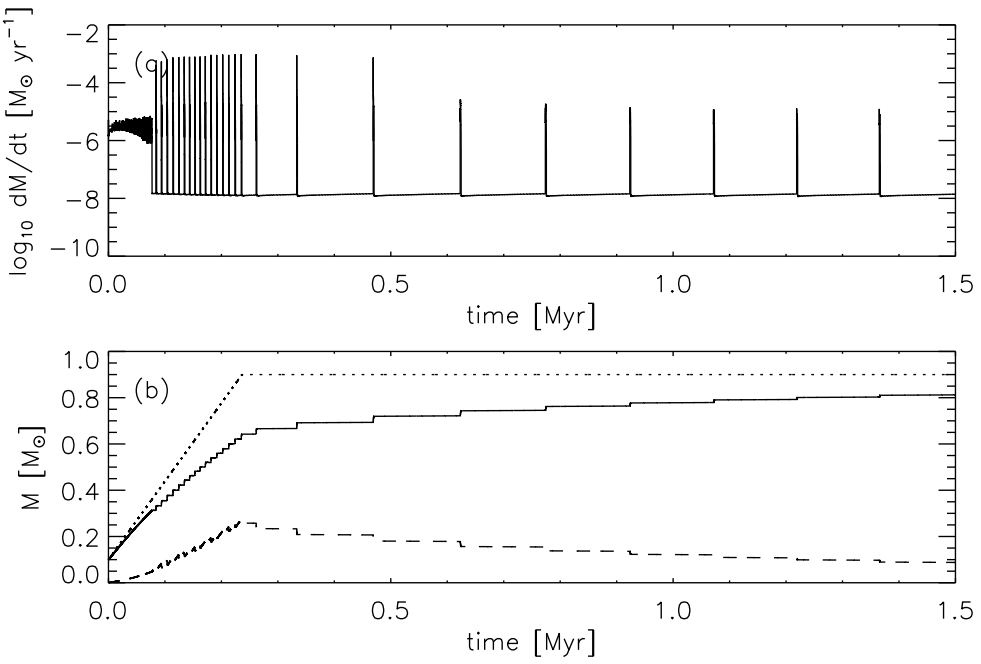

Figure 2.10. (a) Mass accretion rate and (b) mass of the central star + disk (dotted curve), mass of the central star (solid curve), and mass of the disk (dashed curve) of non-zero DZRV model as a function of time, with 10 % of accretion efficiency $f_{\rm rd}$ in the dead zone.

Figure 2.10 shows the mass accretion rate and the mass of the central star, the disk, and the central star + disk as a function of time. Initially, the evolution resembles that of the standard zero DZRV model rather than the non-zero DZRV model; the system shows a distinct outburst phase during infall. This is because the mass that the dead zone can carry is now limited and thus generates less viscous heating at small radii than the standard non-zero DZRV case. Therefore, mass piles up at large radii through the GI before inner disk gets heated and triggers inside-out bursts. After infall ends, however, we still see inside-out bursts with much less frequency than the standard non-zero DZRV model, which is again due to less viscous heating at the inner disk. The duty cycle during T Tauri phase of this model is only 0.015, which is four times smaller than that of the standard non-zero DZRV model. First three outbursts after infall ends are outside-in bursts, since disk already collects enough material at outer disk during infall to make them. This emphasizes importance of understanding the effect of MRI turbulence on dead zones (§2.5).

2.4.6 Dependence on Σ_A and $\alpha_{\rm MRI}$

While we use $\Sigma_A = 100$ g cm^{-2} as our fiducial value, several studies have pointed out that the active layer more likely has a lower surface density (e.g. Sano et al., 2000; Bai & Goodman, 2009). We thus test $\Sigma_A = 20$ g cm^{-2} and adjust the MRI viscosity parameter $\alpha_{\rm MRI} = 0.05$ to maintain roughly the same mass accretion rate ($\dot{M} \propto \alpha\Sigma$) during the quiescent phase as the standard cases (and also in agreement with typical T Tauri accretion rates).

Figure 2.11 shows the mass accretion rates of both zero and non-zero DZRV models adopting the lower value of Σ_A. The mass accretion rate during a single outburst and radial surface density and midplane temperature profiles at the beginning, at the maximum accretion rate, and at the end of a single outburst of the both models are presented in Figure 2.12. Since the outburst timescale depends on the MRI viscosity parameter ($\Delta t_{\rm burst} \propto {\alpha_{\rm MRI}}^{-1}$), the details of the outbursts, such as outburst duration and peak accretion rate, vary. However, the overall evolution as well as the initiation of outbursts remain the same. We see GI-induced MRI-driven outside-in bursts in the zero DZRV case and viscously triggered inside-out bursts in the non-zero DZRV case. This is because the overall evolution and the initiation of outbursts are governed by the mass accretion during the quiescent phase, which we manage to be unchanged. We note that the shorter timescales are in better agreement with FU Ori (see Zhu et al., 2007). The disk properties and outburst details are summarized in Table 2.1.

2.5 Discussion

Our simulations show that it is possible to obtain inside-out triggering of accretion outbursts as well as outside-in bursts (e.g., Zhu et al., 2010a,b), with the former enhanced if there is finite DZRV. The two types of outbursts were also obtained in the model developed by Bell & Lin (1994; BL) for FU Ori outbursts. In the BL model, the outbursts were due to TI, plus an assumed increase in α from a very low value to a much higher value. As Zhu et al. (2007, 2008) showed, the TI model is inconsistent with observations of FU Ori, because the high temperatures required limit the region of rapid accretion to smaller radii than inferred from modeling the spectral energy distribution including *Spitzer Space Telescope*

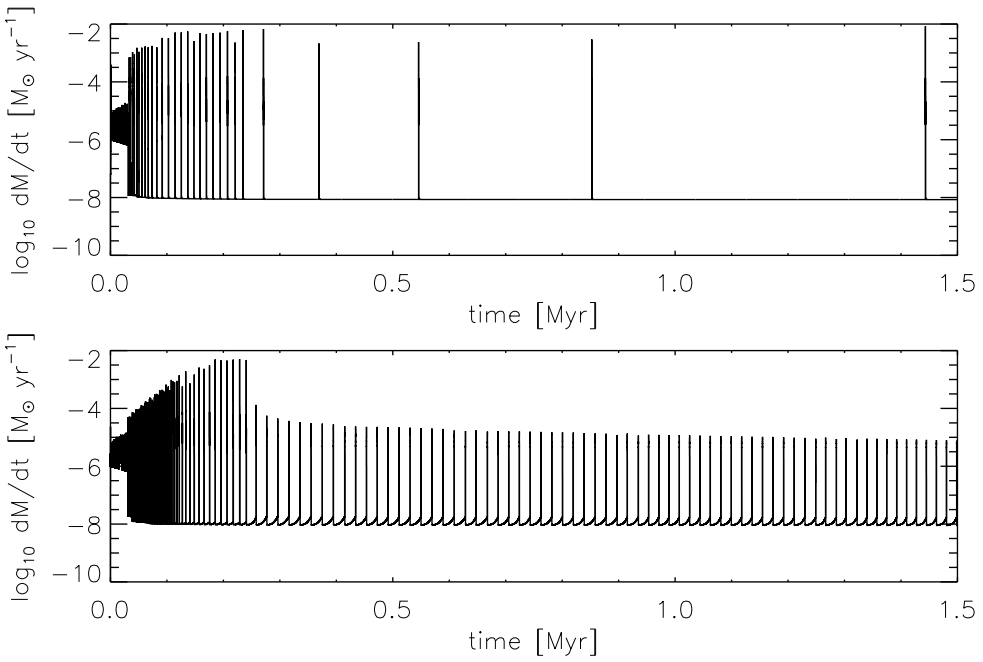

Figure 2.11. Mass accretion rate of zero DZRV model (upper) and non-zero DZRV model (lower) as a function of time, with $\Sigma_A = 20$ g cm^{-2} and $\alpha_{MRI} = 0.05$.

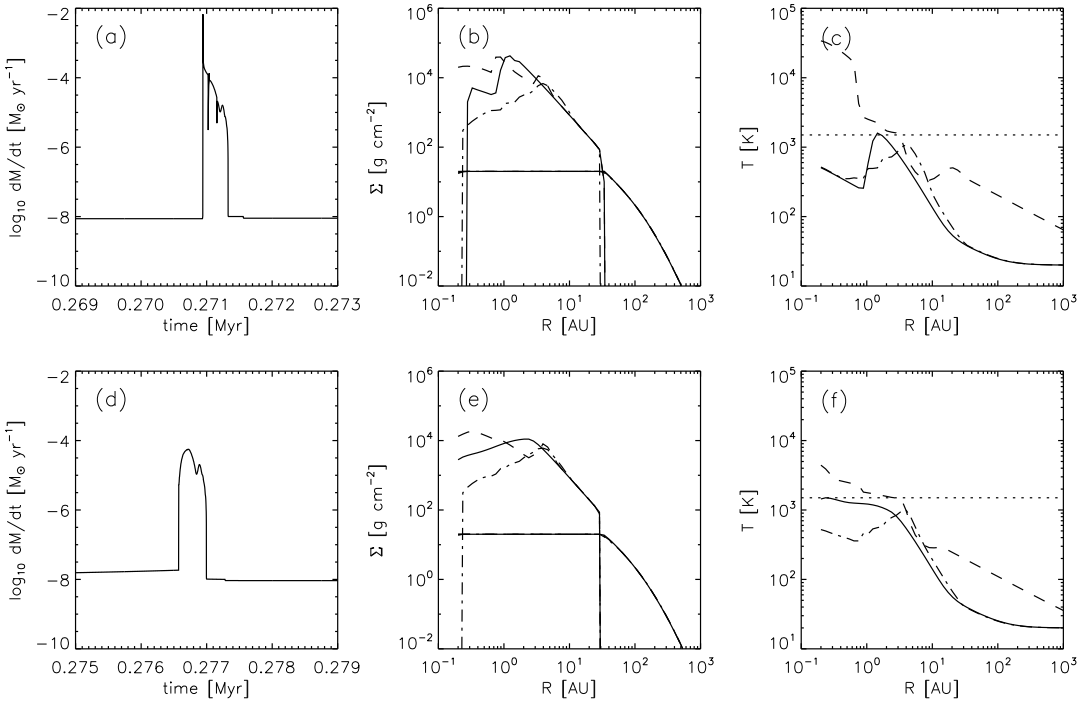

Figure 2.12. Same as Figure 2.5 (upper panels) and 2.9 (lower panels) but with $\Sigma_A = 20$ g cm^{-2} and $\alpha_{MRI} = 0.05$.

data. Nevertheless, the finite DZRV models are qualitatively similar to the basic feature of the BL models which produce inside-out bursts; a small but finite viscosity allows material in the inner disk to produce enough trapping of viscously-generated heat to trigger a higher viscosity and eventually an outburst. As BL showed, such inner disk triggering leads to outbursts with slow rise times, qualitatively consistent with the observed outburst of V1515 Cyg (Herbig 1977; M. Ibrahimov, private communication).

BL showed that outbursts with rapid rise times, such as observed in FU Ori and V1057 Cyg (Herbig, 1977), required outside-in accretion events. In the BL model, a large outer perturbation of the disk was required. In modern models, the event is triggered by GI, which piles up material at larger radii than possible in the TI model (Armitage et al., 2001; Vorobyov & Basu, 2006, 2007, 2009, 2010; Zhu et al., 2010a,b; Martin et al., 2012a,b). Our current results build upon those of Zhu et al. (2010b) in that we clearly identify some inside-out bursts during the main phase of infall (they were actually present in the Zhu et al. simulation as well but were not emphasized).

Our results also bear similarities to outbursts in models of cataclysmic variables (CV). Two different types of outbursts (outside-in and inside-out) in accretion disks around dwarf novae were first predicted by Smak (1984). In CV models, mass transfer from the secondary rises the effective temperature of a disk annulus to 5000–8000 K, which corresponds to hydrogen recombination inside the disk and thus triggers the TI (Menou et al., 1999). While the DZRV parameter is the feature that changes outburst behavior in our model, CV models use the mass transfer rate to generate two different outbursts. If the mass transfer rate is high, the accumulation timescale of transferred material is shorter than the viscous timescale, allowing material piles up at outer disk. Thus, outside-in bursts are triggered. In contrast, if mass transfer rate is low, the accumulation timescale becomes longer than the viscous timescale so that the outbursts outside-in outbursts are replaced by inside-out ones. The resulting outburst behaviors of CV models are similar to ours; inside-out bursts have a smaller accretion peak and a slower rise time than outside-in ones (see Figures 3 and 4 of Hameury et al. 1998).

It is worth emphasizing that the outburst behavior of systems, observed at optical and near-infrared wavelengths, is a result of accretion onto or near the star, i.e. at radial scales

$\lesssim 0.1$ AU. While our models do not reach magnetospheric or stellar radii, our inner boundary radius of 0.2 AU is small enough to capture behavior (TI, inside-out bursts) which cannot be seen in simulations with inner boundaries > 1 AU. Thus, while our own treatment of non-steady accretion has its limitations, time histories of accretion in simulations with large inner disk radii must be treated with special caution. Using an inner boundary of a few AU, as in the series of papers by Vorobyov & Basu (2006, 2007, 2009) or Dunham & Vorobyov (2012), one would not find the outburst behavior characterized by our models or those of Armitage et al. (2001) or Martin et al. (2012a,b).

Along these lines, we have found that the precise duration of the inside-out bursts during infall is sensitive function of the value of the inner radius. We do not explore this further here because there are other major uncertainties in our treatment, such as the assumption of a constant active layer surface density, the characterization of the GI via an α viscosity, and the way in which we implement a finite dead zone viscosity. In the following paragraphs we discuss these issues in turn.

Advanced MHD treatments of the active layer are complex and involve a number of unknowns, such as whether low-energy cosmic rays can penetrate the accretion-driven winds, grain growth and settling, the presence of metal ions, etc. (e.g., Sano et al. 2000; Ilgner & Nelson 2006, 2008; Hirose & Turner 2011; Perez-Becker & Chiang 2011). Martin et al. (2012a,b) argue that a large critical Reynolds number is necessary for transport to occur, resulting "active" regions very different than the constant Σ_a we use. However, Martin et al. (2012b) predict essentially no accretion onto the central star in between outbursts, whereas the pre-outburst spectrum of V1057 Cyg shows emission lines typical of T Tauri stars accreting at $\sim 10^{-8} M_\odot\,\mathrm{yr}^{-1}$ (Herbig 1977). More recently, Miller et al. (2011) showed that the classical (accreting) T Tauri star LkHa 188-G4 underwent an FU Ori-type eruption in 2009. Finally, a pre-outburst spectrum of the FU Ori object V733 Cep (Reipurth et al. 2007) also showed characteristic accreting T Tauri emission lines (B. Reipurth, private communication). Thus the pre-outburst state of at least some FU Ori objects is one of accretion at rates typical of T Tauri stars, which we obtain with our adopted value of $\alpha_a \Sigma_a$, at least in the inner disk.

Similarly, our treatment of the GI with an α viscosity is crude; as in the case of the MRI,

three-dimensional simulations are required to treat the GI properly (e.g., Rice et al. 2003; Boley et al. 2006; Durisen et al. 2007, and references therein). Two-dimensional simulations also do a better job of capturing the GI than our treatment (e.g., Vorobyov & Basu 2006, 2007, 2009). However, as pointed out by Zhu et al. (2009b), and as shown in Zhu et al. (2010a,b) and the present simulations, the GI becomes harder and harder to sustain as one moves to smaller radii, whereas triggering of the MRI becomes easier.

Finally, the presence and behavior of non-zero viscosity in dead zones are highly uncertain. While simulations of resistive, stratified disks in shearing boxes appear to show that the active layer produces a non-zero α in the central "dead" layers (Fleming & Stone 2003; Okuzumi & Hirose 2011; Gressel et al. 2012), the level to which this occurs, the amount of mass transport involved, and precisely where energy is dissipated are unclear. For example, our model assumes that the wave energy is dissipated near the midplane, and thus the heat generated can be trapped radiatively by the opacity of the disk at the midplane; however, it is possible that dissipation is concentrated at higher levels (N. Turner, private communication).

In all, these uncertainties show that our current results must be taken as suggestive rather than predictive for variations of accretion in young stellar objects. Nevertheless, these simple models, which can be evolved easily for significant evolutionary timescales, illustrate the potential information on transport processes in protostellar and protoplanetary disks that might ultimately be gleaned from the observed accretion outbursts. Due to the increasing monitoring of young stellar objects, it is becoming increasingly clear that a wide variety of accretion behavior is exhibited in young stars, emphasizing that further progress on challenging problems of globally simulating MRI and GI in protostellar disks may pay rich dividends.

2.6 Summary

In this Chapter, we have extended the one-dimensional, two-zone model of long-term protostellar disk evolution with infall, which is previously introduced in Zhu et al. (2010a,b). Our modified models include a revised treatment of infall, enhanced disk heating, and possible non-zero viscosity in the dead zone. While the former two changes produce no qualitative

difference in the overall evolution from the Zhu et al. (2010b), we find that the presence of a small but finite dead zone viscosity can trigger inside-out bursts initiated at or near the inner edge of the disk through dead zone viscous heating, instead of GI-induced MRI-driven outside-in bursts with zero dead zone viscosity. These inside-out bursts not only bear a qualitative resemblance to the outburst behavior of one FU Ori objects, V1515 Cyg, but emphasize a careful treatment of the inner disk regions in simulations.

Given the uncertainties, our results are rather suggestive than predictive. However, two types of outbursts seen in FU Ori objects can be successfully reproduced by the simple α treatment in the dead zone. This difference in accretion behavior could be a potential probe of transport efficiency in the dead zone.

2.7 Acknowledgments

The authors acknowledge useful conversations with Bo Reipurth and Neal Turner. This work was supported in part by NASA grant NNX08A139G and by the University of Michigan.

CHAPTER III

Accretion Outbursts in Self-gravitating Protoplanetary Disks

3.1 Abstract

We improve on our previous treatments of long-term evolution of protostellar disks by explicitly solving disk self-gravity in two dimensions. The current model is an extension of the one-dimensional layered accretion disk model of Bae et al. We find that gravitational instability (GI)-induced spiral density waves heat disks via compressional heating (i.e., $P\mathrm{d}V$ work), and can trigger accretion outbursts by activating the magnetorotational instability (MRI) in the magnetically inert disk dead-zone. The GI-induced spiral waves propagate well inside of gravitationally unstable region before they trigger outbursts at $R \lesssim 1$ AU where GI cannot be sustained. This long-range propagation of waves cannot be reproduced with the previously used local α treatments for GI. In our standard model where zero dead-zone residual viscosity ($\alpha_{\rm rd}$) is assumed, the GI-induced stress measured at the onset of outbursts is locally as large as 0.01 in terms of the generic α parameter. However, as suggested in our previous one-dimensional calculations, we confirm that the presence of a small but finite $\alpha_{\rm rd}$ triggers thermally-driven bursts of accretion instead of the GI + MRI-driven outbursts that are observed when $\alpha_{\rm rd} = 0$. The inclusion of non-zero residual viscosity in the dead-zone decreases the importance of GI soon after mass feeding from the envelope cloud ceases. During the infall phase while the central protostar is still embedded, our models stay in a "quiescent" accretion phase with $\dot{M}_{\rm acc} \sim 10^{-8} - 10^{-7}\ M_\odot\,{\rm yr}^{-1}$ over 60 % of the time and spend less than 15 % of the infall phase in accretion outbursts. While our models indicate that episodic mass accretion during protostellar evolution can qualitatively help explain the low accretion luminosities seen in most low-mass protostars, detailed tests of the mechanism

will require model calculations for a range of protostellar masses with some constraint on the initial core angular momentum, which affects the length of time spent in a quasi-steady disk accretion phase. This chapter has been published in the Astrophysical Journal, Volume 795, 161 (2014), in collaboration with Lee Hartmann, Zhaohuan Zhu, and Richard P. Nelson.

3.2 Introduction

Recent infrared surveys have shown that the luminosity functions of protostars peak near 1 $L_\odot$, and have a significant fraction of objects at sub-solar luminosities (Enoch et al., 2009; Evans et al., 2009; Kryukova et al., 2012; Dunham et al., 2013; Stutz et al., 2013, see also Dunham et al. 2014 for review), which seem too low given the need to accrete the central protostar in typical estimated lifetimes (e.g., Kenyon et al., 1990). After many improvements (e.g., Cheng, 1978; Terebey et al., 1984; Fatuzzo et al., 2004; Mac Low & Klessen, 2004) to the singular isothermal sphere collapse model of Shu (1977), theoretical models imply accretion luminosities of 10–100 $L_\odot$ for typical mass and radius of low-mass protostars (0.5 $M_\odot$ and 2 $R_\odot$). One plausible solution to this "luminosity problem" is that mass infall occurs first to the disk, and subsequent disk accretion is low for the most of the time, with occasional short-lived, rapid accretion outbursts (Kenyon et al., 1990). A number of models were developed over decades to explain such episodic accretion events. Possible mechanisms include thermal instability in the inner disk (Bell & Lin, 1994), interactions with companions (Bonnell & Bastien, 1992; Pfalzner et al., 2008; Forgan & Rice, 2010), disk fragmentation plus subsequent migration of clumps generated (Vorobyov & Basu, 2005, 2006, 2010), and a combination of gravitational instability (GI) and the magnetorotational instability (MRI; Armitage et al. 2001; Zhu et al. 2009b, 2010a,b; Martin et al. 2012b; Chapter 2 of this thesis).

One shortcoming of previous work on GI + MRI-driven outbursts is the use of simple parameterized α viscosities (Shakura & Sunyaev, 1973) to represent the mass transport and energy dissipation for the GI and the MRI (Armitage et al. 2001; Zhu et al. 2009b, 2010a,b; Martin et al. 2012b; Chapter 2 of this thesis). This allows one to easily evolve models for the long timescales ($\sim$ Myr) needed to follow disk evolution through the infall phase to the T Tauri phase, and to explore a large parameter space as well. How well the α treatments

mimic the nature of GI and the MRI, however, is still controversial. For example, the intrinsic non-locality of self-gravity can make the appropriateness of an $\alpha_{\rm GI}$ treatment questionable (e.g. Balbus & Papaloizou, 1999), although other studies argue that transport via self-gravity is reasonably well described by α parameterizations when the disk is not too massive (e.g. Gammie, 2001; Lodato & Rice, 2004; Cossins et al., 2009; Vorobyov, 2010).

In Chapter 2, adopting α prescriptions to treat the GI and the MRI, we examined disk evolution and outburst behavior in one-dimensionnal (1D; radial) models. A layered accretion disk model was implemented in that work, where we solved a separate set of viscous-disk equations in each layer: the magnetically active surface layer (hereafter active layer) and the underlying magnetically inert region (hereafter dead-zone). We found that outbursts are triggered as the MRI activates in the dead-zone either thermally or through GI, depending on the dead-zone properties. More specifically, the presence of a small but finite dead-zone residual viscosity generates additional viscous heating in the dead-zone and thus can thermally trigger outbursts starting at or near the inner edge of the disk, instead of the previously found GI + MRI-driven outbursts with zero dead-zone residual viscosity (e.g., Zhu et al., 2010a).

In this Chapter, we improve the treatment of disk self-gravity by moving to two-dimensional (R, ϕ) models. We assume that the disks have a layered structure as in Chapter 2; we show how this can be accommodated solving only one set of hydrodynamic equations. While the overall scenario of accretion outbursts remains valid, the details vary. We find that, in contrast to a local treatment of GI, gravitationally unstable regions generate spiral density waves which can propagate into inner disk regions that are formally GI-stable via the Toomre Q parameter; this triggers the MRI at somewhat smaller radii than would be found with $\alpha_{\rm GI}$ treatments. Also, as we found in Chapter 2, the presence of a small but finite residual viscosity in the dead-zone decreases the importance of GI soon after initial infall phase, and is responsible for thermally driven accretion outbursts instead of GI + MRI-driven bursts with zero $\alpha_{\rm rd}$. Our results emphasize the importance of following the propagation of waves into innermost disk radii for predicting the resulting accretion luminosity as a function of time and thus addressing the protostellar luminosity problem.

3.3 Methods

3.3.1 Basic Equations

We use the FARGO-ADSG code (Baruteau & Masset, 2008) in 2D (R, ϕ) cylindrical coordinates. In addition to the hydrodynamic equations in the public version we add infall, heating sources, and radiative cooling:

$$\frac{\partial \Sigma}{\partial t} + \nabla \cdot (\Sigma v) = \dot{\Sigma}_{\rm in} \tag{3.1}$$

$$\Sigma \left(\frac{\partial v}{\partial t} + v \cdot \nabla v \right) = -\nabla P - \Sigma \nabla \Phi + \nabla \cdot \Pi + F_{\rm in} \tag{3.2}$$

$$\frac{\partial E}{\partial t} + \nabla \cdot (E v) = -P \nabla \cdot v + Q_+ - Q_- + \dot{E}_{\rm in} \, . \tag{3.3}$$

In the above equations Σ is the surface density, v is the velocity, P is the vertically integrated pressure, Φ is the gravitational potential including the disk self-gravitational potential, Π is the viscous stress tensor, E is the vertically integrated thermal energy per unit area, and Q_+ and Q_- are the total heating and cooling rates, respectively. The terms $\dot{\Sigma}_{\rm in}$, $F_{\rm in}$, and $\dot{E}_{\rm in}$ indicate the changes in the equations due to the infall model.

Since the main purpose of Chapter is to compare the driving of accretion outbursts in 2D with the results from our previous 1D models (Chapter 2), in the following we compare the equations we solved to illustrate differences when applicable.

3.3.2 Mass Conservation

We use the infall model introduced in Chapter 2, which is based on the model of Cassen & Moosman (1981) with modifications: (1) mass flux per unit distance is assumed to be constant over radius in order to avoid a singularity at the centrifugal radius and (2) envelope material does not fall onto the disk inside 20 % of the centrifugal radius in order to mimic the effect of collimated jets and outflows to prevent low angular momentum material from being added to the system. The basic idea of the infall model comes from an assumption of infall from a uniformly-rotating, spherically symmetric cloud; thus the axial matter has little angular momentum and falls at small radii, while material originally in (near) the

equatorial plane has the maximum angular momentum per unit mass and thus defines the instantaneous outer radius of infall to the disk (i.e. the centrifugal radius). In addition to the modifications, we apply a 10 % $m = 2$ density fluctuation to infalling material. While the $m = 2$ perturbation is chosen to consider possible non-axisymmetric infall from a filamentary envelope, we emphasize that the manner perturbations applied is not crucial for generating spiral structures as well as triggering outbursts. This is because disk rotates fast enough so that the perturbations smear out. We additionally test with 10 % of random perturbations in each azimuthal grid zone and find no noticeable changes in outcome. However, it turns out that without any non-axisymmetric perturbations infalling material does not generate asymmetric instabilities/spiral features. The mass infall rate of the modified model is

$$\dot{\Sigma}_{\rm in}(R,t) = \frac{\dot{M}_{\rm in}}{2\pi R_c(t) R}\Big[1 + 0.1\cos(2\phi)\Big] \text{ if } 0.2R_c \leq R \leq R_c \tag{3.4}$$

and

$$\dot{\Sigma}_{\rm in}(R,t) = 0 \text{ if } R < 0.2R_c \text{ or } R > R_c, \tag{3.5}$$

where $R_c(t)$ denotes the centrifugal radius at time t and $\dot{M}_{\rm in} = 0.975 c_s^3/G$ is the constant total infall mass rate at a given cloud isothermal sound speed for the singular sphere solution (Shu, 1977). The term $1 + 0.1\cos(2\phi)$ in Equation (3.4) accounts for the $m = 2$ density perturbation in the infall, where ϕ is the angle around the rotational axis of the disk.

With this infall model, the radial component of the mass conservation equation becomes

$$2\pi R\frac{\partial \Sigma}{\partial t} - \frac{\partial \dot{M}}{\partial R} = 2\pi R\dot{\Sigma}_{\rm in} \tag{3.6}$$

where the radial mass flux $\dot{M}$ is defined as $\dot{M} \equiv -2\pi R\Sigma v_R$. Using Equations (3.4) and (3.5), this results in the same form as the mass conservation equation used in Chapter 2 (see Equation 2.1).

3.3.3 Momentum Conservation

Since infalling material arrives at the disk surface with different radial and azimuthal velocities from those of the disk material, there exists a shear force. This can be written as

$F_{R,\rm in} = \dot{\Sigma}_{\rm in}(v_{R,\rm in} - v_{R,\rm disk})$ and $F_{\phi,\rm in} = \dot{\Sigma}_{\rm in}(v_{\phi,\rm in} - v_{\phi,\rm disk})$ and added to Equation (3.2), where $v_{R,\rm in}$ and $v_{\phi,\rm in}$ are the velocities of the infalling material (see Equations A7 and A9) and $v_{R,\rm disk}$ and $v_{\phi,\rm disk}$ are the velocities of the disk, respectively.

To facilitate mass and angular momentum transport, we adopt an α disk model (Shakura & Sunyaev, 1973) where the disk viscosity is calculated as

$$\nu = \alpha \frac{c_s^2}{\Omega}. \tag{3.7}$$

Here, α is a dimensionless parameter characterizing the efficiency of mass transport and energy dissipation and c_s and Ω denote the sound speed and the angular velocity, respectively. In this Chapter, the α parameter accounts for mass transport and energy dissipation through the MRI ($\alpha_{\rm MRI}$), GI if a non-zero $\alpha_{\rm GI}$ is included in the model, and possible hydrodynamic turbulence in the dead-zone ($\alpha_{\rm rd}$, see below).

As our simulations evolve the disk as a single layer that represents the full vertical column density of the disk, while assuming that the underlying disk model has two layers in the vertical direction (an active layer and a dead-zone), we introduce an effective viscosity parameter $\alpha_{\rm eff}$ defined as

$$\alpha_{\rm eff} = \frac{\Sigma_a \alpha_{\rm a} + \Sigma_d \alpha_d}{\Sigma}, \tag{3.8}$$

where Σ_a is the surface density of the active layer, Σ_d is the surface density of the dead-zone, and $\Sigma = \Sigma_a + \Sigma_d$ is the total surface density. α_a and α_d are total viscosity parameters in the active layer and the dead-zone, respectively, which are calculated as $\alpha_a = \alpha_{{\rm MRI},a} + \alpha_{{\rm GI},a}$ and $\alpha_d = \alpha_{{\rm MRI},d} + \alpha_{{\rm GI},d} + \alpha_{\rm rd}$. We explain each term below.

In the model of Gammie (1996) and later treatments of disk structure, the ionization level is not vertically uniform, but varies in a way that it decreases toward the disk midplane with a possible sharp transition. This transition may separate a disk into the magnetically active surface region (i.e. active layer) and the magnetically inert region around the midplane (i.e. dead-zone). In our fiducial models we assume that the active layer can contain $\Sigma_A = 100$ g cm^{-2} at maximum via non-thermal ionization (Gammie, 1996). The MRI viscosity parameter in the active layer ($\alpha_{{\rm MRI},a}$) and the dead-zone ($\alpha_{{\rm MRI},d}$) are assumed to have a fixed value $\alpha_{\rm MRI} = 0.01$ only if a region can sustain the MRI. Thus, $\alpha_{{\rm MRI},a}$ is always set

to $\alpha_{\rm MRI}$ by its definition. On the other hand, $\alpha_{{\rm MRI},d}$ becomes $\alpha_{\rm MRI}$ only if the azimuthally-averaged midplane temperature exceeds the MRI activation temperature $T_{\rm MRI} = 1500$ K so that the collisional ionization of alkali metals (e.g. potassium), or dust sublimation, produces a sufficient ionization level for the dead-zone to thermally sustain the MRI. Otherwise, $\alpha_{{\rm MRI},d}$ is set to zero. We use azimuthally-averaged midplane temperatures when activate the MRI in order to be conservative since our treatment for the MRI activation is crude.

As an aside, we note that the idea of an active layer accreting viscously has been challenged by Bai & Stone (2013a) and Bai (2013, 2014), who find that the inclusion of ambipolar diffusion limits the effectiveness of viscous transport, and argue that magnetically driven winds from upper layers are ultimately responsible for accretion at radii of order 1 to 10–20 AU. As long as there is some mechanism of mass transport other than GI that results in accretion rates less than the infall rate to the disk, the main features of our models should remain relevant and mass will still pile up to produce outbursts.

We consider cases with either zero or non-zero residual viscosity $\alpha_{\rm rd}$ in the dead-zone. This is motivated by recent three-dimensional (3D) magnetohydrodynamic simulations suggesting that the dead-zone can have some non-zero residual viscosity, which can be as large as $\sim 10^{-5}$–10^{-3}, due to hydrodynamic turbulence driven by the Maxwell stress in the active layer (Okuzumi & Hirose, 2011; Gressel et al., 2012). In the non-zero $\alpha_{\rm rd}$ case, we use $\alpha_{\rm rd} = 10^{-4}$. We note that the mass accretion rate of the dead-zone cannot exceed that of the active layer ($\dot{M}_d \leq \dot{M}_a$) if the non-zero $\alpha_{\rm rd}$ is due to turbulence propagated from the active layer. Therefore, we limit $\alpha_{\rm rd}$ as

$$\alpha_{\rm rd} = \min\left(10^{-4},\ \alpha_{\rm MRI}\frac{\Sigma_a}{\Sigma_d}\right). \tag{3.9}$$

To isolate the effects of using a local prescription for the GI from the use of 2D vertically-averaged models, we compute some models with an $\alpha_{\rm GI}$ prescription

$$\alpha_{\rm GI} = e^{-Q^2}, \tag{3.10}$$

where $Q \equiv \pi G\Sigma/\Omega c_s$ is the Toomre parameter. In the models where disk self-gravity is explicitly solved (hereafter self-gravity models), $\alpha_{\rm GI}$ is set to zero.

The azimuthal component of the momentum equation becomes

$$2\pi R\frac{\partial}{\partial t}(\Sigma R v_\phi) - \frac{\partial}{\partial R}(\dot{M} R v_\phi) = 2\pi\frac{\partial}{\partial R}(R^2\Pi_{R\phi}) + 2\pi R^2\dot{\Sigma}_{\rm in} v_{\phi,\rm in} \tag{3.11}$$

where we use Equation (3.6) and axisymmetry is assumed. If we use $v_\phi = R\Omega$ and the infall model given in Equations (3.4) and (3.5), the momentum equation also has the same form as in Chapter (see Equation 2.2). The only concern here is the viscous stress tensor $\Pi_{R\phi}$ because it has viscosity terms in it that vary between the active and dead layers in our underlying model. However, if the stress is defined in terms of α, one can easily show that $\Pi_{R\phi} = \Pi_{R\phi,a} + \Pi_{R\phi,d}$ by using the effective α parameter introduced in Equation (3.8), assuming the disk is vertically isothermal and the two layers share the same velocity field. In this case, the momentum equations for the two layers can be added linearly.

3.3.4 Energy Conservation

We assume that the infalling material has the same temperature as the disk surface (i.e. active layer) at the time of its addition. Thus, we add the corresponding thermal energy $\dot{E}_{\rm in} = k\dot{\Sigma}_{\rm in}T_a/(\gamma-1)\mu m_{\rm H}$ to the disk where T_a denotes the active layer temperature. We note that $\dot{E}_{\rm in}$ accounts only for the thermal energy of infalling material. The heat produced by kinetic energy of infalling material will be discussed below.

The thermal energy of a disk is determined by the balance between total heating and radiative cooling. Heating includes the internal viscous heating, the external irradiation, the infall heating while it exists, the compressional heating (i.e., $P\mathrm{d}V$ work), and the artificial viscosity given by the prescription in VonNeumann & Richtmyer (1950). The von Neumann–Richtmyer viscosity constant, measuring the number of grid zones over which the artificial viscosity spreads a shock, is set to the default value in FARGO-ADSG code, 1.4.

The viscous heating $Q_{{\rm vis},i}$ is defined as

$$Q_{{\rm vis},i} = \frac{1}{2\nu_i\Sigma_i}(\Pi^2_{RR,i} + \Pi^2_{R\phi,i} + \Pi^2_{\phi\phi,i}) + \frac{2\nu_i\Sigma_i}{9}(\nabla\cdot v)^2, \tag{3.12}$$

where ν_i is viscosity calculated as $\nu_i = \alpha_i c_s^2/\Omega$ and $\Pi_{RR,i}$, $\Pi_{R\phi,i}$, and $\Pi_{\phi\phi,i}$ are components of

the viscous stress tensor. The subscript i denotes either the active layer ("a") or the dead-zone ("d"). Note that velocity and temperature are assumed to be the same over the two layers while the surface density and viscosity parameter vary when calculating the viscous dissipation.

The external irradiation flux $Q_{\rm irr}$ is the sum of the fluxes from the central star, accretion luminosity, and the envelope:

$$Q_{\rm irr} \equiv \sigma T_{\rm irr}^4 = \frac{f_* L_*}{4\pi R^2} + \frac{f_{\rm acc} L_{\rm acc}}{4\pi R^2} + \sigma T_{\rm env}^4. \tag{3.13}$$

Here, $T_{\rm irr}$ is the temperature corresponding to the external irradiation flux, L_* and $L_{\rm acc}$ are the stellar and the accretion luminosity, and $T_{\rm env}$ is the envelope temperature. The coefficients f_* and $f_{\rm acc}$ account for the non-normal irradiation of the disk surface and both are set to 0.1 in this Chapter. We increase the stellar luminosity as the central star accretes mass, following the mass-luminosity relation

$$\log_{10}\left(\frac{L_*}{L_\odot}\right) = 0.20 + 1.74 \log_{10}\left(\frac{M_*}{M_\odot}\right) \tag{3.14}$$

which is an approximate power-law fit to the mass–luminosity relation, using the luminosities and effective temperatures from Kenyon & Hartmann (1995) for Taurus pre-main sequence stars and the Siess et al. (2000) evolutionary tracks to convert the HR diagram positions to masses. The accretion luminosity is calculated as

$$L_{\rm acc} = \frac{G M_* \dot{M}}{2 R_\odot}, \tag{3.15}$$

where we assume a typical T Tauri stellar radius of two solar radii.

During the infall phase kinetic energy carried by the infalling material is dissipated in two ways: immediate shock dissipation at the disk surface and readjustment process within the disk. While both processes are accompanied by corresponding energy release, the readjustment process, which is due to smaller specific angular momentum of the infalling material than that of the disk material at the same radius, is taken care in the code by adding the proper shear force in the momentum equation as explained in §3.3.3. The shock heating by

infalling material (see §3.8 for details) corresponding to the infall model outlined in Equations (3.4) and (3.5) is

$$Q_{\rm in} = \frac{GM_*\dot{M}_{\rm in}}{4\pi R_c^3}\frac{2-(R/R_c)}{(R/R_c)^2}\Big[1+0.1\cos(2\phi)\Big] \quad \text{if} \quad 0.2R_c \le R \le R_c \tag{3.16}$$

and

$$Q_{\rm in} = 0 \quad \text{if} \quad R < 0.2R_c \text{ or } R > R_c. \tag{3.17}$$

The dissipation of kinetic energy at the shock is treated as an external heating source since it happens near the disk surface (Cassen & Moosman, 1981). The infall heating term is thus added at the surface of the disk (see below).

The radiative cooling rate Q_- is simply

$$Q_- = 2\sigma T^4 f(\tau), \tag{3.18}$$

where T and τ are temperature and optical depth at the region where the cooling rate is calculated. In Equation (3.18), $f(\tau)$ is defined as

$$f(\tau) = \frac{8}{3}\frac{\tau}{1+\tau^2}, \tag{3.19}$$

which is chosen to accommodate both optically thin and thick cooling (Johnson & Gammie, 2003; Zhu et al., 2010a, 2012a). The optical depth is calculated as $\tau = \Sigma\kappa/2$ where the Rosseland mean opacity κ is taken from Zhu et al. (2009b).

While the mass and momentum conservation equations can simply be compared to those in Chapter 2, the comparison of energy equations is more complicated. The task is to relate the vertically integrated thermal energy per unit area E to the disk midplane temperature. In order to do this, we first assume that the active layer and the dead-zone has their own vertically isothermal temperatures T_a and T_d. If only the active layer exists (because either the dead-zone has been enlivened or surface density is low enough), the energy equation

simply becomes

$$\begin{aligned}\frac{\partial E}{\partial t}+\nabla\cdot(Ev) &= -P\nabla\cdot v+Q_{\rm vis,a}+Q_{\rm in}f(\tau_a)\\ &\quad +2\sigma T_{\rm irr}^4 f(\tau_a)-2\sigma T_a^4 f(\tau_a)+\dot{E}_{\rm in},\end{aligned} \tag{3.20}$$

and we can relate the midplane temperature (T_a in this case) to the vertically integrated thermal energy E. Here, $f(\tau)$ is defined as in Equation (3.19).

If both active layer and dead-zone exist we can write down an energy equation for each separate layer:

$$\begin{aligned}\frac{\partial E_a}{\partial t}+\nabla\cdot(E_a v) &= -P_a\nabla\cdot v+Q_{\rm vis,a}+Q_{\rm in}f(\tau_a)\\ &\quad +2\sigma T_{\rm irr}^4 f(\tau_a)-2\sigma T_a^4 f(\tau_a)+2\sigma T_d^4 f(\tau_d)\\ &\quad -2\sigma T_a^4 f(\tau_d)\end{aligned} \tag{3.21}$$

and

$$\begin{aligned}\frac{\partial E_d}{\partial t}+\nabla\cdot(E_d v) &= -P_d\nabla\cdot v+Q_{\rm vis,d}\\ &\quad +2\sigma T_a^4 f(\tau_d)-2\sigma T_d^4 f(\tau_d)+\dot{E}_{\rm in}.\end{aligned} \tag{3.22}$$

We note that the above two equations are equivalent to the energy equations used in the layered model of Chapter 2 (see Equations 2.12, 2.16, and 2.17). Then, the change in total thermal energy E can be written by adding the two equations,

$$\begin{aligned}\frac{\partial E}{\partial t}+\nabla\cdot(Ev) &= -P_a\nabla\cdot v-P_d\nabla\cdot v+Q_{\rm vis,a}\\ &\quad +Q_{\rm vis,d}+Q_{\rm in}f(\tau_a)+2\sigma T_{\rm irr}^4 f(\tau_a)\\ &\quad -2\sigma T_a^4 f(\tau_a)+\dot{E}_{\rm in}.\end{aligned} \tag{3.23}$$

From Equation (3.21), we can express the term $2\sigma T_a^4$ as

$$\begin{aligned} 2\sigma T_a^4 &= [f(\tau_a)+f(\tau_d)]^{-1}\Big[- P_a\nabla\cdot v + Q_{\mathrm{vis},a} + Q_{\mathrm{in}} f(\tau_a) \\ &\quad +2\sigma T_{\mathrm{irr}}^4 f(\tau_a) + 2\sigma T_d^4 f(\tau_d) - \frac{\partial E_a}{\partial t} - \nabla\cdot(E_a v)\Big]. \end{aligned} \tag{3.24}$$

Then, by substituting Equation (3.24) into Equation (3.23) we obtain

$$\begin{aligned} \frac{\partial E}{\partial t} + \nabla\cdot(Ev) &= -\frac{f(\tau_d)}{f(\tau_a)+f(\tau_d)} P_a \nabla\cdot v - P_d \nabla\cdot v \\ &\quad + \frac{f(\tau_d)}{f(\tau_a)+f(\tau_d)} Q_{\mathrm{vis},a} + Q_{\mathrm{vis},d} \\ &\quad + \frac{f(\tau_a)f(\tau_d)}{f(\tau_a)+f(\tau_d)} Q_{\mathrm{in}} + \frac{f(\tau_a)f(\tau_d)}{f(\tau_a)+f(\tau_d)} 2\sigma T_{\mathrm{irr}}^4 \\ &\quad - \frac{f(\tau_a)f(\tau_d)}{f(\tau_a)+f(\tau_d)} 2\sigma T_d^4 + \dot{E}_{\mathrm{in}} \\ &\quad - \frac{f(\tau_a)}{f(\tau_a)+f(\tau_d)} \left[\frac{\partial E_a}{\partial t} + \nabla\cdot(E_a v)\right] \qquad (3.25) \\ &\approx -\frac{f(\tau_d)}{f(\tau_a)+f(\tau_d)} P_a \nabla\cdot v - P_d \nabla\cdot v \\ &\quad + \frac{f(\tau_d)}{f(\tau_a)+f(\tau_d)} Q_{\mathrm{vis},a} + Q_{\mathrm{vis},d} \\ &\quad + \frac{f(\tau_a)f(\tau_d)}{f(\tau_a)+f(\tau_d)} Q_{\mathrm{in}} + \frac{f(\tau_a)f(\tau_d)}{f(\tau_a)+f(\tau_d)} 2\sigma T_{\mathrm{irr}}^4 \\ &\quad - \frac{f(\tau_a)f(\tau_d)}{f(\tau_a)+f(\tau_d)} 2\sigma T_d^4 + \dot{E}_{\mathrm{in}}. \qquad (3.26) \end{aligned}$$

We find that the last term in Equation (3.25) generally can be neglected in the quiescent state, and is also unimportant during outbursts when the thermal energy change is dominated by that in the dead-zone.

In the limiting case of $\tau_a, \tau_d \gg 1$, the above equation is simplified to

$$\begin{aligned} \frac{\partial E}{\partial t} + \nabla\cdot(Ev) &= -\frac{\tau_a}{\tau} P_a \nabla\cdot v - P_d \nabla\cdot v + \frac{\tau_a}{\tau} Q_{\mathrm{vis},a} + Q_{\mathrm{vis},d} \\ &\quad + \frac{1}{\tau} Q_{\mathrm{in}} + \frac{2}{\tau}\sigma T_{\mathrm{irr}}^4 - \frac{2}{\tau}\sigma T_d^4 + \dot{E}_{\mathrm{in}}, \end{aligned} \tag{3.27}$$

where $\tau \equiv \tau_a + \tau_d$.

3.3.5 Boundary Conditions

A transition is expected in the inner disk from a layered structure to a fully viscous disk at a radius close enough to the central star that stellar irradiation produces high enough temperatures so the MRI can be thermally activated. This transition should occur at a smaller radius ($\sim$ 0.05–0.1 AU) than our inner boundary $R_{\rm in} = 0.2$ AU, but taking a smaller inner radius results in excessive computational times. We therefore mimic the approximate effect of such a transition by assuming that the disk inner boundary is always MRI-active and $\alpha_{{\rm MRI},d}$ varies smoothly over the transition region $\Delta R_{\rm trans} = 0.1$ AU as

$$\begin{aligned} \alpha_{{\rm MRI},d}(R) &= \alpha_{{\rm MRI},d}(R = R_{\rm in} + \Delta R_{\rm trans}) \\ &\quad + [\alpha_{\rm MRI} - \alpha_{{\rm MRI},d}(R = R_{\rm in} + \Delta R_{\rm trans})] \\ &\quad \times \left[1 - \sin\left(\frac{\pi}{2}\frac{R - R_{\rm in}}{\Delta R_{\rm trans}}\right)\right]. \end{aligned} \tag{3.28}$$

We then apply standard open boundary conditions at the inner and outer boundaries: the radial velocity at the inner boundary is set to be the same as that of the first computation zone if the radial velocity is inward, otherwise it is set to 0 in order to avoid any possible inflow.

3.3.6 Initial Conditions and Parameters

We cannot treat the initial collapse phase forming the protostellar core, so we begin the calculations with a 0.2 $M_\odot$ central protostar, using a small surrounding disk of mass 0.007 $M_\odot$ with an initial surface density distribution of $\Sigma(R) = 100\ (R/{\rm AU})^{-1}$ g cm^{-2} to avoid numerical problems (the choice of stellar and disk masses agrees well with those of a recently observed Class 0 protostellar system L1527; Tobin et al. 2012.). In addition, we assume an 1 $M_\odot$ envelope cloud having uniform angular velocity of $\Omega_c = 1.15 \times 10^{-14}$ rad s^{-1} and temperature of $T_{\rm env} = 20$ K. This yields a net constant infall rate of $\sim 3.4 \times 10^{-6}\ M_\odot\,{\rm yr}^{-1}$ for the first ~ 0.24 Myr of calculations, adding 0.8 $M_\odot$ to the central star + disk in total. We use inner and outer boundaries of 0.2 AU and 100 AU, with 128 logarithmically spaced radial grid-cells and 128 linearly spaced azimuthal grid-cells. With this choice, $\Delta R/R$ is constant

Table 3.1. Model Parameters and Results for Two-dimensional Outburst Calculations

$\alpha_{\rm rd}$	$\alpha_{\rm MRI}$	Σ_A (g cm^{-2})	M_*[a] ($M_\odot$)	$M_{\rm disk}$[a] ($M_\odot$)	$M_{\rm burst}$[b] ($M_\odot$)	$\dot{M}_{\rm max}$[b] ($M_\odot$ yr^{-1})	$\Delta t_{\rm burst}$[b] (yr)	D[c]	D_T[d]
0	0.01	100	0.76/0.90	0.24/0.06	1.97×10^{-2}	6.19×10^{-5}	880	0.031	0.007
10^{-4}	0.01	100	0.78/0.93	0.22/0.03	3.73×10^{-3}	1.43×10^{-5}	480	0.058	0.016

[a]Masses are taken at the end of infall (0.24 Myr) and at the end of calculations (1 Myr).

[b]Outburst quantities are averaged over the T Tauri phase.

[c]Duty cycle for the entire calculation.

[d]Duty cycle during the T Tauri phase.

to 0.05 and grid-cells have comparable radial and azimuthal size at all radii. We performed short runs with higher numerical resolutions which are restarted at the end of infall phase, and found that the triggering of accretion outbursts is not affected by the resolution.

In the standard model (§3.4.1), we use $\alpha_{\rm MRI} = 0.01$, $\Sigma_A = 100$ g cm^{-2}, and $\alpha_{\rm rd} = 0$. In a companion model (§3.4.2), we test the effect of non-zero dead-zone residual viscosity with $\alpha_{\rm rd} = 10^{-4}$. Model parameters and outcomes are summarized in Table 3.1.

3.4 Results

3.4.1 Standard Model ($\alpha_{\rm rd} = 0$)

3.4.1.1 $\alpha_{\rm GI}$ Model

We begin with the $\alpha_{\rm GI}$ model. Figure 3.1 presents the mass accretion rate and masses of the central star, the disk, and the envelope as a function of time. The overall behavior is similar to that seen in the 1D calculation of Chapter 2, with outbursts of about $10^{-4}\ M_\odot\,{\rm yr}^{-1}$ superimposed on a roughly steady accretion rate of $\sim 10^{-6}\ M_\odot\,{\rm yr}^{-1}$ for the first 0.05 Myr, where this background "quiescent" rate reduces to $\sim 10^{-8}\ M_\odot\,{\rm yr}^{-1}$ at later times.

Looking in more detail at the behavior during an outburst (Figure 3.2a), the current model does not have such a high initial, short-lived peak in accretion as in the 1D model. This is because radial pressure gradients were not captured in the 1D calculations which in

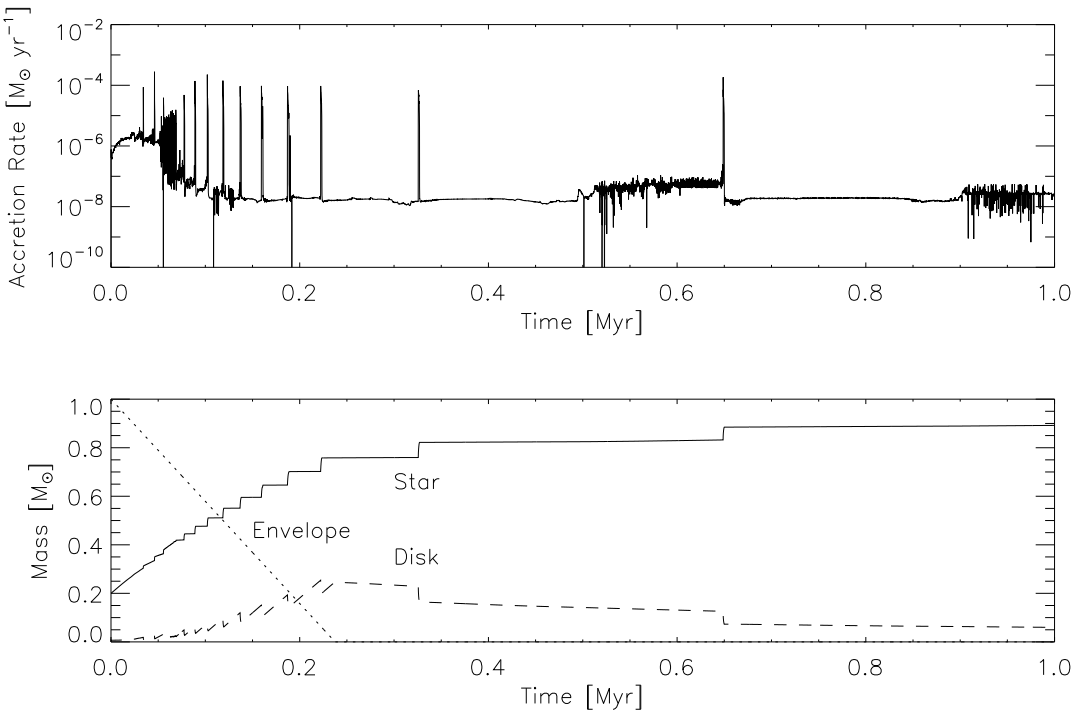

Figure 3.1. (Top) Mass accretion rate and (bottom) masses of the central star (solid curve), the disk (dashed curve), and the envelope cloud (dotted curve) as a function of time for the standard $\alpha_{\rm GI}$ model.

the 2D case help smooth out the burst. In addition, the 1D calculations showed a short-lived drop in the mass accretion rate during the main outburst from $\sim 3 \times 10^{-5}\ M_\odot\,{\rm yr}^{-1}$ to $10^{-6}\ M_\odot\,{\rm yr}^{-1}$ which is not seen in the 2D model.

Figure 3.2 illustrates the physical conditions which produce the outbursts, which are basically the same as in the 1D case. Viscous heating through the MRI and external irradiation provide comparable amounts of heating at $R \lesssim 1$ AU. At $R \gtrsim 20$ AU where disk surface density is low, viscous heating is reduced while external irradiation dominates. At intermediate radii ($1 \lesssim R \lesssim 20$ AU), material piles up due to limited mass transport in the dead-zone. Dissipation by the GI dominates the heating as mass builds up and the outburst is eventually triggered at ~ 2 AU due to the temperature rise driven by the GI heating. The MRI-active front then propagates inward, raising the viscosity in the inner disk. The midplane temperature steeply increases over 10^4 K at the inner $\lesssim 0.5$ AU due to the thermal instability. These features are essentially the same as in 1D.

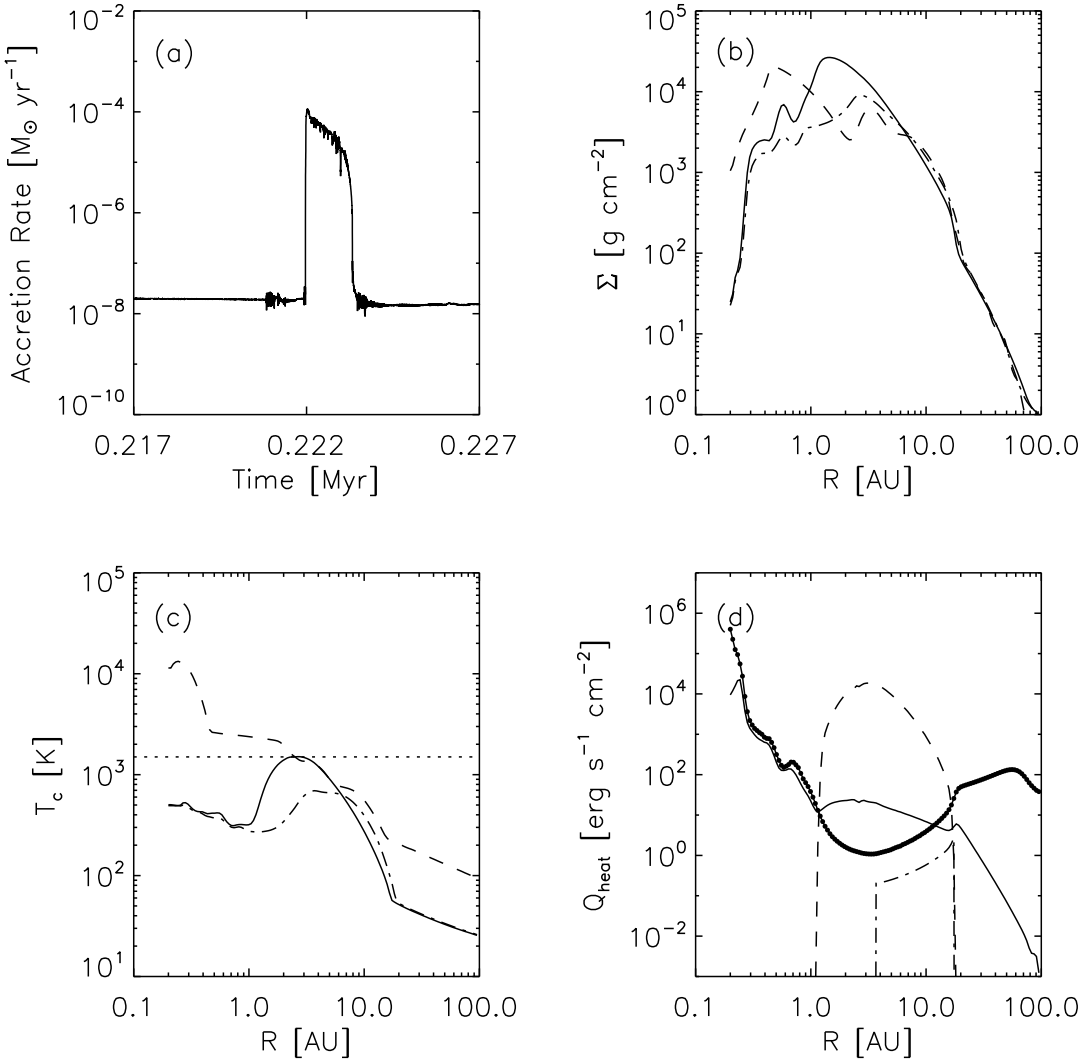

Figure 3.2. (a) Mass accretion rate as a function of time during a single outburst in the standard $\alpha_{\rm GI}$ model. (b) Surface density and (c) midplane temperature distributions at the onset (solid curves), at the peak (dashed curves), and at the end (dash-dotted curves) of the outburst. The horizontal dotted line in panel (c) represents the MRI activation temperature $T_{\rm MRI} = 1500$ K. (d) Contributions of various heating sources at the midplane at the onset of the outburst; external irradiation (solid curve with dots), viscous heating through the MRI (solid curve), GI heating (dashed curve), and infall heating (dash-dotted curve). Radial distributions presented in panels (b) - (d) are taken along the $\phi = 0$ direction.

We note that since disk self-gravity is not explicitly included in the $\alpha_{\rm GI}$ model, no evident spiral structure develops and therefore compressional heating and artificial shock heating are negligible at all radii.

3.4.1.2 Self-gravity Model

Figure 3.3 shows the time evolution of the mass accretion rate and the masses of central star, disk, and envelope for the full 2D self-gravity model. While the overall behavior for the first 0.1 Myr is nearly identical to that of the $\alpha_{\rm GI}$ case, at later times the self-gravity case exhibits more, smaller bursts of accretion that are more irregularly-spaced in time. This is due to the more complex disk structure resulting from the propagation of spiral waves through the disk. The stellar and disk masses at the end of infall phase are 0.76 $M_{\odot}$ and 0.24 $M_{\odot}$, which

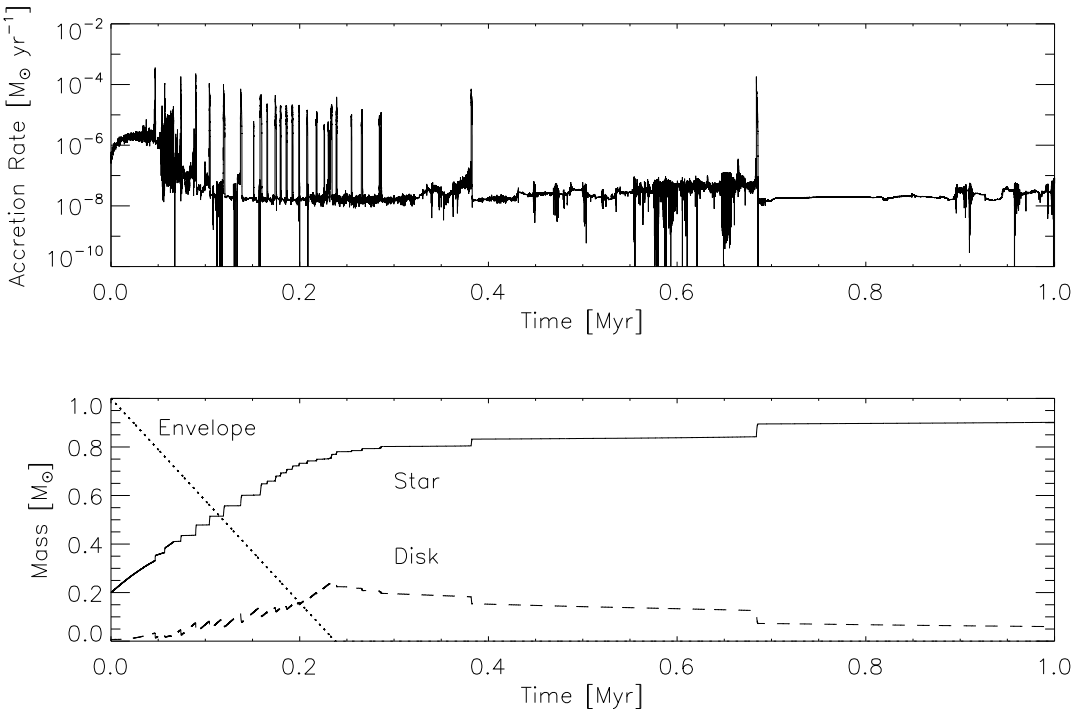

Figure 3.3. (Top) Mass accretion rate and (bottom) masses of the central star (solid curve), the disk (dashed curve), and the envelope cloud (dotted curve) as a function of time for the standard self-gravity model. The drops in accretion rate (shown in this figure and other accretion rate plots) are due to the outflow boundary condition adopted and are not physically realistic.

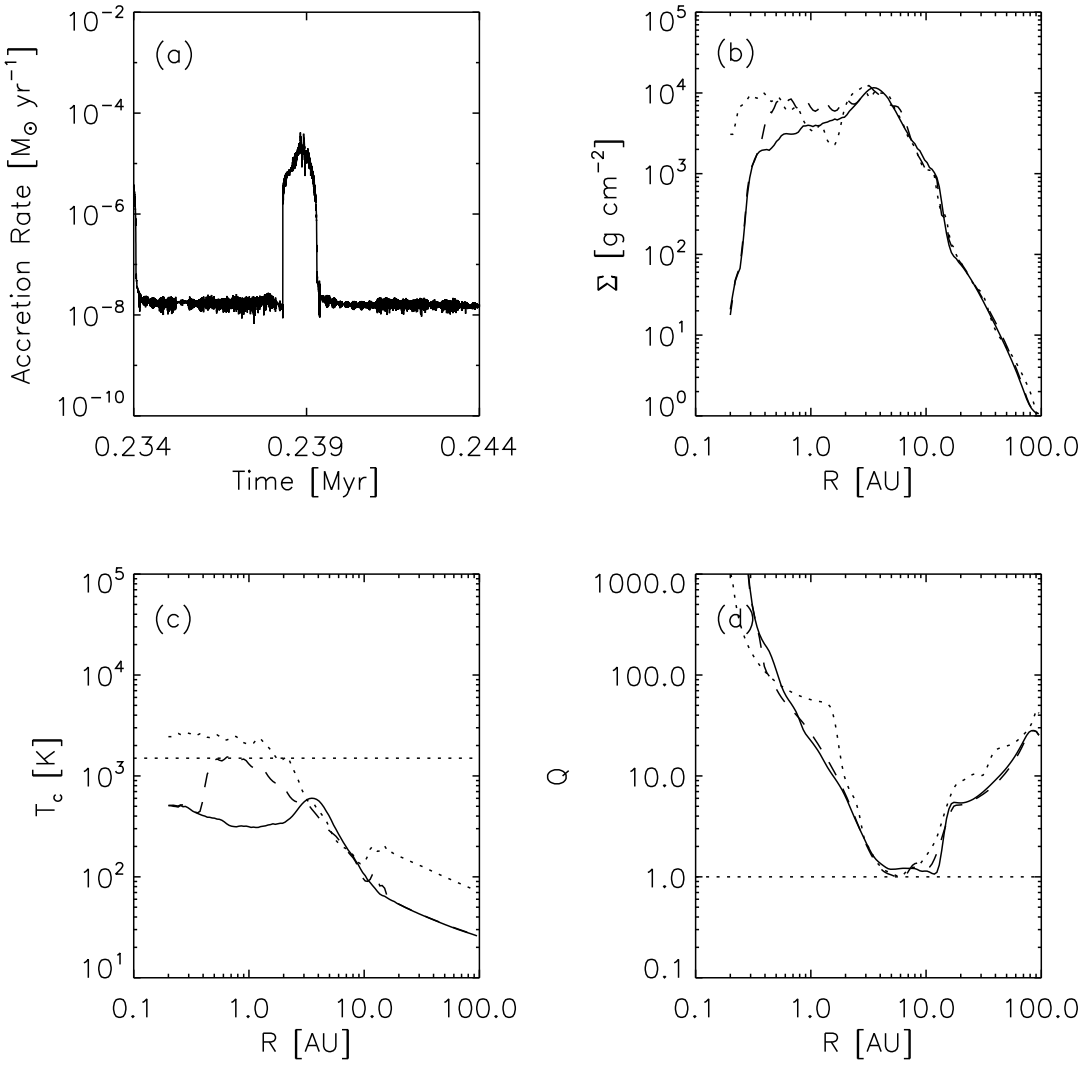

Figure 3.4. (a) Mass accretion rate as a function of time during a single outburst in the standard self-gravity model. (b) Surface density, (c) midplane temperature, and (d) the Toomre Q parameter distributions during quiescent phase (solid curves), at the onset (dashed curves), and at the peak (dotted curves) of the outburst. The horizontal dotted line in panel (c) represents the MRI activation temperature $T_{\rm MRI} = 1500$ K. In panel (d), the dotted line indicates $Q = 1$. Radial distributions are taken along the $\phi = 0$ direction, but the Toomre Q parameter is azimuthally averaged.

give $M_{\rm disk}/M_*$ of 0.32.

Figure 3.4a shows the mass accretion rate during a single outburst, which increases at the beginning of the burst by three orders of magnitude and then gradually increases to $4.1 \times 10^{-5}\ M_\odot\,{\rm yr}^{-1}$ at its peak; the outburst lasts for 1000 yr over which time a total mass of 0.01 $M_\odot$ is accreted. The burst is about a factor of 2–3 lower in peak accretion rate than the $\alpha_{\rm GI}$ model, lasts about two-thirds as long, and exhibits a more "rounded" form. These differences can be traced to differences in the way the outburst is triggered. As shown in Figure 3.4, in the self-gravity case the outburst is triggered at smaller radii and at smaller surface densities, which result in a weaker and shorter accretion episode. The lower maximum accretion rate also results in a failure to trigger the thermal instability, which in turn does not produce the very sharp initial peak in mass accretion seen in Figure 2.

The outburst is triggered differently in the self-gravity case by the propagation of spiral waves into inner disk regions which are formally GI-stable (Figure 3.5). The velocity perturbations of order 0.5 $\rm km\,s^{-1}$ propagate inward and trigger thermal activation of the MRI. Two-dimensional distributions of surface density and midplane temperature before, at the onset, and at the peak of the outburst are presented in Figure 3.6, which also show the propagation of spiral density waves and consequent outburst triggering. Thus, the essentially non-local aspect of GI produces a quantitative difference in the behavior of the outburst.

Figure 3.7 presents contributions of heating sources during the quiescent phase and at

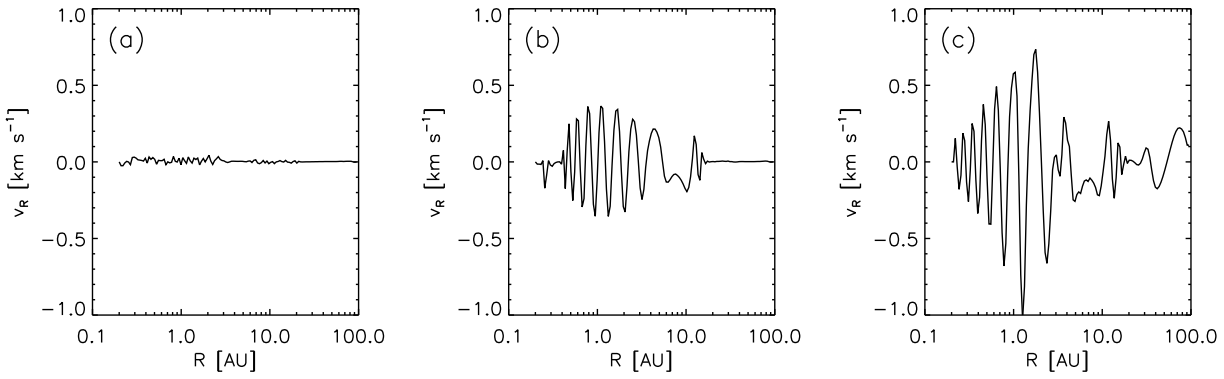

Figure 3.5. Radial velocity profiles along $\phi = 0$ (a) during quiescent phase, (b) at the onset and (c) at the peak of the outburst presented in Figure 3.4. The velocity profiles show the propagation of GI-induced spiral waves.

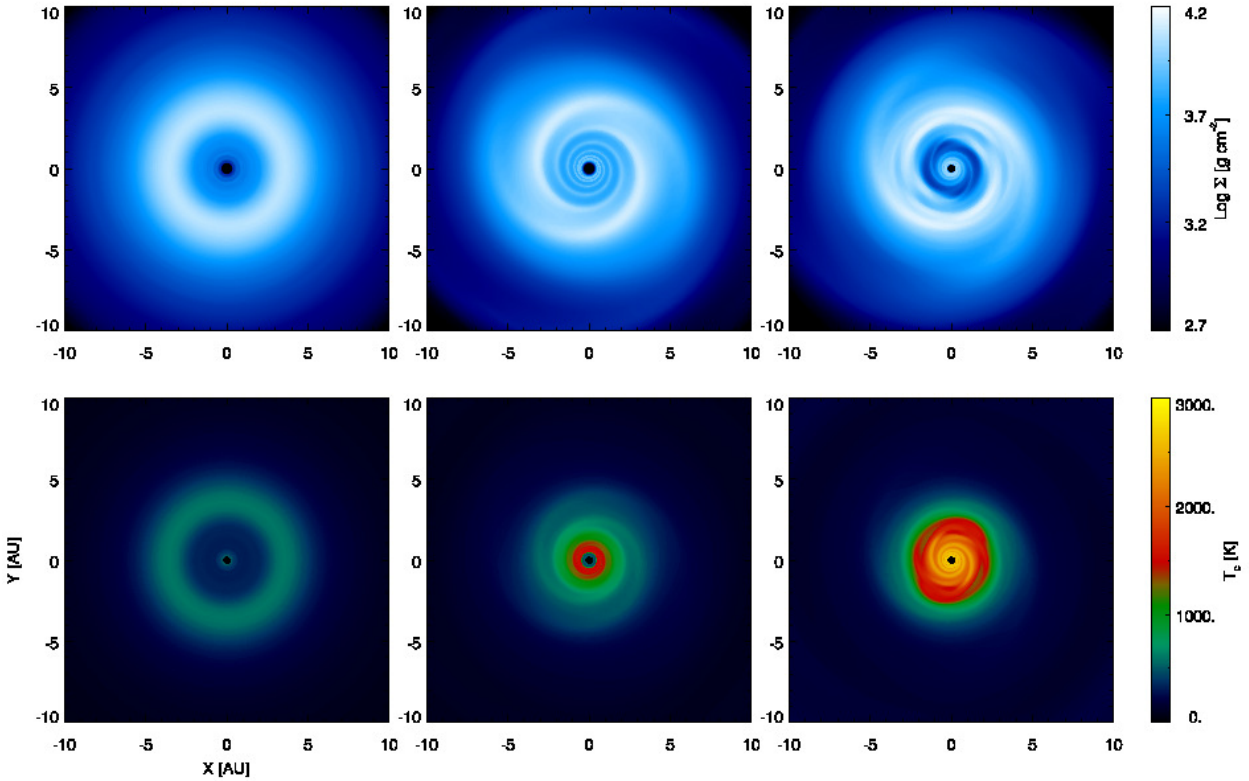

Figure 3.6. (Upper) Surface density and (lower) midplane temperature distributions of the inner 10 AU of the disk (left) during quiescent phase before the outburst presented in Figure 3.4 occurs, and (middle) at the onset and (right) at the peak of the outburst.

the onset of an outburst. During the quiescent phase, external irradiation and viscous heating via the MRI provide comparable amounts of heat, and dominate disk heating at all radii but the outer disk ($R \gtrsim 10$ AU) where external irradiation dominates. The disk is gravitationally stable during the quiescent phase, and thus compressional heating through $P\mathrm{d}V$ work and shock dissipation are less important than other heating sources. As the disk becomes gravitationally unstable, spiral density waves are generated accompanying a rapid inward accretion at inner disk. In this example, the inward radial velocity peaks at ~ 2 AU inside of which radii the compressional heating dominates ($dv_R/dR < 0$). We emphasize that $P\mathrm{d}V$ work is the dominating heating source at the radii providing orders of magnitude greater heat than viscous heating and external irradiation heating. It is also worth to note that rarefactional cooling occurs at ~ 2–10 AU because $dv_R/dR > 0$ over the region.

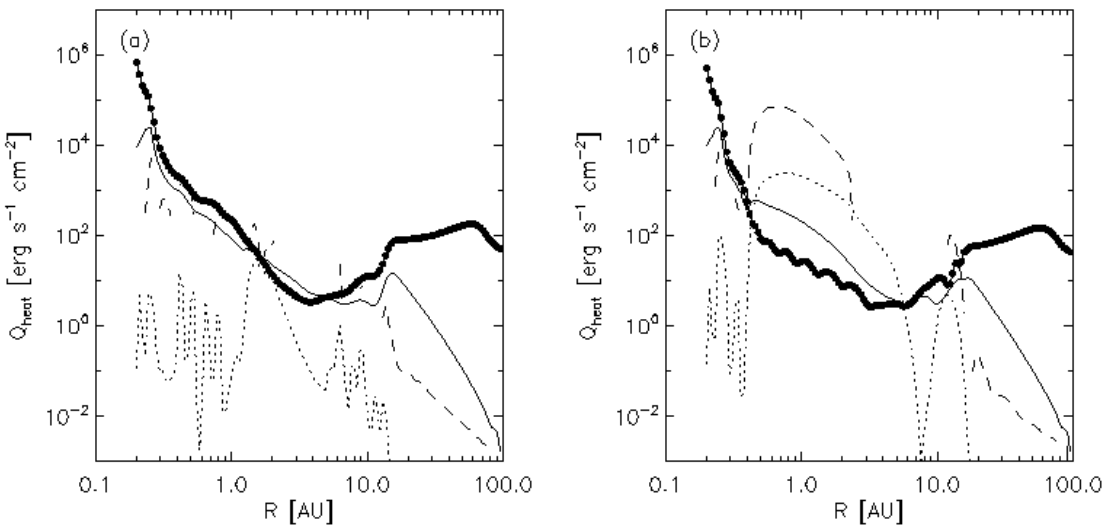

Figure 3.7. Contributions of various heating sources at the midplane (a) during quiescent phase and (b) at the onset of an outburst: external irradiation (solid curve with dots), viscous heating through the MRI (solid curve), compressional heating (dashed curve), and shock dissipation (dotted curve). Compressional and shock dissipation heatings are time-averaged over 1000 yr.

3.4.2 Effect of Non-zero Residual Viscosity in the Dead-zone ($\alpha_{\rm rd} = 10^{-4}$)

3.4.2.1 $\alpha_{\rm GI}$ Model

Figure 3.8 shows the mass accretion rate and the masses of the central star, the disk, and the envelope cloud as a function of time. As in the standard model, the overall evolution shows a qualitative resemblance to the $\alpha_{\rm GI}$ model in 1D (c.f. Figure 2.6 in Chapter 2). However, we note that the outbursts have higher peaks than in the 1D case, which results in faster depletion of the disk.

To compare outburst behaviors we plot the mass accretion rate during a single outburst in Figure 3.9. Radial profiles of surface densities and midplane temperatures at the onset, peak, and end of the outburst, as well as contributions of various heating sources to the midplane temperature are also plotted in the same figure. In the non-zero $\alpha_{\rm rd}$ model, the dead-zone residual viscosity generates a significant amount of heating which dominates at $R \lesssim 3$ AU. It is greater than the external irradiation over these radii by as much as two orders of magnitude. GI heating is significant at $2 \lesssim R \lesssim 20$ AU due to large mass in

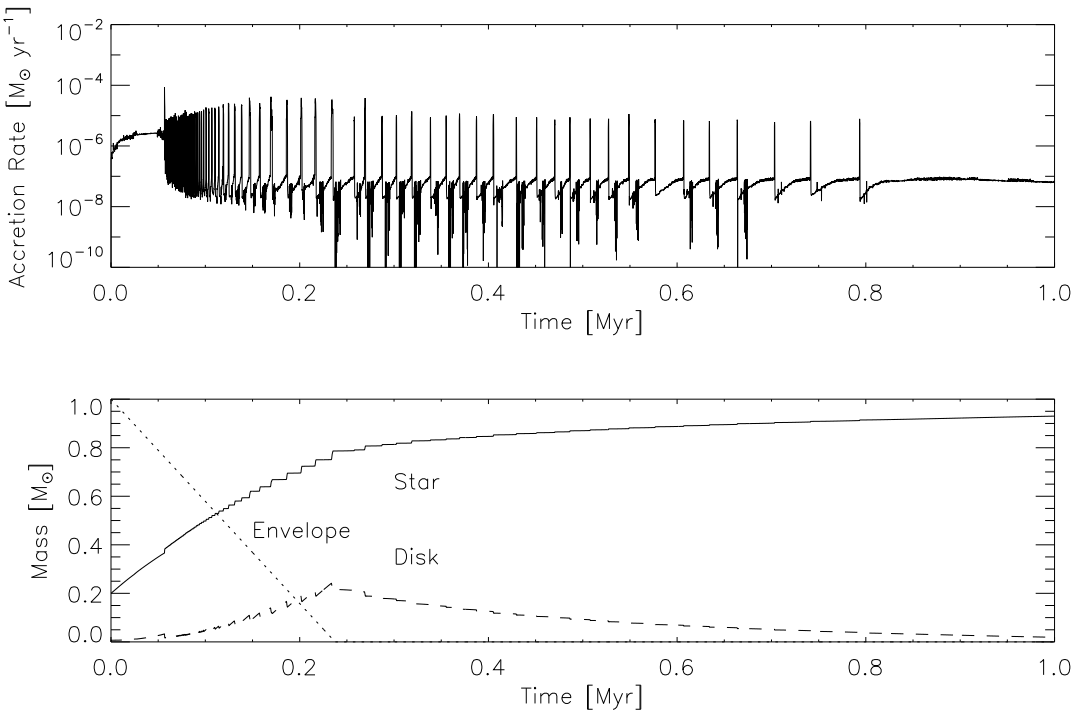

Figure 3.8. (Top) Mass accretion rate and (bottom) masses of the central star (solid curve), the disk (dashed curve), and the envelope cloud (dotted curve) as a function of time for the $\alpha_{\rm GI}$ model with $\alpha_{\rm rd} = 10^{-4}$.

the dead-zone, but outbursts are thermally triggered near the disk inner edge before enough material piles up for GI to initiate outbursts.

3.4.2.2 Self-gravity Model

In Figure 3.10, we plot the mass accretion rate for the non-zero $\alpha_{\rm rd}$ model as a function of time. The mass accretion rate maintains a value of 10^{-8}–10^{-7} $M_\odot\,{\rm yr}^{-1}$ in between bursts, which is in agreement with the zero $\alpha_{\rm rd}$ model, but the outbursts generally have a smaller peak accretion rate $\sim 10^{-6}$–10^{-5} $M_\odot\,{\rm yr}^{-1}$ than the ones in the zero $\alpha_{\rm rd}$ model. At the end of infall phase, stellar and disk masses are 0.78 $M_\odot$ and 0.22 $M_\odot$ giving $M_{\rm disk}/M_*$ of 0.28.

Figure 3.11 shows the accretion rate of an outburst that occurred during the infall phase and the radial profiles of surface density, midplane temperature, and the Toomre Q parameter at the beginning of the outburst. During the infall phase when the disk is fed by infalling material, the outburst-driving mechanism is similar to that of the standard model:

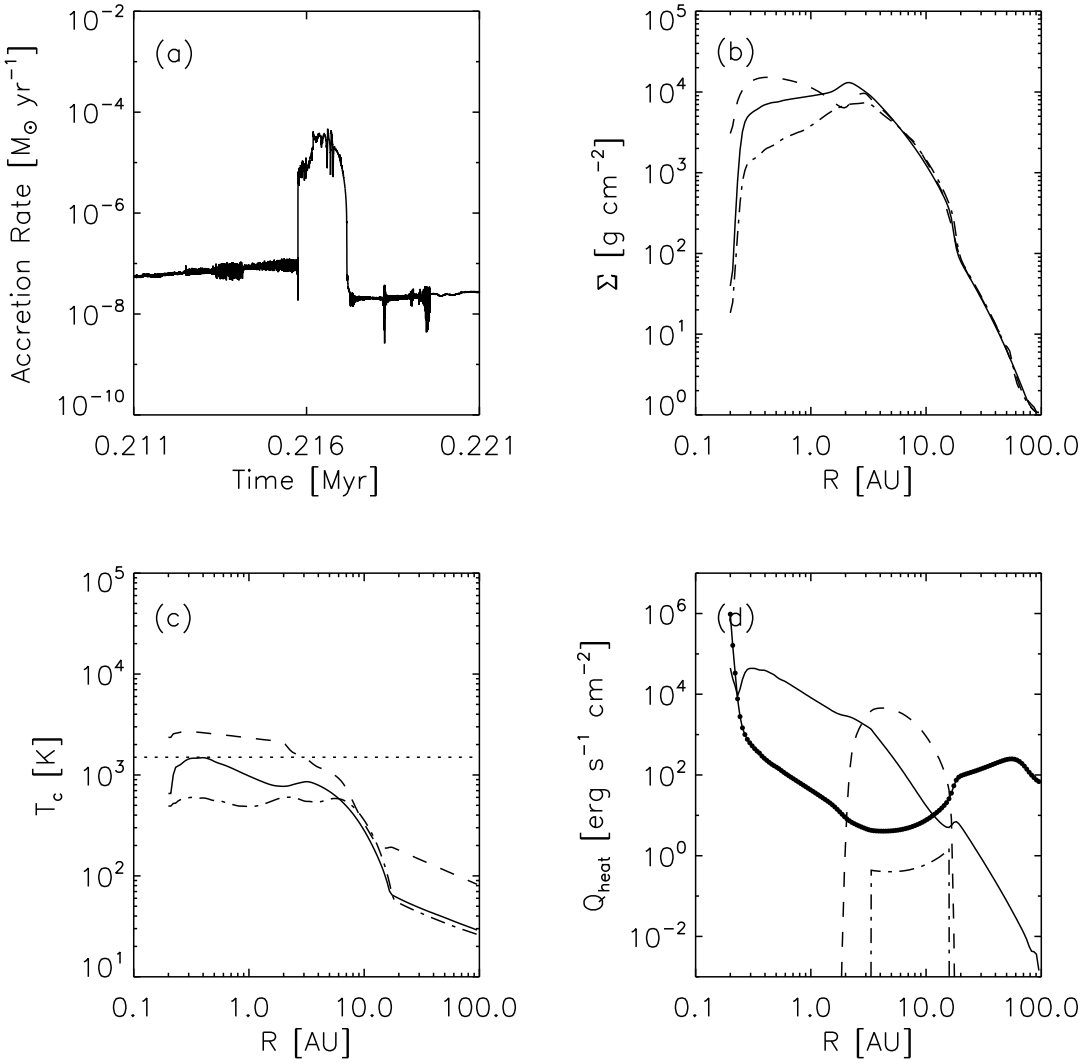

Figure 3.9. Same as Figure 3.2 but for the $\alpha_{\rm GI}$ model with $\alpha_{\rm rd} = 10^{-4}$. In panel (d), the solid curve includes viscous heating through the MRI and hydrodynamic turbulence in the dead-zone (i.e., non-zero $\alpha_{\rm rd}$) as well.

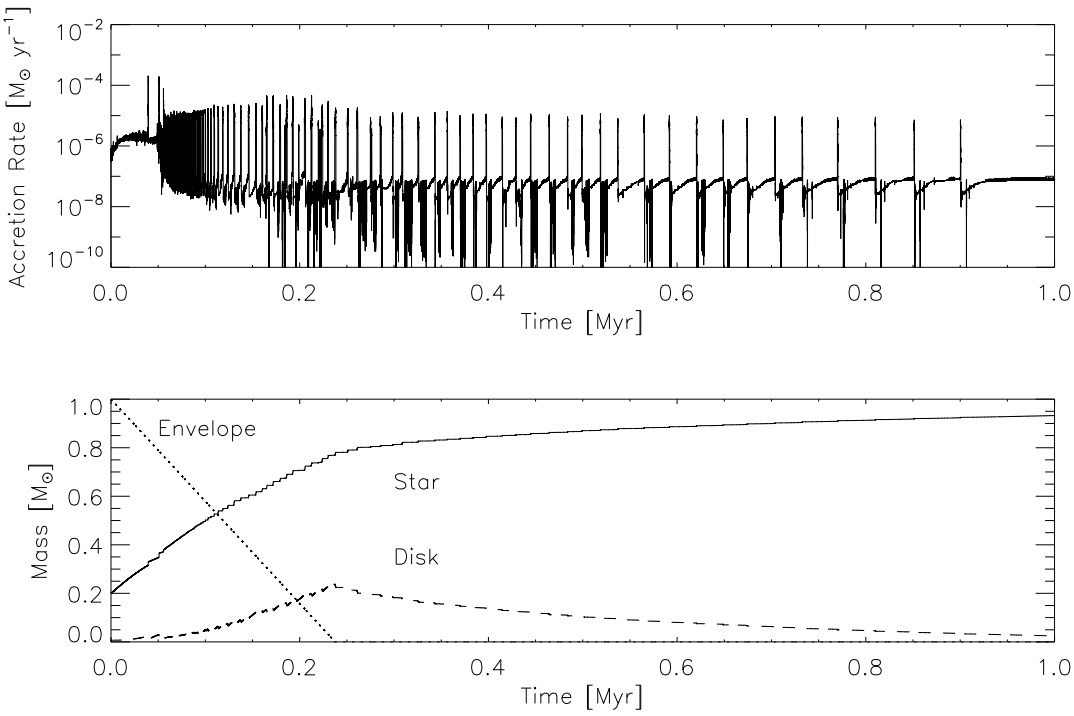

Figure 3.10. (Top) Mass accretion rate and (bottom) masses of the central star (solid curve), the disk (dashed curve), and the envelope cloud (dotted curve) as a function of time for the self-gravity model with $\alpha_{\rm rd} = 10^{-4}$.

spiral density waves propagate inward starting from the gravitationally unstable outer disk, triggering the MRI in the dead-zone through compressional heating. However, after infall stops the inner disk is viscously heated and thermally driven bursts are triggered before material piles up at larger radii. The transition between the GI + MRI-driven outbursts and the thermally driven outbursts occurs soon after the mass feeding from the envelop cloud is ceased, at $t \sim 0.3$ Myr. Figure 3.12 shows the accretion rate and radial profiles of surface density, midplane temperature, and the Toomre Q parameter at the initiation of an outburst occurring after the infall phase. As shown, the outburst is thermally triggered near the disk inner edge before the outer disk becomes gravitationally unstable. We note that there is no signature of spiral waves at the initiation of the burst. Contributions from various heating sources at the onset of thermally driven outburst are plotted in Figure 3.13. As seen, the inner disk ($R \lesssim 10$ AU) is mainly heated by viscous heating in the dead-zone and heating from $P{\rm d}V$ work and shock dissipation is less important.

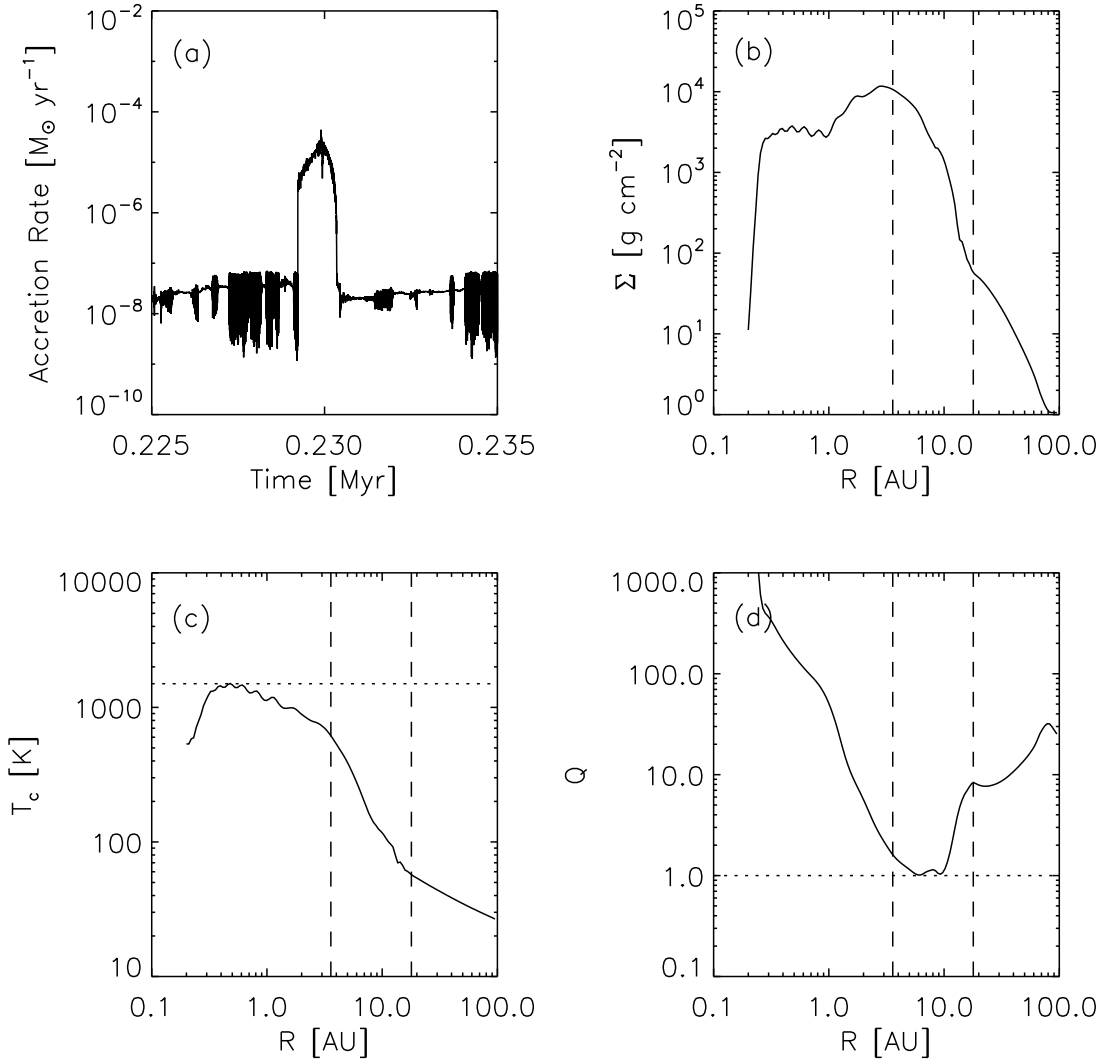

Figure 3.11. (a) Mass accretion rate as a function of time for an outburst occurred during the infall phase ($t \sim 0.23$ Myr) when disk self-gravity is important. Radial distributions of (b) surface density, (c) midplane temperature, and (d) the Toomre Q parameter at the beginning of the outburst are plotted as well. Horizontal dotted line in panel (c) indicates the MRI activation temperature $T_{\rm MRI}$ and the one in panel (d) shows where $Q = 1$. The vertical dashed lines present the radii between which infalling material from the envelop cloud falls on at this time. Radial distributions are taken along the $\phi = 0$ direction, but the Toomre Q parameter is azimuthally averaged.

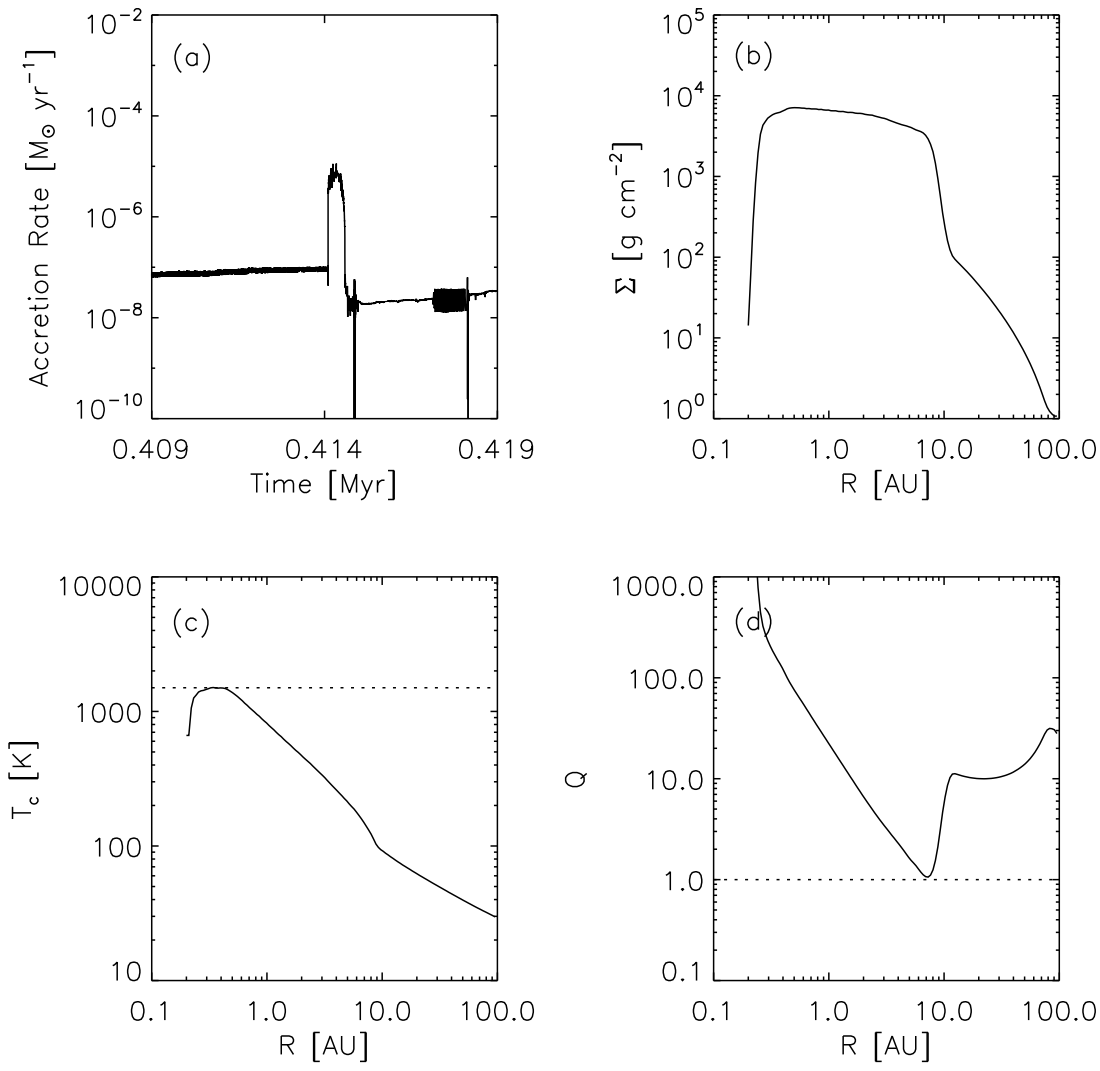

Figure 3.12. Same as Figure 3.11 but for an outburst that occurred during the "T Tauri phase" ($t \sim 0.41$ Myr after infall has stopped) when disk self-gravity becomes negligible. We note that the whole disk is gravitationally stable ($Q > 1$) and there is no signature of spiral waves propagating in the surface density and midplane temperature distributions.

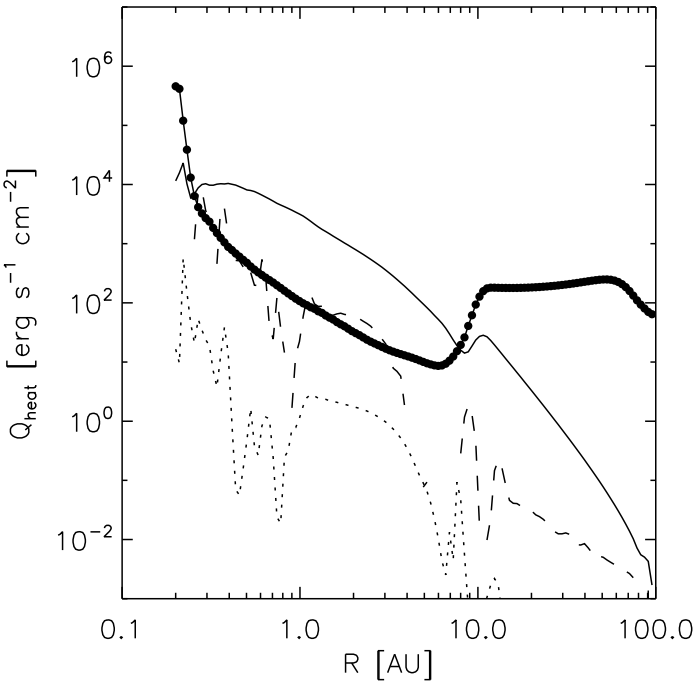

Figure 3.13. Contributions of various heating sources at the midplane at the onset of the thermally-driven outburst presented in Figure 3.12: external irradiation (solid curve with dots), viscous heating through the MRI plus dead-zone residual viscosity (solid curve), compressional heating (dashed curve), and shock dissipation (dotted curve). Compressional and shock dissipation heatings are time-averaged over 1000 yr. Note that the internal viscous heating dominates at $R \lesssim 10$ AU with the help of non-zero $\alpha_{\rm rd}$.

3.5 Discussion

3.5.1 GI-induced Spiral Density Waves

As we have described, the propagation of GI-induced spiral density waves plays a crucial role in triggering accretion outbursts and thus in the evolution of protoplanetary disks. Figure 3.14 illustrates the spatial distribution of perturbations to the surface density $\delta\Sigma/\langle\Sigma\rangle$ in the ϕ–$\log R$ plane at the onset of the GI + MRI-driven outburst presented in Figure 3.4. As seen in the figure, $m = 2$ trailing spiral density waves are dominant. They originate at ~ 7 AU where the disk is gravitationally most unstable, while extending over a range of disk radii from ~ 0.4 AU to ~ 15 AU.

In order to measure the strength of the GI-induced stress, we calculate the gravitational shear stress in terms of an effective α (Lynden-Bell & Kalnajs, 1972; Gammie, 2001) as

$$\alpha_{\rm sg} = -\left(\frac{d\ln\Omega}{d\ln R}\right)^{-1} \frac{\langle\int_{-\infty}^{\infty} g_R g_\phi/(4\pi G)dz\rangle}{\langle\Sigma c_s^2\rangle}, \tag{3.29}$$

where g_R and g_ϕ are self-gravitating acceleration in R and ϕ directions and the brackets denote the azimuthal average. The vertical integration in the above equation is numerically done in the FARGO-ADSG code by changing B^2 to $B^2 + \eta^2$ in Equations (A1) and (A3) of Baruteau & Masset (2008), where η is defined as $z = \eta R$ (see Appendix A of Baruteau et al. 2011). We vary η evenly by 0.01 from 0 to 1 for the integration (C. Baruteau 2014, private communication). In addition to the stress directly generated from the gravitational field, GI also produces density and velocity fluctuations that contribute to mass transport and heat dissipation. This can be quantified using the Reynolds stress calculated as

$$\alpha_{\rm rey} = -\left(\frac{d\ln\Omega}{d\ln R}\right)^{-1} \frac{\langle\Sigma\delta v_R\delta v_\phi\rangle}{\langle\Sigma c_s^2\rangle}, \tag{3.30}$$

where $\delta v_R = v_R - \langle v_R\rangle$ and $\delta v_\phi = v_\phi - \langle v_\phi\rangle$.

The azimuthally-averaged radial profiles of $\alpha_{\rm sg}$ and $\alpha_{\rm rey}$ are plotted on the right panel of Figure 3.14. At the initiation of the outburst, gravitational stress $\alpha_{\rm sg}$ is 0.004 at the radius where the spiral waves are generated. However, the GI-induced spiral waves generate

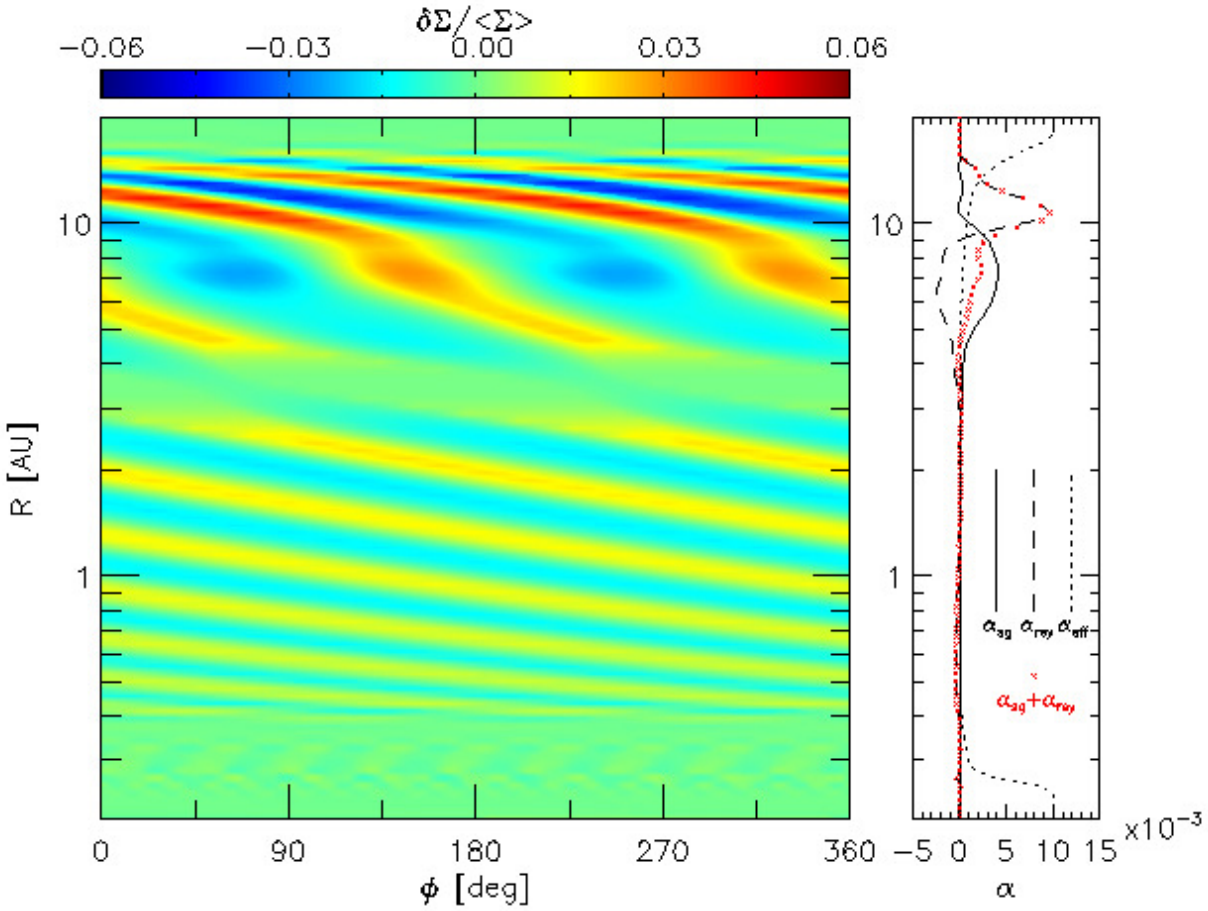

Figure 3.14. (Left) Spatial distribution of surface density enhancement/deficit $\delta\Sigma/\langle\Sigma\rangle$ on the $\phi - \log R$ plane at the onset of the outburst presented in Figure 3.4. (Right) Azimuthally averaged radial profiles of $\alpha_{\rm sg}$, $\alpha_{\rm rey}$, and $\alpha_{\rm eff}$ are plotted. The total stress induced by GI ($\alpha_{\rm sg} + \alpha_{\rm rey}$) is also plotted with red crosses.

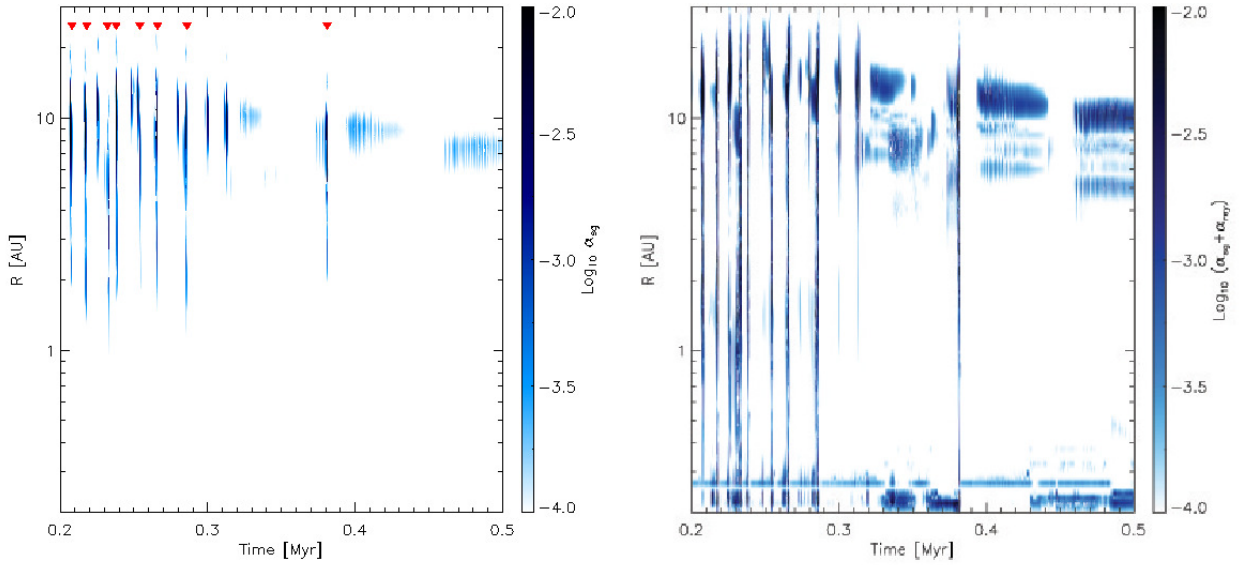

Figure 3.15. Radial profiles of (left) the stress generated directly from the self-gravitating acceleration field $\alpha_{\rm sg}$ and (right) the total stress induced by self-gravity $\alpha_{\rm sg} + \alpha_{\rm rey}$ in logarithmic scale during $t = 0.2$–0.5 Myr for the self-gravity model with zero $\alpha_{\rm rd}$. Red triangles on the left panel indicates the time at which outbursts are occurred.

additional hydrodynamic turbulence across a broader region. In terms of $\alpha_{\rm rey}$, the stress is as large as 0.01 at ~ 10 AU. Also, we note that while gravitationally stable at $R \lesssim 1$ AU the propagating spiral waves provide $\sim 10^{-3}$ of $\alpha_{\rm rey}$ in the region. We note that the mass transport through the MRI across this inner region is limited ($\alpha_{\rm eff} \sim 10^{-4}$) because of relatively large mass in the dead-zone.

In Figure 3.15, we present the time variation of the radial $\alpha_{\rm sg}$ and $\alpha_{\rm rey}$ profiles in the standard self-gravity model over $t = 0.2 - 0.5$ Myr. We emphasize that the disk repeatedly produces GI-induced stresses which are not constant over time or gradually increasing/decreasing, but are rather sporadic. This sporadic feature can be understood as a self-regulation process of a disk that stabilizes itself by redistributing mass through the action of spiral waves.

In terms of the generic α viscosity, this Chapter shows that the total stress driven by GI, while it is a function of time and radius, becomes as large as ~ 0.01 locally. This is comparable to the previously used α treatments of disk self-gravity, where an $\alpha_{\rm GI}$ of 0.01–0.03 (Lin & Pringle 1987, 1990; Armitage et al. 2001; Zhu et al. 2010a,b; Martin & Lubow

2011; Martin et al. 2012b; Chapter 2 of this thesis) is locally assumed for a gravitationally unstable disk region with $Q = 1$.

3.5.2 Accretion Outbursts as a Potential Solution to the Luminosity Problem

As mentioned in the Introduction, time-variable protostellar accretion might help resolve the luminosity problem in low-mass star formation. To address the implications of our calculations, in Figure 3.16 we plot the fractional distributions of the mass accretion rate for the infall phase, during which time the central protostar is still embedded. The highest peak at $\sim 10^{-8}\ M_\odot\,\mathrm{yr}^{-1}$ represents the quiescent disk accretion phase in between outbursts; this accounts for roughly two-thirds of the total time during infall; the peak at $\sim 10^{-6}\ M_\odot\,\mathrm{yr}^{-1}$ corresponds to the early phase of quasi-steady disk accretion at the singular isothermal sphere infall rate, corresponding to about one quarter of the protostellar phase; and the broad peak at $\gtrsim 10^{-5}\ M_\odot\,\mathrm{yr}^{-1}$ is due to outbursts, which corresponds to about 7 % of the infall phase in the zero $\alpha_{\rm rd}$ and about 14 % of the time in the non-zero $\alpha_{\rm rd}$ model. For typical mass-radius relations, accretion at $\lesssim 10^{-7} M_\odot\,\mathrm{yr}^{-1}$ produces low enough luminosities to be compatible with observations (Kenyon et al., 1990; Offner & McKee, 2011).

While our models illustrate the possibility of outburst behavior to help resolve the luminosity problem by having protostars spend most of the infall phase accreting slowly, a real test would require constructing a luminosity function for an entire population of protostars weighted by the stellar mass function (e.g., Offner & McKee, 2011; Dunham & Vorobyov, 2012). In addition, the distribution of initial angular momenta among the different mass protostellar clouds would be an important parameter. The quasi-steady accretion phase, where infall to the inner disk produces high enough temperatures for the MRI to be activated and thus the disk accretes at roughly the same rate as the matter falls onto the disk, can be problematic if it persists for too large a fraction of the infall phase. In turn, the fraction of time spent in the quasi-steady phase is a function of the initial angular momentum, because slower rotation leads to more mass being accreted at small disk radii. Conversely, large initial angular momenta produce large disks with accretion strongly modulated by outbursts, as in the models of Vorobyov & Basu (2005, 2006, 2010). Further progress on this problem would be strongly aided by observational constraints on the angular momentum distributions

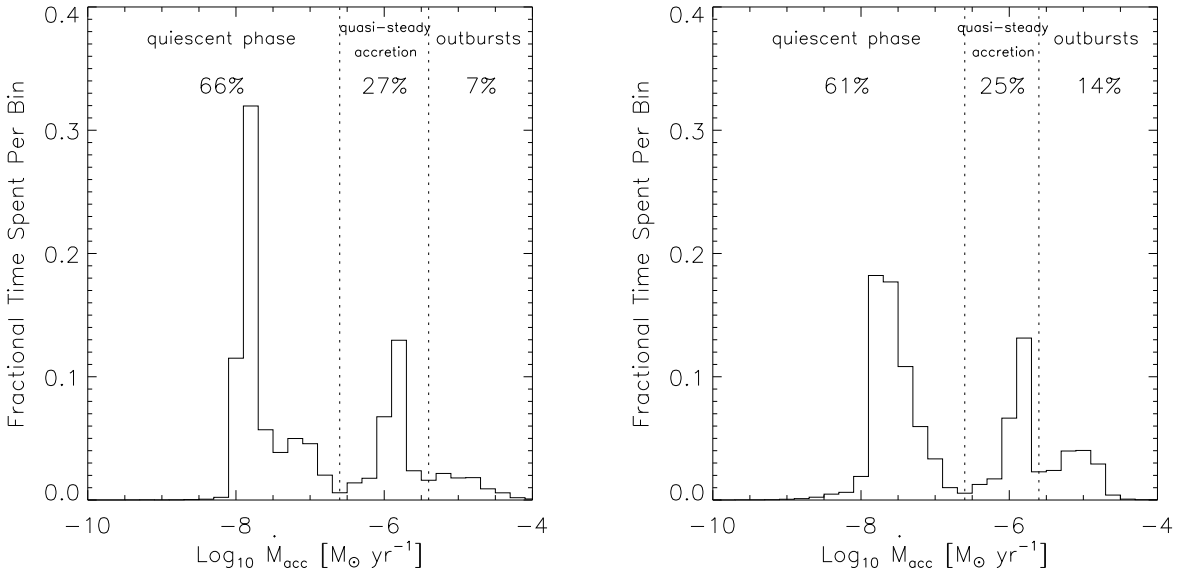

Figure 3.16. Distributions of mass accretion rate during the infall phase with logarithmic bins for self-gravity models with (left) zero and (right) non-zero $\alpha_{\rm rd}$. The histograms can be divided into three phases as indicated by the vertical dotted lines; the early quasi-steady accretion phase, outbursts, and quiescent phase in between bursts. The percentages show fractional time spent in each phase.

among protostellar cores of differing masses.

We note that our models, as in those of Zhu et al. (2010b), also exhibit outbursts in the post-infall or T Tauri phase, for which there is little observational evidence. The mechanisms producing outbursts in the models are sensitive to the amount of radiative trapping of dissipated energy, which thus depends upon the surface density and dust opacity; lowering either of these makes it much more difficult to trigger outbursts. Thus, over T Tauri lifetimes, removal of mass by photoevaporation (e.g., Owen et al., 2011) and dust growth (e.g. Miotello et al., 2014) can reduce the disk opacity and thus radiative trapping of thermal energy in the disk becomes less efficient, lessening the number of outbursts or even preventing them all together.

3.5.3 Comments on Other Possible Outburst-driving Mechanisms

Thermal instability was one of the first proposed mechanisms aiming to explain the accretion outbursts of FU Ori (e.g. Bell & Lin, 1994). The basic idea is that disk opacity steeply

increases between $\sim$ 2000 K and few 10^4 K due to the ionization of hydrogen. However, raising the disk temperature to such high values to initiate thermal instability is limited only to small radii (few $R_\odot$). Zhu et al. (2007) used radiative transfer modeling of FU Ori and found hot inner disk must extend out to $\sim$ 1 AU, concluding the fit is inconsistent with a pure thermal instability model. Therefore, while the thermal instability model should not be completely ruled out, we conjecture the model seems to work better when combined with other mechanisms rather than in isolation.

Vorobyov & Basu (2005, 2006, 2010) suggest that outer disks can fragment and form dense clumps which then migrate inward and eventually accrete onto the central star. Vorobyov & Basu (2010) included the effect of radiative cooling, viscous and shock heating, stellar and background irradiation and solve disk self-gravity to study protostellar evolution starting from the initial collapse phase. They found disks fragment at several tens to hundreds AU, whereas we do not see any disk fragmentation in our calculations. We conjecture this is mainly attributable to the different initial angular momenta assumed in the models. In terms of angular velocity of collapsing core, we use $\Omega_c = 1.15 \times 10^{14}$ rad s^{-1} which is the median value inferred in Chapter 2, in which observed disk frequencies as a function of age where disk dispersal by photoevaporation is assumed. In contrast, the reference model of Vorobyov & Basu (2010) assumed $\Omega_c \sim 9 \times 10^{14}$ rad s^{-1}, which is about an order of magnitude greater than ours. It is also worth to compare the ratio of rotational to gravitational energy $\beta = E_{\rm rot}/|E_{\rm grav}|$. In this Chapter, we use a two-component density profile for the initial Bonnor–Ebert sphere which is described as

$$\rho = \rho_c \text{ at } \xi < \xi_c \tag{3.31}$$

and

$$\rho = 2\rho_c \xi^{-2} \text{ at } \xi_c < \xi < 6.5, \tag{3.32}$$

where ρ_c is the central density and $\xi = r/(c_s^2/4\pi G\rho_c)^{1/2}$ is the non-dimensional radial distance. Note that the density profile beyond $\xi = \xi_c$ has the same profile as the singular isothermal model, and $\xi = 6.5$ corresponds to the critical Bonnor–Ebert sphere radius. As our initial conditions assume the flat, inner part of the Bonnor–Ebert is collapsed to 0.2 $M_\odot$

central protostar leaving outer 1 $M_\odot$ of envelope cloud, the corresponding ξ_c becomes 1.78. With this initial setup $\beta = 3.0 \times 10^{-4}$, which is smaller than the one used in the reference model of Vorobyov & Basu (2010) by a factor of ~ 40.

We also note that while the suggested process in Vorobyov & Basu (2005, 2006, 2010) seems plausible, it is uncertain whether the clumps created at relatively large radii eventually accrete onto the central star and lead to a rise in the accretion rate given their placement of the inner boundary at a relatively large radius ($R_{\rm in} = 5$ AU). For instance, it may be possible that the clumps are tidally destroyed as they migrate (Zhu et al., 2012a). With such a large inner boundary one can also miss important physics including GI + MRI and thermal triggering of outbursts at smaller radii as we show in this Chapter. We tested our model with an inner boundary of $R_{\rm in} = 5$ AU and not surprisingly found that neither GI + MRI-driven nor thermally driven outbursts occur.

3.6 Conclusions

In this Chapter, we explicitly solve disk self-gravity to investigate the triggering of accretion outbursts in two dimension starting from the collapse of an isothermal, uniformly-rotating core. We find that gravitationally unstable disks generate spiral density waves that heat disks via compressional heating and can trigger accretion outbursts by activating the MRI in the disk dead-zone. We emphasize that the GI-induced spiral waves can propagate well inside of the gravitationally unstable region before they trigger outbursts at $R \lesssim 1$ AU; this feature cannot be reproduced with the previously used local $\alpha_{\rm GI}$ treatments. As suggested by the 1D calculations in Chapter 2, we further confirm that the presence of a small but finite $\alpha_{\rm rd}$ of 10^{-4} triggers thermally-driven bursts of accretion soon after mass feeding from envelope cloud is ceased, instead of GI + MRI-driven outbursts. We argue that the episodic mass accretion during protostellar evolution can qualitatively help explain the low accretion luminosities seen in low-mass protostars, while allowing the protostars to grow in mass on the requisite time scales, although a proper test will require calculations for differing final protostellar masses as well as some constraint on the distribution of angular momenta as a function of protostellar core mass.

Our current models include only a very crude treatment of the activation of the MRI, and this can strongly affect the detailed nature of the outbursts in the inner disk. Better predictions of accretion luminosities will require 3D magnetohydrodynamic simulations which can treat the MRI activation in the innermost disk.

3.7 Acknowledgments

This work was supported in part by NASA grant NNX11AK53G, and computational resources and services provided by Advanced Research Computing at the University of Michigan, Ann Arbor. Z.Z. acknowledges support by NASA through Hubble Fellowship grant HST-HF-51333.01-A awarded by the Space Telescope Science Institute, which is operated by the Association of Universities for Research in Astronomy, Inc., for NASA, under contract NAS 5-26555.

3.8 Appendix: Infall Heating

Here, we derive the infall heating by shock dissipation given in Equation (3.16). Assuming an axisymmetric infall model for simplicity, mass, angular momentum, and energy equations in cylindrical coordinates are

$$R\frac{\partial \Sigma}{\partial t} - \frac{1}{2\pi}\frac{\partial \dot{M}}{\partial R} = R\dot{\Sigma}_{\rm in}, \tag{3.33}$$

$$R\frac{\partial}{\partial t}(\Sigma R^2\Omega) - \frac{1}{2\pi}\frac{\partial}{\partial R}(\dot{M}R^2\Omega) = \frac{\partial}{\partial R}(R^2\Pi_{R\phi}) + R^2\dot{\Sigma}_{\rm in}v_{\phi,\rm in}, \tag{3.34}$$

and

$$R\frac{\partial}{\partial t}(\Sigma E) - \frac{1}{2\pi}\frac{\partial}{\partial R}(\dot{M}E) = RQ_+ - 2R\sigma T^4. \tag{3.35}$$

In the above equations Σ is the surface density, $\dot{M}$ is the radial mass flux defined as $\dot{M} \equiv -2\pi R\Sigma v_R$, $\dot{\Sigma}_{\rm in}$ is the infall rate defined as $\dot{\Sigma}_{\rm in} = \dot{M}_{\rm in}/2\pi R_c R$, Ω is the angular velocity, $\Pi_{R\phi}$ is $R-\phi$ component of the viscous stress tensor, M_* is the stellar mass, R_c is the centrifugal radius, E is the total energy per unit mass except thermal energy, Q_+ includes all heating sources except the infall heating, and T is the disk temperature. Assuming instantaneous

centrifugal balance and $\Pi_{R\phi} = R\Sigma\nu d\Omega/dR$, Equations (3.33) and (3.34) can be simplified to

$$\dot{M} = 6\pi R^{1/2}\frac{\partial}{\partial R}(R^{1/2}\Sigma\nu) + \frac{2\pi R^2\Sigma}{M_*}\frac{\partial M_*}{\partial t} - 4\pi R^2\dot{\Sigma}_{\rm in}\left[\left(\frac{R}{R_c}\right)^{1/2} - 1\right]. \tag{3.36}$$

For the next, combining Equations (3.33) and (3.35) gives

$$\Sigma\frac{\partial E}{\partial t} = Q_+ - \dot{\Sigma}_{\rm in}E + \frac{\dot{M}}{2\pi R}\frac{\partial E}{\partial R} - 2\sigma T^4. \tag{3.37}$$

From now on, let us focus on the terms induced from infall only. By substituting $\dot{M}$ in Equation (3.37) with Equation (3.36) we get the total heating due to infall as follows.

$$Q_{\rm in,total} = -\dot{\Sigma}_{\rm in}E - 2R\dot{\Sigma}_{\rm in}\left[\left(\frac{R}{R_c}\right)^{1/2} - 1\right]\frac{\partial E}{\partial R} \tag{3.38}$$

When it arrives at the disk surface infalling material has velocity of

$$v_R = -\left(\frac{GM_*}{R}\right)^{1/2} \tag{3.39}$$

$$v_\theta = \left(\frac{GM_*}{R}\right)^{1/2}\cos\theta_0 \tag{3.40}$$

$$v_\phi = \left(\frac{GM_*}{R}\right)^{1/2}\sin\theta_0 \tag{3.41}$$

where θ_0 is the angle between the orbital plane and the rotation axis of the system and $\sin^2\theta_0 = R/R_c$ at the disk surface (Cassen & Moosman, 1981). Thus, infalling material brings zero total energy ($E_{\rm tot} = E_{\rm kin} + E_{\rm pot} = GM_*/R - GM_*/R = 0$), while disk material has total energy of $-GM_*/2R$ assuming a Keplerian disk. Using Equation (3.38) the total infall heating that corresponds to the additional energy of infalling material is

$$Q_{\rm in,total} = \frac{GM_*\dot{M}_{\rm in}}{4\pi R_c^3}\frac{3 - 2(R/R_c)^{1/2}}{(R/R_c)^2}. \tag{3.42}$$

At the disk surface, only the kinetic energy corresponding to the v_R and v_θ component of the infall is released instantaneously through the shock, which is $(2 - R/R_c)GM_*/2R$. The

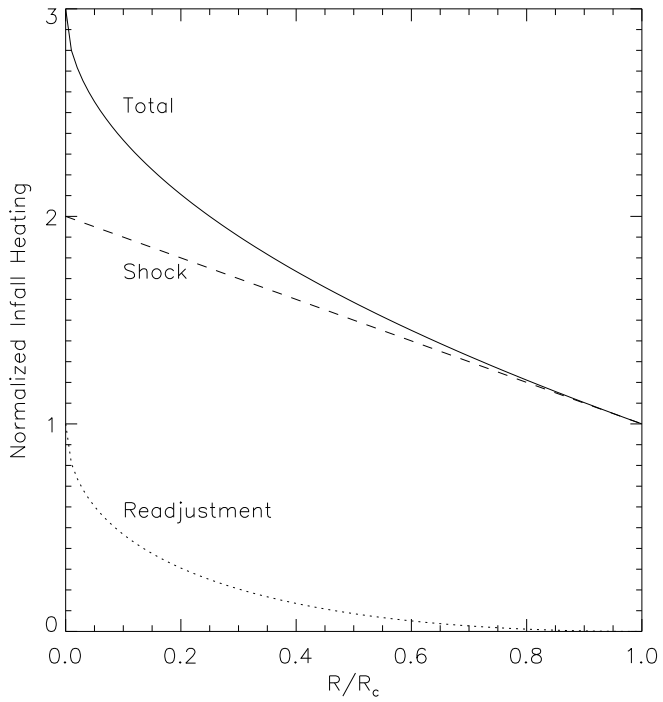

Figure 3.17. Normalized infall heating as a function of radius. The total infall heating is plotted with a solid curve while heating through the instantaneous shock dissipation and the readjustment process are plotted with a dashed and a dotted curve, respectively. At the centrifugal radius R_c infalling material arrives at the disk surface nearly horizontally with the Keplerian azimuthal velocity, so all the kinetic energy is dissipated through shocks.

heat dissipated through the shock dissipation is then

$$Q_{\rm in,shock} = \frac{GM_*\dot{M}_{\rm in}}{4\pi R_c^3}\frac{2-(R/R_c)}{(R/R_c)^2}. \tag{3.43}$$

The rest of the additional energy is taken care by the code with a proper shear force term in the momentum equation, which would correspond to

$$Q_{\rm in,readjust} = \frac{GM_*\dot{M}_{\rm in}}{4\pi R_c^3}\frac{1+(R/R_c)-2(R/R_c)^{1/2}}{(R/R_c)^2}. \tag{3.44}$$

The normalized infall heating profile as a function of radius is presented in Figure 3.17 to show their relative importance at each radius.

CHAPTER IV

Are Protoplanetary Disks Born With Vortices? – Rossby Wave Instability Driven by Protostellar Infall

4.1 Abstract

We carry out two-fluid, two-dimensional global hydrodynamic simulations to test whether protostellar infall can trigger the Rossby wave instability (RWI) in protoplanetry disks. Our results show that infall can trigger the RWI and generate vortices near the outer edge of the mass landing on the disk (i.e. centrifugal radius). We find that the RWI is triggered under a variety of conditions, although the details depend on the disk parameters and the infall pattern. The common key feature of triggering the RWI is the steep radial gradient of the azimuthal velocity induced by the local increase in density at the outer edge of the infall region. Vortices form when the instability enters the nonlinear regime. In our standard model where self-gravity is neglected, vortices merge together to a single vortex within ~ 20 local orbital times, and the merged vortex survives for the remaining duration of the calculation (> 170 local orbital times). The vortex takes part in outward angular momentum transport, with a Reynolds stress of $\lesssim 10^{-2}$. Our two-fluid calculations show that vortices efficiently trap dust particles with stopping times of the order of the orbital time, locally enhancing the dust to gas ratio for particles of the appropriate size by a factor of ~ 40 in our standard model. When self-gravity is considered, however, vortices tend to be impeded from merging and may eventually dissipate. We conclude it may well have that protoplanetary disks have favorable conditions for vortex formation during the protostellar infall phase, which might enhance early planetary core formation. This chapter has been published in the Astrophysical

Journal, Volume 805, 15 (2015), in collaboration with Lee Hartmann and Zhaohuan Zhu.

4.2 Introduction

Dust particles in protoplanetary disks feel drag forces from the gas. In general, the disk gas has outward pressure support and so rotates at sub-Keplerian speeds, whereas grains attempt to move in Keplerian motion. This effect is most significant for the particles that have the stopping time comparable to the orbital time, $t_s\Omega \sim 1$, where t_s and Ω denotes the stopping time and the disk rotation frequency, respectively (Weidenschilling, 1977). Radial drift of dust is thus dependent on the disk conditions under which the particles reside in, but for centimeter to meter-sized particles the resulting radial drift velocity usually reaches a few 10–100 m s^{-1} (Weidenschilling, 1977, 1993; Klahr & Kley, 2006). The corresponding radial drift time at 10 AU, for instance, is less than a few $\times 10^3$ yr which is much shorter than planet formation timescale as well as disk lifetime.

Formation of vortices in protoplanetary disks could be important in the context of planet formation due to their ability to efficiently trap dust particles (Adams & Watkins, 1995; Barge & Sommeria, 1995; Tanga et al., 1996; Bracco et al., 1999; Chavanis, 2000; Fromang & Nelson, 2005; Inaba & Barge, 2006; Heng & Kenyon, 2010; Birnstiel et al., 2013; Zhu & Stone, 2014; Zhu et al., 2014). Anticyclonic vortices – with highest pressure at their centers – are especially important since they can survive long (hundreds of orbits), while cyclonic vortices dissipate quickly (Godon & Livio, 1999). Also, at the core of anticyclones, the radial and azimuthal gas pressure gradients vanish and therefore gas there is in Keplerian motion (Klahr & Kley, 2006). This is an interesting feature of anticyclones because they not only concentrate dust, but once particles reach to the vortex center there is no drag force if turbulence and scattering of particles is absent. Therefore, vortices can be regarded as promising sites of planet formation. In fact, highly non-axisymmetric, vortex-like structures in protoplanetary disks have been observed in submillimeter and millimeter interferometric observations: LkHα 330, SR 21N, HD 135344B (Brown et al., 2009), Oph IRS 48 (van der Marel et al., 2013), HD 142527 (Casassus et al., 2013; Fukagawa et al., 2013), SAO 206462, SR 21 (Pérez et al., 2014), and PDS 70 (Hashimoto et al., 2015).

Possible ways to form vortices in protoplanetary disks are through the Rossby wave instability (RWI; Lovelace et al., 1999; Li et al., 2000, 2001) or the Papaloizou–Pringle instability (Papaloizou & Pringle, 1984, 1985; Hawley, 1987). Generally, the instabilities are triggered by the additional shear arisen from the change of azimuthal velocity gradient over the radius of interest. In two-dimensions, it has been both analytically and numerically shown that the RWI can be triggered at a minimum of the generalized vortensity $\eta \equiv \kappa^2/(2\Sigma\Omega S^{2/\gamma})$ (Lovelace et al., 1999; Li et al., 2000), where κ is the epicyclic frequency, Σ is the surface density, Ω is the rotation frequency, and S is the entropy with the adiabatic index γ. Recent numerical simulations show that the RWI appears to trigger in a similar way in three-dimensions, as in two-dimensions (Meheut et al., 2010, 2012c; Lyra & Mac Low, 2012; Richard et al., 2013; Lin, 2014). The question is then how to make a vortensity minimum in protoplanetary disks? Previously, it has been suggested that a vortensity minimum can form and the RWI is triggered at the edge of the disk dead-zone (Inaba & Barge, 2006; Varnière & Tagger, 2006; Lyra et al., 2008, 2009; Lyra & Mac Low, 2012; Regály et al., 2012) or at the edge of gaps carved by a planet (de Val-Borro et al., 2007; Lin, 2014).

In this Chapter, we propose another mechanism that possibly drives the RWI in protoplanetary disks: protostellar infall. This is partly motivated by the recent ALMA image of HL Tau[1] showing multiple ring and gap structures which might be generated by planets. We focus on the fact that HL Tau is embedded in an envelope from which it still accretes material (Beckwith et al., 1989; Hayashi et al., 1993). If the gaps in the ALMA image are indeed a signature of planets, this implies that planet formation can happen in the very early phase of protostellar evolution. Our simulations show that protostellar infall from natal cloud can generate local vortensity minimum near the centrifugal radius, inside of which radius infalling material falls onto the disk, and can trigger the RWI. While the RWI activity depends on the characteristics of infall model (e.g. radial infall profile, existence of shear between infall and disk material) as well as disk parameters (e.g. viscosity parameter), we find that the RWI can be triggered under a broad circumstance and is a possible way to form vortices. Our results suggest that vortices can form during very early evolution of protostellar systems, and this may ease the timescale problem for giant planet formation.

[1] http://www.eso.org/public/news/eso1436

4.3 Numerical Methods

4.3.1 Infall Model

The infall model is implemented by adding the corresponding terms to the hydrodynamic equations as below.

$$\frac{\partial \Sigma_g}{\partial t} + \nabla \cdot (\Sigma_g v_g) = \dot{\Sigma}_{\rm in} \tag{4.1}$$

$$\Sigma_g \left(\frac{\partial v_g}{\partial t} + v_g \cdot \nabla v_g \right) = -\nabla P_g - \Sigma_g \nabla \Phi + \nabla \cdot \Pi_g + F_{\rm in} \tag{4.2}$$

In the above equations Σ_g is the gas surface density, v_g is the gas velocity, $P_g = \Sigma_g c_s^2$ is the vertically integrated gas pressure, Φ is the gravitational potential including the disk self-gravitational potential (if considered), Π_g is the viscous stress tensor for gas, respectively. The terms $\dot{\Sigma}_{\rm in}$ and $F_{\rm in}$ indicate the changes in the equations due to the infall model, where $\dot{\Sigma}_{\rm in}$ is the mass infall rate and $F_{\rm in}$ is the shear force. We note that in our standard model we look at the effect of density enhancement only by matching velocities of infalling material and disk material ($F_{\rm in} = 0$). The shear term $F_{\rm in}$ in the momentum equation is added later in the model where the shear in between infalling material and disk material is considered (see below and Table 4.1).

In the original work of Ulrich (1976) and Cassen & Moosman (1981), the collapse of an isothermal, spherically symmetric, and uniformly rotating cloud was studied. The infalling material follows parabolic orbits, arriving at the disk surface with different radial and azimuthal velocities from those of the disk material. Therefore, shear force exists which can be written as $F_{R,\rm in} = \dot{\Sigma}_{\rm in}(v_{R,\rm in} - v_{R,\rm disk})$ and $F_{\phi,\rm in} = \dot{\Sigma}_{\rm in}(v_{\phi,\rm in} - v_{\phi,\rm disk})$. Here, $v_{R,\rm in} = -(GM_*/R)^{-1/2}$ and $v_{\phi,\rm in} = (GM_*/R_c)^{-1/2}$ are the velocities of the infalling material with R_c being the centrifugal radius (Cassen & Moosman, 1981), and $v_{R,\rm disk}$ and $v_{\phi,\rm disk}$ are the velocities of the disk, respectively.

We consider two modifications of the infall model introduced in Ulrich (1976) and Cassen & Moosman (1981). First, we simplify the model in a such way that the radial and azimuthal velocities of the infalling material match those of disk material and thus no shear force exists (hereafter UCM model). One notable feature of the infall model of Ulrich (1976) and Cassen

& Moosman (1981) is that because of the solid-body rotation the infalling material near the rotational axis has less angular momentum and thus falls at small radius while the infalling material far from the rotational axis have more angular momentum and falls at large radius. This will concentrate infalling material near the outer edge of the infall (i.e. centrifugal radius). In order to alleviate the relatively strong density enhancement around the centrifugal radius, we consider another modification (hereafter MUCM model). In the MUCM model, the radial infall pattern is modified in a such way that mass flux per unit distance is constant over radius in order to avoid the singularity in density of the infalling material at the centrifugal radius (see below and Figure 2.1 of Chapter 2 for comparison between UCM and MUCM model).

The mass infall rate of the UCM model is

$$\dot{\Sigma}_{\rm in}(R) = \frac{\dot{M}_{\rm in}}{4\pi R_c R}\left(1-\frac{R}{R_c}\right)^{-1/2} \text{ if } R \le R_c \tag{4.3}$$

and

$$\dot{\Sigma}_{\rm in}(R) = 0 \text{ if } R > R_c, \tag{4.4}$$

where $\dot{M}_{\rm in} = 0.975 c_{sc}^3/G$ is the constant total infall mass rate at a given cloud isothermal sound speed c_{sc} for the singular sphere solution (Shu, 1977).

In the MUCM model, the mass infall rate is smoothed as

$$\dot{\Sigma}_{\rm in}(R) = \frac{\dot{M}_{\rm in}}{2\pi R_c R} \text{ if } R \le R_c \tag{4.5}$$

and

$$\dot{\Sigma}_{\rm in}(R) = 0 \text{ if } R > R_c. \tag{4.6}$$

Table 4.1. Model Parameters for Vortex Formation Calculations

Models	Case Name	α	R_c (AU)	Shear Terms	Numerical Resolution ($N_r \times N_\phi$)	Infall Model	Self-gravity
Standard Model (§4.4.1)	S	10^{-4}	25, fixed	N	512×1024	UCM	N
Numerical Resolution (§4.4.2)	NR256	10^{-4}	25, fixed	N	256×512	UCM	N
	NR1024	10^{-4}	25, fixed	N	1024×2048	UCM	N
	NR2048	10^{-4}	25, fixed	N	2048×4096	UCM	N
Viscosity (§4.4.3)	V2	10^{-2}	25, fixed	N	512×1024	UCM	N
	V3	10^{-3}	25, fixed	N	512×1024	UCM	N
	V5	10^{-5}	25, fixed	N	512×1024	UCM	N
Increasing R_c (§4.4.4)	IRC2	10^{-4}	25, linearly increasing 2 AU per 1000 yr	N	512×1024	UCM	N
	IRC5	10^{-4}	25, linearly increasing 5 AU per 1000 yr	N	512×1024	UCM	N
Shear Terms (§4.4.5)	SH	10^{-4}	25, fixed	Y	512×1024	UCM	N
Infall Model (§4.4.6)	MUCM	10^{-4}	25, fixed	N	512×1024	MUCM	N
Self-gravity (§4.4.7)	SG	10^{-4}	25, fixed	N	512×1024	UCM	Y

4.3.2 Dust Component

In order to investigate the dust response to RWI-generated gas structures, we use the FARGO code (Masset, 2000) that is modified to deal with two fluids as introduced in Zhu et al. (2012b). We treat the dust component as an inviscid, pressureless fluid and dust simply feels the drag force in addition to the central stellar potential. Note that the dust component in our calculations evolves passively and does not affect gas evolution and therefore the RWI. Dust feedback may become important at least locally in vortices (e.g. Fu et al., 2014b) but the effect is not considered in the present study.

The drag terms are added in an additional source step as

$$\frac{\partial v_{R,d}}{\partial t} = -\frac{v_{R,d} - v_{R,g}}{t_s} \tag{4.7}$$

and

$$\frac{\partial v_{\phi,d}}{\partial t} = -\frac{v_{\phi,d} - v_{\phi,g}}{t_s}, \tag{4.8}$$

where v_d and v_g denote dust and gas velocities, and t_s is the dust stopping time. With the initial setup explained below in §4.3.3, the mean free path of gas molecules is $\lambda = 3.8\ (R/1\ \mathrm{AU})^{9/4} \exp(R/R_c)$ cm so in our simulation domain the dust particles smaller than ~ 1 m are in the Epstein regime (Whipple, 1972; Weidenschilling, 1977). Therefore, the dust stopping time can be written as

$$t_s = \frac{\rho_p s}{\rho_g v_T}, \tag{4.9}$$

where ρ_p is the dust particle density, s is the dust particle radius, ρ_g is the gas density, and $v_T = \sqrt{8/\pi} c_s$ is the mean thermal velocity with c_s being the gas sound speed (Takeuchi & Lin, 2002). The dust particle density is assumed to be $\rho_p = 1$ g cm^{-3} in this study. With the two-dimensional approach the gas mass density is $\rho_g = \Sigma_g / \sqrt{2\pi} H$ and thus the dust stopping time can also be written as

$$t_s = \frac{\pi \rho_p s}{2 \Sigma_g \Omega}, \tag{4.10}$$

where Ω is the Keplerian angular velocity. The stokes number, or the nondimensional stop-

ping time, T_s is then

$$T_s = t_s \Omega. \tag{4.11}$$

In this work, we consider two different dust sizes: small dust particles that have $T_s \sim 0.1$ and large dust particles that have $T_s \sim 1$, under the initial conditions explained in the next section. In physical size, the former and latter corresponds to 1 cm and 10 cm, respectively.

4.3.3 Initial Conditions

We begin with a 0.5 $M_\odot$ central protostar and a surrounding disk having an initial gas density distribution of $\Sigma(R) = 1000\ (R/\mathrm{AU})^{-1}\exp(-R/R_c)$ g cm^{-2}. Here, R_c is the centrifugal radius which is fixed to 25 AU during the calculations unless otherwise stated. We assume a constant infall rate of $3.0 \times 10^{-6}\ M_\odot\,\mathrm{yr}^{-1}$ which corresponds to a singular isothermal collapse (Shu, 1977) of a 16 K protostellar cloud. The disk mass is 0.014 $M_\odot$ initially and is $\sim 0.11 - 0.13\ M_\odot$ at the end of calculations, depending on model parameters. We adopt a fixed radial temperature distribution ($T \propto R^{-1/2}$) that corresponds to a ratio of disk scale height to radius $H/R = 0.05\ (R/1\ \mathrm{AU})^{0.25}$. Initial random perturbation is applied to surface density at the level of 10^{-4}.

We use inner and outer boundaries of 5 and 100 AU and adopt 512 logarithmically spaced radial grid-cells and 1024 linearly spaced azimuthal grid-cells. With this choice, $\Delta R/R$ is constant to 0.006 and grid-cells have comparable radial and azimuthal size at all radii. In §4.4.2, we discuss the effect of numerical resolution and show the results converge resolutions at 512×1024 and beyond.

We use $\alpha = 10^{-4}$ for our fiducial viscosity parameter. Using a relatively low disk viscosity is motivated by the fact that stellar X-rays and FUV photons are likely to be blocked by infalling material during the protostellar phase so that ionization level at disk surface layers remains low, limiting mass transport through the magnetorotational instability. The effect of the viscosity parameter is tested in §4.4.3. Model parameters are summarized in Table 4.1.

4.3.4 Boundary Conditions

In order to prevent unphysical, rapid depletion of material at the inner boundary, we implement a velocity limiter as introduced in Pierens & Nelson (2008) and Zhu et al. (2012b). To briefly summarize, we limit the radial velocities of the gas component at the inner boundary to be no more than some factors of the viscous radial velocity in a steady state, $v_{R,\mathrm{vis}}$: $v_{R,g} \leq \beta v_{R,\mathrm{vis}}$. Here, $v_{R,\mathrm{vis}} = -3\nu_{\mathrm{in}}/2R_{\mathrm{in}}$ where ν_{in} and R_{in} are the viscosity and radius at the inner boundary. Based on a set of experiments, we find that $\beta = 3$ is most suitable for this study.

A similar approach is implemented for the dust component, following Zhu et al. (2012b). In case of dust, we limit radial velocity to be no more than three times of the dust drift speed in a viscous disk $v_{R,\mathrm{drift}}$, where $v_{R,\mathrm{drift}}$ is defined as

$$v_{R,\mathrm{drift}} = -\frac{(3\nu_{\mathrm{in}}/2R_{\mathrm{in}})T_s^{-1} + \eta v_K}{T_s + T_s^{-1}}. \tag{4.12}$$

Here, η is the ratio between the pressure gradient and gravitational force defined as $\eta \equiv -(R\Omega^2\rho_g)^{-1}\partial P/\partial R$, and v_K is the Keplerian speed.

At the outer boundary, standard open boundary conditions are implemented for both gas and dust components.

4.4 Results

4.4.1 Standard Model: Results With the UCM Model

We start with our standard model, showing details of the launching, growth, and saturation of the RWI and dust's response. Then, in the following subsections we present how varying disk conditions and infall pattern affect the RWI activity.

4.4.1.1 Launching of the RWI

In two-dimensions, one can analytically show that the RWI can be triggered at a radial minimum of the generalized vortensity η, where

$$\eta = \frac{\kappa^2}{2\Sigma\Omega}\frac{1}{S^{2/\gamma}} \tag{4.13}$$

(Lovelace et al., 1999; Li et al., 2000). Here, $\kappa = [R^{-3}d(R^4\Omega^2)/dR]^{1/2}$ is the epicyclic frequency, Σ is the surface density, Ω is the rotational frequency, and $S = P/\Sigma^\gamma$ is the entropy. Given that we assume a locally isothermal temperature profile which is unchanged over time, the above equation can be written as

$$\eta = \frac{\kappa^2}{2\Sigma\Omega}\frac{1}{c_s^4}. \tag{4.14}$$

For convenience we call the quantity η as vortensity hereafter.

Figure 4.1 shows radial distributions of azimuthally averaged gas surface density, azimuthal velocity, epicyclic frequency, and vortensity at the time of the launching of the RWI. The density gradient and thus the pressure gradient becomes steeper on the outer part of the density bump as infall adds mass onto the disk. The steep pressure gradient then generates a steeper azimuthal velocity profile in order to maintain the radial force balance. The resulting azimuthal velocity slope deviates from -0.5, which is for the Keplerian rotation, and approaches to -1. We note that the -1 slope is important in triggering the RWI since κ^2 and η change sign at $v_\phi \propto R^{-1}$. This can be simply shown by substituting κ^2 into Equation (4.14):

$$\eta = \frac{1}{2\Sigma\Omega}\frac{1}{c_s^4}\frac{1}{R^3}\frac{d}{dR}(R^2 v_\phi^2). \tag{4.15}$$

In Keplerian disks where $v_\phi \propto R^{-1/2}$, η is always positive. However, η becomes zero if $v_\phi \propto R^{-1}$ and is negative if v_ϕ has a steeper slope than -1.

Figure 4.2 presents the maximum value of non-axisymmetric density perturbation $\delta\Sigma_g/\langle\Sigma_g\rangle$ as a function of time, where $\delta\Sigma_g = \Sigma_g - \langle\Sigma_g\rangle$ and the brackets denote the azimuthal average.

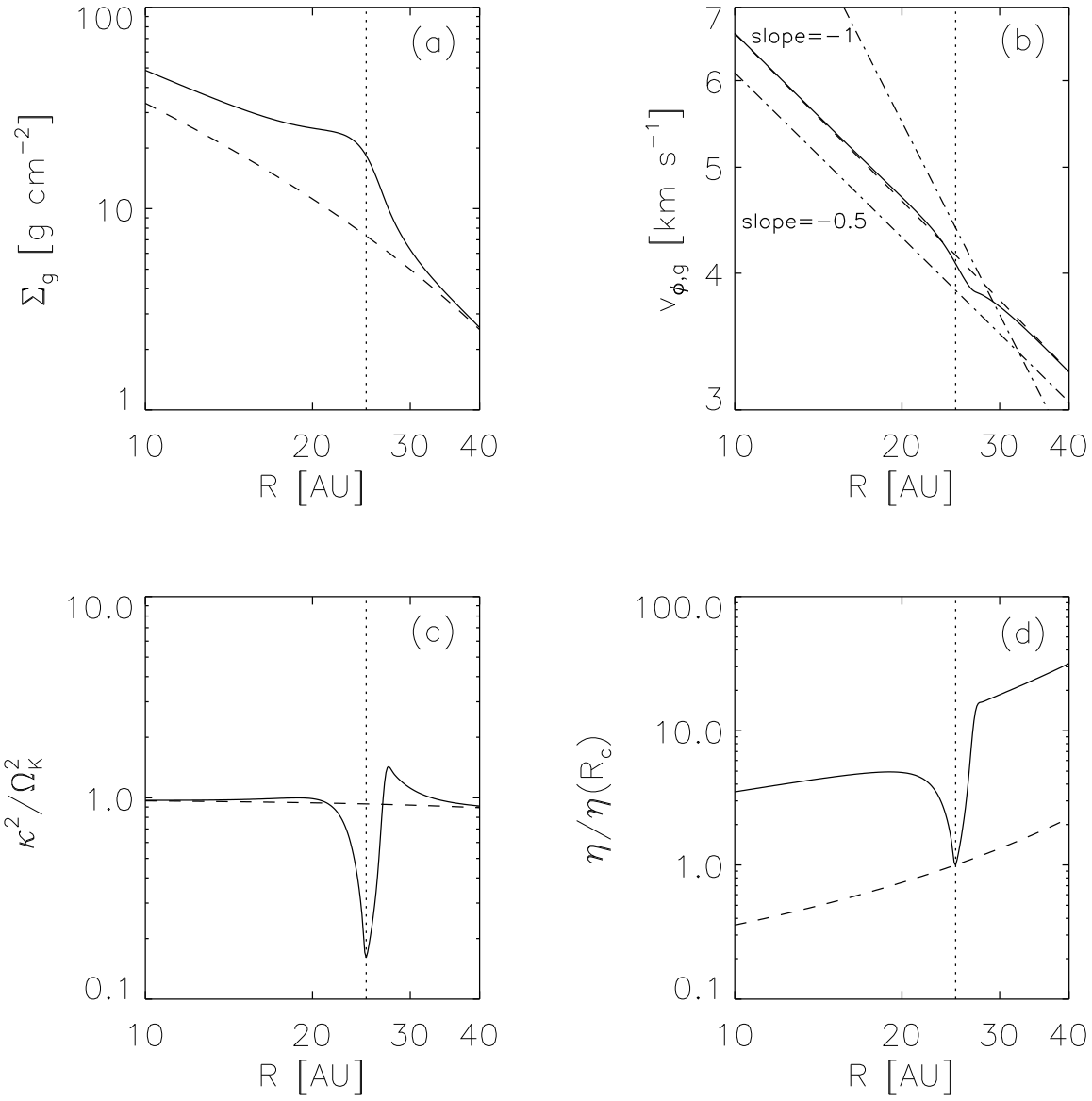

Figure 4.1. Radial distributions of azimuthally averaged (a) gas surface density Σ_g, (b) gas azimuthal velocity $v_{\phi,g}$, (c) epicyclic frequency κ^2/Ω_K^2, and (d) vortensity $\eta/\eta(R_c)$ at the launching of the RWI ($t = 14$ orbital times at R_c; see Figure 4.2) for the standard model. Dashed curves show the initial distributions. The centrifugal radius R_c is indicated with vertical dotted lines. In panel (b), two dotted–dashed lines show slopes of -1 and -0.5, respectively. We note that the density bump generates a steep azimuthal velocity gradient around R_c in order to maintain the radial force balance, which results in the κ^2 and η minima.

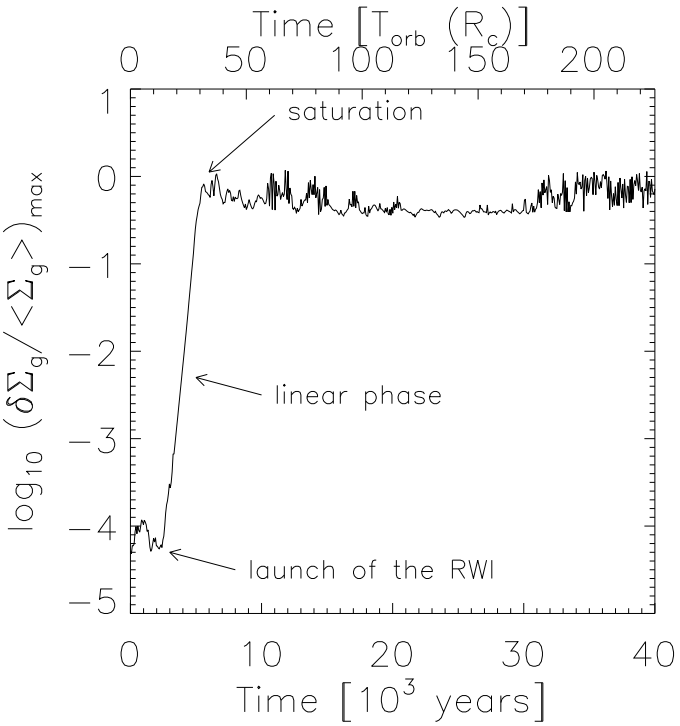

Figure 4.2. The maximum value of non-axisymmetric gas density perturbation $\delta\Sigma_g/\langle\Sigma_g\rangle$ is shown as a function of time. The instability triggers at 14 $T_{\rm orb}$ and grows exponentially during the 'linear' phase ($14\ T_{\rm orb} \lesssim t \lesssim 30\ T_{\rm orb}$). Then the instability saturates and turns into the nonlinear regime thereafter.

Initially before the RWI triggers, the maximum perturbed density maintains $\sim 10^{-4}$ which corresponds to the initial random component. The vortensity minimum develops gradually until the instability triggers at $t \sim 14\ T_{\rm orb}$, where $T_{\rm orb}$ hereafter denotes the local orbital time at the centrifugal radius.

4.4.1.2 Growth and Saturation of the RWI

After the instability is triggered, it grows in the 'linear' regime where the growth of the perturbed density is well described by the linearized continuity equation $\partial(\delta\Sigma)/\partial t = -i\tilde{\omega}\delta\Sigma$, where $\tilde{\omega} = \omega + i\gamma$ is a complex frequency, ω is the real mode frequency, and γ is the growth rate. This is clearly seen in Figure 4.2 – the instability grows exponentially during the linear phase ($14\,T_{\rm orb} \lesssim t \lesssim 30\,T_{\rm orb}$). The growth timescale $T_{\rm growth}$, during which time the maximum perturbed density increases by a factor of e, is 1.8 $T_{\rm orb}$. After spending 16 $T_{\rm orb}$ in the linear phase, the instability saturates and enters the nonlinear regime.

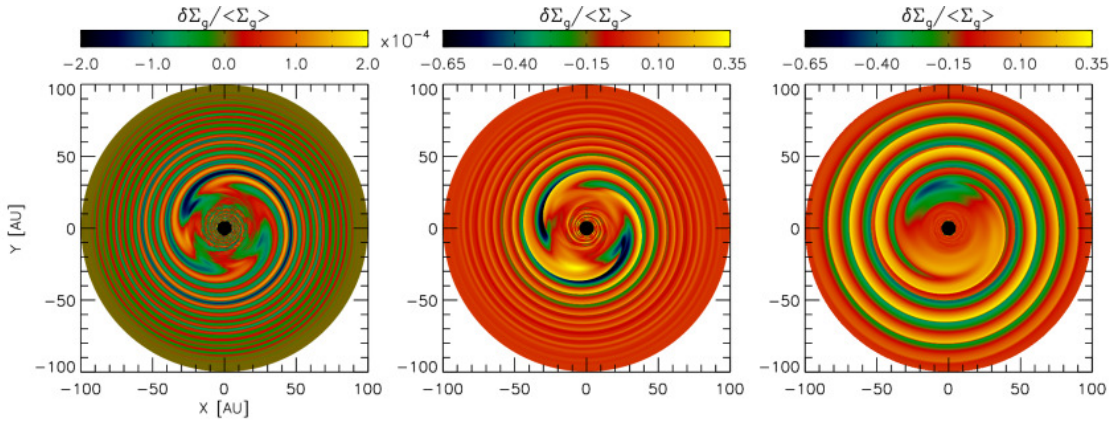

Figure 4.3. Perturbed gas density distributions $\delta\Sigma_g/\langle\Sigma_g\rangle$ of the standard model at the launching of the instability, at the saturation, and at the end of the simulation (from left to right). These correspond to 14, 30, and 226 local orbital times at R_c or $t = 2.5, 5.3$, and 40×10^3 yr. Note that the scale for the leftmost panel is different from the other two.

Figure 4.3 shows the spatial distributions of the perturbed gas density at the launching of the instability ($t = 14\ T_{\rm orb}$), at its saturation ($t = 30\ T_{\rm orb}$), and at the end of the simulation ($t = 226\ T_{\rm orb}$). Initially, the $m = 4$ mode is dominant but it quickly merges to $m = 3$ mode during the linear phase, and eventually merges to $m = 1$ mode which is maintained until the end of the calculation.

4.4.1.3 Vortex Formation and Dust Response

The RWI accompanies vortex formation as the instability enters the nonlinear regime. Figure 4.4 illustrates gas vorticity, gas surface density, and surface densities of 1 cm and 10 cm dust particles on the $\phi - R$ coordinates. The (negative) vorticity minimum grows at R_c as infall proceeds. At the time the RWI initiates ($t = 14\ T_{\rm orb}$), the non-axisymmetric features are still too small to be seen. As the instability grows, the radial vorticity minimum starts to develop structure and finally breaks into vortices when the instability enters the nonlinear regime ($t = 30\ T_{\rm orb}$). Vortex formation during nonlinear evolution of the RWI is in good agreement with previous hydrodynamic simulations (e.g. Li et al., 2001). The important feature is that the vortices have a local vorticity minimum at its center – the vortices are anticyclones. The vortices wander in azimuth, merge together, and form a single vortex within $\sim 20\ T_{\rm orb}$ from their formation. The merged vortex survives until the end of the calculation and we did not follow its evolution thereafter.

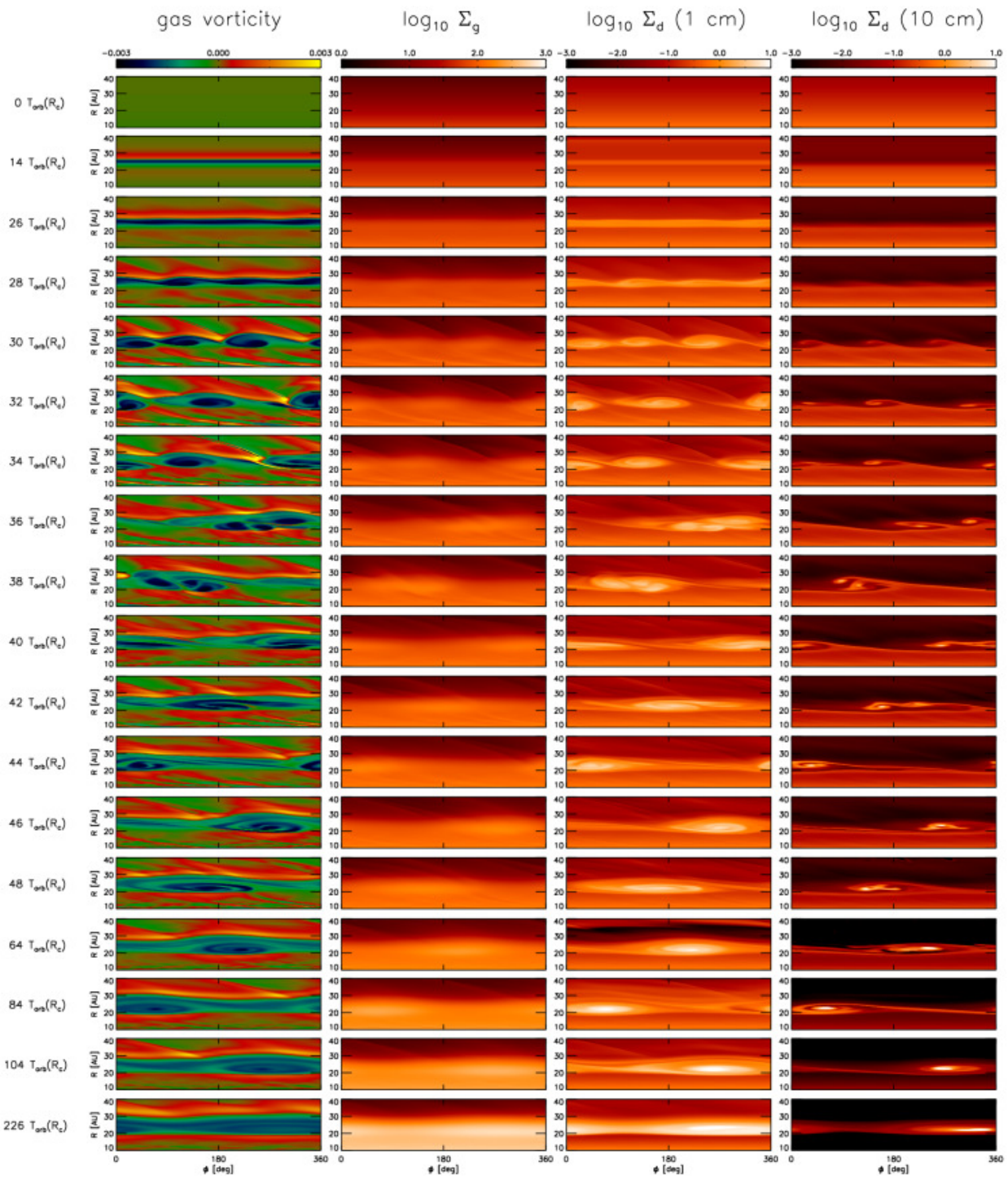

Figure 4.4. Snapshots of gas vorticity $\nabla \times v_g$, gas density, 1 cm particle density, 10 cm particle density at selected times. Times are presented on the left side in units of $T_{\rm orb}$. The Keplerian component in the azimuthal velocity is subtracted when calculating the vorticity. Densities are in cgs units and displayed in the logarithmic scale.

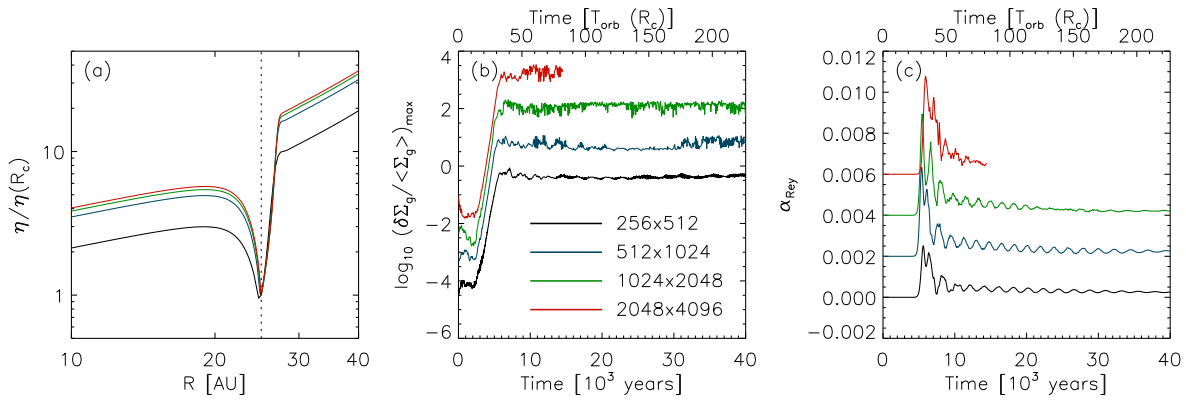

Figure 4.5. (a) Radial distribution of the azimuthally averaged $\eta/\eta(R_c)$ at $t = 14\ T_{\rm orb}$. (b) Maximum perturbed gas density $\delta\Sigma_g/\langle\Sigma_g\rangle$ as a function of time. (c) The Reynolds stress as a function of time. In panel (b) and (c), the plots are shifted vertically by 1 and 0.002, respectively, for better view. We note that the oscillating feature of $\alpha_{\rm Rey}$ is due to the epicyclic motion of gas inside vortices against the geometric center of the vortices. Since it requires a lot of computational resources the highest resolution run is conducted only for 80 $T_{\rm orb}$.

Before the vortices form, dust particles are concentrated at the vorticity minimum while the small and the large dust behave somewhat differently. Initially when the instability grows in the linear phase, small dust concentrate around the gas pressure maximum. On the other hand, the large particles have the greatest inward drift velocity at the centrifugal radius ($T_s \sim 1$ at R_c), so the density drops at the radius. The large dust distribution shows a steep density change around R_c (see Figure 4.4 at $t = 14$ and 26 $T_{\rm orb}$). This is because infall adds gas inside R_c and thus the dust stopping time correspondingly decreases significantly at the region, slowing down the large dust migrating inward.

After the vortices form, they efficiently trap dust particles so that the dust distributions show stronger asymmetry than the gas distribution. While the small particles are well coupled to gas and follow the gas vorticity distribution well, the large particles show highly perturbed behavior. The accumulated cores of large dust are often offset from the vortex cores. This is more significant in earlier times when the vortices merge (see Figure 4.4 at $t = 38$ and 40 $T_{\rm orb}$ for example). Also, the large dust particles show more dramatic concentration than small dust particles. We will discuss dust trapping and its implication later in §4.5.1.

4.4.2 Effect of Numerical Resolution

As mentioned in §4.3.1, the UCM model has a singularity (infinite mass infall rate per unit area) at the centrifugal radius while the total infall rate is finite. With finite grids this can cause non-convergent behavior at different numerical resolutions. Thus, we need to show that our results are not dependent on the numerical resolution before we go to further analysis. We test with four different numerical resolutions of $(N_R, N_\phi) = (256, 512), (512, 1024), (1024, 2048)$, and $(2048, 4096)$.

We use three different diagnostics to check the numerical convergence. First, we check the position, shape, and depth of the vortensity minimum since it is crucial for triggering the RWI. Second, we use the maximum value of the perturbed gas density. For the last, we calculate the Reynolds stress which is defined as

$$\alpha_{\rm Rey} = \frac{\int \Sigma_g \delta v_{R,g} \delta v_{\phi,g} \, dS}{\int \Sigma_g c_s^2 \, dS}, \tag{4.16}$$

where the integration is done in a volume-averaging manner, and $\delta v_{R,g} = v_{R,g} - \langle v_{R,g} \rangle$ and $\delta v_{\phi,g} = v_{\phi,g} - \langle v_{\phi,g} \rangle$. The first two quantities check the convergence of local features whereas $\alpha_{\rm Rey}$ checks the numerical convergence in a globally averaged sense.

The three diagnostics are presented in Figure 4.5. All diagnostics converge well at 512×1024 and beyond. With 256×512 grid cells, the region around the R_c is not very well resolved so that the infall rate seems underestimated at the region. The vortensity minimum with 256×512 grids is significantly shallower and broader than others (see also Table 4.2 for the minimum κ^2/Ω_K^2 values), and thus the instability growth and the Reynolds stress are less significant.

4.4.3 Effect of Viscosity

Since larger gas viscosity more efficiently spreads out the density enhancement, it is possible to broaden the vortensity minimum and limit the RWI growth. We tested different viscosity parameters to see the effect of disk viscosity; $\alpha = 10^{-2}, 10^{-3}, 10^{-4}$, and 10^{-5}. As expected, Figure 4.6 shows that the vortensity minimum becomes broader as α increases. Especially with $\alpha = 10^{-2}$, the minimum is very shallow and broad. In this case, the RWI triggers but

Table 4.2. Results for Vortex Formation Calculations

Case Name	RWI	κ^2/Ω_K^2 [a]	$T_{\rm launch}$ [b] ($T_{\rm orb}$)	$T_{\rm sat}$ [b] ($T_{\rm orb}$)	$T_{\rm growth}$ [b] ($T_{\rm orb}$)	Vortex Formation
S	Y	0.16	14	30	1.8	Y
NR256	Y	0.24	13	29	2.1	Y
NR1024	Y	0.15	14	30	1.7	Y
NR2048	Y	0.15	16	32	1.7	Y
V2	Y[c]	0.62	22	-	2.2	N
V3	Y	0.25	18	36	2.1	Y
V5	Y	0.15	14	30	1.8	Y
IRC2	Y	0.28	22	33	2.2	Y
IRC5	Y[c]	0.60	24	-	5.3	N
SH	Y	0.03	8	19	1.2	Y
MUCM	Y	0.35	54	110	5.5	Y
SG	Y	0.15	14	32	1.9	Y[d]

[a]The κ^2/Ω_K^2 values are measured at the launching of the RWI.

[b]The times correspond to the launching of the RWI ($T_{\rm launch}$), the saturation of the RWI ($T_{\rm sat}$), and the exponential growing timescale ($T_{\rm growth}$).

[c]The instability is triggered but stays only in the linear regime and withers away before it enters the nonlinear phase.

[d]Multiple vortices form as the RWI enters the nonlinear regime, but they later dissipate as the disk becomes gravitationally unstable.

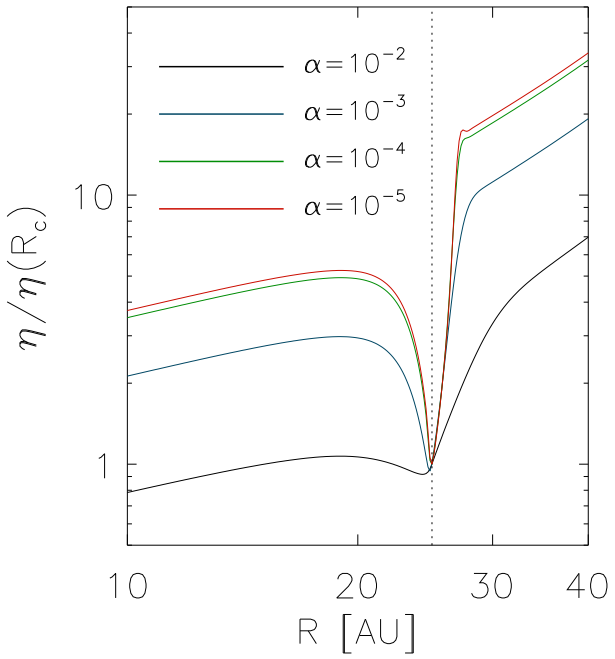

Figure 4.6. Radial distribution of azimuthally averaged $\eta/\eta(R_c)$ at $t = 14\,T_{\rm orb}$ with $\alpha = 10^{-2}$, 10^{-3}, 10^{-4} (standard model), and 10^{-5}. The vortensity minimum is very shallow and broad with $\alpha = 10^{-2}$. In this case, the RWI grows only in the linear regime and does not further develop to the nonlinear regime.

it only stays in the linear regime and does not turn into the nonlinear regime – we therefore do not observe any vortices forming and concentration of dust particles.

It has been empirically shown that the width of the vortensity minimum has to be $\lesssim 2H$ in order for the RWI to develop (Lyra et al., 2009; Regály et al., 2012). If we adopt this criterion, the RWI growth can be limited if the local viscous timescale at R_c, in which time the disk can viscously spread out the bump by $\sim H$, is shorter than the RWI growing timescale. The local viscous timescale estimated at R_c is $t_\nu = H^2/\nu \sim (0.11R)^2/\nu \sim 90/\alpha$ yr. With $\alpha = 10^{-2}$, the local viscous timescale is ~ 9000 yr (or $\sim 51\,T_{\rm orb}$) which is approximately the timescale of the linearly growing part of the RWI. Thus, it makes sense that the instability with $\alpha = 10^{-2}$ does not further grow and turn into the nonlinear regime. On the other hand, viscosity does not affect triggering of the RWI when the viscous timescale is much longer than the RWI growing timescale.

4.4.4 Effect of Linearly Increasing Centrifugal Radius With Time

In protoplanetary disks, the centrifugal radius will generally not be constant with time as material with even greater angular momentum falls in; this will spread the vortensity minimum. Instead of implementing a more self-consistent time evolution of the centrifugal radius (e.g. Cassen & Moosman, 1981), we mimic the effect by simply linearly increasing R_c as a function of time. We test with two different rates: R_c increases at 2 and 5 AU per 1000 yr.

In order to see how the R_c increasing rates translate to initial core rotation, let us assume that the protostellar system we consider in this study evolves from the initial Bonner–Ebert sphere-like two-component density profile (see Zhu et al., 2010b), and the inner flat core has collapsed to a 0.1 $M_\odot$ central protostar and the rest of the cloud collapses as a rotating singular isothermal sphere. If we further assume that the disk mass inside of our inner boundary ($R_{\rm in} = 5$ AU) is negligible, our model is $\sim 1.3 \times 10^5$ yr past from the initial core collapse. Then, the increasing rates of R_c we adopt here correspond to the instantaneous R_c increasing rate of uniformly rotating cores at $\Omega_c = 5.3 \times 10^{-14}$ and 8.3×10^{-14} rad s^{-1}. The rotation frequencies are 20 and 30 % of the breakup angular frequency at the outer edge of an 1 $M_\odot$ cloud. It is worth to point out that the rotation frequencies are large compared to the median value of 3 % inferred later in Chapter 8 of this thesis; the value was required to reproduce the observed circumstellar disk frequencies as a function of age, assuming disk dispersal by photoevaporation.

Figure 4.7 shows radial distributions of vortensity minimum for the models. The RWI excites and generates vortices with small increasing rate of 2 AU per 1000 yr. However, if R_c increases fast at 5 AU per 1000 yr the RWI triggers but stays only in the linear regime. The instability with the large rate eventually withers away and no vortices form in this case. Although a more self-consistently evolved model is require to conclude, in very rapidly rotating systems the centrifugal radius may move outward so fast that the RWI may not have chance to form vortices.

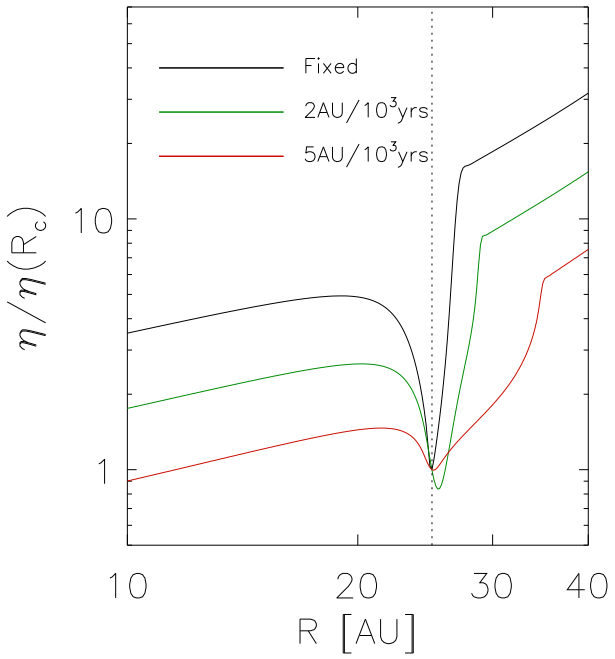

Figure 4.7. Radial distributions of the azimuthally averaged $\eta/\eta(R_c)$ with fixed R_c at 25 AU (standard model) and linearly increasing R_c at rates of 2 AU and 5 AU per 1000 yr. Although the vortensity minimum is seen in all models, the RWI grows only in the linear regime when the centrifugal radius increases 5 AU per 1000 yr.

4.4.5 Effect of Shear Terms

In actual protostellar systems, the infalling material must have different specific angular momentum or azimuthal velocity than the disk material when it lands on the disk. Otherwise, the mass would not fall in. We test the effect of shear by adopting velocity fields of infalling material that follows parabolic orbits. Following Ulrich (1976) and Cassen & Moosman (1981), the infalling material has radial and azimuthal velocities of $v_{R,\rm in} = -(GM_*/R)^{-1/2}$ and $v_{\phi,\rm in} = (GM_*/R_c)^{-1/2}$. So at $R = R_c$ both radial and azimuthal velocities of infalling material are the same as the Keplerian velocity at the radius. We note that the radial velocity of infalling material is extremely large when compared to the accretion velocity in the steady-state α disk. In an α disk, the accretion rate can be described as $\dot{M}_{\rm acc} \simeq 3\pi\nu\Sigma$ since we are interested in the region far from the stellar surface. Then, if we relate it to $\dot{M}_{\rm acc} = -2\pi R\Sigma v_{R,\rm disk}$ we get $v_{R,\rm disk} = -(3/2)\alpha c_s(H/R)$. Thus, $v_{R,\rm disk}/v_{R,\rm in} = (3/2)\alpha(H/R)^2 \ll 1$.

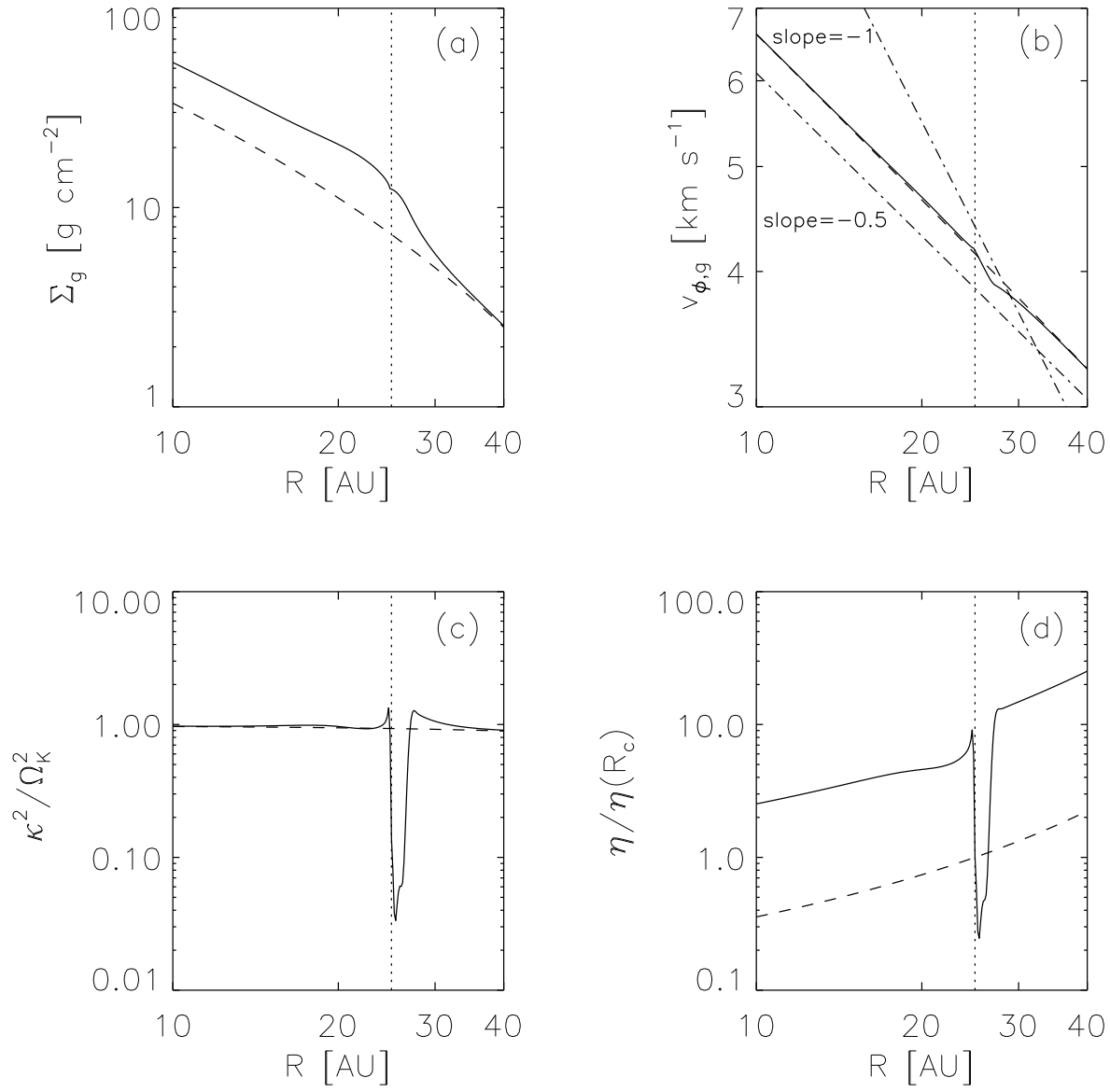

Figure 4.8. Same as Figure 4.1 but at $t = 8\ T_{\rm orb}$ for the SH model (shear terms are included). We emphasize that the vortensity minimum is much sharper and narrower compared to the standard model (see Figure 4.1d).

Due to the large inward radial velocity of the infalling material, the disk develops a very sharp density jump at the centrifugal radius. Therefore, compared to the standard model where no shear terms are included, the vortensity minimum is much sharper and narrower as seen in Figure 4.8. In this model the shear from infall rapidly builds the vortensity minimum, whereas in the standard model the disk has to wait until enough mass is added to build the density bump. Thus, no evident density bump is developed around R_c at the time of RWI initiation. Another notable feature is that the RWI initially triggers with an extremely high order mode of $m = 9$ as seen in Figure 4.9, at which mode the linear growth rate is the highest in this model. The perturbed density peaks rotate at slightly different velocities and thus one catches another as time goes. They eventually merge to $m = 1$ mode at $t \sim 100\ T_{\rm orb}$.

4.4.6 Effect of Infall Profile: With the Modified UCM Model

The UCM model, as pointed out earlier, adds a large fraction of infalling material near the centrifugal radius. In order to see if the RWI can be limited by more gentle infall pattern, we match the radial infall pattern to the initial disk surface density distribution ($\Sigma_g, \dot{\Sigma}_{\rm in} \propto R^{-1}$). Even with the smoothed infall profile we find that the RWI excites. Figure 4.10 presents radial distributions of azimuthally averaged gas surface density, azimuthal velocity, epicyclic

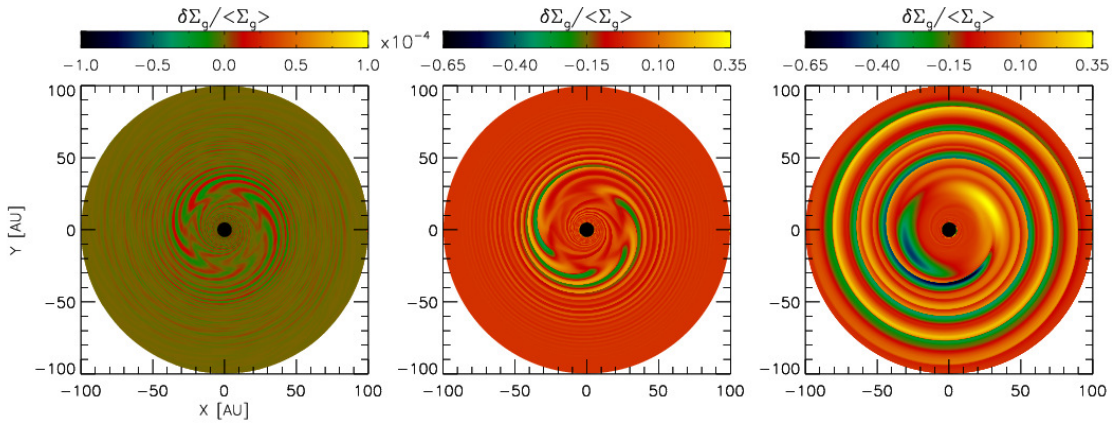

Figure 4.9. Perturbed gas density $\delta\Sigma_g/\langle\Sigma_g\rangle$ distributions at the launching of the instability, at the saturation, and at the end of the simulation (from left to right) for the SH model (shear terms are included). These correspond to $t = 8, 19$, and 226 $T_{\rm orb}$ or 1.4, 3.4, and 40×10^3 yr. Note that the scale for the leftmost panel differs from the other two.

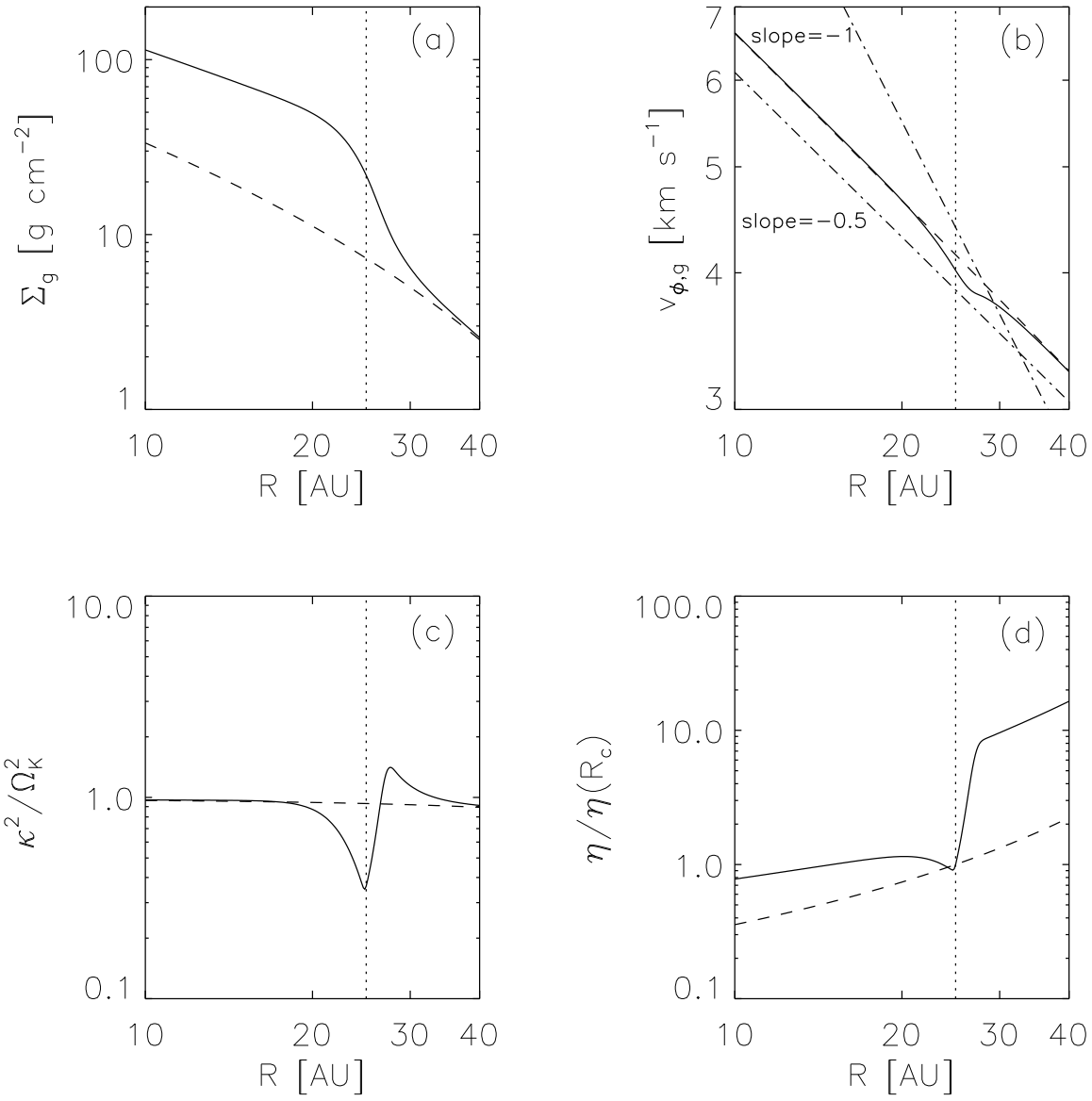

Figure 4.10. Same as Figure 4.1 but for the MUCM model.

frequency, and vortensity at the time of the launching of the RWI ($t = 54\ T_{\rm orb}$). The vortensity minimum is shallow and broad, but since infall keeps adding material at the same radius the RWI triggers. The density around R_c increases steeply but does not develop bumpy structures. We note that the instability very slowly grows, having three times longer $T_{\rm growth}$ compared to the standard model (see Table 4.2).

4.4.7 Effect of Self-gravity

In our standard run, the azimuthally averaged Toomre Q parameter around R_c is $\lesssim 1$ at $T \gtrsim 200\ T_{\rm orb}$. At this point (or even earlier), we expect disk self-gravity becomes important and may alter the later disk evolution including possible activation of gravitational instability (GI). We thus conducted a calculation with disk self-gravity included, using FARGO-ADSG code (Baruteau & Masset, 2008).

Before looking at numerical results, one may predict the role of self-gravity in triggering the RWI through a simple back-of-the-envelope calculation using the connection between the vortensity η and the Toomre Q parameter, where the vortensity is again

$$\eta = \frac{\kappa^2}{2\Omega\Sigma}\frac{1}{c_s^4}, \tag{4.17}$$

and the Toomre Q parameter is

$$Q = \frac{\kappa c_s}{\pi G\Sigma}. \tag{4.18}$$

At a given radii, under the locally isothermal assumption, $\eta \propto \kappa^2/\Sigma$ and $Q \propto \kappa/\Sigma$. Remember that both RWI and GI acts in a way to redistribute mass in the disk so the disk stabilizes against the instabilities. In other words, the instabilities broaden the density enhancement and increase the epicyclic frequency close to Keplerian speeds. If a disk is under the circumstance that RWI and GI competes, this process will increase η faster than Q so that the RWI will stabilize first. Therefore, one can expect RWI will still trigger while a disk is gravitationally stable ($Q \gg 1$) but as the disk becomes gravitationally unstable ($Q \sim 1$) GI can eventually take part in, in which case the RWI can be quenched.

Figure 4.11 depicts perturbed density distributions at three selected times ($t = 30, 44$, and $160\ T_{\rm orb}$), together with the distributions of the standard run for comparison. During

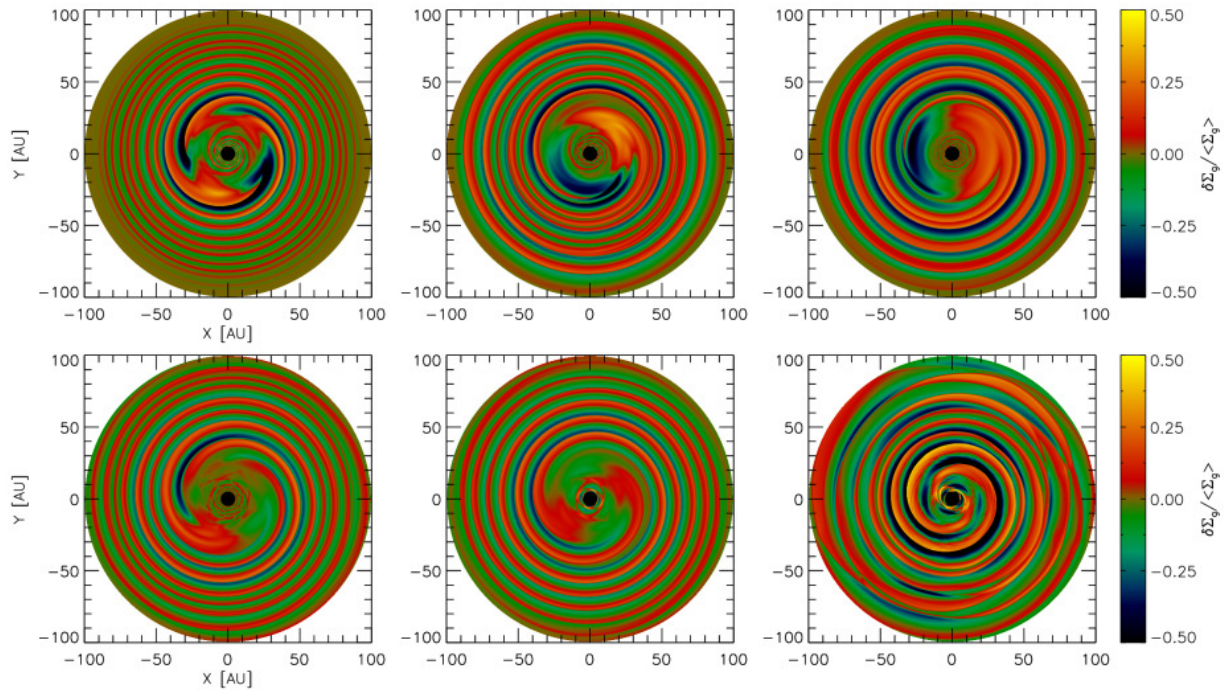

Figure 4.11. Perturbed gas density $\delta\Sigma_g/\langle\Sigma_g\rangle$ distributions at $t = 30, 44$, and 160 $T_{\rm orb}$ (from left to right) for the standard run (upper panels) and the self-gravity run (lower panels). The azimuthally averaged Toomre Q parameters of the self-gravity run at the three epochs are 5.3, 3.2, and 1.3.

the period the RWI linearly evolves, the azimuthally averaged Toomre Q parameter in the disk is > 5; the disk is gravitationally stable. The RWI thus triggers as we predict above and vortices form. Vortices form as the RWI enters the nonlinear regime and merge together over time. However, in the presence of self-gravity the merging tends to be impeded and results in $m = 2$ mode, instead of a single vortex. At $t = 44\ T_{\rm orb}$, azimuthally averaged the Toomre Q parameter is 3.2 at the radial density bump while Q is locally as small as 2.4 at the core of the vortices. As the disk further obtains material and becomes gravitationally unstable, the vortices dissipate and the GI eventually triggers generating strong $m = 2$ trailing spiral arms. The evolution of vortices under the influence of self-gravity seen in our calculation agrees well with previous two- and three-dimensional simulations showing that vortex merging can be delayed in weakly self-gravitating disks and global spiral waves develop instead of vortex formation if self-gravity is sufficiently strong (Lin & Papaloizou, 2011; Lin, 2012).

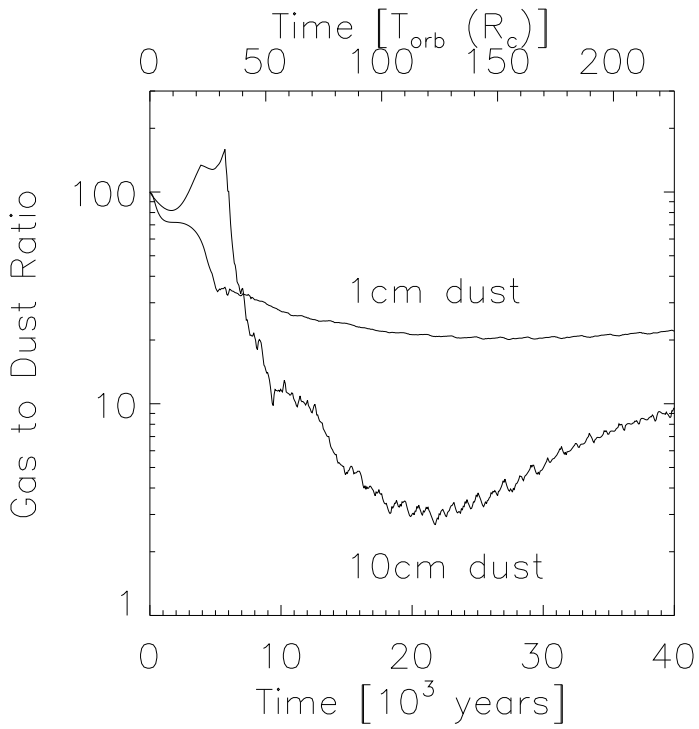

Figure 4.12. Time evolution of the minimum gas to dust ratio for the standard model. The ratio drops significantly as the instability enters the nonlinear regime and vortices form. Because the large dust at the outer disk are depleted due to rapid radial drift and there are no more supply from the region, the ratio for the 10 cm particles after $\sim 120\ T_{\rm orb}$ increases.

4.5 Discussion

4.5.1 Dust Trapping in Vortices and Observational Implications

Our two-fluid approach shows that vortices formed by the RWI efficiently trap dust particles of appropriate size. Figure 4.12 shows the time evolution of the minimum gas to dust ratio for the standard model. Although the detailed evolution of the ratio for the small (1 cm) and large (10 cm) dust particles are different, in overall, the ratios tend to decrease by more than a factor of few. The small dust particles are well coupled to gas as we see in §4.4.1.3 and therefore the decrease of the ratio is relatively smooth and only moderate. The ratio has a minimum of $\sim 20:1$. For the large dust particles, the ratio slightly increases initially because they migrate inward rapidly (remember $T_s \sim 1$ at R_c), while gas surface density interior of R_c increases due to the infall. As vortices form, however, they efficiently trap the large dust particles and the gas to dust ratio drops to $\sim 2.7:1$ at $t \sim 120\ T_{\rm orb}$. The

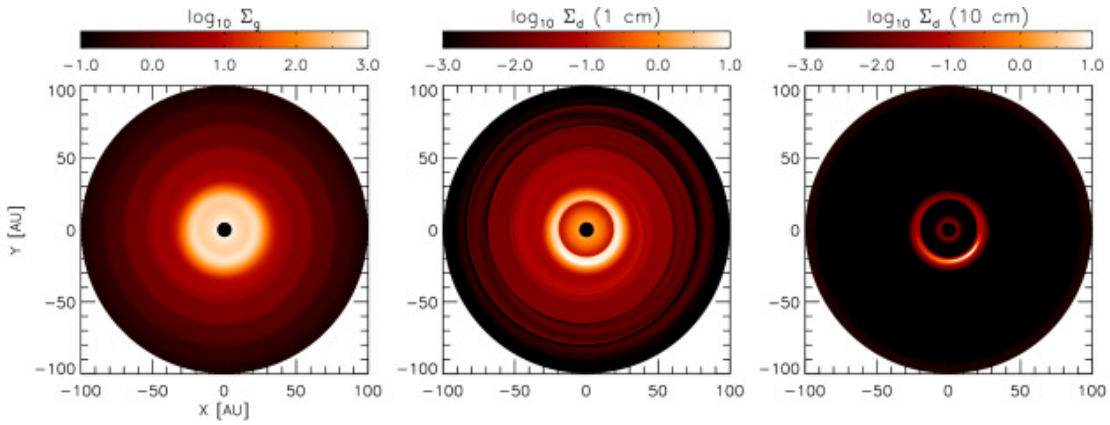

Figure 4.13. Surface density distributions of (left) gas, (middle) 1 cm dust particles, and (right) 10 cm dust particles at the end of the simulation for the standard model. Densities are in cgs units and displayed in the logarithmic scale.

ratio then increases after $\sim 120\ T_{\rm orb}$ but this is because the large dust at the outer disk are depleted due to rapid radial drift and there are no more supply from the region.

Figure 4.13 displays surface density distributions of gas, small dust, and large dust at the end of the standard run. Clear dust concentration in the vortex is shown for both small and large dust particles. Another notable feature is that the inner disk is depleted of dust because of the dust trapping by the vortex. Again, this effect is more prominent for the larger dust particles. As seen in the figure, existence of vortices can not only form azimuthal asymmetry of dust that can be directly observed via interferometric observations but also build radial structures that can be inferred by single-dish observations at multiple wavelengths. The deficit of dust at inner disk regions can affect the spectral energy distributions of the disk and such disks can be interpreted as transitional disks (Calvet et al., 2005). The disks still can have enough gas at the inner disk (see Figure 4.13) that can probably maintain high accretion rate observed in some transitional disks (e.g. Espaillat et al., 2010, 2011; Andrews et al., 2011; Kim et al., 2013).

The significant dust concentration in vortices suggests that the vortices can provide favorable conditions for the planet and/or planetesimal formation. In terms of vortex formation via the RWI, it would prefer higher infall rate and lower disk mass although a thorough parameter study is desired in the future regarding infall rate and disk mass. This means that, with the example of HL Tau suggesting that planet formation can start early even during

the infall phase, RWI might be one mechanism to accelerate planet formation. On the other hand, the longevity of vortices has to be further tested since vortices may not survive forever (e.g. Meheut et al., 2012a), although dust can still remain concentrated after gas vortices disappear (Birnstiel et al., 2013).

4.5.2 Angular Momentum Transport

Li et al. (2001) has shown that RWI-driven anticyclones and trailing spiral waves are responsible for outward angular momentum transport. In Figure 4.14 we display spatial distribution of the perturbed gas density along with the radial distribution of azimuthally averaged Reynolds stress. At the time the instability saturates, the dominant $m = 3$ mode is clearly seen at all radii: the trailing spiral waves propagate both interior and exterior of R_c. The measured Reynolds stress has the maximum value of ~ 0.015 around R_c. Inside of R_c the Reynolds stress is measured to $\sim 10^{-3}$ while at $R > 60$ AU the stress is in the range of $\alpha_{\rm Rey} \sim 10^{-4} - 10^{-6}$. At later time, the vortices merge and the hydrodynamic turbulence around the vortex becomes less significant; $\alpha_{\rm Rey} \sim 10^{-3}$. Instead, the trailing one-armed spiral wave generate stronger turbulence very broadly in the disk that corresponds to $\alpha_{\rm Rey} \sim 10^{-4} - 3 \times 10^{-3}$. The measured Reynolds stress driven by the RWI and the subsequent vortex formation is as strong as the ones induced by other instabilities in protoplanetary disks, such as GI (e.g., Chapter 3) and magnetorotational instability (e.g. Stone et al., 1996).

As a result of exchange of angular momentum between the vortex and the surrounding disk material, the vortex is subject to migration (Paardekooper et al., 2010). More specifically, the vortex loses angular momentum and migrates inward if the trailing waves emitted by the vortex are stronger at the outer disk region than the inner disk region (Paardekooper et al., 2010). We measure the migration rate starting from the time vortices merge together in a single, stable vortex, which is $t \sim 80\ T_{\rm orb}$ in the standard model for example (see Figure 4.4). However, we do not see the vortex migrating until the end of the simulation in our models. It has to be noted though that this can be due to finite numerical resolution. Since the radial grid size at R_c is ~ 0.15 AU, in the standard run we are able to observe migration only if the rate is $\gtrsim 6 \times 10^{-6}$ AU yr^{-1}. We also do not observe vortex migrating

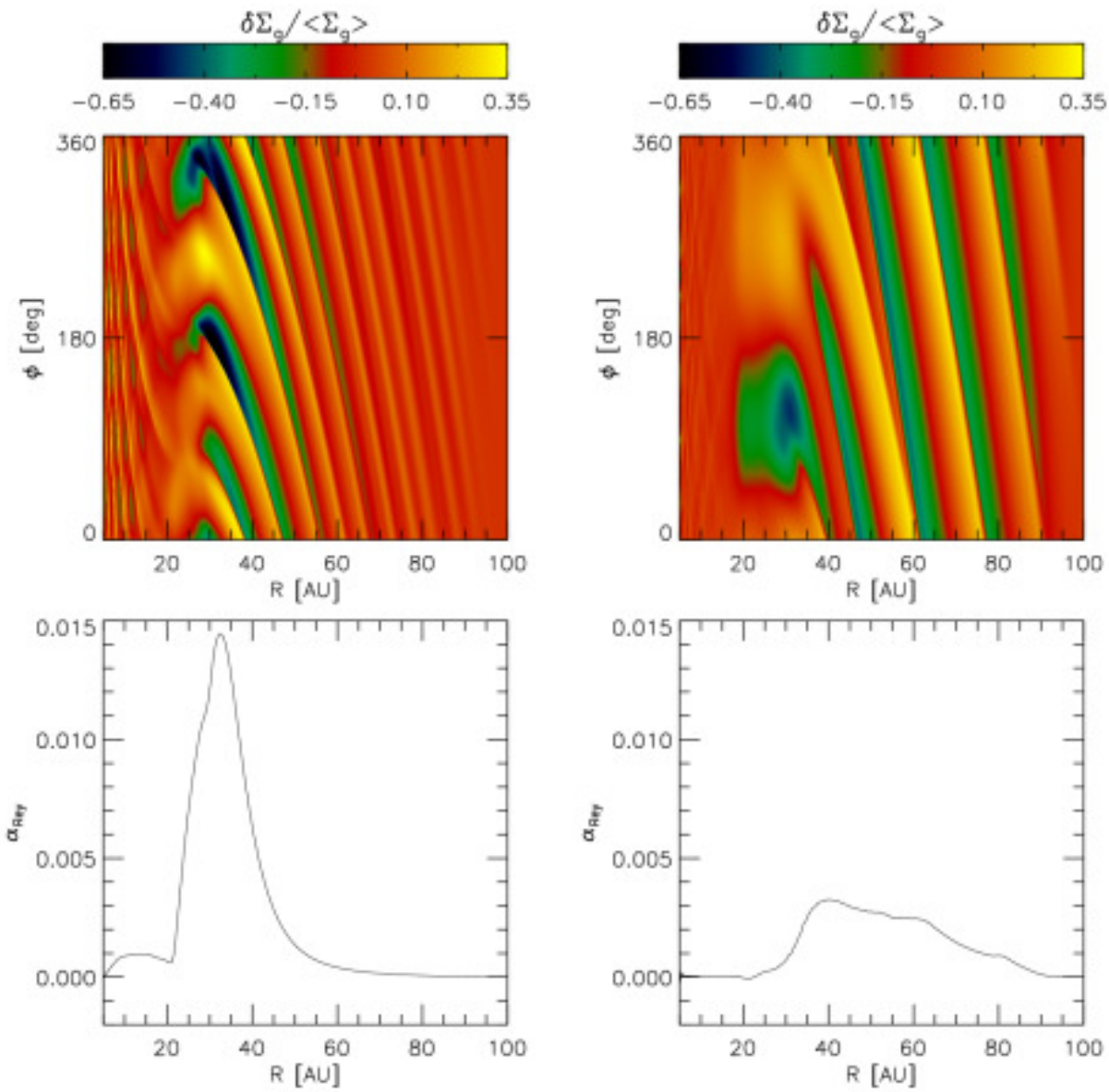

Figure 4.14. (Top) Perturbed gas density $\delta\Sigma_g/\langle\Sigma_g\rangle$ distributions on the $R-\phi$ coordinates. (Bottom) Azimuthally averaged Reynolds stress as a function of radius. The snapshots are taken from the standard model at $t = 30\ T_{\rm orb}$ (left) and 226 $T_{\rm orb}$ (right).

in the higher resolution run with 1024×2048 grid cells, which reduces the migration rate to $\lesssim 3 \times 10^{-6}$ AU yr^{-1}. The fact that the vortex migrates only very slowly, if it does, is important because the vortex might prevent centimeter to meter-sized objects from rapidly migrating inward in a few $\times 10^3 - 10^4$ yr via the aerodynamic drag, retaining material for planet formation.

Generally, it is known that vortices migrate toward high pressure regions (Paardekooper et al., 2010; Meheut et al., 2012a). If a disk around a vortex has constant pressure, competing effects that determine vortex migration cancel each other and thus the vortex is likely to be locked in its location (Paardekooper et al., 2010; Lyra & Mac Low, 2012; Meheut et al., 2012a). In our models, we find that the radial pressure gradient around merged vortices is shallow, in many cases close to zero, and this is presumably why we do not observe vortices migrating. However, we caution that migration of vortices could depend on many other complications (e.g. Richard et al., 2013; Faure et al., 2015), which are beyond the scope of two-dimensional adiabatic calculations.

4.5.3 Caveats and Future Work

It is likely that actual patterns of protostellar infall will be much more complex, possibly having filamentary infall pattern, as inferred from observations (e.g. Tobin et al., 2010, 2011, 2012; Yen et al., 2014) and suggested by numerical simulations (e.g. Seifried et al., 2015). These more complex patterns of mass and angular momentum addition might yield differing structures and other instabilities including RWI. Three-dimensional simulations are needed to take the next steps toward understanding the development of structure in protoplanetary disks.

It is possible that vortices generated during the protostellar infall phase dissipate during the subsequent disk evolution, especially under the influence of disk self-gravity as we show in §4.4.7. In our example, however, the disk becomes gravitationally unstable quickly because we add infalling material at the same disk regions over time, whereas infall is likely to occur at larger radii as time passes, due to the addition of material with higher angular momentum (e.g. Cassen & Moosman, 1981). Further studies of the longevity of vortices formed during the infall phase which incorporate a self-consistent and realistic evolutionary model are thus

required.

Some other limitations of the current work include lack of the three-dimensionality of the RWI and vortex structure, proper thermodynamics which is especially important when self-gravity is considered, and more accurate dust physics such as dust growth and dust feedback.

4.6 Conclusion

We propose protostellar infall as a possible mechanism to trigger the RWI. Our work demonstrates that the RWI enables early vortex formation in protoplanetary disks, during the infall phase. This, along with the emerging observation evidences may suggest that planet/planetary core formation can start earlier than previously expected.

By implementing infall models, we carry out two-fluid, two-dimensional global hydrodynamic simulations. Our results show that the RWI triggers at a radial minimum of the vortensity which is in agreement with previous works. In our model the vortensity minimum develops near the density enhancement at the outer edge of the mass landing on the disk (centrifugal radius). The key feature of triggering the RWI is the steep radial gradient of the azimuthal velocity close to R^{-1} instead of $R^{-0.5}$ for Keplerian rotation, which is induced by the local increase in density at the centrifugal radius. The instability initially grows in the linear regime where the growth is well described by the linear theory. The vortensity minimum keeps growing as infall proceeds, and the instability eventually saturates, followed by subsequent nonlinear evolution.

We conduct a parameter study to investigate the RWI activity under a variety of disk conditions. The major findings are as follows: (1) the RWI triggers with disk viscosity of our interests ($\alpha \leq 10^{-2}$), with larger α weakening the RWI activity; (2) the RWI tends to weaken if centrifugal radius increases over time; (3) in case infalling material has faster inward radial velocity than the disk material on its landing, the vortensity minimum becomes sharper and narrower, resulting in more rapid growing of the RWI; (4) with a gentle mass addition where the radial infall pattern is matched on purpose to the initial disk surface density distribution, the RWI develops more slowly.

Vortex formation occurs when the instability enters the nonlinear phase. Multiple vortices ($m \geq 3$) form initially but they merge to a single vortex in a few tens of local orbital time from their formation, in the absence of self-gravity. Vortices generate trailing spiral waves that are responsible for outward angular momentum transport, with a Reynolds stress of $\lesssim 10^{-2}$. However, no vortex migration was observed in our simulations. Dust particles are well trapped in vortices in general, showing most prominent dust concentration for the particles with stopping times of the order of the orbital time ($T_s \sim 1$). Dust trapping in vortices enhances the local dust to gas ratio significantly by a factor of ~ 40 in our standard run.

With the evolutionary model and parameters we use in this study, the disk is gravitationally stable until the RWI saturates; thus the launching and growth of the RWI is not affected by self-gravity. Due to continuous mass addition through infall and the presence of self-gravity, however, vortex merging tends to be impeded and the vortices eventually dissipate.

In this work, various disk conditions and infall patterns were tested sequentially to better isolate their effects on the RWI activity and the evolution of vortices. The situation is much more complicated in actual protoplanetary disks. In order for better understanding of the longer-term disk evolution, a more self-consistent and realistic long-term evolutionary model is desired in the future. Also, long-term evolution and survival of vortices has to be tested under the consideration of disk turbulence and other instabilities that might be responsible for destroying vortices (e.g. Kerswell, 2002; Lesur & Papaloizou, 2009).

4.7 Acknowledgments

This research was supported in part through computational resources and services provided by Advanced Research Computing at the University of Michigan, Ann Arbor. J.B. acknowledges Richard P. Nelson for carefully reading the manuscript and providing helpful comments.

CHAPTER V

Planetary Signatures in the SAO 206462 (HD 135344B) Disk: A Spiral Arm Passing Through Vortex?

5.1 Abstract

The disk surrounding SAO 206462, an 8 Myr-old Herbig Ae star, has recently been reported to exhibit spiral arms, an asymmetric dust continuum, and a dust-depleted inner cavity. By carrying out two-dimensional, two-fluid hydrodynamic calculations, we find that a planetary-mass companion located at the outer disk could be responsible for these observed structures. In this model, the planet excites primary and secondary arms interior to its orbit. It also carves a gap and generates a local pressure bump at the inner gap edge where a vortex forms through Rossby wave instability. The vortex traps radially drifting dust particles, forming a dust-depleted cavity in the inner disk. We propose that the vortex is responsible for the brightest southwestern peak seen in infrared scattered light and sub-millimeter dust continuum emission. In particular, it is possible that the scattered light is boosted as one of the spiral arms passes through the high density vortex region, although the vortex alone may be able to explain the peak. We suggest that a planetary companion with a mass of $10 - 15\ M_J$ is orbiting SAO 206462 at 100–120 AU. Monitoring of the brightest peak over the next few years will help reveal its origin because the spiral arms and vortex will show distinguishable displacement. This chapter has been published in the Astrophysical Journal, Volume 819, 134 (2016), in collaboration with Zhaohuan Zhu and Lee Hartmann.

5.2 Introduction

The protoplanetary disk around SAO 206462 is one of the few systems so far to exhibit asymmetric features in both near-infrared scattered light and sub-millimeter thermal emission. Direct polarimetric imaging revealed two spiral arms in the H and K_s bands (Muto et al., 2012; Garufi et al., 2013), and the dust continuum emission at sub-millimeter wavelengths observed with ALMA showed a vortex-like feature as well as a dust-depleted inner cavity (Pérez et al., 2014; van der Marel et al., 2015, 2016). One possibly interesting feature is that the scattered light observations indicate an abrupt change in brightness and pitch angle in one of the arms, while most models show smooth spiral structure (e.g. Fung & Dong, 2015).

Recent studies have shown that planet-driven spiral arms may explain the observed scattered light in near-infrared (e.g. Dong et al., 2015; Zhu et al., 2015). Upon their formation, planets excite density waves in disks with different azimuthal modes. While the different modes tend to interfere with each other and merge to a single spiral arm (Ogilvie & Lubow, 1999), it is found that a secondary can also exist and the separation between these two arms increases with the planet mass (e.g. Zhu et al., 2015; Fung & Dong, 2015). Planets are also capable of generating vortices at the inner and outer gap edge, where pressure has local maxima (Koller et al., 2003; Li et al., 2005; de Val-Borro et al., 2007; Lin & Papaloizou, 2010; Lyra & Lin, 2013; Fu et al., 2014a,b; Zhu et al., 2014; Zhu & Stone, 2014). The vortices efficiently trap dust particles and impede dust migrating inward, possibly forming a dust-depleted inner cavity.

The scattering of optical and near-infrared light and the thermal sub-millimeter emission reflect not only the gas structure but the spatial distribution of the dust particles with different sizes. The small dust responsible for the scattered light should be well-coupled to the gas, but larger grains responsible for millimeter-wave emission can be concentrated by pressure gradients.

In this work, we test whether a planetary-mass companion is able to generate various structures observed in the SAO 206462 disk. In order to test our models against near infrared scattered light and sub-millimeter thermal emission, we perform two-fluid calculations where we can simulate dust as well as gas structures. Based on the calculations, we show that the

observed structures are well reproduced with a $10 - 15\ M_J$ planet orbiting SAO 206462 at 100–120 AU. The abrupt change in brightness in one of the arms could be produced as the arm passes through the high density vortex region, though vortex alone may be able to explain the bright scattered light peak. We discuss possible future observations that will help reveal the origin of the structures seen in SAO 206462 disk and better constrain planetary mass and position.

5.3 Numerical Methods

5.3.1 Disk Model

We begin with an initial power-law surface density of the disk gas

$$\Sigma_g(R) = \Sigma_p \left(\frac{R}{R_p}\right)^{-1}, \tag{5.1}$$

where Σ_g is the gas surface density and Σ_p is the gas surface density at the semi-major axis of the planetary orbit R_p. The power-law density slope of -1 is consistent with the best solution of Carmona et al. (2014, see their model 5) found in between 30 and 200 AU. We choose Σ_p such that the initial total gas mass is 0.026 $M_\odot$ (Andrews et al., 2011).

In these two-dimensional (R, ϕ) simulations, we use a fixed radial temperature distribution with the isothermal equation of state, which implies that the ratio of disk scale height to radius is

$$\frac{H}{R} = \left(\frac{H}{R}\right)_p \left(\frac{R}{R_p}\right)^{0.25}, \tag{5.2}$$

where $(H/R)_p$ is the aspect ratio at planet's semi-major axis. We use $(H/R)_p = 0.1$ which results in the corresponding disk temperature profile

$$T = 44\ \mathrm{K} \left(\frac{R}{R_p}\right)^{-0.5} \left(\frac{R_p}{100\ \mathrm{AU}}\right)^{-1} \tag{5.3}$$

with $M_* = 1.7 M_\odot$ and mean molecular weight of 2.4. The temperature profile is roughly consistent with detailed flared disk models, including good agreement with estimates of the disk scale heights for SAO 206462 from Andrews et al. (2011) and Carmona et al. (2014).

Also, the temperature dependence on radius is consistent with the assumption of a constant α and $\Sigma \propto R^{-1}$ (for a steady disk).

For the gas component a uniform viscosity parameter $\alpha = 10^{-4}$ is implemented. Vortex formation through the Rossby wave instability (RWI) could be dependent on the choice of α value as seen in numerical simulations (e.g., Chapter 4 of this thesis). Empirically, it has been shown that the width of the gas pressure maximum has to be $\lesssim 2H$ in order for the RWI to develop (Lyra et al., 2009; Regály et al., 2012). Although determining the critical upper α value for which our results remain valid could be done only numerically given the complexity of the disk structure (planet, spiral arms, vortex, their interaction, etc.), adopting this criterion, one could make a simple argument that the viscous timescale at the inner gap edge (t_ν; the timescale that the disk viscously spreads out the gas pressure bump by $\sim H$) has to be longer than the vortex formation timescale. In an alpha disk, the corresponding viscous timescale can be written as $t_\nu = H^2/\nu = P/(2\pi\alpha)$, where $\nu = \alpha H^2 \Omega$ is the viscosity and $P = 2\pi/\Omega$ is the local orbital period. We find that vortices form at the inner gap edge within $10 - 20$ local orbital time; thus, unless the viscosity parameter is as large as ~ 0.01 our results should remain valid.

We adopt inner and outer boundaries at 20 and 300 AU. We use 288 logarithmically spaced radial grid-cells and 688 linearly spaced azimuthal grid-cells, with which choice $\Delta R/R$ is constant to 0.009 and grid-cells have comparable radial and azimuthal sizes at all radii.

5.3.2 Dust Component

The dust response to planet-generated gas structures is calculated with the two-fluid FARGO code introduced in Zhu et al. (2012b), in which the dust component is added to the standard FARGO code (Masset, 2000). To briefly summarize, we solve an additional mass and momentum equation set for the dust component. We treat the dust component as an inviscid, pressureless fluid so dust simply feels the drag force in addition to the central stellar potential. The drag terms are added to the momentum equation as an additional source step

$$\frac{\partial v_{R,d}}{\partial t} = -\frac{v_{R,d} - v_{R,g}}{t_s} \tag{5.4}$$

and

$$\frac{\partial v_{\phi,d}}{\partial t} = -\frac{v_{\phi,d} - v_{\phi,g}}{t_s}, \tag{5.5}$$

where v_R and v_ϕ are radial and azimuthal velocities, and the subscripts g and d denote gas and dust components. The dust stopping time is $t_s = \pi \rho_p a / 2\Sigma_g \Omega$ with ρ_p and a being dust particle density and size.

Since dust particles can diffuse in the gaseous disk due to turbulence, dust diffusion is implemented in the operator split fashion in the source step of the dust component (Clarke & Pringle, 1988):

$$\frac{\partial \Sigma_d}{\partial t} = \nabla \cdot \left(D \Sigma_g \nabla \left(\frac{\Sigma_d}{\Sigma_g} \right) \right). \tag{5.6}$$

In the above equation, $D = \nu / Sc$ is the turbulent diffusivity where ν is the gas viscosity and $Sc = 1 + (\Omega t_s)^2$ is the Schmidt number (Youdin & Lithwick, 2007).

We perform calculations with five different dust sizes: 30, 100, 300, 1000, 3000 μm, which represent particles in size bins of [17 μm, 53 μm], [53 μm, 170 μm], [170 μm, 530 μm], [530 μm, 1700 μm], [1700 μm, 5300 μm], respectively. We assume that the dust particles have a power-law size distribution $n(a) \propto a^{-3.5} da$ in between $a_{\rm min} = 0.1$ μm and $a_{\rm max} = 5.3$ mm. We note that we do not perform calculations for the particles with $a < 17$ μm, and simply assume that those particles perfectly follow the gas distribution when producing synthetic ALMA observations in Section 5.5. The dust mass in each size bin is determined based on the particle size distribution of $n(a) \propto a^{-3.5} da$, which provides the surface density as a function of a: $\Sigma_d(a) \propto a^{-0.5} da$. The mass fractions in each size bin of [0.1 μm, 17 μm], [17 μm, 53 μm], [53 μm, 170 μm], [170 μm, 530 μm], [530 μm, 1700 μm], [1700 μm, 5300 μm], are 5.3 %, 4.4 %, 7.9 %, 13.8 %, 25.1 %, 43.6 %, respectively. The total initial dust surface density is assumed to be 1 % of the gas density. We assume that the dust density is 3 g cm^{-3}.

We vary the planet's mass and semi-major axis to model the SAO 206462 disk. The model parameters are summarized in Table 5.1.

Table 5.1. Model Parameters for SAO 206462 Disk Calculations

Parameter	Value
Stellar mass (M_*)	1.7 $M_\odot$[a]
Disk mass ($M_{\rm disk}$)	0.026 $M_\odot$[b]
Disk aspect ratio at planet's orbit ($(H/R)_p$)	0.1
Planet mass (M_p)	$5, 7.5, 10, 12.5, 15, 17.5, 20$ M_J
Semimajor axis of the planet (R_p)	$80, 90, 100, 110, 120, 130, 140$ AU
Minimum grain size ($a_{\rm min}$)	0.1 μm
Maximum grain size ($a_{\rm max}$)	5.3 mm

[a]Müller et al. (2011)

[b]Andrews et al. (2011)

5.4 Results

All the calculations were run for 100 T_p where T_p refers to the orbital time at the planet's location. We find that the spiral structure is well developed within 2 T_p and remains steady afterward. The planet carves a gap and generates a horseshoe orbit region around its orbit. It also generates vortices at the inner and outer gap edges. The vortex at the inner gap edge forms within ~ 5 T_p and survives until the end of the calculations. The duration of the calculations is thus long enough for the structures to fully develop in the disk.

Figure 5.1 shows gas, 30 μm dust, and 300 μm dust distributions at 50 T_p with a 10 M_J planet orbiting at 100 AU. The horseshoe region, primary and secondary inner spiral arms, and an azimuthally elongated vortex can be clearly seen. Dust depletion takes place in the inner disk ($\sim$ 40–50 AU for $a = 30$ μm, $\sim$ 30–50 AU for $a = 300$ μm) and it is more significant for larger dust particles because they suffer stronger drag. The inner dust cavity grows over time, and at the end of the calculation ($t = 100$ T_p) particles with $a \geq 1$ mm are completely cleared from the inner disk. The outer vortex is prominent in our simulations, but not seen in the ALMA sub-millimeter thermal emission map presumably because the actual SAO 206462 disk has a faster decline in surface density with radius than in our model at large radii ($\gtrsim$ 100 AU; Andrews et al., 2011): our model disk has more mass in the outer disk than the observational estimates for the actual disk. It is also possible that a slow dust

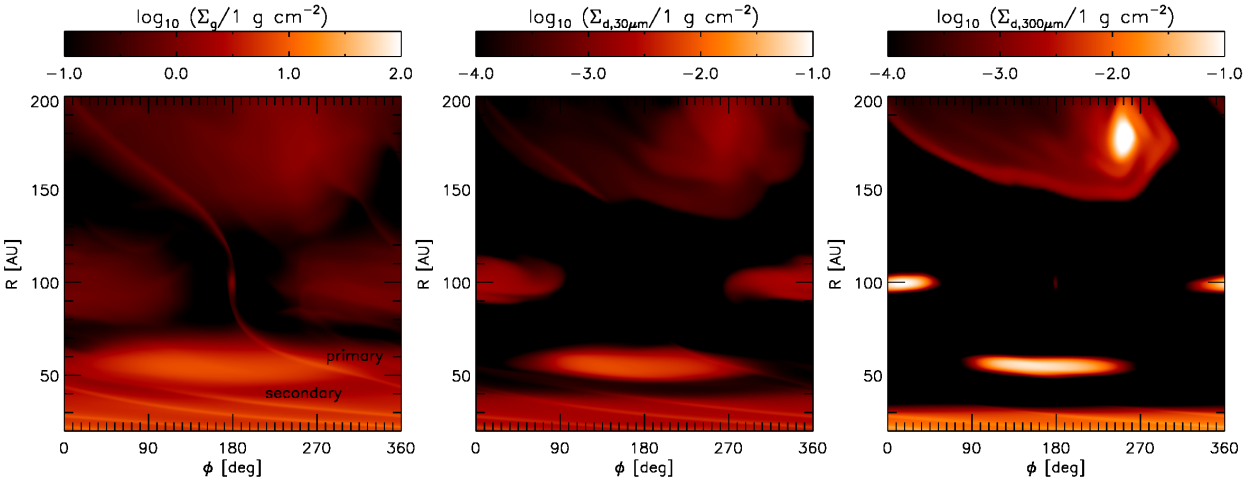

Figure 5.1. Distributions of (left) gas, (middle) 30 μm dust, and (right) 300 μm dust at $t = 50\ T_p$ in $\phi - R$ coordinates. $M_p = 10\ M_J$ and $R_p = 100$ AU were used. The planet excites primary and secondary arms at the inner disk. It also generates a horseshoe region and opens a gap. Two vortices are formed at the inner and the outer gap edge. The image is shifted in azimuth from its original in a way that the planet locates at $\phi = 180°$.

growth rate at large radii limits dust mass with $a \gtrsim 100\ \mu$m in the outer disk of SAO 206462, which is responsible for the sub-millimeter thermal emission.

The width of the horseshoe region ($x_{\rm hs}$) is about 25 AU, which is in good agreement with a known relation between the local disk aspect ratio $h = H/R$ and the planet-to-star mass ratio $q = M_p/M_*$: $x_{hs} \sim R_p\sqrt{q/h}$ (Masset et al., 2006; Baruteau & Masset, 2008; Paardekooper & Papaloizou, 2008).

The vortex efficiently traps dust particles, particularly the ones with a stopping time of the order of the local orbital time as expected in typical anticyclonic vortices (e.g., Barge & Sommeria 1995; Inaba & Barge 2006; Meheut et al. 2012b; Fu et al. 2014b; Zhu & Stone 2014; Chapter 4 of this thesis). As a result the dust-to-gas mass ratio inside the vortex becomes as large as $\sim 1:25$. In Figure 5.2, we present the distribution of the Stokes number T_s that corresponds to the model presented in Figure 5.1. The Stokes number in the vortex is about $10^{-3} - 10^{-2}$ for the 30 μm particles and is close to unity for millimeter-sized particles. As the Stokes number increases against the particle size ($T_s \propto a$), larger particles exhibit a more compact structure. For the 300 μm-sized dust, the vortex extends $\sim 180°$ in azimuth. The total (gas+dust) mass in the inner vortex varies over time, but is about 3 M_J at 50 T_p,

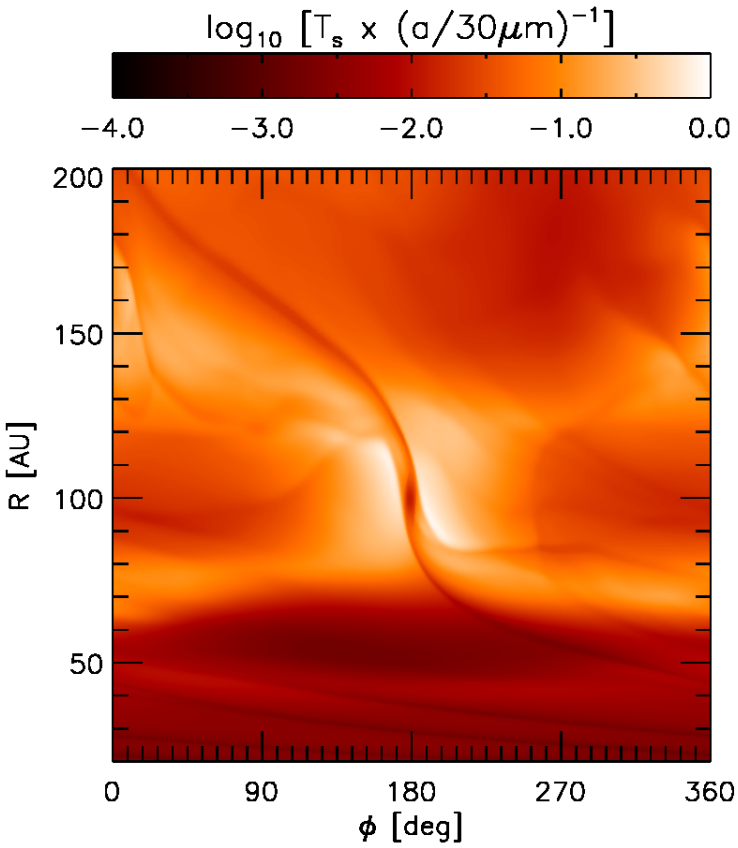

Figure 5.2. Distribution of the Stokes number T_s corresponding to the gas distribution shown in Figure 5.1. Note that the numbers given in the colorbar are for the particles with $a = 30$ μm.

which is roughly consistent to the mass constrained by sub-millimeter observation (2 M_J; Pérez et al., 2014).

Regarding the inner arms, we find that the secondary arm becomes significantly fainter outside of ~ 60 AU, whereas the primary arm extends further out to the planet. The faint secondary arm at $\gtrsim 60$ AU may be due to the fact that less material exists because of the gap opened by the planet. However, this may also be because the second spiral arm is excited at $m = 2$ Lindblad resonance which resides at $R \sim 0.63\ R_p$. We note that the pitch angle of the primary arm increases as a function of radius, especially near the planet, while that of the secondary arm is nearly constant over radius. It is also worth pointing out that the vortex and the inner spiral arms rotate at different frequencies: the vortex orbits at the local Keplerian speed whereas the spiral arms corotate with the planet.

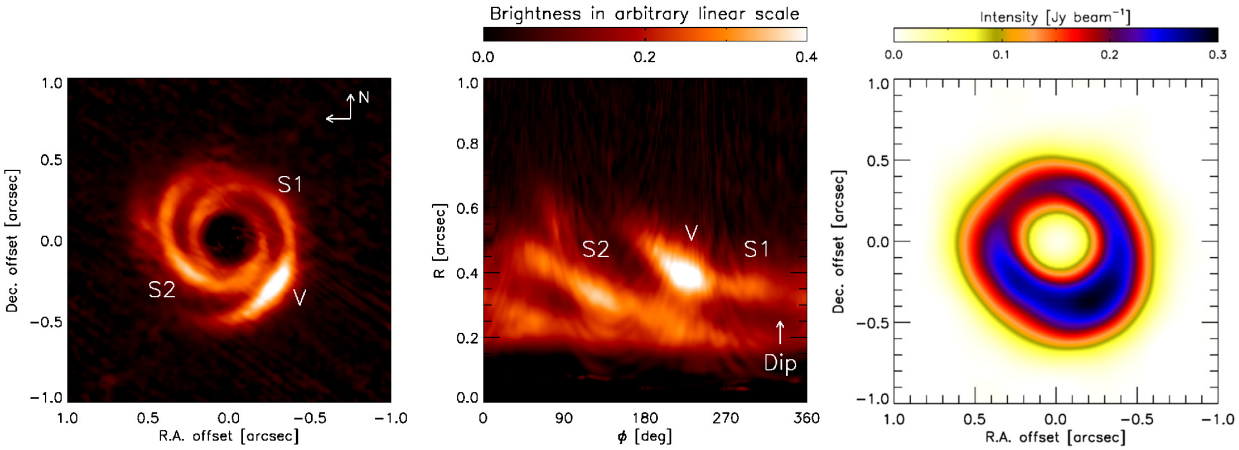

Figure 5.3. (Left) Polarized scattered light observed in K_s band by Garufi et al. (2013). The brightness is scaled with R^2 to compensate for stellar light dilution, and is in arbitrary linear scale. We used publicly available data from Vizier online catalog (http://vizier.cfa.harvard.edu/viz-bin/VizieR?-source=J/A+A/560/A105). (Middle) Same as the left panel but in $\phi - R$ coordinates where ϕ is defined as the angle measured counter-clockwise from the North. (Right) Dust continuum emission obtained with ALMA at 690 GHz by Pérez et al. (2014). We used public data available from the ALMA archive. In the left and middle panels we label some important structures: S2 refers to the arm on the eastern side, S1 refers to the arm extends from the north to west, and V refers to the brightest peak on the southwestern side.

5.5 Discussion

In Figure 5.3 we display the scattered light image at the K_s band (Garufi et al., 2013), and the dust continuum emission at 690 GHz (Pérez et al., 2014). In the scattered light image, the disk shows two well-established spiral arms; one on the western side (hereafter S1) and the other on the eastern side (hereafter S2). It also shows a bright azimuthal feature (hereafter V) at $(\Delta\text{R.A.}, \Delta\text{Dec.}) = (-0.25'', -0.3'')$. Interestingly, the bright feature in S1 in the scattered light is spatially coincident to the southwestern dust emission peak.

When the scattered light is plotted in $\phi - R$ coordinates, however, the pitch angle of the western arm changes abruptly in between S1 and V. This raised us the following question: do S1 and V form a single spiral arm and share a common physical origin? Or do they have different physical origins, but are just spatially coincident?

In order to infer the origin of the structures and to estimate the planet's mass and location, we compare the simulated surface density distribution and synthetic ALMA observations

to the observed data. We note that comparison between the simulated surface density distribution and the scattered light image should be treated with caution for several reasons.

The near-infrared scattered light only traces the fluctuations of the disk atmosphere since the disk is highly optically thick at these wavelengths. Furthermore, the spiral shocks complicate the three-dimensional structure (Zhu et al., 2015). Therefore, it is not straightforward to directly relate the disk surface density to the scattered light images. However, the shape of the spiral arms are similar at different heights in the disk (Figure 2 of Zhu et al. 2015) and similar to the spiral shape in the modeled scattered light images (Figure 2 of Fung & Dong 2015). Thus, we compare the morphology of the arms and density distribution in a qualitative manner, rather than in quantitative manner.

The synthetic ALMA observations are produced as follows. We use the Mie theory to calculate the dust opacity at 690 GHz. For particle sizes of 30, 100, 300, 1000, 3000 μm, the dust opacities are 12.0, 12.9, 7.6, 2.3, 0.6 $\mathrm{cm^2 g^{-1}}$, respectively. For particles smaller than 17 μm, we use the opacity at $a = 3\mu$m as a representative value (2.4 $\mathrm{cm^2 g^{-1}}$). We note that the resulting synthesized images are not sensitive to the choice of the opacity of $a < 17$ μm particles because the mass fraction for the particles are only 5.3 % (see Section 5.3.2). Then, we calculate the optical depth of the disk as

$$\tau = S \sum_i W_i \Sigma_{d,i} \kappa_i, \tag{5.7}$$

where W_i is the mass fraction ($0 \leq W_i \leq 1$, $\sum W_i = 1$) of each dust size bin, and $\Sigma_{d,i}$ and κ_i are the dust surface density and the opacity for each dust size bin, respectively. The scaling factor S is introduced to calibrate the overall dust-to-gas ratio in a way that the simulated thermal emission matches to the observed intensity. In the models introduced below, we use $S \sim 2$, which implies that the dust-to-gas mass ratio is presumably smaller than the one assumed in our calculations (1:100). The total flux distribution is calculated with the temperature profile given in Equation (5.3), assuming the blackbody radiation with the effect of optical depth taken into account: $F = B_\nu(T) \exp(1 - \tau)$ where F is the flux, B_ν denotes the Planck function, and τ is the optical depth. Finally, the flux is synthesized with

the ALMA beam using CASA[1]. Thermal noise from the atmosphere and from the ALMA receivers is added by setting the *thermalnoise* option in the *simobserve* task to *tsys-atm*. We use the ALMA cycle 0 extended configuration to compare our models to the data presented in Pérez et al. (2014, see also Figure 5.2 of this Chapter). The distance of 140 pc (Müller et al., 2011, and references therein), PA and inclination of 63° and 16° (van der Marel et al., 2016) were used.

For the entire duration of our simulations (100 $T_p \lesssim 10^5$ yr) μm-sized dust particles are not completely depleted from the inner disk, while sub-millimeter and millimeter continuum observations suggest a significant reduction of dust density in the inner cavity (Lyo, 2011; van der Marel et al., 2015, 2016). This is probably because the duration of the simulations is much shorter than the actual age of the system, although we cannot rule out the existence of a second companion inside the cavity. In order to reduce the excess dust emission from the inner disk, we decrease the dust density at the inner 35 AU by a factor of 100 when we produce synthetic ALMA observations.

Zhu et al. (2015) and Fung & Dong (2015) recently showed that the azimuthal separation of scattered light from the primary and secondary arms is a function of planet-to-star mass ratio q. In addition, the azimuthal separation of the arms is generally smaller than 180° unless q becomes very large ($q > 0.01$; Fung & Dong 2015); so the secondary is generally ahead of the primary at the same radius. The observed azimuthal separation between S1 and S2 ($|\phi_{S1} - \phi_{S2}|$) in SAO 206462 at $R = 0.3 - 0.35$" largely varies from 160° to 260°,[2] partly because of the dip due to the depolarization effect around the minor-axis (see Garufi et al., 2013). Given the difficulties discriminating the primary and secondary, we test two scenarios: (1) S1 being the primary and (2) S1 being the secondary. In both scenarios, we find that a vortex has to be located at the southwestern side to explain the observed sub-millimeter dust emission peak.

In Figure 5.4, we present the gas surface density distribution in the inner 1" and the simulated ALMA observation. The upper panels show the first scenario in which S1 is assumed to be the primary arm, with $M_p = 10\ M_J$ and $R_p = 100$ AU. Interestingly, the

[1]http://casa.nrao.edu

[2]Since it is not clear whether or not V is part of S1 at this point, we measure the separation between S1 and S2.

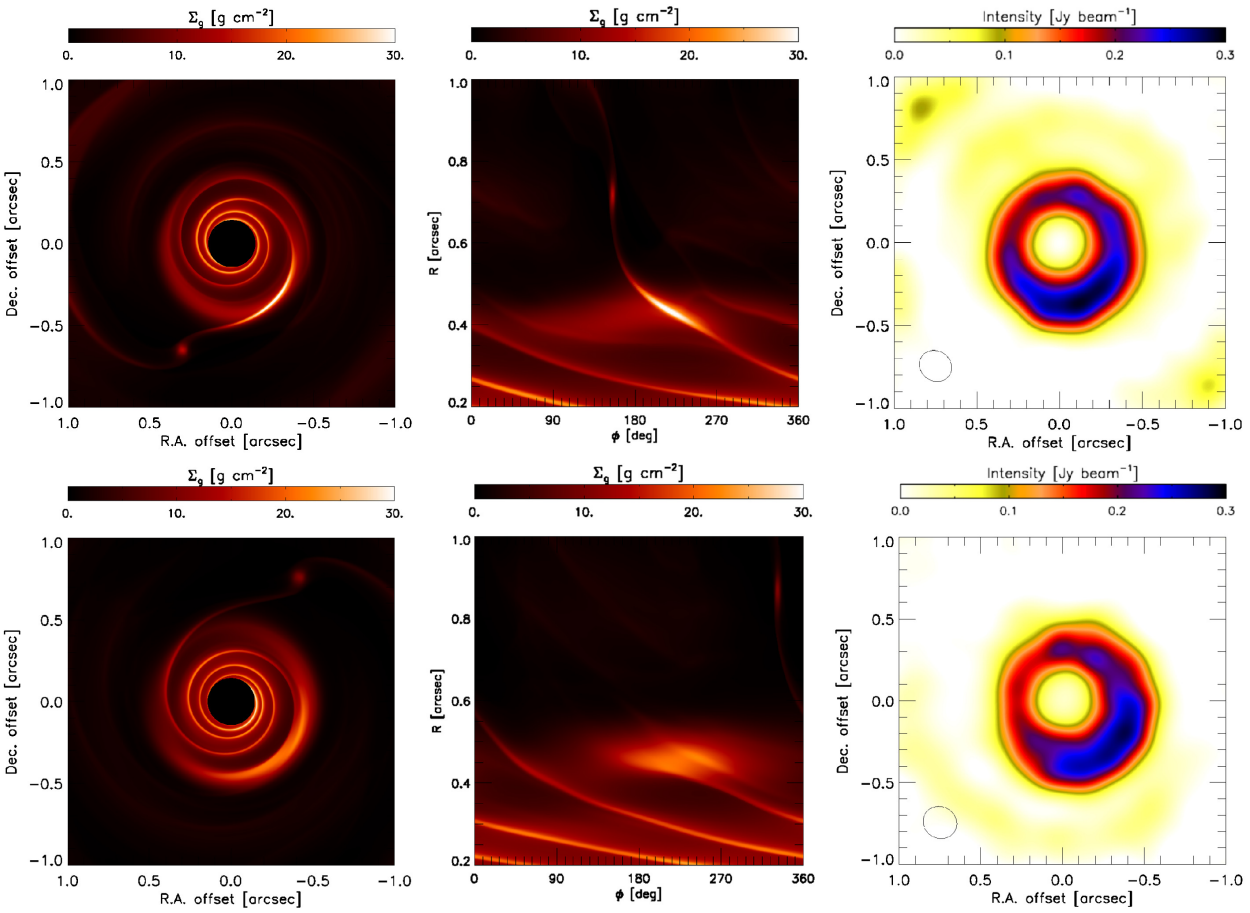

Figure 5.4. *Upper panels:* when S1 is assumed to be the primary arm. $M_p = 10\ M_J$ and $R_p = 100$ AU were used. (Left) Gas density distribution in the inner 140 AU disk (=1") from this work. The planet is located at $(\Delta\text{R.A.}, \Delta\text{Dec.}) = (0.3'', -0.65'')$. (Middle) Same as the left panel, but in $\phi - R$ coordinates where ϕ is measured counter-clockwise from the north. The primary and secondary inner spiral arms as well as the vortex are clearly seen. (Right) ALMA simulated image with the cycle 0 extended configuration. The synthesized beam is displayed in the lower-left corner. *Lower panels:* same as the upper panels, but when S2 is the primary arm. $M_p = 15\ M_J$ and $R_p = 120$ AU were used. The planet is located at $(\Delta\text{R.A.}, \Delta\text{Dec.}) = (-0.4'', 0.75'')$ in the left panel.

primary arm passes through the vortex at the inner gap edge. While relating surface density to scattered light has to be done with caution as pointed out earlier, it is plausible that a spiral passing through a denser region would also produce higher density at the scattering surface. Also, because the primary arm generally extends further out and has a larger pitch angle than the secondary, the lopsided vortex-like structure can be naturally explained. The large separation between the secondary and the primary arms in this scenario is still a question.

When S2 is assumed to be the primary arm, V and S1 in the scattered light probably have a different origin because it is unlikely that (1) the secondary arm extends further out than the primary and (2) the pitch angle of the secondary arm abruptly changes at large radii, though interaction with a vortex may produce an unexpected outcome. In order to reproduce the lopsided dust emission, a larger planetary mass of $M_p = 15\ M_J$ is assumed so that the planet generates a stronger pressure bump at the gap edge. Also, because a more massive planet opens a gap further away $R_p = 120$ AU is used: recall that the vortex forms at the inner gap edge whose position is a function of planetary mass. Since there is no boost via interaction between the spiral and vortex as in the other scenario, significant vertical motion inside the vortex will be required to explain the bright scattered light at the vortex position. In fact, it is possible that a vortex has a three-dimensional vertical motion, which can lift small particles to the disk atmosphere, potentially enhancing the scattered light intensity (Meheut et al., 2012b).

It is possible that the spiral arms generate strong shocks and thus produce a high temperature near the surface (Zhu et al., 2015). Regarding the sub-millimeter flux, however, high temperature near the surface would not provide significant flux given that the disk is optically thin at 690 GHz as seen in Figure 5.5 and most of the mass is concentrated near the midplane.

The vortex and the inner spiral arms not only orbit at different frequency as pointed out earlier, but they move in a different manner. Figure 5.6 shows time evolution of the bright southwestern peak. If the peak is originated from a spiral arm interacting with vortex it will appear to be more opened over time, showing both circular and lateral displacement. On the other hand, if the peak is due to the vortex alone, it will move only circularly. Assuming

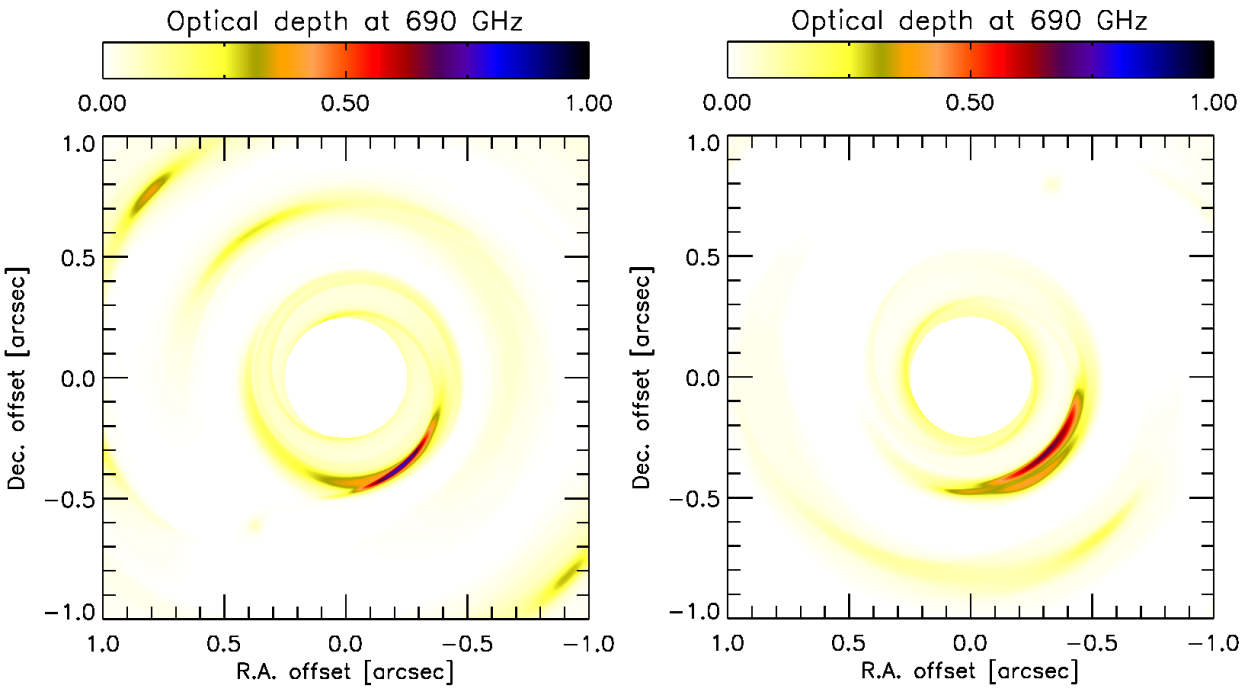

Figure 5.5. Distribution of optical depth at 690 GHz for the two models presented in Figure 5.4. We note that the entire disk is optically thin at this frequency, and only the core of the vortex is marginally optically thick.

the vortex center is at $0.4'' = 56$ AU, the peak will rotate about 1.1° per year. Since the two scenarios show noticeably different evolution, monitoring of the brightest peak over the next few years will help reveal the origin of the structures.

Pinilla et al. (2015) pointed out that the southwestern dust emission peak is shifted over time by comparing two ALMA data sets obtained in 2012 and 2014. The shift is however much more significant than what would be expected from our models. Instead, given that the two ALMA data sets are taken at different frequencies (690 and 340 GHz) it is possible that the observations show offsets among dust particles with different sizes as particles with Stokes number closer to the unity are known to show more violent movement inside a vortex (e.g., Chapter 4).

We note that the observations made so far were not able to reach the detection limit of $\sim 10\ M_J$ at 100 AU in SAO 206462 (e.g. Vicente et al., 2011), because the thermal emissions from such planets are too small compared to the central star. Future observations with GPI and SPHERE will be able to provide stronger constraints, if not detect a planet candidate.

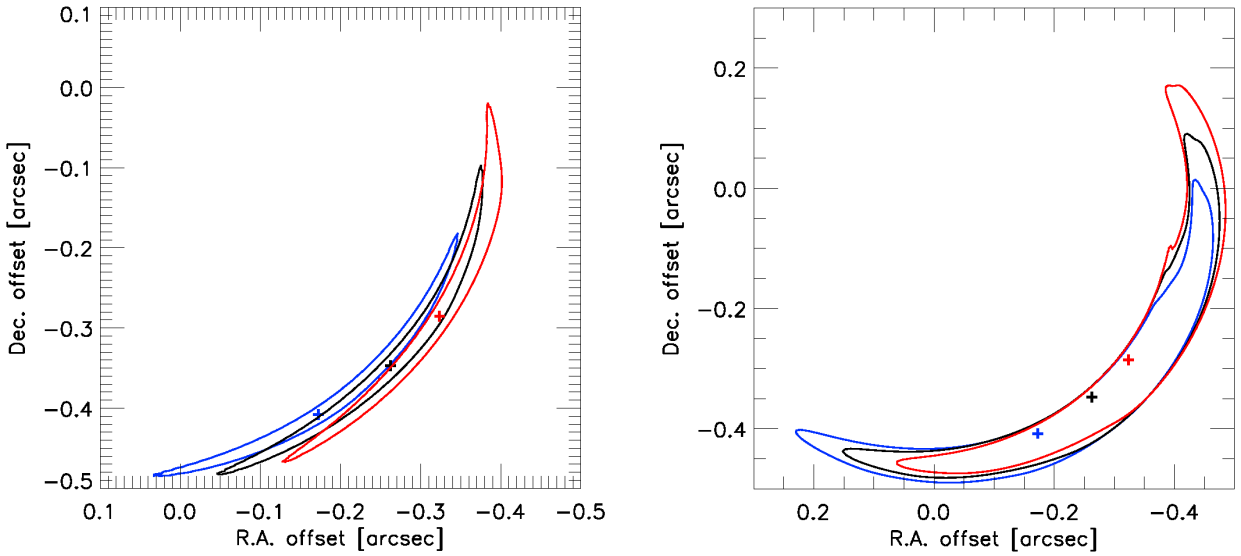

Figure 5.6. Iso-density contours ($\Sigma_g = 20$ g cm^{-2}) showing time evolution of the bright southwestern feature in the two scenarios: (left) S1 is the primary arm and (right) S1 is the secondary arm. The black contours show positions at the same time as in Figure 5.4. The blue and red contours show positions at -10 and $+10$ years from the black contours, respectively. If the bright feature originates from the vortex alone (scenario 2) it will move circularly over time, whereas the displacement will be circular + lateral if it is from a spiral arm passing through vortex (scenario 1). The cross symbols indicate the positions where the density peaks in the structures.

Our calculations are limited to two dimensions and, therefore, we are unable to conclude which scenario would be preferred over the other at this point. Future three-dimensional simulations and radiative transfer calculations will be able to provide a more robust prediction. In addition, knowing more accurate estimates of the vortex position and disk temperature profile will help constrain the planetary mass and position for future searches.

5.6 Conclusions

We have constructed two-dimensional models with dust drift, which show vortex and spiral structure similar to that observed in SAO 206462. We further suggest that an interaction between a spiral arm and the vortex accounts for the abrupt change in brightness seen in the scattered light observations, although vortex alone may also explain the bright scattered light peak. Monitoring of the brightest peak over the next few years and higher resolution ALMA observations can help test our models and perhaps suggest which of our two preferred

scenarios is more likely.

5.7 Acknowledgments

The authors thank the anonymous referee for a helpful report that improved the initial manuscript. The authors also thank Jeffrey Fung and Antonio Garufi for valuable discussion, and Antonio Garufi et al. for making their data publicly available. Z.Z. greatly appreciates Laurent Pueyo sharing his unpublished results and providing very helpful suggestions. This research was supported in part by the University of Michigan, and computational resources there provided by Advanced Research Computing. Z.Z. is supported by NASA through Hubble Fellowship grants HST–HF–51333.01–A awarded by the Space Telescope Science Institute, which is operated by the Association of Universities for Research in Astronomy, Inc., for NASA, under contract NAS 5-26555. This Chapter makes use of the following ALMA data: ADS/JAO.ALMA #2011.0.00724.S. ALMA is a partnership of ESO (representing its member states), NSF (USA) and NINS (Japan), together with NRC (Canada), NSC and ASIAA (Taiwan), and KASI (Republic of Korea), in cooperation with the Republic of Chile. The Joint ALMA Observatory is operated by ESO, AUI/NRAO and NAOJ. The National Radio Astronomy Observatory is a facility of the National Science Foundation operated under cooperative agreement by Associated Universities, Inc.

5.8 Appendix: Resolution Test

We double the resolution in order to check numerical convergency, with a 10 M_J planet orbiting at 100 AU. We test with a particle size of $a = 300$ μm as a representative case because (1) dust evolution does not affect to gas evolution in our calculations and thus the gas structure remains identical no matter which dust particle size is used, and (2) the dust stopping time often limits the time step in two-fluid calculations, especially when a small dust particle size is assumed. For instance, when $a = 30$ μm is assumed, the dust stopping time is locally more than three orders of magnitude shorter than the orbital time (see Figure 5.2), and therefore causes a very small time step.

In Figure 5.7, we display two-dimensional distributions of gas and 300 μm dust, and their

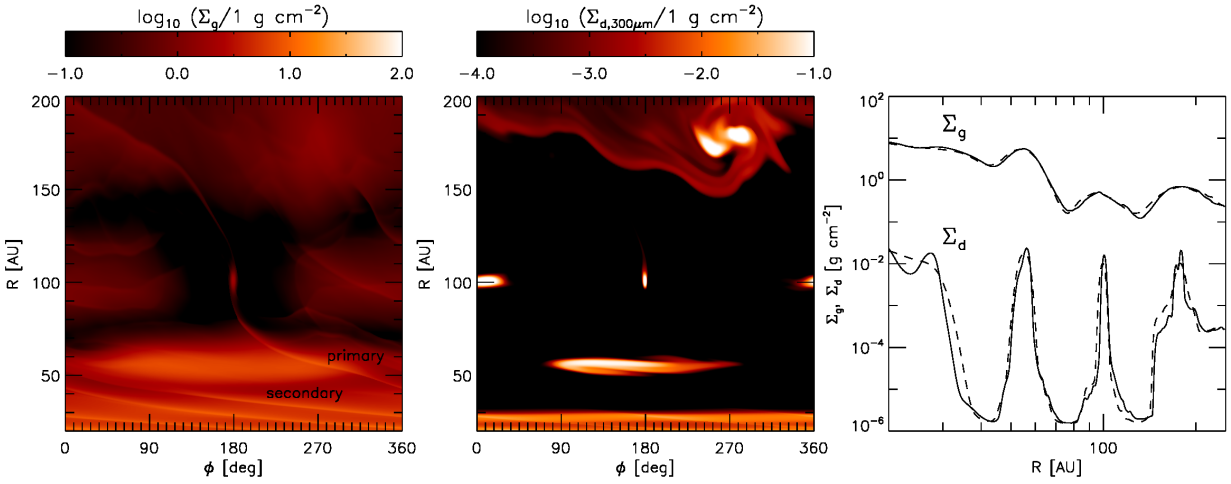

Figure 5.7. Distributions of (left) gas, (middle) 300 μm dust in $\phi - R$ coordinates, and (right) azimuthally averaged radial profiles of the gas and dust distributions at $t = 50.6\ T_p$. The same model parameters are used as in Figure 5.1, but with twice higher resolution $(n_R \times n_\phi) = (576 \times 1376)$. In the right panel, the solid curves show high-resolution (576×1376) results and the dashed curves show low-resolution (288×688) results.

azimuthally averaged radial profiles. While the high-resolution run shows more small-scale structures, the overall morphology is in good agreement with the low-resolution run presented in Figure 5.1. The azimuthally averaged radial density distributions are also consistent with each other.

CHAPTER VI

Self-destructing Spiral Waves: Global Simulations of a Spiral Wave Instability in Accretion Disks

6.1 Abstract

We present results from a suite of three-dimensional global hydrodynamic simulations which show that spiral density waves propagating in circumstellar disks are unstable to the growth of a parametric instability that leads to break-down of the flow into turbulence. This spiral wave instability (SWI) arises from a resonant interaction between pairs of inertial waves, or inertial-gravity waves, and the background spiral wave. The development of the instability in the linear regime involves the growth of a broad spectrum of inertial modes, with growth rates on the order of the orbital time, and results in a nonlinear saturated state in which turbulent velocity perturbations are of a similar magnitude to those induced by the spiral wave. The turbulence induces angular momentum transport, and vertical mixing, at a rate that depends locally on the amplitude of the spiral wave (we obtain a stress parameter $\alpha \sim 5 \times 10^{-4}$ in our reference model). The instability is found to operate in a wide-range of disk models, including those with isothermal or adiabatic equations of state, and in viscous disks where the dimensionless kinematic viscosity $\nu \leq 10^{-5}$. This robustness suggests that the instability will have applications to a broad range of astrophysical disk-related phenomena, including those in close binary systems, planets embedded in protoplanetary disks (including Jupiter in our own Solar System) and FU Orionis outburst models. Further work is required to determine the nature of the instability, and to evaluate its observational consequences, in physically more complete disk models than we have considered in this Chapter. This chapter

has been published in the Astrophysical Journal, Volume 829, 13 (2016), in collaboration with Richard P. Nelson, Lee Hartmann, and Samuel Richard.

6.2 Introduction

Spiral density waves are excited in circumstellar disks by a variety of processes, and play an important role in the dynamical evolution and observational appearance of these systems. They arise as normal modes in self-gravitating disks (Lin & Shu, 1964), where they provide an efficient mechanism for the transport of mass and angular momentum through gravitational torques and an advective wave flux (Lynden-Bell & Kalnajs, 1972; Papaloizou & Savonije, 1991; Laughlin & Bodenheimer, 1994). Spiral shocks can be excited by stellar companions in close binary systems, including cataclysmic variables, X-ray binaries and T Tauri binaries (Lin & Papaloizou, 1979; Sawada et al., 1986; Artymowicz & Lubow, 1994). The excitation of nonlinear spiral waves by giant planets also plays an important role in structuring protoplanetary disks, and in driving the migration of embedded planets (Bryden et al., 1999; Kley, 1999; Nelson et al., 2000). Models for the origin of FU Orionis outbursts have been presented where spiral waves, originating in the gravitationally unstable outer regions of protostellar disks during the early infall phase, propagate into the inner disk regions and trigger the magnetorotational instability by heating and ionizing the disk gas there (Gammie 1999; Armitage et al. 2001; Zhu et al. 2010a; Chapter 3 of this thesis). Recent work has also shown that the infall of low angular momentum material onto a protostellar disk during the early infall phase can also generate global spiral waves (Lesur et al., 2015).

In this Chapter, we show that spiral waves in circumstellar disks are unstable to the growth of a parametric instability that leads to the disk flow becoming turbulent. We came across this phenomenon while extending the two-dimensional hydrodynamic simulations of triggered FU Orionis outbursts in Chapter 3 to three dimensions. The instability arises because pairs of inertial waves, or inertial-gravity waves, couple resonantly to the spiral wave, leading to the extraction of energy and angular momentum from it and the growth of a broad spectrum of inertial waves. Similar parametric instabilities, leading to the growth of inertial waves and the generation of small scale turbulence, have been reported to arise in numerous

circumstances where disk fluid elements are subjected to periodic forcing. Goodman (1993) and Ryu & Goodman (1994) showed that a parametric instability arises due to the elliptical distortion of a disk caused by an external orbiting companion. Warped disks have been shown to be subject to parametric instability (Gammie et al., 2000; Ogilvie & Latter, 2013), as have globally eccentric disks (Papaloizou, 2005a,b; Barker & Ogilvie, 2014). In a study similar to the one that we present here, Fromang & Papaloizou (2007) used shearing box simulations and analytical calculations to show that axisymmetric, nonlinear sound waves traveling in disks are also subject to parametric instability.

In this Chapter, we examine the stability of propagating $m = 2$ spiral waves in circumstellar disks, by carrying out three-dimensional global hydrodynamic simulations at high resolution. We consider a broad range of simplified disk models and input physics, including both isothermal and adiabatic equations of state, viscous and inviscid disks, and vertically stratified and non-stratified density profiles. Simulations are computed with four independent numerical codes, and the outcomes are found to be in good agreement with each other. Our main result is that the spiral density waves are unstable to the growth of the aforementioned parametric instability, leading to the development of turbulence in the disk models. We refer to the instability as the spiral wave instability (SWI). The SWI is found to be robust across the full range of models that we considered, suggesting that it will be influential in the dynamical evolution of disks that contain nonlinear spiral density waves of whatever origin.

This Chapter is organized as follows. In Section 6.3, we discuss the theoretical background to the SWI to set the scene for the numerical simulations. We describe our numerical methods in Section 6.4, including the basic equations solved and the disk models examined. In Section 6.5, we present results from cylindrical disk models as a demonstration of the instability in the simplest global model with a non-stratified, globally isothermal initial setup. Results from vertically stratified disk models with isothermal and adiabatic equations of state are discussed in Sections 6.6 and 6.7, respectively. We discuss the application of the SWI to various astrophysical disk phenomena, with a particular emphasis on protoplanetary disks, in Section 6.8, and we provide concluding remarks in Section 6.9. A reader who is mainly interested in the physical manifestation of the instability, and its potential applications, can

safely skip Sections 6.3 – 6.5 and read from Section 6.6 onwards.

6.3 Theoretical Background

Working in the context of a cylindrical coordinate system (R, ϕ, Z), we consider the situation where a spiral density wave, with azimuthal mode number m, propagates inwards in a quasi-Keplerian disk. The disk is assumed to be isothermal in the vertical direction (i.e. temperature independent of Z). We consider models in which the thermodynamic response of the gas is adiabatic, such that $\gamma > 1$, and models where the disk gas responds isothermally such that $\gamma = 1$. Under these conditions, the sound speed of the gas is independent of Z, and according to linear theory a spiral density wave that is launched from an inner Lindblad resonance (ILR) and has no vertical structure should propagate inwards maintaining its two-dimensional nature (Lin et al., 1990). Here, the absence of vertical structure simply means that perturbed quantities associated with the wave are independent of height.

A parametric instability may arise when an oscillator is subjected to a particular form of forcing at twice the natural frequency of the oscillator (e.g. a swinging pendulum with a moment of inertia that varies sinusoidally at twice the pendulum's mean natural frequency). In the context of astrophysical disks, parametric instabilities have been examined that arise from the excitation of pairs of inertial modes in disks that are elliptical due to tidal distortion by an external binary companion (Goodman, 1993) or due to the propagation of axisymmetric, nonlinear sound waves (Fromang & Papaloizou, 2007), where the two excited inertial waves have frequencies that satisfy the resonance condition $\omega_{\mathrm{i},1} + \omega_{\mathrm{i},2} = \omega_{\mathrm{F}}$, where the frequency of the forcing disturbance is ω_{F}. Viewed in a frame corotating with a fluid element in the disk, the frequency associated with a spiral wave that propagates interior to its inner Lindblad resonance is given by $\omega_{\mathrm{s}} = m(\Omega - \Omega_{\mathrm{p}})$, where Ω is the local orbital angular frequency and Ω_{p} is the pattern speed of the spiral wave measured in the inertial frame. In the specific case of an external companion on a circular orbit, Ω_{p} would be the angular frequency of the companion's orbit.

The WKBJ dispersion relation for local disturbances in a differentially rotating disk is

given by (Goodman, 1993)

$$\frac{\omega^2/c_s^2}{\omega^2 - N^2} - \frac{k_Z^2}{\omega^2 - N^2} - \frac{k_R^2}{\omega^2 - \kappa^2} = 0, \tag{6.1}$$

where ω is the mode frequency, κ is the epicyclic frequency defined as

$$\kappa^2 = \frac{1}{R^3}\frac{d}{dR}(R^2\Omega)^2, \tag{6.2}$$

N is the Brunt-Väisälä frequency defined as

$$N^2 = g\left(\frac{1}{\gamma P}\frac{dP}{dZ} - \frac{1}{\rho}\frac{d\rho}{dZ}\right), \tag{6.3}$$

k_R and k_Z are the wave numbers associated with the wave vector $\mathbf{k} = k_R\hat{\mathbf{e}}_R + k_Z\hat{\mathbf{e}}_Z$ and c_s is the sound speed. In the high frequency limit, $\omega^2 \gg N^2$, κ^2, Equation (6.1) supports acoustic waves where $\omega^2 \simeq c_s^2 k^2$. In the low frequency limit, where $\omega^2 \ll c_s^2 k^2$, the dispersion relation becomes

$$\omega_{\rm i}^2 = \kappa^2 \cos^2\theta + N^2 \sin^2\theta, \tag{6.4}$$

where the angle between the wave vector $\mathbf{k}$ and the Z-axis $\theta = \tan^{-1}(k_R/k_Z)$. Equation (6.4) governs the behavior of inertial-gravity modes. These correspond to fluid elements undergoing epicyclic motions, with the fluid motions being confined to planes that are tilted by an angle θ with respect to the disk midplane, and which are perpendicular to the wave vector, $\mathbf{k}$. Coriolis and buoyancy forces provide the restoring forces in the horizontal and vertical directions, respectively. In the absence of vertical buoyancy, as in a disk with an isothermal response to perturbations ($N^2 = 0$ when $\gamma = 1$), the dispersion relation simplifies to one that describes inertial waves

$$\omega_{\rm i}^2 = \kappa^2 \cos^2\theta. \tag{6.5}$$

To simplify the discussion, we use the term *inertial modes/waves* to denote inertial-gravity waves (supported by Coriolis and buoyancy forces) and inertial waves (supported only by the Coriolis force) from now on.

We might expect parametric instability to arise locally, through the coupling of a pair of

inertial waves to an incoming spiral wave with doppler-shifted frequency $\omega_{\rm s}$, when the two inertial waves have frequencies that obey the relation $\omega_{\rm i,1} + \omega_{\rm i,2} = \omega_{\rm s}$. Working in the high wave number limit where $\omega_{\rm i,1} \simeq \omega_{\rm i,2}$ (Fromang & Papaloizou, 2007), we have

$$2\omega_{\rm i} \simeq m(\Omega - \Omega_{\rm p}). \tag{6.6}$$

For the specific case of an $m = 2$ spiral wave, as considered in this Chapter, this becomes

$$\omega_{\rm i} = \Omega - \Omega_{\rm p}. \tag{6.7}$$

We see that the frequencies of inertial waves are independent of wave number, and simply depend on the orientation of the wave vector. For a disk that is finite in both radius and height, the wave numbers, k_R and k_Z, and associated wave frequencies, will be discrete. Considering a situation where the radial and vertical wavelengths are given by $\lambda_R = H/n_R$ and $\lambda_Z = H/n_z$, respectively (where H is the scale height), such that $k_R = 2\pi n_R/H$, $k_Z = 2\pi n_Z/H$ and (n_R, n_Z) are integers, then we have

$$\omega_{\rm i}^2(n_R, n_Z) = \frac{n_Z^2}{n_R^2 + n_Z^2}\kappa^2. \tag{6.8}$$

It is obvious from Equation (6.8) that if we consider arbitrarily large n_R and n_Z, then $\omega_{\rm i}$ can be matched with arbitrary precision to the value of $\Omega - \Omega_{\rm p}$, where $0 < \Omega_{\rm p} < \Omega$. In other words, inertial waves have a dense spectrum, and the resonance condition can always be matched to high precision for large enough k. Fromang & Papaloizou (2007), considering a disk with an isothermal equation of state, comment on the fact that the density of inertial modes is greater in a disk with vertical density stratification than in a non-stratified disk because of the larger range of length scales. Here, we also note that an adiabatic disk with $N^2 > 0$ also increases the density of inertial modes, because N^2 scans a range of frequencies as a function of height, and so increases the probability that the resonant condition for the parametric instability can be met at any given radius (i.e. one combination of n_R and n_Z may satisfy the resonance condition near the midplane where $N^2 \simeq 0$, and another combination may satisfy the resonance condition away from the midplane where $N^2 > 0$).

6.3.1 Wavelengths of Parametrically Excited Inertial Modes

Obtaining a full and detailed understanding of which specific pairs of inertial modes will couple to an incoming spiral wave by satisfying the resonance condition $\omega_{\mathrm{i},1} + \omega_{\mathrm{i},2} = \omega_{\mathrm{s}}$ would require determination of the radial and vertical eigenmode structure, and associated eigenfrequencies, for the global disk models that we consider. This goes beyond the scope of this Chapter (but see Barker & Latter (2015) for a study of a similar problem in the context of the vertical shear instability). Instead, we use simple arguments, based on a local WKBJ picture, to consider the approximate wave numbers associated with unstable inertial modes to help interpret and understand the simulations presented in later sections.

The WKBJ dispersion relation for a spiral wave with azimuthal mode number m (in the absence of self-gravity) is given by (assuming $k_Z = 0$)

$$m^2(\Omega - \Omega_{\mathrm{p}})^2 = \kappa^2 + c_s^2 k_{R,\mathrm{s}}^2, \tag{6.9}$$

giving a radial wave number interior to the ILR

$$k_{R,\mathrm{s}}^2 = \frac{m^2(\Omega - \Omega_{\mathrm{p}})^2 - \kappa^2}{c_s^2}. \tag{6.10}$$

Inertial modes that are excited by the spiral wave must occur on radial length scales similar to or smaller than the incoming wavelength, so for simplicity we write the wave number of the excited inertial waves (assuming they have very similar spatial structure and frequencies, appropriate to the high wave number limit) $k_{R,\mathrm{i}} = n k_{R,\mathrm{s}}$, where n is an integer. Given the radial wave number and the frequency of the spiral wave (in the local fluid frame), we can estimate the vertical wave number of the excited inertial waves using the dispersion relation from Equation (6.1), written using the modified notation

$$\frac{k_{Z,\mathrm{i}}^2}{\omega_{\mathrm{i}}^2 - N^2} + \frac{k_{R,\mathrm{i}}^2}{\omega_{\mathrm{i}}^2 - \kappa^2} - \frac{\omega_{\mathrm{i}}^2/c_s^2}{\omega_{\mathrm{i}}^2 - N^2} = 0, \tag{6.11}$$

giving

$$k_{Z,\mathrm{i}}^2 = -\frac{n^2 k_{R,\mathrm{s}}^2}{\omega_{\mathrm{i}}^2 - \kappa^2}(\omega_{\mathrm{i}}^2 - N^2) + \frac{\omega_{\mathrm{i}}^2}{c_s^2}. \tag{6.12}$$

Substituting the resonance condition $\omega_{\rm i} = \omega_{\rm s}/2$ and $k_{R,{\rm s}}^2 = (\omega_{\rm s}^2 - \kappa^2)/c_s^2$ into Equation (6.12) gives

$$k_{Z,{\rm i}}^2 = \frac{(\omega_{\rm s}/2)^2}{c_s^2} - n^2 \frac{\omega_{\rm s}^2 - \kappa^2}{c_s^2} \frac{(\omega_{\rm s}/2)^2 - N^2}{(\omega_{\rm s}/2)^2 - \kappa^2}. \tag{6.13}$$

First, we consider the behavior of $k_{Z,{\rm i}}$ for disks in which $N^2 = 0$

$$k_{Z,{\rm i}}^2 = \frac{(\omega_{\rm s}/2)^2}{c_s^2} \left(1 - n^2 \frac{\omega_{\rm s}^2 - \kappa^2}{(\omega_{\rm s}/2)^2 - \kappa^2} \right). \tag{6.14}$$

For $k_{Z,{\rm i}}$ to be real, such that inertial waves can be excited, we require that $\omega_{\rm s}^2 > \kappa^2$ and $(\omega_{\rm s}/2)^2 < \kappa^2$, and these conditions are both satisfied at all radii interior to the inner Lindblad resonance of an $m = 2$ spiral wave in a Keplerian disk. (These conditions, however, are not satisfied everywhere for a spiral wave that propagates outwards from an outer Lindblad resonance, as we discuss later in Section 6.8.) Considering the influence of buoyancy in Equation (6.13), we see that $k_{Z,{\rm i}}$ can become imaginary when $(\omega_{\rm s}/2)^2 < N^2$, indicating that inertial modes will not be excited at certain locations above the midplane where the buoyancy frequency is large. Taking the large n limit, the transition occurs at $(\omega_{\rm s}/2)^2 = N^2$. Given that the resonance condition for the excited inertial waves is $\omega_{\rm i} = (\omega_{\rm s}/2)$, this indicates that inertial modes cannot be excited where $\omega_{\rm i} < N$. Later in the Chapter, we use Equation (6.13) to construct maps of stable and unstable regions of our disks for comparison with the simulation results, and to consider the influence of numerical resolution on our ability to resolve unstable inertial waves that arise on small scales.

As we have emphasized, there are a number of caveats that should be considered before applying the above arguments to the simulation results. The most obvious is the fact that a local WKBJ analysis, that applies to modes where $k_Z H \gg 1$ and $k_R H \gg 1$, is not strictly applicable to modes with $k_R \sim 1/H$, as may be excited by spiral waves in a global disk model. Furthermore, for simplicity we have assumed that there is an integer relation between the wavelengths of the excited inertial waves and the incoming spiral modes, and this is not precisely the situation that should arise because the linear inertial modes supported in the global disk model should be quantized to fit within the radial boundaries of the disk, and hence are not expected to have an integer relation with the spiral waves. A full analysis of the modes that can be excited should take account of the full structure of the eigenfunctions

in both radial and vertical directions, and their frequencies, which represents a significant computational problem (e.g. Barker & Latter, 2015), and goes beyond the scope of this Chapter. It is noteworthy, however, that Lubow & Pringle (1993) compute the vertical structure of inertial-gravity waves in vertically isothermal disks that support buoyancy forces, and demonstrate that inward traveling waves have their wave energy increasingly confined towards the midplane as they enter disk radii where large fractions of the disk vertical domain have $N^2 > \omega_{\rm i}^2$, since this defines the region of space where the waves can (or cannot) propagate. Similar forbidden zones arise in the above WKBJ analysis for essentially the same reason, as we have described above.

6.3.2 Nonlinear Wave Propagation in Vertically Stratified Disks

In linear theory, a two-dimensional spiral wave without any vertical structure, launched at an inner Lindblad resonance in a vertically isothermal disk with sound speed independent of Z, should propagate towards the star with wave fronts remaining perpendicular to the midplane. As described in the next section, the underlying axisymmetric disk model will normally have midplane density varying according to $\rho(R,0) = \rho(R_0,0)(R/R_0)^p$, with $p < 0$, and variation with height scaling as $\rho(R,Z) \sim \rho(R,0)\exp\left(-Z^2/(2H^2)\right)$, where H is the density scale height. For such a model, the wave front associated with an inward propagating wave will see an increasing midplane density as it moves in, but at high altitudes the wave front will see a sharply decreasing density. We might then expect that nonlinear effects experienced by the wave to be greater at high altitudes than near the midplane. These effects include distortion of the wave form and an enhanced propagation speed due to advection of the wave by the perturbed radial velocity. We expect this will result in curvature of the spiral wave fronts as these waves propagate towards the star. An important consequence of this is that vertical hydrostatic equilibrium will not be maintained at the wave fronts, resulting in the generation of vertical motions as the wave moves inwards, and an oscillating non-axisymmetric corrugation of the disk surface.

6.4 Numerical Methods

6.4.1 Basic Equations

We solve the hydrodynamic continuity, momentum, and internal energy equations:

$$\frac{\partial \rho}{\partial t} + \nabla \cdot (\rho v) = 0, \tag{6.15}$$

$$\rho \left(\frac{\partial v}{\partial t} + v \cdot \nabla v \right) = -\nabla P - \rho \nabla (\Phi_* + \Phi_p) + \nabla \cdot \Pi, \tag{6.16}$$

$$\frac{\partial e}{\partial t} + \nabla \cdot (ev) = -P \nabla \cdot v, \tag{6.17}$$

where ρ is the mass density, v is the velocity, P is the pressure, Φ_* is the gravitational potential due to the central object, Φ_p is the spiral potential (see Section 6.4.3), Π is the viscous stress tensor, and e is the internal energy per unit volume.

We make use of both cylindrical (R, ϕ, Z) and spherical (r, θ, ϕ) coordinates. We consider cylindrical disk models where we neglect the vertical component of gravity from the central object, so the gravitational potential is $\Phi_* = GM_*/R$, where G is the gravitational constant, M_* is the mass of the central object and R is the cylindrical radius. These models are computed using cylindrical coordinates. The purpose of using non-stratified, cylindrical models is to illustrate the nature of the instability as clearly as possible, by removing/minimizing complications that may arise from spherical geometry, concave wave structure (see Section 6.6.1), etc. Furthermore, adopting a cylindrical disk model allows us to run models with periodic boundary conditions in the vertical direction, and hence allows us to demonstrate that the existence of the instability is independent of the chosen boundary conditions.

We also consider models where the density is vertically stratified. The gravitational potential is then $\Phi_* = GM_*/r$, where $r = \sqrt{R^2 + Z^2}$ is the spherical radius. These models are computed using spherical coordinates.

We make use of two forms of equation of state. In the isothermal calculations, we use an isothermal equation of state $P = \rho c_s^2$, where c_s is the isothermal sound speed, and do not solve the internal energy equation. In the adiabatic calculations, we relate the gas pressure

and the internal energy through $P = (\gamma - 1)e$, where γ is the adiabatic index, and solve the internal energy equation. We do not include the effects of cooling in the internal energy equation. Instead, we explore the effects of cooling by changing the adiabatic index value. The idea is that a disk with very rapid cooling acts as if it is isothermal, and hence has an effective $\gamma \sim 1$, whereas a disk with very slow cooling acts as if it is adiabatic, and thus its effective γ is equal to the actual ratio of specific heats in the disk, here taken to be $\gamma = 1.4$. Intermediate values of the effective γ correspond to intermediate cooling rates. We take this approach because determining the Brunt-Väisälä frequency is not trivial in the presence of cooling, making comparison between numerical results and theoretical predictions difficult.

We include physical and artificial viscosity (Stone & Norman, 1992). Lyra et al. (2016) has recently considered the local generation of entropy through strong spiral shocks induced by massive planets, that could in turn drive local convective motions. We have confirmed, however, that the shock dissipation heating is negligible in our adiabatic calculations because the spiral waves considered in this work are much weaker.

6.4.2 Disk Models

We begin with an initial radial power-law temperature distribution in the disk that is independent of height

$$T(R) = T_0 \left(\frac{R}{R_0} \right)^q , \tag{6.18}$$

where T_0 is the temperature at $R_0 = 1$. In all models presented, T_0 is chosen such that the ratio of disk scale height to radius at R_0 is $H_0/R_0 = 0.05$. The isothermal sound speed is related to the temperature by $c_s^2 = \mathcal{R}T/\mu$, where $\mathcal{R}$ is the gas constant and μ is the mean molecular weight. Thus, Equation (6.18) corresponds to the radial sound speed distribution given by

$$c_s(R) = \frac{H_0}{R_0} \left(\frac{R}{R_0} \right)^{q/2} . \tag{6.19}$$

For the main simulation set we assume $q = 0$, so that the disk has the same temperature everywhere. This temperature structure might not be very realistic, especially when the simulation domain extends more than an order of magnitude in radius. On the other hand, one can safely ignore the vertical shear instability in these models, because the instability

Table 6.1. Model Parameters for Globally Isothermal SWI Calculations

Run Label	Code	Numerical Resolution (N_R or $N_r \times N_\phi \times N_z$ or N_θ)	$\mathcal{A}$	Kinematic Viscosity ν	γ
CYL-F	FARGO3D	$512 \times 128 \times 128$	5.0×10^{-4}	0	1.0
CYL-N	NIRVANA	$3200 \times 128 \times 128$	5.0×10^{-4}	0	1.0
CYL-P	PLUTO	$512 \times 128 \times 128$	5.0×10^{-4}	0	1.0
CYL-I	INABA3D	$3200 \times 128 \times 128$	5.0×10^{-4}	0	1.0
R512	FARGO3D	$512 \times 128 \times 128$	5.0×10^{-4}	0	1.0
R128	FARGO3D	$128 \times 32 \times 32$	5.0×10^{-4}	0	1.0
R256	FARGO3D	$256 \times 64 \times 64$	5.0×10^{-4}	0	1.0
R768	FARGO3D	$768 \times 192 \times 192$	5.0×10^{-4}	0	1.0
AMP0.625	FARGO3D	$512 \times 128 \times 128$	6.25×10^{-5}	0	1.0
AMP1.25	FARGO3D	$512 \times 128 \times 128$	1.25×10^{-4}	0	1.0
AMP2.5	FARGO3D	$512 \times 128 \times 128$	2.5×10^{-4}	0	1.0
AMP10	FARGO3D	$512 \times 128 \times 128$	1.0×10^{-3}	0	1.0
V6	FARGO3D	$512 \times 128 \times 128$	5.0×10^{-4}	10^{-6}	1.0
V5	FARGO3D	$512 \times 128 \times 128$	5.0×10^{-4}	10^{-5}	1.0
V4	FARGO3D	$512 \times 128 \times 128$	5.0×10^{-4}	10^{-4}	1.0
GAM01	FARGO3D	$512 \times 128 \times 128$	6.25×10^{-5}	0	1.01
GAM05	FARGO3D	$512 \times 128 \times 128$	6.25×10^{-5}	0	1.05
GAM1	FARGO3D	$512 \times 128 \times 128$	6.25×10^{-5}	0	1.1
GAM2	FARGO3D	$512 \times 128 \times 128$	6.25×10^{-5}	0	1.2
GAM3	FARGO3D	$512 \times 128 \times 128$	6.25×10^{-5}	0	1.3
GAM4	FARGO3D	$512 \times 128 \times 128$	6.25×10^{-5}	0	1.4

requires a non-zero vertical gradient in the disk angular velocity which arises when there is a radial temperature gradient (Nelson et al., 2013). In the Appendix, we present models with a radial temperature gradient ($q = -1$). In those models, we find that the spiral wave instability and the vertical shear instability coexist in the absence of kinematic viscosity, and thus identifying intrinsic features arising from the SWI is challenging. The vertical shear instability can be suppressed with a non-zero kinematic viscosity, but adding kinematic viscosity not only suppresses the vertical shear instability but also damps the growth of small scale unstable modes excited by the SWI. To summarize, by assuming the globally isothermal temperature structure, we aim to illustrate the nature of the SWI as clearly as possible, in the absence of any other hydrodynamic instabilities.

The initial density and azimuthal velocity profiles are constructed to satisfy hydrostatic equilibrium (e.g. Nelson et al., 2013):

$$\rho(R, Z) = \rho_0 \left(\frac{R}{R_0}\right)^p \exp\left(\frac{GM_*}{c_s^2}\left[\frac{1}{\sqrt{R^2 + Z^2}} - \frac{1}{R}\right]\right) \tag{6.20}$$

and

$$v_\phi(R, Z) = \left[(1+q)\frac{GM_*}{R} + (p+q)\, c_s^2 - q\frac{GM_*}{\sqrt{R^2+Z^2}}\right]^{1/2}. \tag{6.21}$$

The midplane density at $R = R_0$, ρ_0, is chosen such that the total disk mass is 10 % of the central object's mass. When vertical stratification of the disk is ignored in the cylindrical disk models, the above equations simplify to:

$$\rho(R, Z) = \rho_0 \left(\frac{R}{R_0}\right)^p \tag{6.22}$$

and

$$v_\phi(R, Z) = \left[\frac{GM_*}{R} + (p+q)\, c_s^2\right]^{1/2}. \tag{6.23}$$

We fix the radial power-law index of the midplane gas density to $p = -1.5$ for all models. The initial radial and vertical/meridional velocity are set to zero, but uniformly distributed random perturbations are added as white noise, at the level of 10^{-6} c_s, to the initial vertical/meridional velocity in order to seed the instability. We have tested the effects of changing the amplitudes of the random perturbations, and found that the growth rate and the satu-

ration level of the instability are not sensitive to the initial noise level.

Our simulation domain extends from 0.5 to 10 in radius and from 0 to 2π in azimuth. In cylindrical models, the vertical domain extends from $Z = -0.1$ to 0.1. In spherical models, the meridional domain covers $\pm 4H_0/R_0$ above and below the midplane. The model parameters are summarized in Table 6.1.

6.4.3 Spiral Potential

In order to excite spiral waves, we adopt the following potential Φ_p:

$$\Phi_p(R, \phi, t) = \mathcal{A} \cos[m(\phi - \Omega_p t)] e^{-(R-R_p)^2/\sigma_p^2}, \tag{6.24}$$

where $\mathcal{A}$ is the amplitude, assumed to be constant over time, m is the azimuthal mode number, Ω_p is the pattern speed, R_p is the radius about which the potential is centered, and σ_p is the radial width of the potential. We adopt the values $R_p = 5$ and $\sigma_p = 1$, and assume that the pattern speed is the local Keplerian frequency at its central position: $\Omega_p = (GM_*/R_p^3)^{1/2}$. In this work, we only focus on spiral potentials with $m = 2$.

Our fiducial model assumes potential amplitude of $\mathcal{A} = 5.0 \times 10^{-4}$. With this amplitude we intend to produce velocity perturbations at $R = 1$ that are about $\sim 20\%$ of the local sound speed[1]. The effect of varying the spiral potential strength on the spiral wave instability is investigated in Section 6.6.3.

Prior to discussing the results of simulations in any detail, we briefly illustrate the effects of changing the spiral wave amplitude on the wave forms and propagation speeds of the waves in the midplane of a stratified disk. In Figure 6.1, we present the radial velocity profiles in the disk midplane of a stratified disk model, driven by two spiral potential amplitudes of $\mathcal{A} = 5.0 \times 10^{-4}$ and $\mathcal{A} = 6.25 \times 10^{-5}$. As shown, the overall structure of the spiral waves driven in the numerical simulations agrees well with theoretical expectations: from the WKBJ dispersion relation for a non self-gravitating disk one expects to see waves propagating interior and exterior to the inner and outer Lindblad resonances, with the waves being

[1]As we mentioned in the introduction, the spiral wave instability was found while studying spiral wave propagation as part of a study of accretion outbursts in FU Orionis systems. This spiral amplitude produces velocity and density fluctuations in the inner disk similar to the ones produced by the gravitationally unstable outer disk, with which an accretion outburst was triggered (see Figure 5b of Chapter 3).

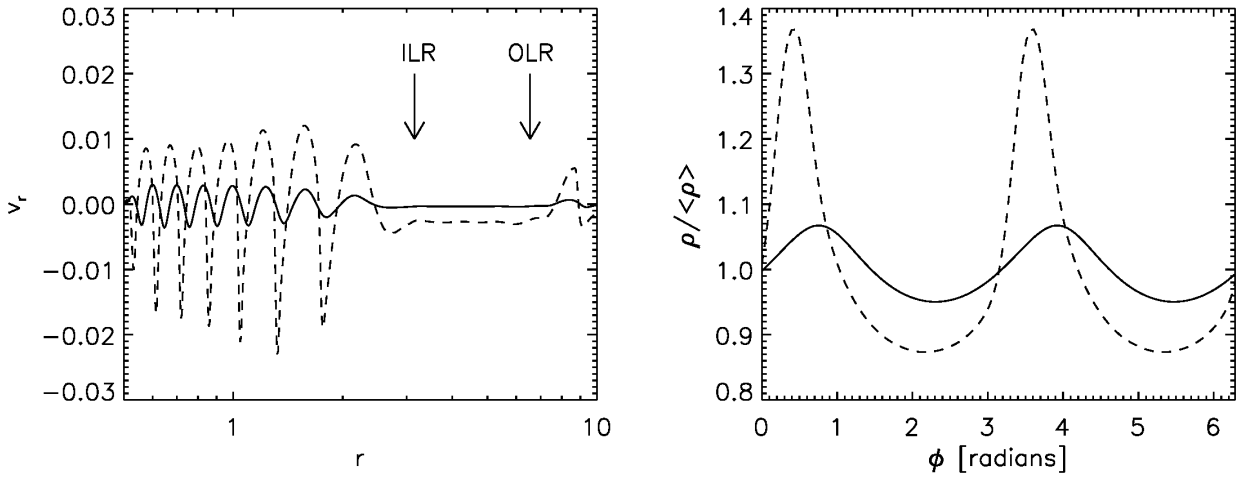

Figure 6.1. (Left) The radial velocity v_r in the disk midplane induced by the spiral potential with amplitudes of (solid) $\mathcal{A} = 6.25 \times 10^{-5}$ from model AMP0.625 and (dashed) $\mathcal{A} = 5 \times 10^{-4}$ from model R512. The arrows indicate the location of the inner and outer Lindblad resonances (ILR and OLR). (Right) The azimuthal distribution of the midplane density at $r = 0.6$, normalized by the azimuthal average. As in the left panel, the solid and dashed curves are when $\mathcal{A} = 6.25 \times 10^{-5}$ and $\mathcal{A} = 5 \times 10^{-4}$, respectively. The data are taken after the spiral waves are well established over the entire disk, but before the spiral wave instability perturbs the wave structures.

evanescent in the region between the resonances (Lin & Shu, 1964; Goldreich & Tremaine , 1978, 1979). The wave with the small potential amplitude $\mathcal{A} = 6.25 \times 10^{-5}$ is nearly sinusoidal. In the inner disk, the velocity amplitude is about a few per cent of the sound speed and is nearly constant over radius. When the spiral potential amplitude is increased to $\mathcal{A} = 5 \times 10^{-4}$, on the other hand, the waves are rather strong, generating sharp wave fronts that have radial velocities up to about 40 % of the sound speed. At $r = 0.6$, the two spiral potential amplitudes generate relative density enhancements of $\sim 7\%$ ($\mathcal{A} = 6.25 \times 10^{-5}$) and $\sim 37\%$ ($\mathcal{A} = 5 \times 10^{-4}$) above the azimuthal average. In addition to these differences in perturbed velocities and densities, we also note that the propagation speed of the higher amplitude wave is slightly faster than that of the lower amplitude wave. This is a nonlinear effect arising from the fact that the magnitude of the perturbed velocity contributes to the wave speed through the advection term in the momentum equation. The magnitude of this effect as a function of height in the disk plays an important role in determining the shape of the spiral wave fronts in the stratified disk models, as discussed in Section 6.3 and demonstrated in Section 6.6.

6.4.4 Boundary Conditions

One needs to take particular care with the boundary conditions when simulating an instability, in order to ensure that what is being observed is not an artifact generated by the boundaries. The requirement that models with vertical stratification are able to maintain hydrostatic equilibrium has forced us to pay particular attention to the meridional boundary conditions. The radial boundary condition is chosen to have a zero gradient for all variables in all models, and a wave damping zone is implemented (de Val-Borro et al., 2006) in the intervals $R = [0.5, 0.6]$ and $R = [9, 10]$. We choose one local orbital time for the wave damping timescale. As the simulation domain covers 2π in azimuth, periodic boundary conditions are used in azimuth.

Vertical periodic boundary conditions are used in models where we neglect vertical stratification. In the stratified models, we use an outflow meridional boundary condition such that all velocity components in the ghost zones have the same values as the last active zones, but the meridional velocity is set to 0 if directing toward the disk midplane. In adiabatic calculations, the temperature in the ghost zones is set to have the same value as in the last active zones. The density in the ghost zone is then obtained by solving the hydrostatic equilibrium in the meridional direction:

$$\frac{1}{\rho}\frac{\partial}{\partial\theta}(\rho c_s^2) = \frac{v_\phi^2}{\tan\theta}. \tag{6.25}$$

In order to investigate the influence of the meridional boundaries in the stratified models, we tested various boundary conditions including the zero-gradient boundary condition, the standard outflow boundary condition, the reflecting boundary condition, and the wave-damping boundary conditions. We find that the choice of the meridional boundary condition does not affect the triggering of the parametric instability. For the Godunov codes, however, we find that enforcing hydrostatic equilibrium in the meridional ghost zones using Equation (6.25) maintains the low-density surface region more stably than with other boundary conditions, allowing us to better observe the early development of the instability.

6.4.5 Codes

We use four independent grid-based codes: FARGO3D, NIRVANA, PLUTO, and INABA3D. These include two finite difference codes and two Godunov codes, to ensure the robustness of the results.

FARGO3D is a finite difference code developed with special emphasis on disk simulations (Benítez-Llambay & Masset, 2016). An orbital advection algorithm is implemented as in its two-dimensional predecessor FARGO (Fast Advection in Rotating Gaseous Objects; Masset 2000) code. We have tested with and without the FARGO algorithm and found that the result is not dependent on the use of the FARGO algorithm.

Similar to FARGO3D, NIRVANA uses an algorithm very similar to that used in the ZEUS code to solve the equations of ideal MHD (Ziegler & Yorke, 1997; Stone & Norman, 1992). This scheme uses operator splitting, dividing the governing equations into source and transport terms. Advection is performed using the second-order monotonic transport scheme (van Leer, 1977).

PLUTO is a general-purpose Godunov code (Mignone et al., 2007). We employ the piece-wise parabolic reconstruction and third-order Runge-Kutta time integration. We note that lower-order schemes, e.g. the piece-wise linear reconstruction and second-order Runge-Kutta time integration, do not produce a converged Riemann solution for the problem considered in this work. The FARGO orbital advection module was enabled for the calculations with PLUTO.

INABA3D is a finite volume code using an unsplit MUSCL Hancock scheme, which is a second order method in time and space. The physical values on the faces of each cells are calculated through an exact Riemann solver. The code is based on the 2D code described in Inaba et al. (2005), and the third dimension has been implemented as in Richard et al. (2013).

As shown in Table 6.1, most simulations in this Chapter were computed using the FARGO3D code. We note that FARGO3D and PLUTO use a logarithmically spaced radial grid, whereas NIRVANA and INABA3D use a uniform mesh. The innermost grid cell size in the FARGO3D and PLUTO runs was $\Delta r = 0.002934$, and this value was used for the

uniform meshes in the NIRVANA and INABA3D runs.

6.4.6 Code Units

We choose code units such that $GM_* = R_0 = \Omega(R = R_0) = 1$. Since we do not include cooling, all the calculations are scalable to any system of interest. In the following sections we will use the orbital time at $R = 1$ as the time unit. We will denote this quantity as 1 $T_{\rm orb}$. One orbital time at the spiral potential center $R = R_p$, T_p, corresponds to 11.2 $T_{\rm orb}$.

6.4.7 Diagnostics

In order to examine the growth and evolution of the spiral wave instability we calculate the volume-integrated vertical kinetic energy, e_Z, in non-stratified disk models (as these are computed using cylindrical coordinates) and the volume-integrated meridional kinetic energy, e_θ, in the stratified disk models (as these use spherical polar coordinates):

$$e_{Z,\theta} = \frac{1}{2}\int_V \rho v_{Z,\theta}^2 \; dV. \tag{6.26}$$

The volume integration is performed in between $R = 0.6$ and $R = 1.0$, in order to capture growth in a local region of the disk to better measure exponential growth rates.

6.5 Non-stratified Disk Models

We start discussion of the simulations by describing results of the non-stratified disk models. In Figure 6.2, we present the time evolution of the integrated vertical kinetic energy e_Z, where we see that this quantity exponentially increases at early times ($t \lesssim 40$) before saturating to a quasi-steady value at late times, indicating the presence of an instability.

In Figures 6.3 and 6.4, we display the two-dimensional distributions of the vertical and radial velocities at some selected times. Since vertical density stratification of the disk is neglected, and the sound speed is independent of height, the spiral waves propagate purely radially before the SWI sets in, maintaining wave fronts that are perpendicular to the disk midplane, as seen in the first two panels of Figure 6.4. Hence, the spiral waves in themselves

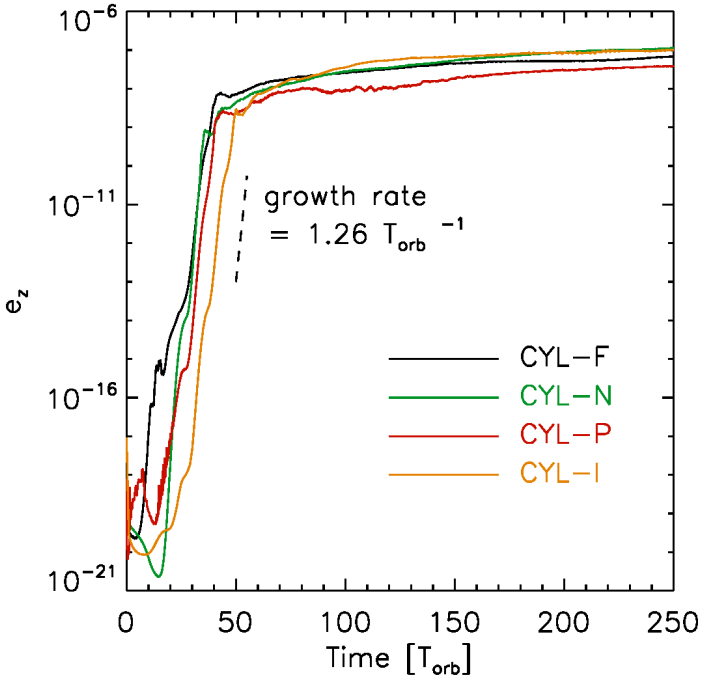

Figure 6.2. Time evolution of the integrated vertical kinetic energy e_Z for non-stratified models with different codes (CYL-F, CYL-N, CYL-P, CYL-I). The black dashed line corresponds to the growth rate of 1.26 $T_{\rm orb}^{-1}$.

are not expected to generate any vertical motion in the disk. We see that the inertial modes grow fastest in the inner disk regions, as their frequencies and growth rates are larger there, and the instability spreads to larger radii as time progresses. At $t = 20$, the inertial modes that are excited by the spiral wave form a checkerboard pattern in the vertical velocities, as seen in Figure 6.3. Close visual inspection of the plot, combined with a Fourier analysis, shows that in the disk inner regions around $R = 0.6$, the vertical wavelength associated with the excited inertial modes $\lambda_Z \simeq 0.004$ and the radial wavelength $\lambda_R \simeq 0.04$. These wavelengths correspond to approximately 3 and 12 grid cell spacings in the vertical and radial directions, respectively, indicating that the fastest growing modes have the shortest wavelengths that can be represented on the computational grid, presumably limited by the vertical resolution in this case. This is in agreement with Fromang & Papaloizou (2007), who showed that short wavelength inertial waves excited by axisymmetric, nonlinear sound waves have higher growth rates than longer wavelength modes.

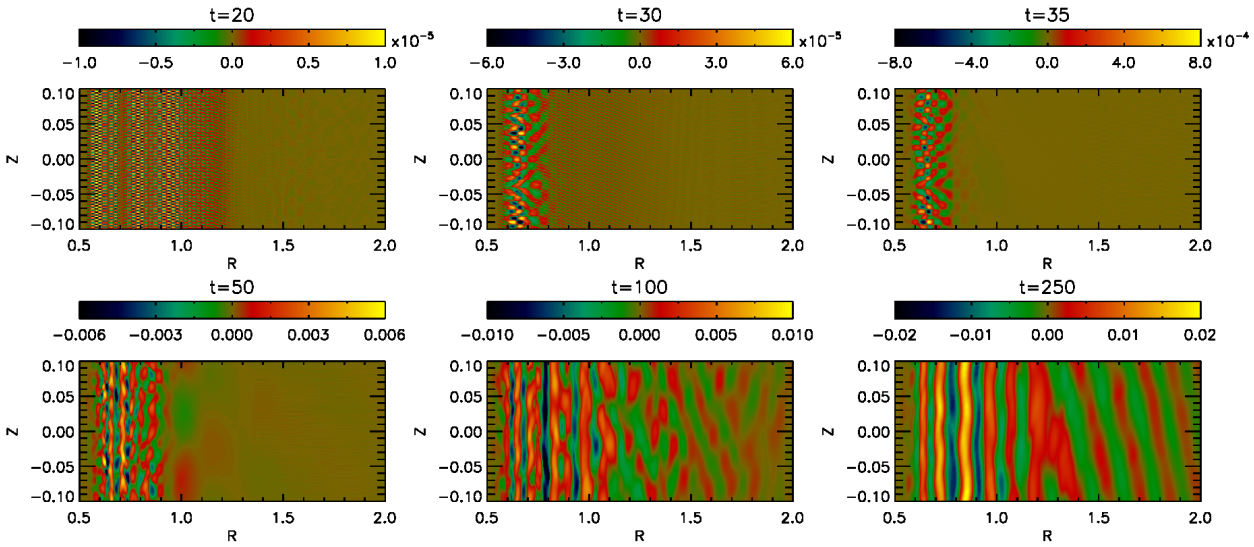

Figure 6.3. Distributions of the vertical velocity in a $R - Z$ plane ($\phi = 0$) interior to $R = 2$ at various times for model CYL-F. The upper panels show the linear growth phase of the SWI. The instability saturates when the perturbed vertical velocity of the unstable modes is comparable to the radial velocity of the imposed spiral waves.

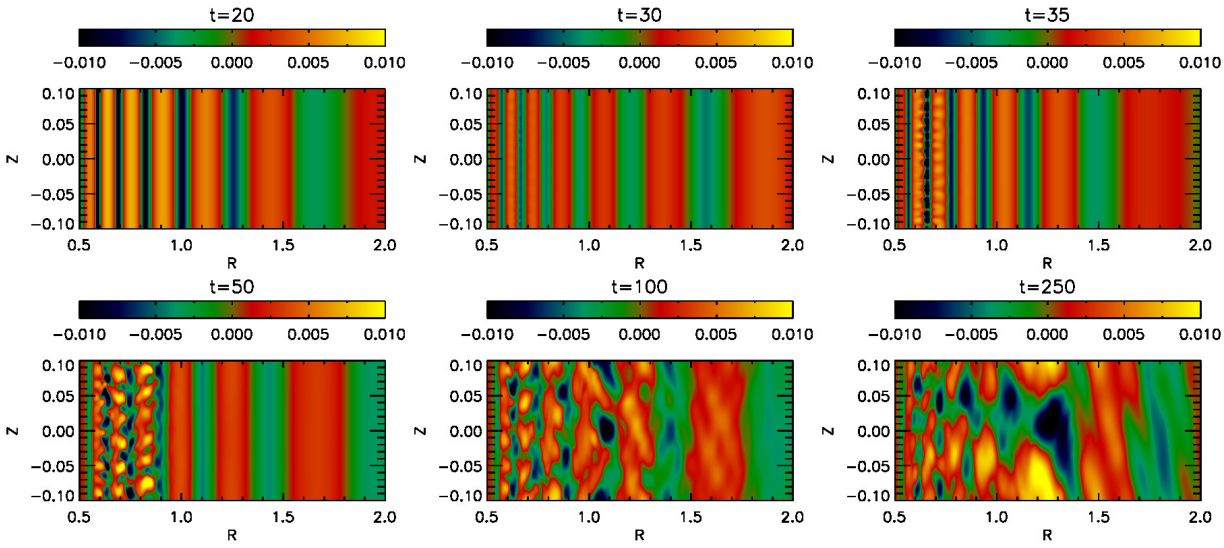

Figure 6.4. Same as Figure 6.3, but for the radial velocity.

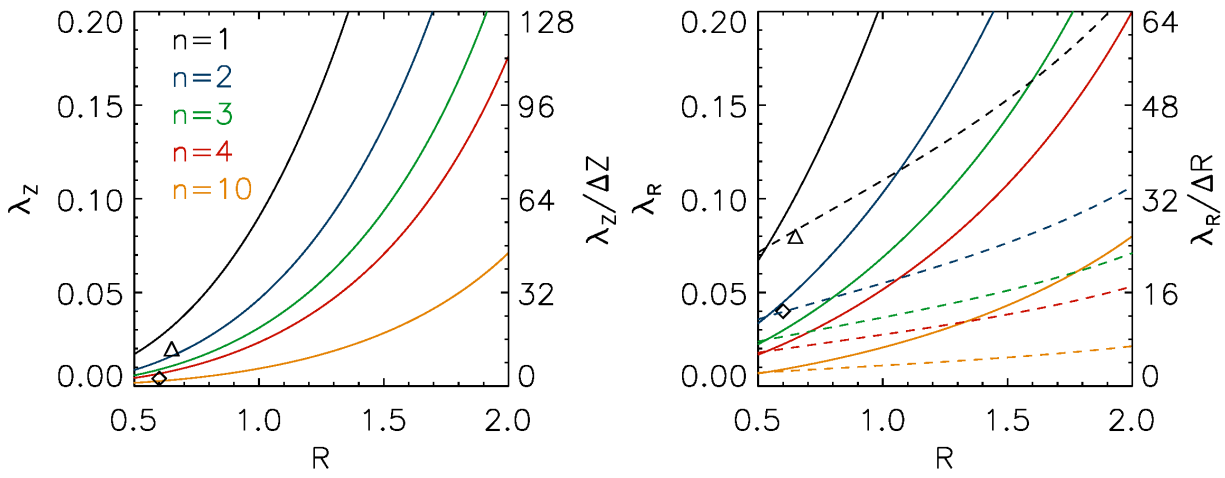

Figure 6.5. The predicted (left) vertical and (right) radial wavelengths of the unstable modes λ_Z and λ_R as a function of radius, calculated from the relation given in Equation (6.13) and Equation (6.10) with $k_{R,\mathrm{i}} = nk_{R,\mathrm{s}}$, where n is an integer, and $k_{R,\mathrm{s}}$ and $k_{R,\mathrm{i}}$ are the wave numbers of the spiral wave and the excited inertial modes, respectively. The over-plotted symbols indicate the measured vertical and radial wavelengths of the unstable inertial modes at the innermost spiral arm location at $t = 20$ ($R \sim 0.6$; diamonds) and 30 ($R \sim 0.65$; triangles). In the right panel, the solid curves present the radial wavelengths and the dashed curves show the number of radial grid cells in one inertial mode wavelength ($\lambda_R/\Delta R$).

Figure 6.3 shows that at slightly later times, $t = 30$, the length scales associated with the most prominent perturbations have increased substantially, presumably indicating that these longer wavelength modes grow on longer time scales, but may also contain more energy than the shorter wavelength modes seen to grow earlier. This latter point may, however, be affected by numerical diffusion damping the smallest scale modes, so some caution is required when interpreting this result. Inspection of the figure, and Fourier analysis, indicate that these modes have wavelengths $\lambda_Z \simeq 0.02$ and $\lambda_R \simeq 0.08$. We have plotted these and the earlier wavelength values in Figure 6.5, which shows the vertical and radial wavelengths of the inertial modes that are predicted to be excited by the spiral wave using the simple local analysis presented in Section 6.3. Noting the caveats associated with the analysis discussed earlier in the Chapter, we see that the early growing modes have radial wavelengths that are $\sim 1/3$ that of the incoming spiral wave, and the later growing modes have radial wavelengths very similar to the spiral wave. The numbers of grid cells covered by the different wavelengths are also indicated in this figure, demonstrating that the earlier growing modes occur on

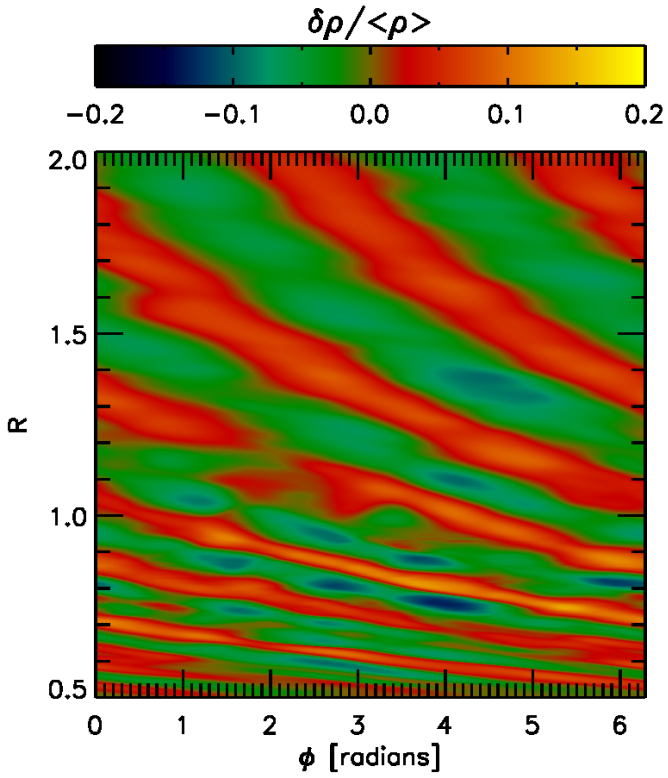

Figure 6.6. Distribution of the normalized perturbed density $\delta\rho/\langle\rho\rangle$ in the $Z = 0$ plane at $t = 250$ from the CYL-F model.

length scales close to the grid scale, whereas the later growing modes are more comfortably represented on the grid.

The growth rate measured during the exponential growth phase shown in Figure 6.2 is measured to be 1.26 $T_{\rm orb}^{-1}$. While this represents the growth associated with the superposition of numerous growing inertial modes between the radii $R = 0.6-1$, it is likely to be dominated by the longer wavelength modes. The instability saturates at about $t = 50$. As shown in Figure 6.3 and 6.4, the maximum perturbed vertical and radial velocities of the unstable inertial modes at saturation are on the order of the radial velocity of the background wave. This is presumably an indication of the fact that the linear instability saturates when the perturbed velocity grows large enough to disrupt the structure of the background wave, as also argued by Fromang & Papaloizou (2007). During the non-linear phase of the instability, the checkerboard shaped cells merge together, creating alternating vertical flows. At $t = 250$, the vertical flows are locally as fast as $\sim 50\%$ of the sound speed.

In Figure 6.6, we present the perturbed density distribution $\delta\rho/\langle\rho\rangle$ in a horizontal (R, ϕ)

plane at $t = 250$, where the angled brackets denote an azimuthal average and $\delta\rho = \rho - \langle\rho\rangle$. As expected from the snapshots in the vertical plane, the spiral arms are highly perturbed, showing fragmentary structures. Moving along the azimuth at any given radius shows a clear asymmetry. We will further discuss the appearance of the disrupted spiral structures in Section 6.8.2.3, along with their observational implications.

6.5.1 Code Comparison

In order to demonstrate the robustness of the instability we have run the same calculation with the four independent codes introduced in Section 6.4.5. As shown in Figure 6.2, clear exponential growth of the instability is observed with all codes. The growth time measured during the linear phase ranges between $\sim 1.2 - 1.4\ T_{\rm orb}^{-1}$. The saturated perturbed energy levels also show good agreement with each other, being within a factor ~ 3 at $t = 250$.

We note, however, that the early evolution of the perturbed kinetic energy ($t \lesssim 30$) seems to be more code dependent than the later evolution. In particular, the exponential growth seen at $5 \lesssim t \lesssim 15$ in the CYL-F model is not observed with the other codes. As discussed earlier, this is when the small scale modes, with wavelengths comparable to grid cell size, grow in the models. The growth rates of such small wavelength modes are inevitably dependent on the dissipative properties of each code.

In Figure 6.7, we present contour plots of the vertical velocity obtained with NIRVANA, PLUTO and INABA3D. Although the detailed evolution of the instability may slightly differ, it is clear that the same instability is being captured by all codes – the instability exhibits a checkerboard pattern during the linear phase, and alternating vertical flows when saturated.

As mentioned in Section 6.4.2, we initially add small, random, vertical velocities to seed the instability. Adding noise puts energy into the inertial modes in the disk. When the initial random perturbation is not added, we note that the cylindrical model does not trigger the SWI with the finite volume codes PLUTO and INABA3D. These codes do an excellent job of maintaining the symmetry associated with the initial conditions because the conservative properties of these codes are enforced by the pairwise exchange of fluid properties between neighboring grid cells. In the finite difference codes, however, we find that the SWI still develops when starting without the initial perturbations, presumably

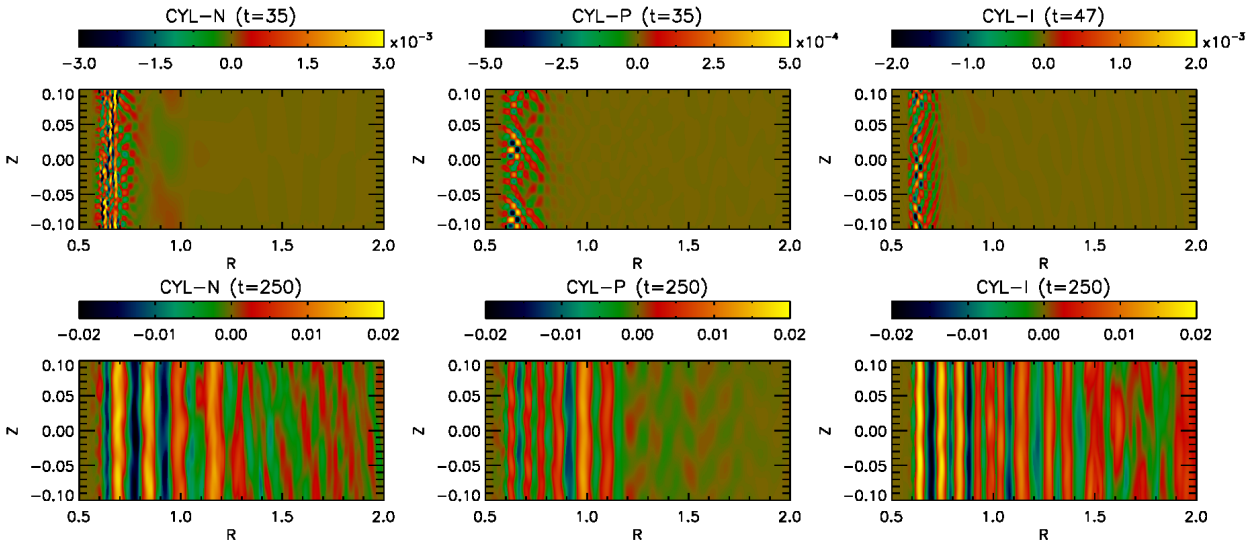

Figure 6.7. The upper panels present the distribution at $t = 35$ to compare the early evolution of the instability with CYL-F model. For the CYL-I model, we present the data taken at $t = 47$ since the growth of the instability starts at a later time (see Figure 6.2). The lower panels present the distribution at the end of calculations ($t = 250$).

because machine precision level errors are introduced by the use of finite differences.

6.6 Vertically Stratified, Isothermal Disk Models

In this section, we present results of vertically stratified models with an isothermal equation of state. The calculations are initiated with the vertically stratified density structure and the corresponding azimuthal velocity that satisfy the hydrostatic equilibrium, as introduced in Equations (6.20) and (6.21). We first introduce our reference model, for which the spiral wave amplitude $\mathcal{A} = 5.0 \times 10^{-4}$ and which has zero kinematic viscosity. The numerical resolution is $(N_r \times N_\phi \times N_\theta) = (512 \times 128 \times 128)$. The effects of varying the numerical resolution, spiral potential amplitude, and viscosity will be discussed in the following sections.

As discussed in Section 6.3, we expect that the spectrum of inertial modes that can be excited by the spiral waves will be dense, and therefore it is difficult to identify individual growing modes during the simulations. The best way of doing this would be to compute the eigenfunctions associated with these modes, such that they could be seeded in the initial conditions and their growth rates measured. We take a different approach by using white noise to perturb the initial conditions, thereby adding energy to the full spectrum of inertial

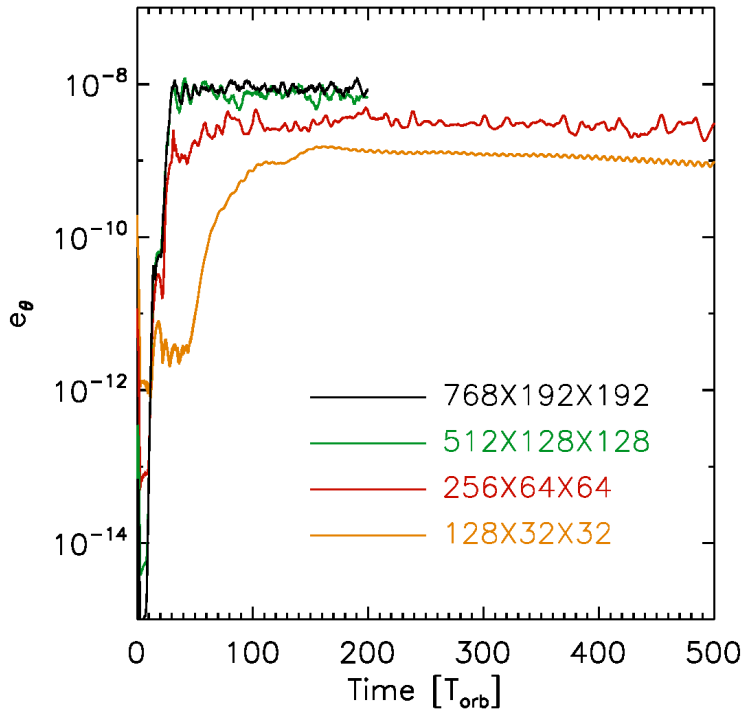

Figure 6.8. Time evolution of the integrated meridional kinetic energy e_θ. Results with four different resolutions are plotted. The plot indicates that the numerical results more or less converge at $(N_r \times N_\phi \times N_\theta) = (512 \times 128 \times 128)$ and beyond. We run the two low resolution models for a longer time to see if the saturation level eventually converges toward the value with higher resolutions, but find that the perturbed energy level does not further increase after 200 $T_{\rm orb}$ in both $(N_r \times N_\phi \times N_\theta) = (256 \times 64 \times 64)$ and $(128 \times 32 \times 32)$ run.

modes, and ensuring the robustness of the SWI by examining the triggering of the instability under a variety of disk conditions, instead of identifying and characterizing individual unstable modes.

6.6.1 A Reference Run (R512)

In Figure 6.8, we present the time evolution of the integrated meridional kinetic energy e_θ. Contour plots of the meridional kinetic energy density ρv_θ^2 are plotted in Figure 6.9. We make use of the meridional kinetic energy density ρv_θ^2 for the stratified models, instead of the meridional velocity, in order to better illustrate the development of the instability in the main body of the disk.

As shown in Figure 6.8, e_θ increases rapidly very early in the simulations at $10 \lesssim t \lesssim 15$. This initial increase does not represent the growth of unstable inertial modes. As shown in

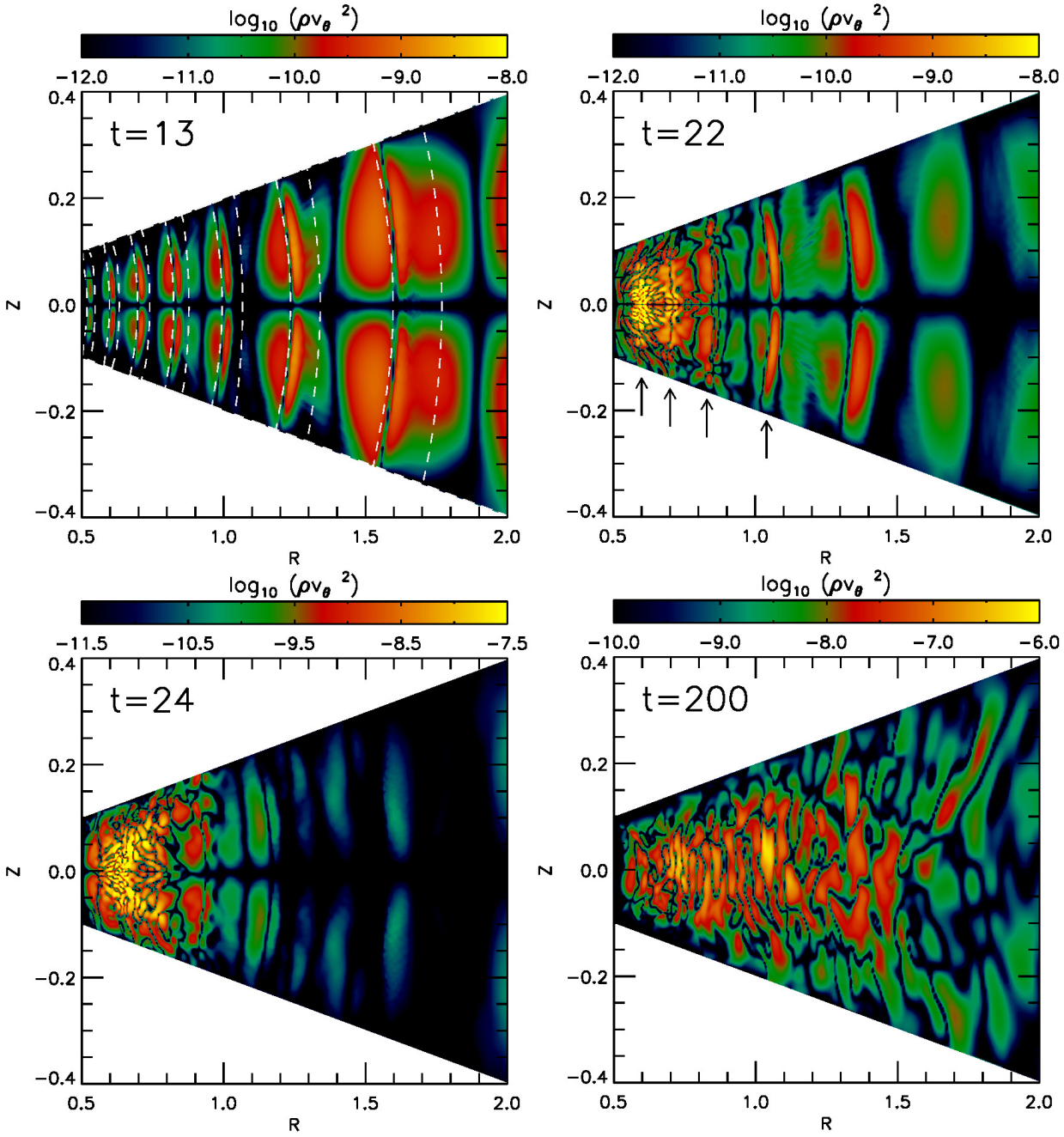

Figure 6.9. Contour plots presenting two-dimensional distributions of the meridional kinetic energy density ρv_θ^2 in a vertical plane ($\phi = 0$). The snapshots are taken (upper-left) before the spiral wave instability is triggered, (upper-right) at the beginning of the linear growth phase, (lower-left) at the middle of the linear growth phase, and (lower-right) at the end of the calculation when the instability is fully saturated. The white dashed contours in the upper-left panel show the $v_r = 0$ surface. Note that the wave fronts are curved towards the midplane due to nonlinear advection of the wave. The arrows in the upper-right panel indicate the four locations where the spiral arms intersect the $\phi = 0$ plane at that time.

the first panel of Figure 6.9, the spiral waves are not perpendicular to the disk midplane in the stratified models, but instead have a concave shape that develops as they propagate towards the star. As discussed in Section 6.3, this seems to arise as a nonlinear effect due faster advection of the wave at higher altitudes in the disk because the initial planar wave fronts move through steeply decreasing density profiles there, whereas the density increases near the midplane as the wave moves inwards. The curvature results in a loss of vertical hydrostatic equilibrium in the vertical direction, giving rise to the meridional kinetic energy.

The exponential growth associated with the SWI starts at $t \sim 20$, and e_θ saturates at $t \sim 30$. The second and third panel of Figure 6.9 show the linear growth and saturation of unstable modes at the innermost spiral arm. The unstable modes grow faster at smaller radii as shown, because of the higher mode frequencies and growth rates closer to the central object. When the instability is saturated ($t = 200$), the disk ends up in a complicated quasi-steady turbulent state. We discuss the turbulence produced via the SWI and its implications for angular momentum transport and vertical mixing later in Section 6.8.2.1.

6.6.2 Effect of Numerical Resolution

In order to test the effect of numerical resolution, we run the reference model with four different resolutions: $(N_r \times N_\phi \times N_\theta) = (128 \times 32 \times 32), (256 \times 64 \times 64), (512 \times 128 \times 128)$, and $(768 \times 192 \times 192)$. Increasing the numerical resolution should allow the growth of smaller scale inertial modes.

As seen in Figure 6.8, the growth rate and the saturated perturbed energy are reasonably well converged at $(N_r \times N_\phi \times N_\theta) = (512 \times 128 \times 128)$ and beyond. As expected, the highest resolution run displays the highest level of perturbed energy in the saturated state on average, because of the excitation of smaller scale modes, but the difference between the $(512 \times 128 \times 128)$ and $(768 \times 192 \times 192)$ runs is modest, indicating that the modes containing the largest amount of energy are captured in the lower resolution calculation. We note that there is a significant difference between the two higher resolution cases and the $(256 \times 64 \times 64)$ and $(128 \times 32 \times 32)$ cases, with the lowest resolution run in particular showing a much lower growth rate and saturation level.

In Figure 6.10, we present contour plots of the meridional kinetic energy density for R768

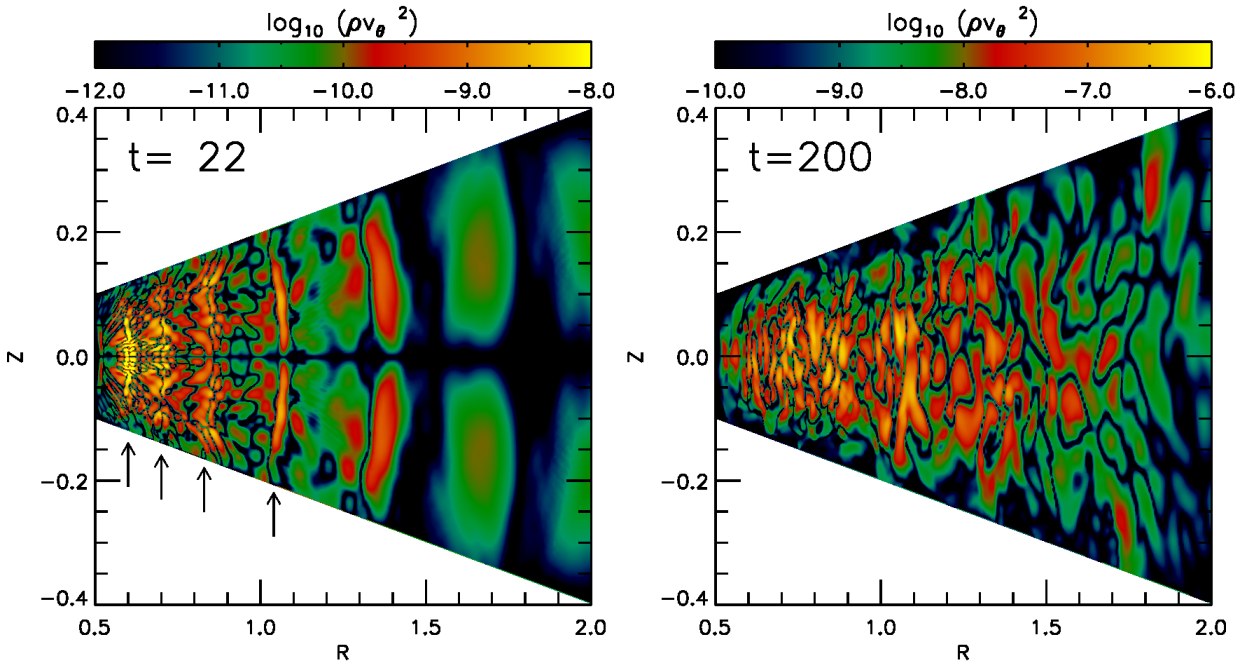

Figure 6.10. Contour plots of the meridional kinetic energy density ρv_θ^2 in a vertical plane ($\phi = 0$), obtained with $(N_r \times N_\phi \times N_\theta) = (768 \times 192 \times 192)$ grid cells.

model at $t = 22$ and 200. Compared to the results obtained with $(512 \times 128 \times 128)$ grid cells presented in Figure 6.9, one can see more fine scale structures developing at the beginning of the instability ($t = 22$). It is also apparent that, with the higher resolution, the unstable modes have grown faster at the third and fourth innermost spiral arms. In the R768 model, we find that the spiral waves create a larger density enhancement at the wave fronts than in the reference model: at $r = 0.6$, the spiral waves induce 39% of density enhancement in the midplane in R768 model, whereas the enhancement is 37% in the reference model. Since the growth rate of unstable modes is an increasing function of the wave amplitude (Fromang & Papaloizou, 2007, and see below), the stronger perturbations lead to faster growth of the unstable modes, in addition to there being more modes excited at high resolution.

6.6.3 Effect of Spiral Potential Amplitude

In this section, we explore the effect of varying the imposed spiral potential strength. We increase the spiral potential amplitude by factors of two from the smallest value, $\mathcal{A} = 6.25 \times 10^{-5}$, up to the largest value $\mathcal{A} = 1.0 \times 10^{-3}$.

Figure 6.11 shows the time evolution of e_θ. It is immediately obvious from the figure that

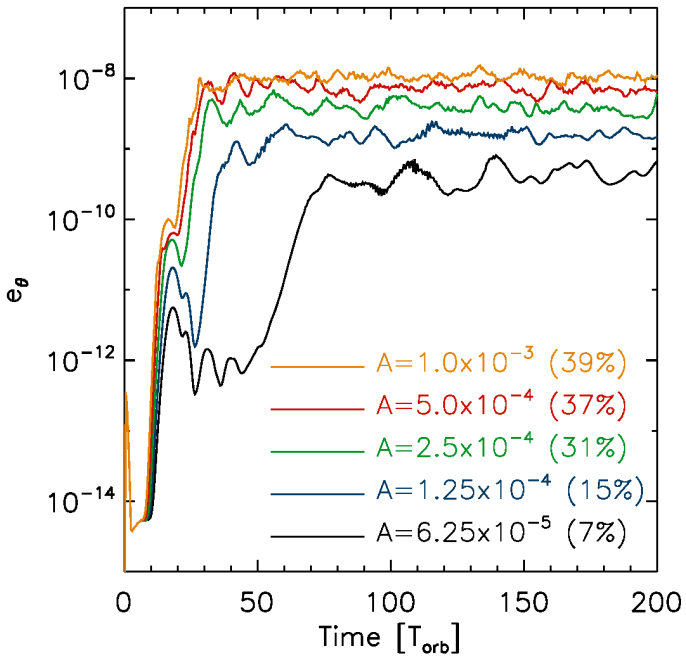

Figure 6.11. Time evolution of the meridional kinetic energy e_θ for different potential amplitude $\mathcal{A}$. The percentage in the parentheses indicate the density enhancement induced by the imposed spiral waves at $r = 0.6$ (refer to the right panel of Figure 6.1).

the instability has a higher perturbed energy level with stronger spiral waves. During the initial phase when the spiral waves propagate into the inner disk ($t \lesssim 20$), stronger spiral waves create more vertical motion. In addition, the linear growth phase begins at an earlier time with a stronger spiral amplitude. In the case with $\mathcal{A} = 6.25 \times 10^{-5}$, for example, the instability starts at about $t = 50$, while in the reference model the instability starts almost immediately after the initial propagation of the waves.

From $\mathcal{A} = 6.25 \times 10^{-5}$ to $\mathcal{A} = 2.5 \times 10^{-4}$, the density enhancement doubles when the spiral potential amplitude is doubled. However, the density enhancement induced by the spiral waves does not linearly increase with the potential strength when $\mathcal{A} > 2.5 \times 10^{-4}$. Comparing $\mathcal{A} = 2.5 \times 10^{-4}$ model with $\mathcal{A} = 10^{-3}$ model, the density enhancement increases only by about 25%, presumably as a result of nonlinear dissipation. The nonlinear dissipation is observed over a broad disk region ($r \lesssim 1.6$), and interestingly, it is more significant at smaller radius.

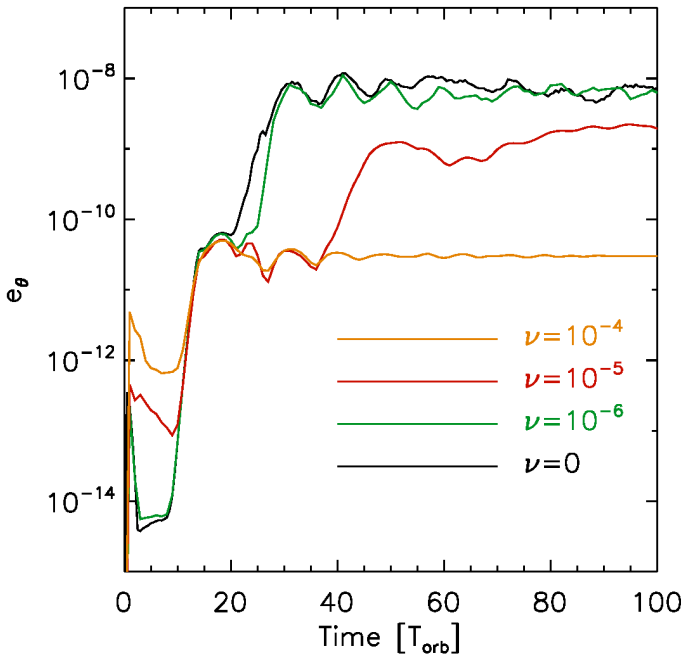

Figure 6.12. Time evolution of the meridional kinetic energy e_θ for different values of the kinematic viscosity. Note that the spiral wave instability operates with $\nu \leq 10^{-5}$, while the instability is suppressed when $\nu = 10^{-4}$.

6.6.4 Effect of Viscosity

We add a constant kinematic viscosity to our reference model to study the triggering and the evolution of the SWI in the presence of viscous dissipation. We test with three different kinematic viscosities: $\nu = 10^{-6}, 10^{-5}$, and 10^{-4}. In the canonical α prescription of Shakura & Sunyaev (1973), the kinematic viscosity ν corresponds to

$$\alpha(R) = 1.1 \times 10^{-3} \left(\frac{\nu}{10^{-6}}\right) \left(\frac{R}{0.5}\right)^{-1.5} . \tag{6.27}$$

If we assume that radii are measured in units of AU, then a value of $\nu = 10^{-5}$ corresponds to $\alpha = 3.9 \times 10^{-3}$ at 1 AU, and $\alpha = 3.5 \times 10^{-4}$ at 5 AU. In Figure 6.12, we plot the time evolution of the integrated meridional kinetic energy. As the plot indicates, the SWI operates with $\nu \leq 10^{-5}$, but is completely suppressed when $\nu = 10^{-4}$. The linear growth of the instability begins at a later time with a larger viscosity, probably because the viscosity

damps the smaller scale fastest growing modes. Also, the saturated energy level is reduced with a larger viscosity, for the same reason, although the difference between $\nu = 0$ and $\nu = 10^{-6}$ models is only marginal, suggesting that numerical diffusion operates with a value that is moderately below $\nu = 10^{-6}$ in the inviscid model.

Contour plots of meridional kinetic energy density are shown in Figure 6.13. As inferred from the energy evolution, one can see that the SWI operates with $\nu \leq 10^{-5}$. With $\nu = 10^{-4}$, we do not find any signatures of the instability growing throughout the duration of the calculation. Comparing with the results of the reference model at $t = 24$ presented in Figure 6.9, we find that the small scale unstable modes are absent with $\nu = 10^{-6}$. With $\nu = 10^{-5}$, small scale modes are further suppressed, and the unstable modes that have grown in the model have noticeably larger length scales than in the $\nu = 0$ and $\nu = 10^{-6}$ models. Fromang & Papaloizou (2007) show that, except for the largest wavelength inertial modes, the growth rates are almost constant. Given that we expect modes to be viscously damped when the damping rate exceeds the growth rate, and the viscous damping rate scales as $\sim k^2\nu$, this demonstrates that we expect the high k (small λ) modes to be preferentially damped.

We emphasize that the instability operates with fairly large viscosity of $\nu = 10^{-5}$. In terms of the canonical α description, $\nu = 10^{-5}$ corresponds to $\alpha \sim 0.008$ at $R = 0.6$ (right outside of the inner damping zone) and $\alpha \sim 0.001$ at $R = 2$. The fact that the spiral wave instability operates in quite dissipative disks may be important for disks that sustain fully developed MHD turbulence, such as the accretion disks around cataclysmic variables and/or black holes. Furthermore, the growth rate of the instability depends on the amplitude of the spiral wave, so the value of ν for which the SWI operates will depend on the incoming wave amplitude.

6.7 Vertically Stratified, Adiabatic Disk Models

In this section, we adopt an adiabatic equation of state to investigate the influence of the thermodynamics on the growth and development of the SWI. We consider six different adiabatic index values: $\gamma = 1.01, 1.05, 1.1, 1.2, 1.3, 1.4$. By using different values of γ, we mimic a disk that experiences cooling at different rates. Reducing γ acts as if the disk has more

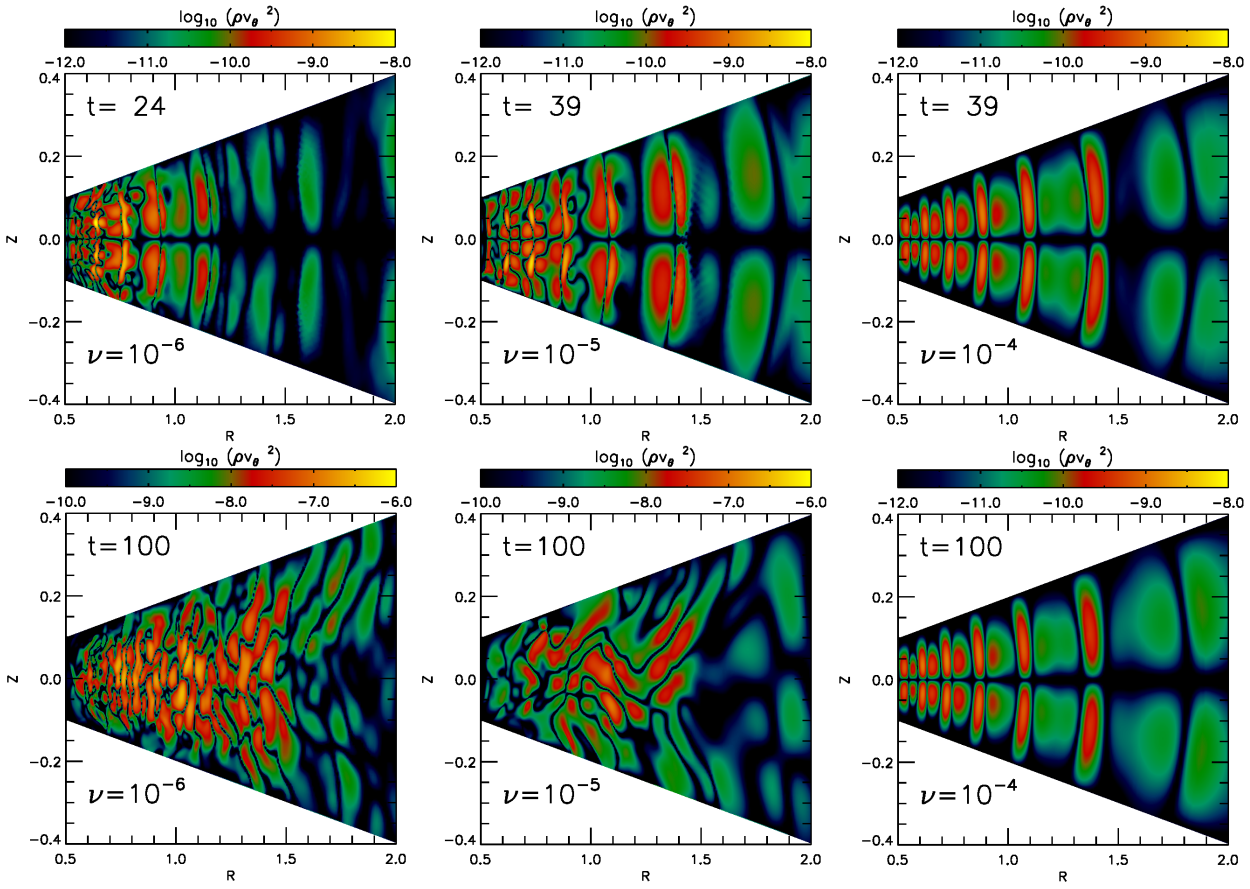

Figure 6.13. Contour plots showing two-dimensional distributions of the meridional kinetic energy density ρv_θ^2 in the vertical plane with different kinematic viscosities. The upper panels show the distributions at the beginning of the linear growth phase, and the lower panels show the distributions at $t = 100$. Note that the instability operates with (left) $\nu = 10^{-6}$ and (middle) $\nu = 10^{-5}$, but is suppressed with (right) $\nu = 10^{-4}$.

efficient cooling. Using the broad range of γ values, we aim to demonstrate that the SWI operates in both optically thin regions (isothermal) and optically thick regions (adiabatic). As we shall show below, the disks become more susceptible to the SWI with stronger adiabatic responses (i.e. larger γ value). In contrast to the reference model that we have presented earlier in this Chapter, we use a smaller spiral potential amplitude of $\mathcal{A} = 6.25 \times 10^{-5}$ to allow us to capture the growth of the instability at early times.

In Figure 6.14, we present the time evolution of the integrated meridional kinetic energy. When the spiral waves initially propagate into the inner disk ($t \lesssim 20$), a more rapid and higher amplitude growth of e_θ is observed with a larger γ value, and it is clear that the SWI triggers at earlier times with larger γ values. For example, the linear growth of the

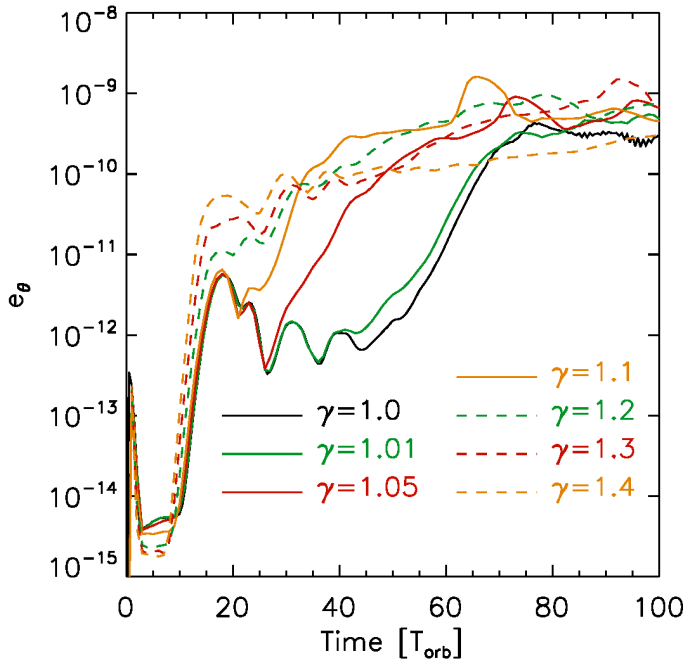

Figure 6.14. Time evolution of the meridional kinetic energy e_θ for different adiabatic indices γ.

instability begins at $t \sim 45$ with $\gamma = 1.01$, but at $t \sim 30$ with $\gamma = 1.05$ and at $t \sim 25$ with $\gamma = 1.1$. For $\gamma = 1.4$, it is difficult to disentangle the initial growth of the perturbed kinetic energy due to the spiral wave propagation from the growth of the instability.

As we discussed in Section 6.3, the Brunt-Väisälä frequency varies over a wide range of values over height in adiabatic disks, with the range of values covered being a function of the value of the effective γ adopted. This suggests that at each radius in an adiabatic disk, the spiral modes will have a larger number of inertial modes with which to resonantly interact, with the number being larger for larger values of γ. We might therefore expect to see a more rapid growth of the SWI for the larger values of γ, and this expectation is borne out by the simulation results.

We also pointed out in Section 6.3 that there can be forbidden regions for the SWI in adiabatic disks. The existence of these can be inferred from Equation (6.13), which shows that the vertical wave number has no physical solution in disk regions where $(\omega_s/2)^2 \lesssim N^2$ in the large n limit. Although in global models, such as those we present here, the analysis

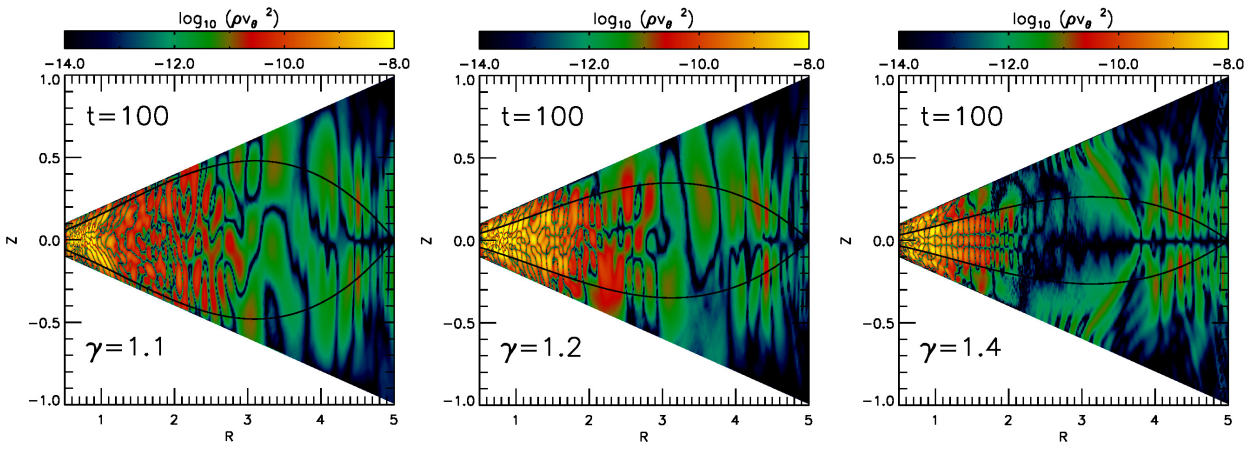

Figure 6.15. Contour plots of the meridional kinetic energy density ρv_θ^2 for adiabatic models with different γ values. The black curves indicate where the local buoyancy frequency equals to a half of the local Doppler-shifted frequency of the spiral waves: $N^2 = (\omega_s/2)^2$. The results from the $\gamma = 1.4$ run demonstrate the fact that the region where the SWI develops is confined to the regions where $N^2 \lesssim (\omega_s/2)^2$.

of the properties of the inertial waves should also be global and not local. The analysis of the vertical structure of inertial mode eigenfunctions by Lubow & Pringle (1993) also shows that the energy in the modes is confined near the midplane, and the modes do not propagate in regions where the inertial mode frequencies $\omega_i^2 < N^2$.

In Figure 6.15, we display contour plots of the meridional kinetic energy density at the end of calculations ($t = 100$) with $\gamma = 1.1$, 1.2, and 1.4. In the figure, the black curves connect the disk regions where the local Brunt-Väisälä frequency matches to a half of the Doppler-shifted spiral wave frequency: $N^2 = (\omega_s/2)^2$. As discussed above, the region surrounded by the black curves is where the inertial waves are expected to be confined. The forbidden region is not clearly seen in the $\gamma = 1.1$ and 1.2 models (although there is a strong hint of it in the latter model), because the $N^2 = (\omega_s/2)^2$ region is located near the meridional boundary, and acoustic waves excited by the SWI are likely to be present there along with vertical motions induced by the spiral waves. We note, however, the strong signature of inertial mode confinement near the midplane in the $\gamma = 1.4$ model.

Finally, we note that varying the adiabatic index affects the shape and strength of spiral waves. As γ is increased, spiral waves are more openly wound, due to the larger sound speed, and the density enhancement at wave fronts is reduced. These, in turn, can have influence

on the growth rate of the SWI and the saturated energy level, although the existence of the SWI in adiabatic disks is clearly robust. At $r = 0.6$, for example, the density perturbation $\rho/\langle\rho\rangle$ before the SWI sets in is ~ 7 % with $\gamma = 1.0$, ~ 4 % with $\gamma = 1.1$, and only ~ 1 % with $\gamma = 1.4$. The reduction in density enhancement at spiral wave fronts for larger values of γ may explain why the saturated state of the model with $\gamma = 1.4$ is somewhat smaller than in the other models (as seen in Figure 6.14), in spite of the obvious faster growth rate associated with this run.

6.8 Discussion

Our results suggest that the SWI can operate under a broad range of disk conditions. In addition, the instability presumably operates regardless of the origin of spiral waves, as long as the waves maintain a fixed period until the instability develops[2]. This implies a potential significance of the SWI in various astrophysical disks.

6.8.1 Why Has the Instability Not Been Reported Previously?

At this point, one might wonder why the SWI has not been reported previously if it operates under a broad range of disk conditions as we claim.

First of all, it is possible that the SWI has been present in previous studies, but masked by turbulence driven via other processes. For instance, the recent study of nonlinear spiral waves in a disk excited by a massive planet by Lyra et al. (2016) used high resolution in an essentially inviscid disk, but the violence of the disk response to the strong nonlinear forcing, combined with the presence of convective motions, probably masked the presence of the SWI in that study. Also, we speculate the SWI might have been present in the recent 3D MHD calculation of accretion disks in cataclysmic variable (CV) systems by Ju et al. (2016). In this study, however, the SWI must be obscured by the vigorous MRI turbulence.

Considering the reference run R512, this was computed using a logarithmic radial grid, where the grid cell size at $r = 0.5$ was $\Delta r = 0.002934$. Similarly, the run undertaken by NIRVANA, described in the appendix, used a uniform radial mesh with the same grid

[2]We have confirmed that the SWI develops for the spiral waves driven by a companion in a disk.

spacing, corresponding to $N_r = 3200$ grid cells. This is higher resolution than is usually undertaken in global simulations of giant planets embedded in protoplanetary disks, for example, although high resolution in the vicinity of the planet is often achieved with local mesh refinement (e.g Kley et al., 2001; Klahr & Kley, 2006; Gressel et al., 2013; Szulágyi et al., 2014). Viscosity, with $\nu \geq 10^{-5}$, is also often included in these models, which has the effect of partially damping the instability. We note that simulations with low-mass planets are unlikely to show growth of the SWI within the typical durations of three-dimensional calculations, since the smaller the mass of companion, the weaker the instability and the longer it takes for it to develop (see Figure 6.11). In addition, the primary and secondary arm separation is known to be less than 180° for low-mass planets (e.g. Fung & Dong, 2015; Zhu et al., 2015), in which case the resonance between the spiral arms and inertial modes is not exact. In this case, the SWI may grow at a reduced rate, requiring a longer simulation duration to observe the instability develop.

In Figure 6.16, we present two-dimensional maps showing the vertical and radial wavelengths of the inertial modes that satisfy the resonance conditions with the imposed spiral waves. The wavelengths are calculated using Equations (6.10) and (6.13), using the background disk structure and computational domain used in the adiabatic simulation labelled as GAM4 in Table 6.1. Purely for the purposes of illustration, we present maps for the inertial modes predicted to arise when $n = 4$, where n is defined as $k_{R,\mathrm{i}} = nk_{R,\mathrm{s}}$. However, since the second term in Equation (6.13) is typically smaller than the first term, the contour plots can be linearly scaled to other modes[3] as indicated in the color bar labels.

The maps imply that there is a resolution limit on which modes can be represented by the computational grid. For $n = 4$, the midplane region interior to $R \sim 0.9$ is poorly resolved by $\lesssim 8$ grid cells in both the vertical and radial directions, indicating that these inertial modes cannot be well represented on the mesh there. Smaller values of n are hence expected to be associated with the modes seen to grow in this region, in agreement with the results described in Section 6.5. Moving out to the midplane region beyond $R = 1$, the vertical and radial wavelengths of the excited modes start to exceed ~ 10 grid cell spacings, suggesting

[3]We confirmed that this is invalid only in a very narrow region near the boundary between the SWI forbidden and permitted regions where $(\omega_{\mathrm{s}}/2)^2 \simeq N^2$.

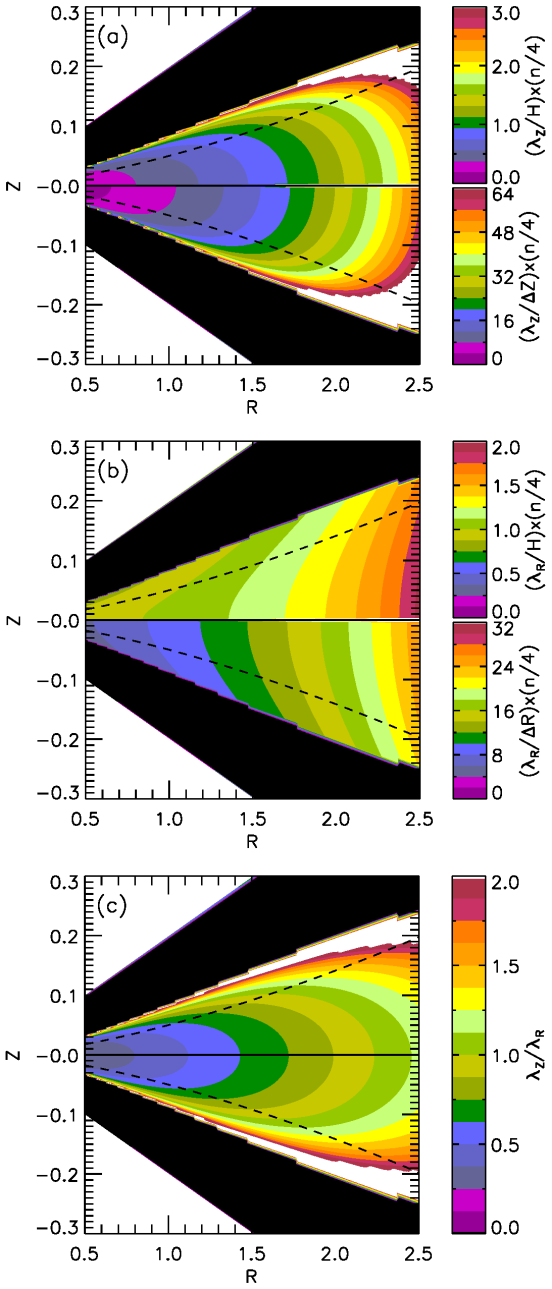

Figure 6.16. (a) Contour plots of the vertical wavelength of the inertial modes λ_Z that are subject to the resonant interaction with the imposed spiral waves assumed in this work. (b) Same as (a) but for the radial wavelength λ_R. (c) The ratio of vertical to radial wavelength of the inertial modes. In all panels, the dashed curves indicate where $Z = \pm 1H$. The black regions are where the dispersion relation does not have a physical solution. In (a) and (b), the upper half of the disk shows the wavelength in units of disk scale height at each radius, whereas the lower half of the disk shows the wavelength in units of vertical and radial grid cell size at each position. We use the $n = 4$ mode as a representative, but the numbers on the colorbars can be linearly scaled to other modes as noted in the labels.

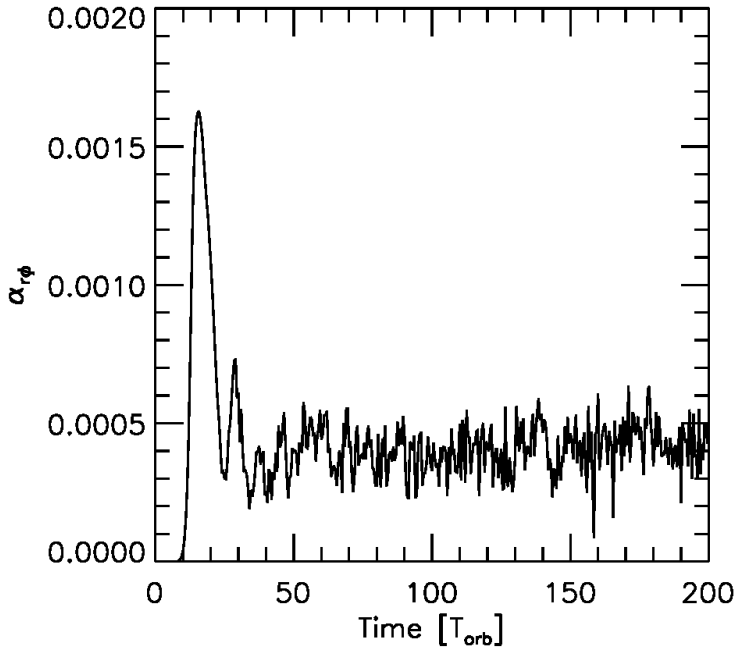

Figure 6.17. Time evolution of Shakura-Sunyaev parameter $\alpha_{r\phi}$, averaged over θ in between $r = 0.5$ and 2.

that these modes can be represented on the grid.

6.8.2 Implications

6.8.2.1 Angular Momentum Transport

In order to estimate the rate of angular momentum transport induced by the turbulent flow arising from the SWI, we calculate the Shakura-Sunyaev stress parameter $\alpha_{r\phi}$ for the reference model R512 according to $\alpha_{r\phi}(r,\theta) \equiv \langle \rho \delta v_r \delta v_\phi \rangle / \overline{P}(r)$ where $\overline{P}(r)$ is a density-weighted mean pressure at radius r. The simple arithmetic average of $\alpha_{r\phi}$ over θ in between $r = 0.5$ and 2 is plotted in Figure 6.17 as a function of time. We see that the advected flux of angular momentum due to the spiral waves at the beginning of the simulation gives rise to an apparent Reynolds stress $\alpha_{r\phi} \sim 0.0016$. This is not the accretion stress experienced by the disk, but instead represents the negative angular momentum flux associated with the spiral wave as it propagates inwards, and only that fraction of the wave angular momentum that is deposited in the gas through wave dissipation acts to drive accretion. Once the SWI develops we see that the correlated velocity fluctuations generate a sustained accretion stress

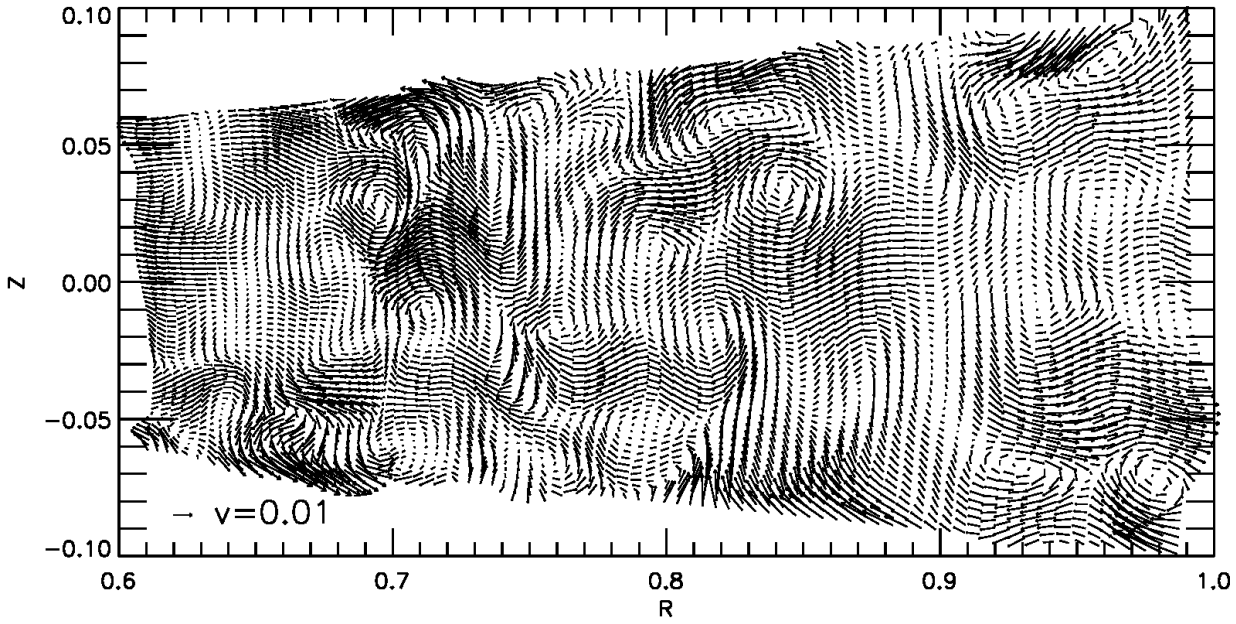

Figure 6.18. Velocity vectors in a $R - Z$ plane at $t = 200$ from the R512 model. The map shows only $Z = -2H$ to $+2H$ due to large velocity in the upper layer. Note the turbulent eddies generated by the spiral wave instability. A velocity vector with $v = 0.2c_s = 0.01$ is shown on the lower-left corner.

$\alpha_{r\phi} \sim 5 \times 10^{-4}$. This value is naturally smaller than that associated with the unattenuated spiral wave because the SWI operates over a range of radii in the disk, and the energy and angular momentum associated with the wave are injected into the disk matter over this radial range via the breakdown into turbulence.

6.8.2.2 Vertical Mixing

In Figure 6.18, we present velocity vectors in a vertical plane at the end of the reference run. As can be seen, the SWI creates a set of turbulent eddies that will be effective at inducing vertical mixing of the gas, and any dust particles that it contains. It is also the case that forces arising from the turbulent density fluctuations will induce stochastic migration and eccentricity/inclination excitation of larger bodies, such as planetesimals and protoplanets, in a protoplanetary disk in which nonlinear spiral waves propagate, similar to what is observed in disks that sustain magneto-rotational turbulence (Nelson & Papaloizou, 2004; Nelson, 2005). We estimate the vertical diffusion coefficient associated with the correlated vertical velocity fluctuations using the approximation $\mathcal{D}_Z = \langle v_Z^2 \rangle \tau_{\rm corr}$, where $\tau_{\rm corr}$ is the correlation

time of the vertical velocity fluctuations, v_Z (Fromang & Papaloizou, 2006). In obtaining an estimate for $\tau_{\rm corr}$, we generate a time series for v_Z at different locations in the disk, defined by the region $|Z| < 1H$ at $r = 1$, and filter these time series to remove the sinusoidal component induced by the spiral wave. We then compute the autocorrelations of these time series, to which we fit the function $\exp(-t/\tau_{\rm corr})$, leading to an average of the measured correlation times $\tau_{\rm corr} \simeq 0.12{\rm T_{orb}}$. Using natural units, the diffusion coefficient is estimated to be $\mathcal{D}_Z \simeq 9 \times 10^{-6}$, such that the time scale for vertical mixing $t_{\rm mix} = H^2/\mathcal{D}_Z \simeq 44$ orbits.

Particles in the Epstein drag regime have a settling time that can be expressed as $t_{\rm settle} = (2\pi t_{\rm s}\Omega)^{-1}$ orbits. $t_{\rm s}$ is the stopping time defined by $t_{\rm s} = (\rho_{\rm grain}a)/(\rho v_{\rm therm})$ (Weidenschilling, 1977), where $\rho_{\rm grain}$ is the internal density of the grain particles (typically ~ 2 g cm^{-3}), a is the grain size and $v_{\rm therm}$ is the thermal velocity of gas molecules. Assuming that particles are significantly mixed by the turbulence when $t_{\rm mix} \sim t_{\rm settle}$, we expect this to occur for particles with Stokes numbers ${\rm St} \equiv t_s\Omega \leq 0.004$. This corresponds to a particle size $a \sim 2$ cm at 1 AU and $a \sim 2$ mm at 5 AU in the midplane of a minimum mass solar nebula (Hayashi, 1981).[4]

6.8.2.3 Non-axisymmetric Spiral Features

Recent near-IR scattered light observations have revealed complex spiral arm morphologies in some protoplanetary disks (e.g. Garufi et al., 2013; Benisty et al., 2015; Garufi et al., 2016), thanks to the advent of extreme adaptive optics. The scattered light is believed to trace (sub-)μm-sized dust grains in the disk atmosphere since protoplanetary disks are highly optically thick at near-IR wavelength. Interestingly, even in nearly face-on systems exhibiting well-defined spiral arms, the brightness of the spiral arms at the same distance from the central object significantly differ from each other (e.g. SAO 206462; Garufi et al. 2013, MWC 758; Benisty et al. 2015).

In Figure 6.19, we present two-dimensional distributions of the azimuthal density variation at various heights in the disk, and in Figure 6.20, we show how the perturbed density varies with azimuth at different disk heights. We see that spiral waves are disturbed by the instability at all heights, but with more prominent disruption occurring higher in the disk.

[4]We note that the mean free path of molecules is ~ 1 cm at 1 AU, so using the Epstein drag formula here is only marginally justified for 2 cm-sized pebbles.

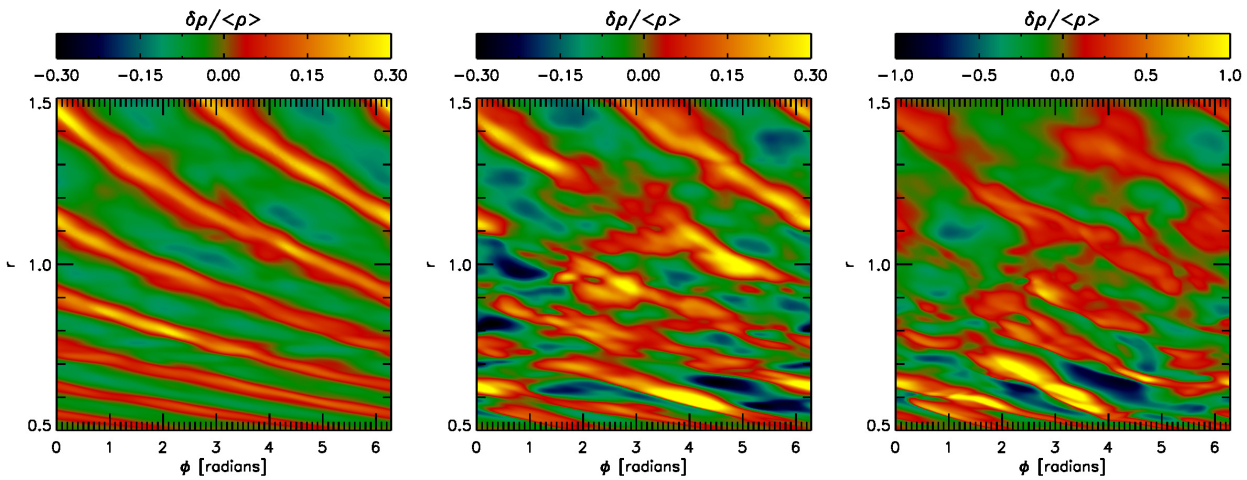

Figure 6.19. Distribution of $\delta\rho/\langle\rho\rangle$ at $t = 200$ in the (left) $Z = 0$ plane, (middle) $Z = 2H$ plane, and (right) $Z = 3H$ plane for R512 model.

This will obviously have significant implications when attempting to predict the appearance of spiral waves for comparison with observations (e.g. Dong et al., 2016)

6.8.3 Future Work

Our results suggest that the SWI is robust, and possibly operates under a variety of disk conditions. The simplified disk models assumed in the present work help to illuminate the nature of the instability, but the significance of the instability will have to be tested with more realistic disk models.

The influence of thermodynamic effects on the instability will need to be tested using a more realistic model for the thermal evolution, including processes such as radiation transport and external irradiation. We have shown that the SWI is likely to operate in both optically thin (isothermal) and thick (adiabatic) disk regions. On the other hand, the outcome of the instability is quite sensitive to the disk thermal model, as we showed by varying the adiabatic index. Real disks are likely to behave adiabatically near the midplane and isothermally near the surface, so the outcome of t-he instability in such disks will be more complicated than shown by the models we have presented here. In particular, the forbidden zones, where inertial waves cannot be excited, will depend on the detailed thermodynamics due to the dependency on the local Brunt-Väsälä frequency.

Our simulations have shown that the SWI can operate in viscous disks, suggesting that it

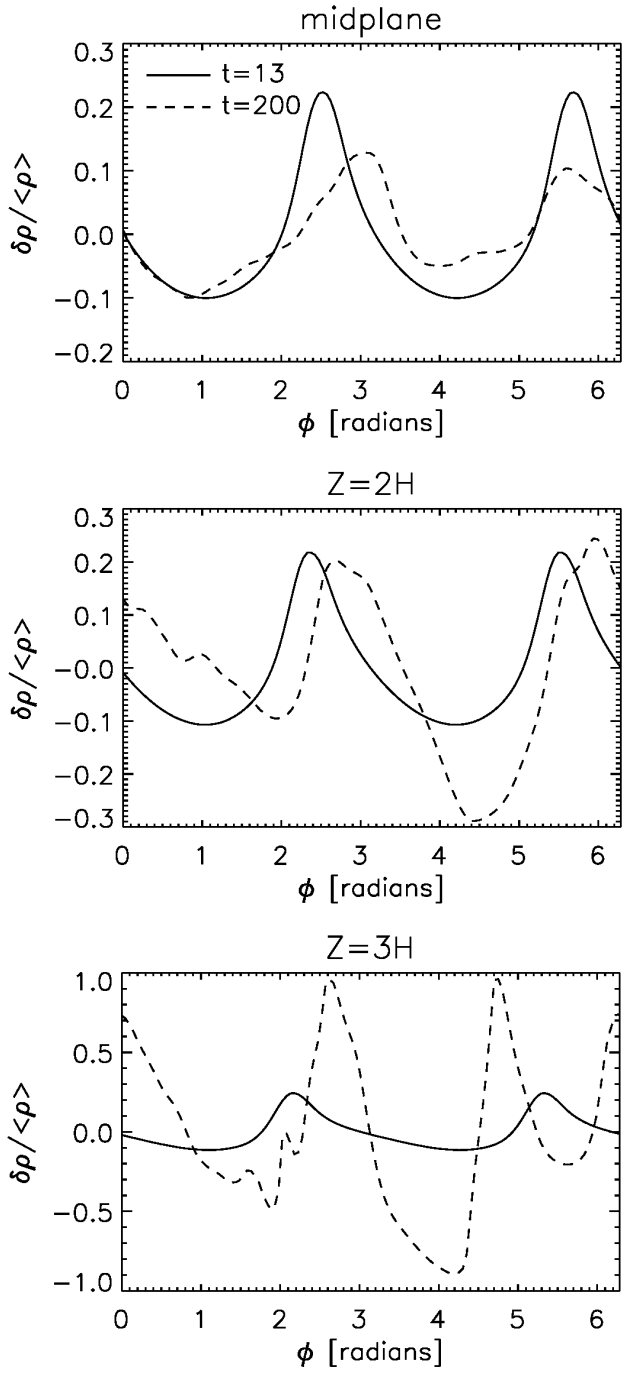

Figure 6.20. Azimuthal distributions of the perturbed density $\delta\rho/\langle\rho\rangle$ at different heights in the disk at $r = 0.65$. The solid curves show the distributions before the SWI sets in, and the dashed curves show the distributions when the instability is saturated.

might also operate in disks that sustain turbulence through the magnetorotational instability (MRI) (Balbus & Hawley, 1991). It certainly appears to be the case that the instability could operate in dead zones (Gammie, 1996), and regions where non ideal MHD effects such as ambipolar diffusion act to moderate the strength of MRI turbulence (Bai, 2015). Precisely how the SWI operates under these conditions will require high resolution MHD simulations of spiral waves propagating in magnetized disks.

In addition to understanding how the inclusion of additional physical processes could modify the SWI, future work is needed to examine how the SWI changes our understanding of astrophysical phenomena where spiral waves play an important role. The list of these includes the following:

1. Spiral wave propagation in disks with external binary companions, such as protoplanetary disks, CV systems and X-ray binaries. Issues of interest include how efficiently the spiral waves are damped by the SWI and how this affects the wave amplitude as a function of position in the disk, and whether or not the turbulent stresses associated with the SWI modify the outburst cycles associated with CV systems. In recent work, Ju et al. (2016) showed that spiral shocks can co-exist with MRI turbulence in CV systems, so it will be interesting to investigate applications of the SWI in the systems.

2. FU Orionis outbursts driven by spiral waves excited by self-gravity in disks around young stars. The idea here is that spiral waves launched in the outer disk during the infall phase can heat the inner disk sufficiently to ionize it, and drive accretion onto the star by switching on the MRI (Zhu et al. 2010a; Chapter 3 of this thesis). We came across the SWI while conducting 3-D simulations designed to address this very issue, and in the future we will present a study that examines the viability of this picture.

3. Planet formation in disks with external binary companions. Numerous exoplanets are known to orbit one star that is a member of a binary system, perhaps the most famous of these being γ Cephei (Hatzes et al., 2003). The excitation of spiral waves in a protoplanetary disk by an external binary is already known to have a strong influence on planet formation (Kley & Nelson, 2008; Paardekooper et al., 2008). The excitation of turbulence by the SWI will also have an important influence, particularly on the

settling of dust grains and the growth of small particles.

4. Formation of circumbinary planets. The situation regarding the growth of the SWI for spiral waves that propagate outwards from an outer Lindblad resonance is different than for an inward propagating wave. Ignoring the effects of buoyancy, and noting that inertial wave frequencies must lie in the range $0 < \omega_{\rm i} \leq \Omega$, we infer that the resonant excitation of inertial waves by an inner companion occurs in a relatively narrow range of radii where the doppler-shifted frequency of the spiral $\omega_{\rm s} \simeq \omega_{\rm i}/2$. A fluid element at large radius in a disk sees a large value for $\omega_{\rm s}$, such that the resonance condition cannot be satisfied, unless buoyancy forces are also included in a disk where the Brunt-Väsälä frequency is large. This suggests that there may be a range of radii in circumbinary disks where the SWI operates, making it difficult for small particles to grow there, and for planets to form in situ. The details will depend on the disk thermodynamics.

5. Formation of planets in the presence of a giant planet. It is generally believed that Jupiter was the first planet to form in the Solar System, and its early presence has been invoked to explain a number of physical and dynamical features that are observed today, such as the dynamical state of the asteroid belt and the small mass of Mars (Walsh et al., 2011). It will be of interest to examine how the onset of the SWI, induced by the spiral waves excited by a growing Jupiter, influenced the orbits of asteroids though stochastic forcing, and modified the growth of the terrestrial planets or their precursor embryos. The influence could be strong if this occurred mainly through chondrule/pebble accretion, as explored recently by Johansen et al. (2015) and Levison et al. (2015b).

6.9 Conclusion

We have presented the results of high resolution, 3-D simulations of circumstellar disks that are perturbed by two-armed spiral density waves, and we have shown that a broad range of disk models are subject to a parametric instability involving the excitation of pairs of inertial waves that interact resonantly with the spiral wave. This spiral wave instability (SWI) gives rise to turbulence that transports angular momentum and causes vertical mixing. The

apparent robustness of the SWI under changes to physical conditions in the disks suggests that it may arise in a broad range of astrophysical settings. Future work is required to understand and evaluate its influence on the physical evolution and observational appearance of these systems.

6.10 Acknowledgments

Authors thank the anonymous referee for a helpful report that improved the initial manuscript. J.B. thanks Fred Adams and Steve Lubow for valuable conversations, and Charles Gammie for insightful comments on the initial manuscript. This research was supported in part through computational resources and services provided by Advanced Research Computing at the University of Michigan, Ann Arbor, and by HPC resources provided by IT Services at Queen Mary University of London. This work used the Extreme Science and Engineering Discovery Environment (XSEDE), which is supported by National Science Foundation grant number ACI-1053575. The authors acknowledge the San Diego Supercomputer Center at University of California, San Diego and the Texas Advanced Computing Center at The University of Texas at Austin for providing HPC resources that have contributed to the research results reported within this Chapter. This work used the DiRAC Complexity system, operated by the University of Leicester IT Services, which forms part of the STFC DiRAC HPC Facility (www.dirac.ac.uk). The equipment is funded by BIS National E-Infrastructure capital grant ST/K000373/1 and STFC Operations grant ST/K0003259/1. DiRAC is part of the national E-Infrastructure.

6.11 Appendix: Vertically Stratified, Locally Isothermal Models

We introduce locally isothermal disk models, in which a radial temperature gradient is imposed by assuming $H_0/R_0 = 0.05$ and $q = -1$, and an isothermal equation of state is adopted. With this setup, the disk aspect ratio maintains a constant value at all radii. Since the radial temperature gradient produces a non-zero vertical gradient in the disk rotation (see Equation 6.21), this model is susceptible to the vertical shear instability (Nelson et al., 2013). We implement the density slope $p = -1.5$, so the initial disk structure is identical

Table 6.2. Model Parameters for Locally Isothermal SWI Calculations

Run label	Code	Numerical Resolution ($N_r \times N_\phi \times N_\theta$)	q	$\mathcal{A}$	Kinematic Viscosity ν	γ
VISO-V0	FARGO3D	$512 \times 128 \times 128$	-1	5.0×10^{-4}	0	1.0
VISO-V6	FARGO3D	$512 \times 128 \times 128$	-1	5.0×10^{-4}	10^{-6}	1.0
VISO-V5	FARGO3D	$512 \times 128 \times 128$	-1	5.0×10^{-4}	10^{-5}	1.0
VISO-V4	FARGO3D	$512 \times 128 \times 128$	-1	5.0×10^{-4}	10^{-4}	1.0
VISO-N	NIRVANA	$3200 \times 128 \times 128$	-1	5.0×10^{-4}	10^{-6}	1.0
VISO-P	PLUTO	$512 \times 128 \times 128$	-1	5.0×10^{-4}	10^{-6}	1.0
VISO-I	INABA3D	$3200 \times 128 \times 128$	-1	5.0×10^{-4}	10^{-6}	1.0

to the T1R-0 and T1R-0-3D models of Nelson et al. (2013). The model parameters are summarized in Table 6.2.

In order to check whether or not the vertical shear instability develops in the absence of imposed spiral waves, we first run calculations with the spiral potential turned off ($\Phi_p = 0$). We vary the kinematic viscosity using the values $\nu = 0, 10^{-6}, 10^{-5}$. As inferred from the time evolution of the integrated meridional kinetic energy presented in Figure 6.21, the vertical shear instability develops when $\nu = 0$ but is suppressed with $\nu \geq 10^{-6}$, which is in good agreement with Nelson et al. (2013). The small fluctuations at $t \gtrsim 30$ in the VISO-V6 model and at $t \gtrsim 130$ in the VISO-V5 model are signatures of the vertical shear instability, but note that they do not grow over time and damp out because of viscous dissipation.

Having confirmed that the disk is stable to the vertical shear instability with $\nu \geq 10^{-6}$, we now introduce spiral waves into the disk. We test with four different kinematic viscosity values: $\nu = 0, 10^{-6}, 10^{-5}$, and 10^{-4}. As shown in Figure 6.21, the result is consistent with the globally isothermal models: the spiral wave instability is triggered with $\nu \leq 10^{-5}$ and is completely suppressed with $\nu = 10^{-4}$. Also, the saturated energy level is smaller with larger viscosity, as expected.

We run the $\nu = 10^{-6}$ model with the four codes introduced in Section 6.4.5. As we discussed earlier, the detailed evolution is not identical because of the difference in dissipative properties of the codes, and the fact that NIRVANA and INABA3D use uniform radial meshes, whereas FARGO3D and PLUTO use logarithmically spaced grid cells. Nevertheless,

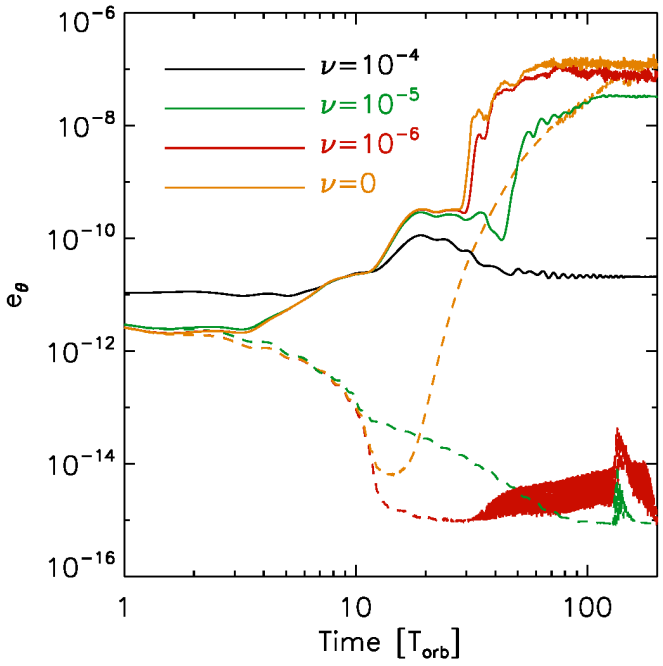

Figure 6.21. Time evolution of the meridional kinetic energy e_θ for vertically isothermal models with different kinematic viscosities. The solid curves show the results with the spiral potential amplitude of $\mathcal{A} = 5.0 \times 10^{-4}$, while the dashed curves show the results with $\mathcal{A} = 0$ to check whether the vertical shear instability develops in the absence of spiral waves. The vertical shear instability is suppressed with $\nu \geq 10^{-6}$, which is in good agreement with Nelson et al. (2013, see their Figure 9). The spiral wave instability is suppressed with $\nu = 10^{-4}$ as in the globally isothermal models.

the results show reasonably good agreement with each other and all codes reproduce the SWI, as shown in Figure 6.22.

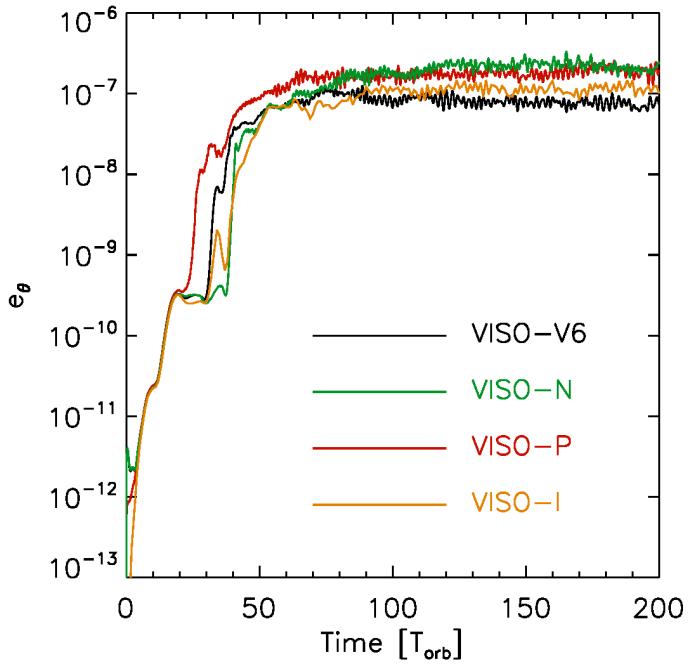

Figure 6.22. Time evolution of the meridional kinetic energy e_θ for the vertically isothermal models with different codes (VISO-V6, VISO-N, VISO-P, VISO-I).

CHAPTER VII

The Spiral Wave Instability Induced By a Giant Planet: I. Particle Stirring in The Inner Regions of Protoplanetary Disks

7.1 Abstract

We have recently shown that spiral density waves propagating in accretion disks can undergo a parametric instability by resonantly coupling with and transferring energy into pairs of inertial waves (or inertial-gravity waves when buoyancy is important). In this Chapter, we perform inviscid three-dimensional global hydrodynamic simulations to examine the growth and consequence of this instability operating on the spiral waves driven by a Jupiter-mass planet in a protoplanetary disk. We find that the spiral waves are destabilized via the spiral wave instability (SWI), generating hydrodynamic turbulence and sustained radially-alternating vertical flows that appear to be associated with long wavelength inertial modes. In the interval $0.3\ R_p \leq R \leq 0.7\ R_p$, where R_p denotes the semi-major axis of the planetary orbit (assumed to be 5 au), the estimated vertical diffusion rate associated with the turbulence is characterized by $\alpha_{\rm diff} \sim (0.2 - 1.2) \times 10^{-2}$. For the disk model considered here, the diffusion rate is such that particles with sizes up to several centimeters are vertically mixed within the first pressure scale height. This suggests that the instability of spiral waves launched by a giant planet can significantly disperse solid particles and trace chemical species from the midplane. In planet formation models where the continuous local production of chondrules/pebbles occurs over Myr time scales to provide a feedstock for pebble accretion onto these bodies, this stirring of solid particles may add a time constraint: planetary embryos and large asteroids have to form before a gas giant forms in the outer

disk, otherwise the SWI will significantly decrease the chondrule/pebble accretion efficiency. This chapter has been published in the Astrophysical Journal, Volume 833, 126 (2016), in collaboration with Richard P. Nelson and Lee Hartmann.

7.2 Introduction

When they form, planets leave traces of their presence in the disks they reside in. The most suggestive signatures include spiral arms, of which we might already have observational snapshots (e.g., Muto et al., 2012; Garufi et al., 2013; Grady et al., 2013; Currie et al., 2014; Benisty et al., 2015; Garufi et al., 2016; Stolker et al., 2016), though the physical origin of the observed spiral arms as well as the presence of planet(s) in the systems are yet to be confirmed.

In our recent work, we have shown that propagating spiral density waves, such as the ones that could be excited by a planet embedded in a gaseous protoplanetary disk, or by gravitational instability (GI), can become unstable to a spiral wave instability (SWI; Chapter 6). The instability arises because the periodic forcing due to the spiral waves resonantly couples with, and transfers energy into, pairs of inertial waves (or inertial-gravity waves) at the expense of the spiral wave itself, such that the spiral waves partially dissipate. When the instability tends towards nonlinear saturation, the flow breaks down into hydrodynamic turbulence, which in turn can act as an efficient source of vertical mixing of trace chemical species and solid particles (Chapter 6).

The level of turbulence in protoplanetary disks plays an important role in determining the ability of solid particles to grow from ISM sizes to eventually become planets. Solid particles grow to millimeters to centimeters in size through direct sticking collisions, after which point the so-called "bouncing barrier" limits further growth by hit-and-stick coagulation (see review by Testi et al. 2014 and references therein). If decimeter-sized particles are able to form in abundance then streaming instabilities can concentrate these "pebbles" and "boulders" via aerodynamic drag, and the resulting particle clumps can collapse gravitationally to form planetesimals of between 25 to 200 km in size (Youdin & Goodman, 2005; Johansen et al., 2007, 2015). Once large planetesimals are present, gas drag acting on the remaining

pebbles can produce rapid accretion – pebble accretion (Johansen & Lacerda, 2010; Ormel & Klahr, 2010; Lambrechts & Johansen, 2012; Morbidelli & Nesvorny, 2012). Pebble accretion involving millimeter-sized chondrules can help to build up planetary embryos to the size of Mars, and can also help to grow 100 km sized asteroids that form as a result of streaming instabilities into significantly larger bodies that resemble the largest asteroids in the asteroid belt (e.g., Johansen et al., 2015). While the former process – the streaming instability – has been shown to operate in the presence of moderately strong turbulence with $\alpha \sim 10^{-3}$ (Johansen et al., 2007), where α denotes the canonical Shakura & Sunyaev (1973) stress parameter, for the latter process – pebble accretion – to work efficiently, it is necessary to concentrate pebbles into a thin layer at the disk midplane such that the scale height of the pebbles is smaller than the Hill radius of pebble-accreting planetesimals (Lambrechts & Johansen, 2012). Under typical disk conditions, this requires the scale height of pebbles to be less than ~ 1 % of that of gas, which can only be satisfied with very low turbulence to avoid stirring up the pebbles. A turbulence level of $\alpha \gtrsim 10^{-4}$ may result in a too long timescale for the formation of planetary embryos or large asteroids (e.g., Johansen et al., 2015).

In the present Chapter, we perform three-dimensional global hydrodynamic simulations to demonstrate that the SWI operates in the presence of spiral waves excited by a Jovian mass giant planet, and to estimate the level of SWI-induced turbulence and the consequent vertical mixing of solid particles in the terrestrial body-forming and asteroid belt regions. Our simulations show that the SWI develops for the spiral waves on timescales on the order of the planetary orbital time. When the instability is fully saturated, the vertical diffusion rate estimated from gas motions in the interval $0.3R_p \leq R \leq 0.7R_p$, where R_p is the semi-major axis of the planetary orbit (assumed to be 5 au in this work), is such that particles with sizes up to a few centimeters are vertically mixed within the first pressure scale height of the gas disk. This result suggests that the instability acting on the spiral waves from a gas giant can have significant influence on the dust dynamics and chemical mixing in protoplanetary disks. In particular, if accretion of chondrules/pebbles dominates the growth of terrestrial embryos in the terrestrial planet region, or large asteroids in the asteroid belt, then we suggest that the SWI can have a strong influence by limiting chondrule/pebble accretion efficiency when

a gas giant planet such as Jupiter forms in the outer disk.

This Chapter is organized as follows. In Section 7.3, we discuss the expected wavelengths of the unstable inertial waves and the regions of a disk in which the SWI operates, based on the WKBJ dispersion relations. We describe our computational setup in Section 7.4, with a special emphasis on the choice of numerical resolution that suits for capturing unstable inertial modes. In Section 7.5, we begin by describing numerical results obtained with perturbations having *monochromatic* azimuthal modes with $m = 2$ and $m = 3$, with which the spiral arms are evenly spaced in azimuth. We then describe results obtained with a full planetary potential. We present the analysis on the vertical mixing of particles arising from the SWI and discuss implications to the formation and growth of terrestrial bodies and large asteroids in Section 7.6, and draw conclusions in Section 7.7.

7.3 Theoretical Expectations

7.3.1 Monochromatic Spiral Waves

Before we consider spiral density waves launched by planets, which consist of a superposition of various azimuthal components (Goldreich & Tremaine , 1979), we briefly discuss theoretical expectation for the SWI driven by monochromatic $m = 2$ and $m = 3$ spiral waves to gain insight into the instability. These modes are chosen because they appear prominently in our simulations with Jupiter-mass planets, as discussed below. We focus mainly on spiral waves that propagate in the disk regions that lie interior to the planet in this Chapter, and leave discussion of outward propagating spiral waves for future work. Throughout the Chapter, we use the term *monochromatic modes/waves* to denote the spiral waves that are evenly spaced in azimuth. For a more detailed discussion of the theoretical background, we refer readers to Section 2 of Chapter 6 and references therein.

In a differentially rotating disk, the WKBJ dispersion relation for local disturbances can be written as (Goodman, 1993)

$$\frac{\omega^2/c_s^2}{\omega^2 - N^2} - \frac{k_Z^2}{\omega^2 - N^2} - \frac{k_R^2}{\omega^2 - \kappa^2} = 0. \tag{7.1}$$

In the dispersion relation, ω is the mode frequency, κ is the epicyclic frequency, N is the vertical Brunt-Väisälä frequency, k_R and k_Z are the radial and vertical wave numbers associated with the wave vector $\mathbf{k} = k_R\hat{\mathbf{e}}_R + k_Z\hat{\mathbf{e}}_Z$, and c_s is the sound speed.

The WKBJ dispersion relation for a spiral wave with azimuthal mode number m is given by

$$m^2(\Omega - \Omega_\mathrm{p})^2 = \kappa^2 + c_s^2 k_{R,\mathrm{s}}^2, \tag{7.2}$$

when self-gravity is neglected and $k_{Z,\mathrm{s}} = 0$ is assumed. Interior to the inner Lindblad resonance (ILR), this gives a radial wave number $k_{R,\mathrm{s}}$ of

$$k_{R,\mathrm{s}}^2 = \frac{\omega_s^2 - \kappa^2}{c_s^2}, \tag{7.3}$$

where $\omega_s = m(\Omega - \Omega_p)$ is the Doppler-shifted frequency of the incoming waves, and Ω_p is the pattern speed of the spiral wave measured in the inertial frame.

Inertial modes excited by a spiral wave must have radial length scales that are similar to or smaller than the wavelength of the incoming wave. Thus, assuming that the excited inertial modes have very similar spatial structure and frequencies, which is appropriate to the high wave number limit, we can relate the wave number of the excited inertial waves $k_{R,\mathrm{i}}$ to $k_{R,\mathrm{s}}$ as

$$k_{R,\mathrm{i}} = n k_{R,\mathrm{s}}, \tag{7.4}$$

where n is an integer. As noted in Chapter 6, this integer relationship holds for waves in periodic shearing boxes, and is introduced for the global models that we consider here for the purpose of choosing a simple relation between the wavelengths of the spiral and inertial waves. Given the radial wave number and the frequency of the spiral wave (in the local fluid frame), we can estimate the vertical wave number of the excited inertial waves $k_{Z,\mathrm{i}}$ using the dispersion relation in Equation (7.1) and the resonance condition $\omega_\mathrm{i} = \omega_\mathrm{s}/2$ in the high wave number limit ($n \gg 1$; Fromang & Papaloizou, 2007). This results in

$$k_{Z,\mathrm{i}}^2 = \frac{(\omega_\mathrm{s}/2)^2}{c_s^2} - n^2 \frac{\omega_\mathrm{s}^2 - \kappa^2}{c_s^2} \frac{(\omega_\mathrm{s}/2)^2 - N^2}{(\omega_\mathrm{s}/2)^2 - \kappa^2}, \tag{7.5}$$

when the Brunt-Väisälä frequency, N, is important or

$$k_{Z,\mathrm{i}}^2 = \frac{(\omega_\mathrm{s}/2)^2}{c_s^2}\left(1 - n^2\frac{\omega_\mathrm{s}^2 - \kappa^2}{(\omega_\mathrm{s}/2)^2 - \kappa^2}\right) \tag{7.6}$$

when N is negligible. In order for $k_{Z,\mathrm{i}}$ to be real for arbitrary values of n from Equation (7.6), such that inertial waves can be excited, one requires

$$(\omega_\mathrm{s}/2)^2 < \kappa^2 < \omega_\mathrm{s}^2 \tag{7.7}$$

to be satisfied.

In rotating disks, inertial modes have frequencies in the interval $0 \leq \omega_i \leq \Omega$. This, together with Equation (7.7), implies that for an arbitrary perturbation with azimuthal mode number $m \geq 1$ the SWI operates in the radial region of

$$\left(\frac{m-2}{m}\right)^{2/3} R_p \leq R \leq \left(\frac{m-1}{m}\right)^{2/3} R_p \tag{7.8}$$

in the inner disk and

$$\left(\frac{m+1}{m}\right)^{2/3} R_p \leq R \leq \left(\frac{m+2}{m}\right)^{2/3} R_p \tag{7.9}$$

in the outer disk. Focusing on the inner disk, there will always be inertial mode pairs available for a resonant interaction with $m = 2$ spiral waves having a Doppler-shifted frequency $\omega_s = 2(\Omega - \Omega_p) < \Omega$ inside the ILR. On the other hand, for $m \geq 3$ waves, the SWI cannot operate in disk regions where $R \leq ((m-2)/m)^{2/3} R_p$, because the spiral wave frequency at these radii is too large, so no inertial modes can participate in a resonant interaction.

In Figure 7.1, we present two-dimensional maps showing the vertical and radial wavelengths of the inertial modes that satisfy the resonance conditions for monochromatic $m = 2$ and $m = 3$ spiral waves, assuming an adiabatic response of gas with $\gamma = 1.4$ and the disk model that will be introduced in Section 7.4.2. The wavelengths are calculated using Equations (7.3), (7.4), and (7.5).

We point out two important features from the figure. First, as we have shown above, there is a limited region where the SWI can be triggered for a given monochromatic perturbation.

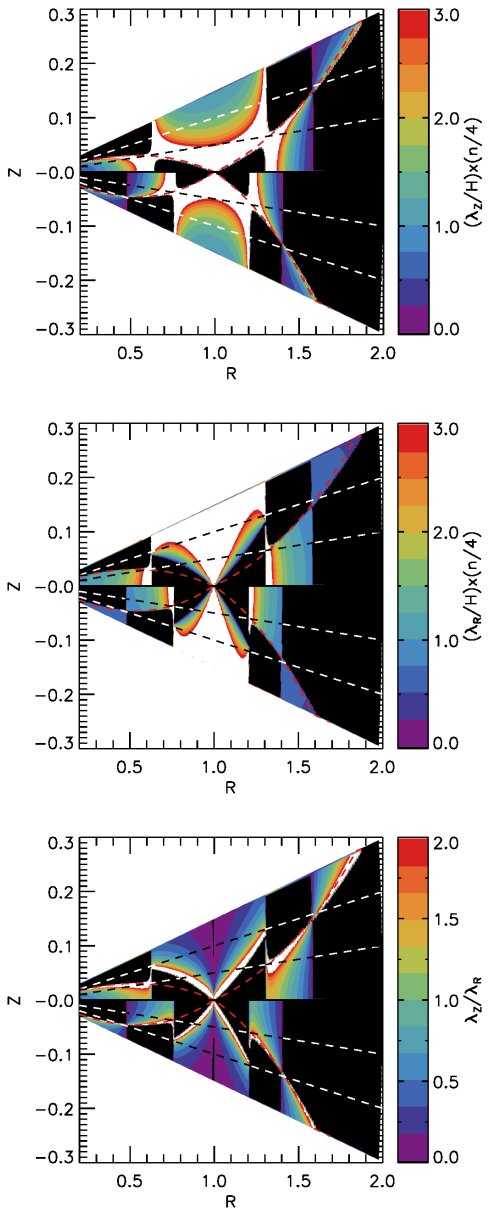

Figure 7.1. (a) Contour plots of the vertical wavelength of the unstable inertial modes λ_Z, in units of local scale height, calculated with Equation (7.5) and the disk model that will be introduced in Section 7.4.2. (b) Same as (a) but for the radial wavelength λ_R. (c) The ratio of vertical to radial wavelength of the inertial modes. In all panels, the black and white dashed lines indicate where $Z = \pm 1H$ and $\pm 2H$. The black regions are where the dispersion relation does not have a physical solution, and thus the SWI is believed to be forbidden. The red dashed curves indicate where the local buoyancy frequency equals to a half of the doppler-shifted frequency of the spiral waves: $N^2 = (\omega_s/2)^2$. The upper half of each panel presents the wavelengths of unstable inertial modes in response to monochromatic $m = 2$ waves, whereas the lower half of each panel shows those in response to monochromatic $m = 3$ waves. We use $n = 4$ as a representative example purely for the purposes of illustration, but the numbers on the colorbars can be linearly scaled to other modes as noted in the labels.

At the midplane, where the Brunt-Väisälä frequency becomes zero, the SWI can operate in the entire region inside of the ILR for $m = 2$ waves ($R \lesssim 0.63\ R_p$), whereas it can only operate in the region $0.48\ R_p \lesssim R \lesssim 0.76\ R_p$ for $m = 3$ waves. Second, when buoyancy is considered, the SWI-permitted regions are confined towards the midplane at the radii where the SWI can operate because the SWI can operate only in disk regions where $(\omega_s/2)^2 \lesssim N^2$ is satisfied (Chapter 6). The vertical extent of this SWI-permitted region is $\sim 1H$ above and below the midplane, and this is where we will focus on in this Chapter. While $m \geq 3$ modes can trigger the SWI near the surface region ($|Z| \gtrsim 2H$) at $R \leq ((m-2)/m)^{2/3} R_p$ because of buoyancy, and this may have important implications for the morphology of spiral arms traced by observations of infrared scattered light, we do not consider this further here as we are mainly concerned with the mixing of solid particles located near the midplane.

7.3.2 Planet-induced Spiral Waves

A Jovian planet on a circular orbit will excite a spiral wave pattern that is a superposition of components with different azimuthal mode numbers, but with each component displaying a pattern speed, $\Omega_{\rm p}$, that is equal to the Keplerian angular velocity of the planet. Nonlinear effects may cause the relation between the different components to vary as a function of radius. As shown later in this Chapter via a Fourier analysis, the spiral wave pattern at any radius interior to the Lindblad resonances due to a Jovian planet can be decomposed into a sum of modes where the dominant contributors are the $m = 2$ and $m = 3$ modes. At any point in time, one can assume that a protoplanetary disk will support the whole spectrum of possible inertial modes, which, in the absence of a strong excitation mechanism, will be present with very low amplitudes. The presence of a spiral wave pattern consisting of different azimuthal components, each with different Doppler-shifted frequencies as observed by fluid elements orbiting in the disk, will lead to excitation of those inertial modes that can resonantly interact with any of the azimuthal mode components that make up the incoming spiral wave. As such, we expect that a giant planet-induced spiral wave will lead to the excitation of inertial modes in a manner that is similar to a superposition of the response to both the $m = 2$ and $m = 3$ spiral modes described above. For lower mass planets, where the strengths of the spiral wave components will not be so strongly concentrated towards

the $m = 2$ and $m = 3$ modes, the SWI may also be excited by the higher-m modes.

Although our focus in this Chapter is on planets with circular orbits, it is worthwhile briefly discussing how the above picture changes if orbital eccentricity is considered. If the planet is on an eccentric Keplerian orbit, then m-fold spiral waves are excited at Lindblad resonances with pattern speeds $\Omega_{\rm p} = (m \pm k)\,\Omega_{\rm pl}/m$, where k is a positive integer and $\Omega_{\rm pl}$ is the mean motion of the planet (Goldreich & Tremaine, 1980). When considering planet-disk interactions at Lindblad resonances, the strength of the torque exerted on the disk by the planet, Γ, scales as $\Gamma \sim e^2 k$, where e is the orbital eccentricity. Therefore, increasing the planet eccentricity gives rise to new spiral waves, associated with higher values of k, being excited, with their amplitudes increasing as the eccentricity increases. Considering Lindblad resonances located interior to the planet that launch inward propagating spiral waves, these additional spiral waves can have higher pattern speeds than the equivalent m-fold spirals associated with planets on circular orbits. For example, taking $m = 2$ and $k = 1$, we have a wave that is excited with pattern speed $\Omega_{\rm p} = 3/2\Omega_{\rm pl}$ instead of $\Omega_{\rm p} = \Omega_{\rm pl}$ as is the case for a planet on a circular orbit. Clearly, introducing the possibility of eccentric orbits increases the range of inertial mode frequencies that can be resonantly excited.

7.4 Numerical Methods

7.4.1 Basic Equations

We solve the hydrodynamic equations for mass, momentum, and internal energy conservation in the three-dimensional spherical coordinates (r, θ, ϕ):

$$\frac{\partial \rho}{\partial t} + \nabla \cdot (\rho v) = 0, \tag{7.10}$$

$$\rho \left(\frac{\partial v}{\partial t} + v \cdot \nabla v \right) = -\nabla P - \rho \nabla (\Phi_* + \Phi_p), \tag{7.11}$$

$$\frac{\partial e}{\partial t} + \nabla \cdot (ev) = -P \nabla \cdot v + Q_{\rm cool}. \tag{7.12}$$

In the above equations, ρ is the mass density, v is the velocity, P is the pressure, $\Phi_* = GM_*/r$ is the gravitational potential from the central star, Φ_p is the external potential (see below),

e is the internal energy per unit volume, and $Q_{\rm cool}$ is the cooling rate (see below).

In the case of monochromatic spiral waves, we implement the following potential form:

$$\Phi_p = \mathcal{A}\cos[m(\phi - \Omega_p t)]e^{-(R-R_p)^2/\sigma_p^2}. \tag{7.13}$$

Here, $\mathcal{A}$ determines the spiral wave amplitude which is assumed to be constant over time t, m is the azimuthal mode number, Ω_p is the pattern speed, $R = r\sin\theta$ is the cylindrical radius, R_p is the radius about which the potential is centered, and σ_p is the radial width of the potential. We assume that the pattern speed is the local Keplerian frequency at its central position $\Omega_p = (GM_*/R_p^3)^{1/2}$ and that $\sigma_p = 0.2R_p$.

When a planetary companion is considered, its potential is included as

$$\Phi_p = -\frac{GM_p}{(|\mathbf{r} - \mathbf{r_p}|^2 + b^2)^{1/2}}, \tag{7.14}$$

where M_p is the planetary mass, $\mathbf{r}$ and $\mathbf{r_p}$ are the radius vectors of the center of grid cells in question and of the planet, and b is the smoothing length. We increase the planetary mass from zero to its full mass (i.e., 1 M_J) over ten orbital times. In three-dimensional calculations, the smoothing length is used only to avoid singularities in the potential on the grid scale. We thus adopt the cell diagonal size $((\Delta r)^2 + (r\Delta\theta)^2 + (r\Delta\phi)^2)^{1/2}$ at the position of the planet as the smoothing length. With the disk model introduced in Section 7.4.2, the smoothing length corresponds to about 18% of a scale height, or about 13% of the Hill radius when the planet is fully grown to 1 M_J. In the planet run, we also include the indirect potential that arises because the origin of the coordinate system is based on the central star and not the center of the mass of the system.

We make use of an adiabatic equation of state. The gas pressure and the internal energy are thus related through $P = (\gamma - 1)e$, with an adiabatic index $\gamma = 1.4$ adopted. To realize the radiative cooling of the disk we implement a simple, but physically motivated, cooling scheme. This assumes relaxation of the internal energy towards the background disk temperature T_0 at each location on the cooling timescale $t_{\rm cool}$. Then, the cooling rate can be

written as

$$Q_{\rm cool} = -\rho c_v \frac{T - T_0}{t_{\rm cool}}, \tag{7.15}$$

where c_v denotes the heat capacity at constant volume.

The cooling timescale is calculated every time step for each grid cell, using the optical depth and the temperature. We follow the approach used in Lyra et al. (2016) and previously in Lyra et al. (2010) and Horn et al. (2012) in a vertically-integrated two-dimensional approximation. To briefly summarize, the cooling timescale is estimated to be the radiative timescale that is defined as

$$t_{\rm cool} \equiv \frac{\int e dV}{\int F \hat{\mathbf{n}} \cdot d\mathbf{A}}, \tag{7.16}$$

where $e = \rho c_v T$ and $F = |\mathbf{F}| = \sigma T^4 / \tau_{\rm eff}$ with σ and $\tau_{\rm eff}$ being the Stefan-Boltzmann constant and the effective optical depth. The effective optical depth $\tau_{\rm eff}$ is given by

$$\tau_{\rm eff} = \frac{3}{8}\tau + \frac{\sqrt{3}}{4} + \frac{1}{4\tau} \tag{7.17}$$

to take account of both optically thick and thin limits (Hubeny, 1990; D'Angelo et al., 2003).

The integration in Equation (7.16) is done over a sphere that has a radius equal to the local pressure scale height. This results in a cooling time of

$$t_{\rm cool} = \frac{\rho c_v H \tau_{\rm eff}}{3\sigma T^3}. \tag{7.18}$$

To obtain the optical depth τ, we first calculate the optical depth due to the material above and below each grid cell as

$$\tau_{\rm upper} = \int_z^{z_{\rm max}} \rho(z')\kappa(z')dz' \tag{7.19}$$

and

$$\tau_{\rm lower} = \int_{z_{\rm min}}^{z} \rho(z')\kappa(z')dz'. \tag{7.20}$$

In practice, the integration is done in θ, instead of z, for simplicity. Then, we calculate the optical depth as $1/\tau = 1/\tau_{\rm upper} + 1/\tau_{\rm lower}$ to give a correct midplane cooling rate (Lyra et al., 2016). For the opacity κ in the above equations, we use the Rosseland mean opacity of

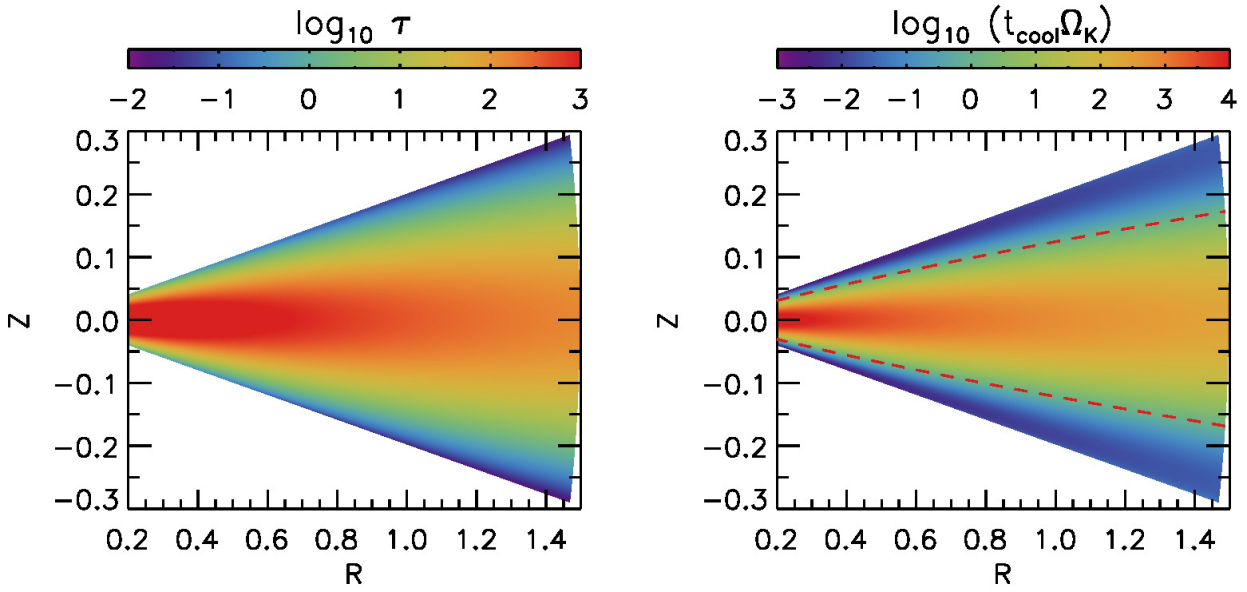

Figure 7.2. Two-dimensional $R - Z$ distributions of (left) optical depth τ and (right) the dimensionless cooling time $\beta = t_{\rm cool}\Omega_K$ for the initial disk. The red dashed curves in the right panel indicate where $t_{\rm cool}\Omega_K = 1$. The main body of the disk is expected to behave adiabatically, since the cooling timescale is much longer than the dynamical timescale in the region.

Zhu et al. (2009b).

The optical depth and the cooling time of the initial disk are presented in Figure 7.2. As shown, the main body of the disk is optically thick, with the cooling time much longer than the dynamical time: $t_{\rm cool} \gg 1/\Omega_K$. Therefore, we expect that the main body of the disk behaves essentially adiabatically, and hence will be stable against the growth of the vertical shear instability (Nelson et al., 2013).

Our calculations are inviscid, but artificial viscosity and the associated heating are included in the momentum and internal energy equations (Stone & Norman, 1992). As discussed in Chapter 6, the effective dimensionless kinematic viscosity associated with the numerical diffusion for FARGO3D (Benítez-Llambay & Masset, 2016) operates with a value that is below $\nu = 10^{-6}$.

7.4.2 Disk Models

We begin with an initial radial power-law temperature distribution in the disk that is independent of height:

$$T(R) = T_p \left(\frac{R}{R_p} \right)^q , \tag{7.21}$$

where T_p is the temperature at the location of the perturber $R = R_p$. The isothermal sound speed is related to the temperature by $c_s^2 = \mathcal{R}T/\mu$, where $\mathcal{R}$ is the gas constant and μ is the mean molecular weight. Thus, Equation (7.21) corresponds to the radial sound speed distribution given by

$$c_s(R) = \frac{H_p}{R_p} \left(\frac{R}{R_p} \right)^{q/2} . \tag{7.22}$$

In all models, we adopt $H_p/R_p = 0.05$ and $q = -1$ such that the entire disk has the aspect ratio of 0.05.

The initial density and azimuthal velocity profiles are constructed to satisfy hydrostatic equilibrium (e.g., Nelson et al., 2013):

$$\rho(R, Z) = \rho_p \left(\frac{R}{R_p} \right)^p \exp \left(\frac{GM_*}{c_s^2} \left[\frac{1}{\sqrt{R^2 + Z^2}} - \frac{1}{R} \right] \right) \tag{7.23}$$

and

$$v_\phi(R, Z) = \left[(1 + q) \frac{GM_*}{R} + (p + q)\, c_s^2 - q \frac{GM_*}{\sqrt{R^2 + Z^2}} \right]^{1/2} . \tag{7.24}$$

We choose the initial density distribution in such a way that the vertically-integrated surface density Σ becomes $\Sigma = 5\Sigma_{\rm MMSN}$, where $\Sigma_{\rm MMSN}$ is the minimum mass solar nebular (MMSN) model of Hayashi (1981). A value of $p = -5/2$ is adopted accordingly, to have the surface density power-law slope that matches to the slope of the MMSN model, $-3/2$.

The initial radial and meridional velocities are set to zero, but uniformly distributed random perturbations are added as white noise, at the level of $10^{-6}\ c_s$, to the initial meridional velocity field in order to seed the instability.

7.4.3 Computational Setup

We expect the main body of the disk to behave adiabatically, since the disk cooling timescale is much longer than the dynamical timescale in the region (see Figure 7.2). Thus, the regions in which the SWI is allowed to operate can be inferred using the linear analysis described in Section 7.3 and depicted in Figure 7.1, assuming an adiabatic equation of state with $\gamma = 1.4$.

As seen in Figure 7.1, the SWI-permitted regions are confined around the midplane, with a thickness that is as small as $\sim 1H$ above and below the midplane. Therefore, we aim to have a numerical resolution with which unstable inertial modes with $\lambda_Z \simeq 1H$ can be well captured. At the midplane, the ratio of the vertical to radial wavelengths of unstable inertial modes increases over radius, except near the ILR where a singularity appears. The largest ratio of λ_Z/λ_R for perturbations with $m \geq 2$ is $\simeq 1.5$ (see Figure 7.1), and thus the radial wavelength that we aim to resolve will be $\lambda_R \simeq (2/3)H$.

Since inertial modes can have arbitrarily small length scales, smaller scale unstable modes can only be captured with higher resolutions than the one used in the present work. On the other hand, it seems that the modes with the largest length scale contain the largest amount of kinetic energy (Chapter 6). In the simulations presented in Section 7.5 as well as the ones in Chapter 6, we observe that smaller scale modes grow at earlier times, but only with small velocity amplitudes. These modes are then masked by larger scale modes that grow at later times with larger velocity amplitudes, supporting the conjecture that the modes with the largest length scales contain most of the kinetic energy as the system approaches the nonlinear saturated state. One effect of under-resolving the small scale modes, however, is that the development of a realistic breakdown into hydrodynamic turbulence may be prevented, as the cascade of energy from large to small scales in the fully saturated nonlinear regime will be prevented, affecting the nature of the flow and the statistics of the quasi-turbulent flow that develops due to the SWI.

Our simulation domain extends from $r_{\rm in} = 0.2R_p$ to $r_{\rm out} = 1.5R_p$ in radius, from $\pi/2 - 0.2$ to $\pi/2 + 0.2$ in the meridional direction (covering 4 scale heights above and below the midplane), and from 0 to 2π in azimuth. We have tested with various numerical resolutions and find that 12 grid cells per wavelength is required to properly resolve unstable inertial

modes. To achieve $\Delta r = (1/12)\lambda_R = (1/12) \times (2/3)H$, or equivalently $\Delta r/r = (1/18)H/R$ at the midplane, we adopt 726 logarithmically-spaced radial grid cells. We adopt 144 and 754 uniformly-spaced grid cells in the meridional and the azimuthal directions, respectively, with which choice $\Delta r : r\Delta\theta : r\Delta\phi \simeq 1 : 1 : 3$.

The radial boundary condition is chosen to have a zero gradient for all variables. We further implement a wave damping zone (de Val-Borro et al., 2006) in the intervals $r = [r_{\rm in}, 1.2r_{\rm in}]$ and $r = [0.9r_{\rm out}, r_{\rm out}]$, since reflected waves at the radial boundaries may affect triggering and growth of the SWI, as they have the same pattern speed as the incoming waves. Periodic boundary conditions are used in azimuth since the simulation domain covers 2π. At the meridional boundaries, we use an outflow boundary condition such that all velocity components in the ghost zones have the same values as the last active zones, but the meridional velocity is set to 0 if directed toward the disk midplane. The temperature in the ghost zones is set to have the same value as in the last active zones. The density in the ghost zone is then obtained by solving the hydrostatic equilibrium in the meridional direction:

$$\frac{1}{\rho}\frac{\partial}{\partial\theta}(\rho c_s^2) = \frac{v_\phi^2}{\tan\theta}. \tag{7.25}$$

We make use of FARGO3D (Benítez-Llambay & Masset, 2016), which runs on both central processing units (CPUs) and graphics processing units (GPUs). In order to deal with the high numerical resolution, our calculations use a cluster of GPUs, which allows us to perform the calculations within a reasonable time frame thanks to a large speed up with respect to CPUs. With four NVIDIA Tesla K20x GPUs on the University of Michigan high-performance computing cluster[1], it takes about one month for the planet run in Section 7.5.2 to evolve for 200 orbits. We enable the FARGO (Fast Advection in Rotating Gaseous Objects) orbital advection module (Masset, 2000).

In the following sections we will use the orbital distance of the planet (or perturbing potential) R_p as the length unit (assumed to be 5 au), and the orbital time 1 $t_{\rm orb}$ at $R = R_p$ as the time unit.

Since we adopt physical units to consider cooling, the models are not scalable in principle.

[1]http://arc-ts.umich.edu/systems-and-services/flux/

However, we believe that the results can be qualitatively applicable as far as the main body of a disk is sufficiently optically thick, because the disk response to spiral waves is not very sensitive to the cooling timescale when $\beta \equiv t_{\rm cool}\Omega_K \gtrsim 1$ (Zhu et al., 2015, and also from our test runs during early phases of the present work).

7.4.4 Diagnostics

In order to examine the growth and the saturation of the SWI, we compute the volume-integrated meridional kinetic energy e_θ:

$$e_\theta = \frac{1}{2}\int_V \rho v_\theta^2 \, dV. \tag{7.26}$$

While the velocity perturbation driven by spiral waves is larger at high altitude than near the midplane in general, e_θ traces perturbations near the midplane region because of the vertically stratified density structure.

In the figures presenting the meridional kinetic energy, we normalize e_θ by $e_{\rm th}$ which we define as the volume-integrated kinetic energy of gas parcels assuming that they move at the local sonic velocity:

$$e_{\rm th} = \frac{1}{2}\int_V \rho {c_s}^2 \, dV. \tag{7.27}$$

We also compute the Shakura-Sunyaev stress parameter $\alpha_{r\phi}$ as

$$\alpha_{r\phi}(r,\theta) = \frac{\langle \rho \delta v_r \delta v_\phi \rangle}{\overline{P}(r)}, \tag{7.28}$$

where $\overline{P}(r)$ is a density-weighted mean pressure at radius r, in order to examine the sustained level of angular momentum transport driven by the turbulent flow at saturation of the instability (although we note that a contribution to $\alpha_{r\phi}$ also arises from the propagating spiral waves that is difficult to disentangle from that arising from the SWI-induced turbulence).

7.5 Results

7.5.1 Results with Monochromatic Waves

Before we describe our main results with a planet, we introduce models with monochromatic perturbations. The perturbing waves are imposed using Equation (7.13) with azimuthal mode numbers $m = 2$ (Section 7.5.1.1; hereafter $m = 2$ model) or $m = 3$ (Section 7.5.1.2; hereafter $m = 3$ model). The potential amplitudes are chosen so that the linear phase of the instability spans several orbital times, and therefore the growth of individual unstable modes can be captured: $\mathcal{A} = 4 \times 10^{-3}$ for the $m = 2$ model and $\mathcal{A} = 5 \times 10^{-4}$ for the $m = 3$ model.

7.5.1.1 $m = 2$ Model

In Figure 7.3, we present the density distribution $\rho/\langle\rho\rangle$ for $m = 2$ model, where the brackets denote an azimuthal average, along with the meridional velocity distribution near the midplane where the SWI is expected to operate. The density perturbation is about 10% in the midplane and about 30% at the surface when the spiral waves are fully established. The larger perturbation towards the surface is presumably because of a nonlinear effect due to faster advection of the wave at higher altitudes in the disk (Chapter 6; see also Zhu et al. 2015).

The checkerboard pattern shown in the meridional velocity distribution is a generic feature of the linear growth phase of the SWI (Chapter 6), and was also observed by Fromang & Papaloizou (2007) in their shearing box simulations of nonlinear, axisymmetric sound waves propagating in astrophysical disks. As expected from the dispersion relations, the regions in which the SWI develops are confined toward the midplane, because the large Brunt-Väisälä frequency near the surface does not allow any inertial modes there to resonantly interacting with the incoming $m = 2$ waves. During the linear phase, the magnitude of the perturbed meridional velocity increases over time, but remains a few to about ten percent of the local sound speed. The wavelengths of the dominant unstable inertial modes varies over radius: at the midplane, $\lambda_R \simeq \lambda_Z \simeq 1H$ at $R \sim 0.4$, whereas $\lambda_R \simeq 1H$ and $\lambda_Z \simeq 2H$ at $R \sim 0.6$.

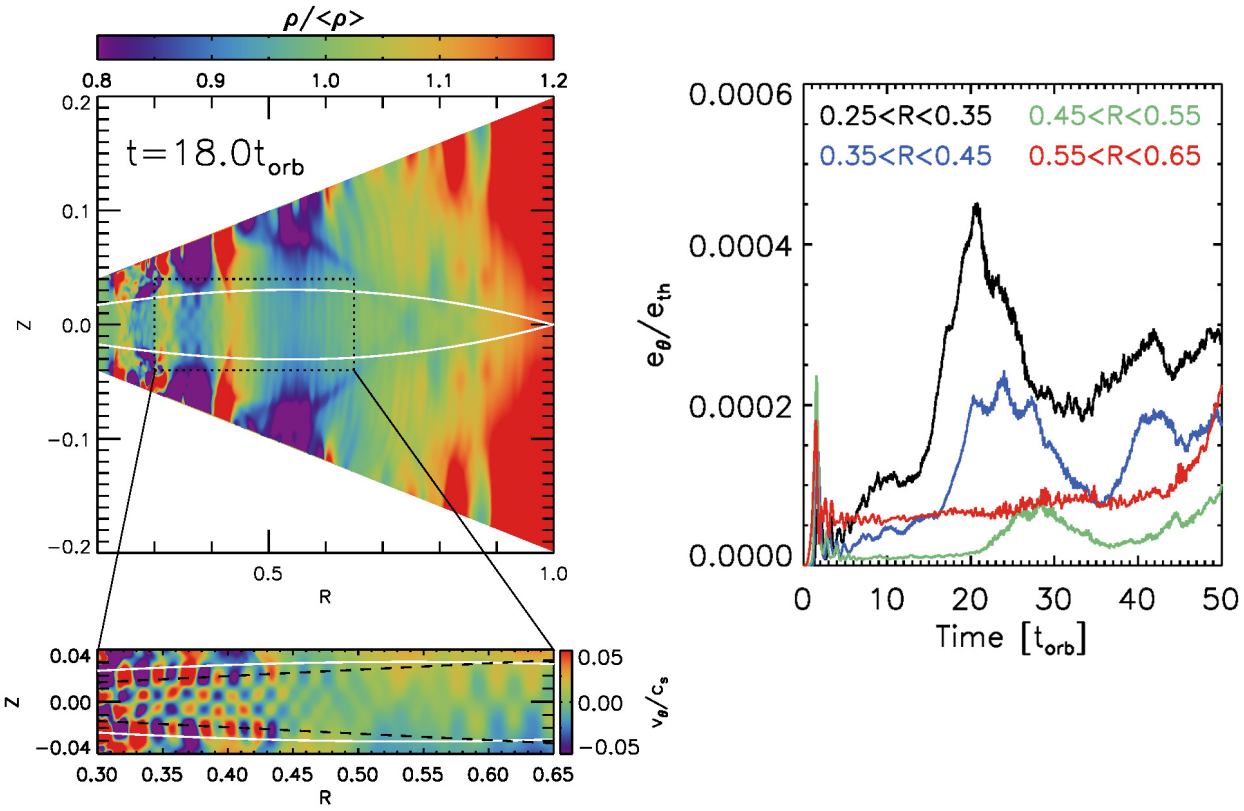

Figure 7.3. (Left Top) Two-dimensional distribution of density perturbation $\rho/\langle\rho\rangle$ in a $R-Z$ plane for $m = 2$ model. The two white curves near the midplane indicate where the local Brunt-Väisälä frequency equals to one half of the doppler-shifted wave frequency of spiral waves ($N^2 = (\omega_s/2)^2$), between which region is expected to be unstable to the SWI. (Left Bottom) Contour plots of the meridional velocity normalized by the local sound speed, for the dotted rectangle region in the left top panel. The x and y axes are drawn isotropically so that the radial and vertical wavelengths of unstable inertial modes can be compared with each other from the figure. The black dashed lines indicate where $Z = \pm 1H$. Note that the SWI has grown in the entire disk region inside the ILR. (Right) Time evolution of the meridional kinetic energy e_θ at various radius bins, normalized by $e_{\rm th}$ in each bin. Note that the exponential growth of the instability appears at earlier times for smaller radii.

The ratio of vertical to radial wavelengths of the unstable inertial modes increases toward larger radii and height. Note that these unstable mode properties are well described by the linear analysis introduced in Section 7.3.

Also shown in Figure 7.3 is the time evolution of the volume-integrated meridional kinetic energy e_θ for various radius bins. The exponential growth of e_θ, for example during $t \sim 15 - 21\ t_{\rm orb}$ at $0.25 < R < 0.35$, indicates the development of the SWI. At smaller radii the instability becomes apparent at earlier times because of the shorter interaction period

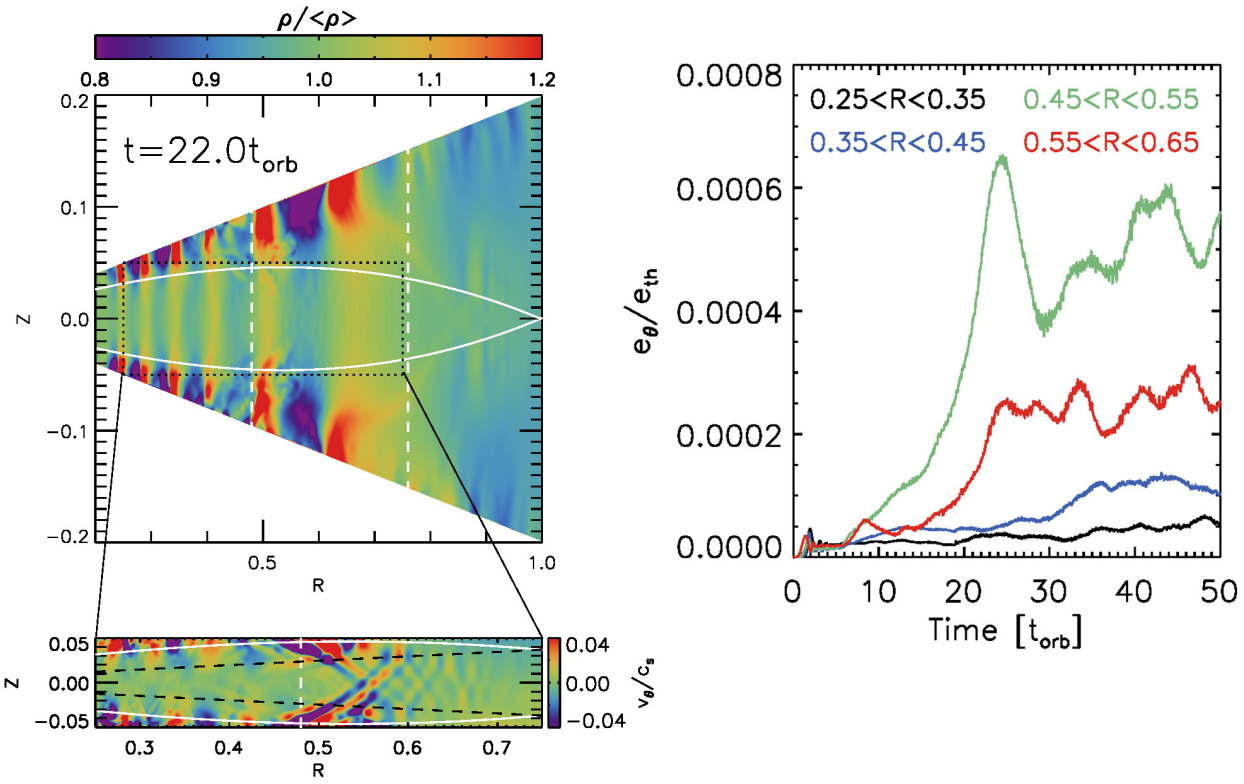

Figure 7.4. Same as Figure 7.3, but for $m = 3$ model. Note that the instability has grown beyond $R \sim 0.5$, but not inward of the radius as no inertial modes there have an adequate frequency to satisfy the resonant condition with the incoming spiral waves. Also, the exponential growth in e_θ appears for $0.45 < R < 0.55$ and $0.55 < R < 0.65$ but not at the inner two radius bins, supporting the fact that the SWI does not operate at $R \lesssim 0.5$. The increase in e_θ in the inner two radius bins at later times ($t \gtrsim 30\ t_{\rm orb}$) is presumably because the spiral waves propagate through the SWI-turbulent region.

between inertial modes and the spiral waves.

7.5.1.2 $m = 3$ Model

Figure 7.4 displays the density distribution $\rho/\langle\rho\rangle$ for the $m = 3$ model. The density perturbation is about 5% in the midplane and about 20% at the surface when the $m = 3$ spiral waves are fully established. As seen in the figure, the instability is developing beyond $R \gtrsim 0.5$ at $t = 22\ t_{\rm orb}$. The SWI does not operate inward of this radius because the Doppler-shifted perturbation frequency from the incoming $m = 3$ waves is too large to excite any inertial modes, which is in very good agreement with the expectation from the dispersion relations. As in the $m = 2$ model, the ratio of vertical to radial wavelength of unstable inertial modes

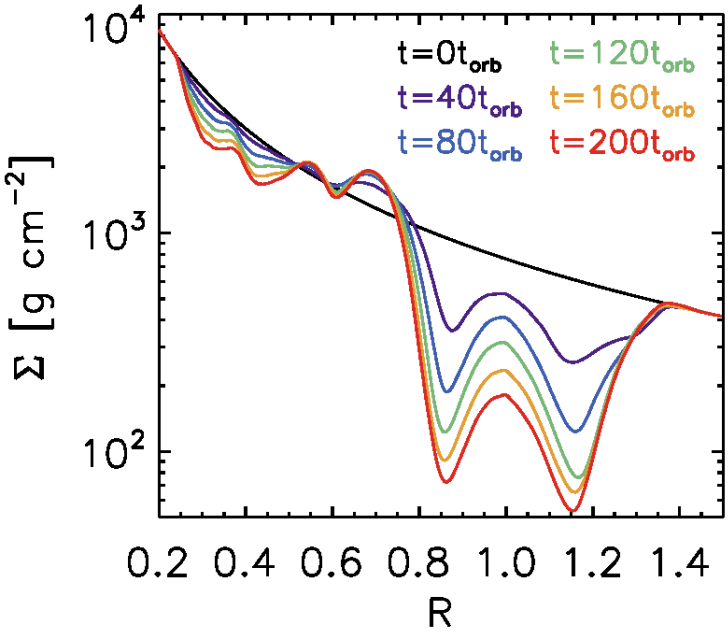

Figure 7.5. Radial distributions of the azimuthally averaged surface density at $t = 0$, 40, 80, 120, 160, and 200 $t_{\rm orb}$.

increases towards larger radii and height.

The time evolution of e_θ is presented in Figure 7.4. The exponential growth of e_θ is only observed in $0.45 < R < 0.55$ and $0.55 < R < 0.65$, supporting the conjecture that the instability is forbidden at smaller radii. The increase in e_θ at later times (e.g., $t \gtrsim 30\ t_{\rm orb}$) in the inner disk regions of $R < 0.45$ is probably because the spiral waves propagate through the turbulent region of $R > 0.45$, and hence generate some vertical motion there due to the curvature of the spiral wave fronts in the meridional plane discussed in Chapter 6.

7.5.2 Results with a Perturbing Planet

We now describe the results for the planet run. We first discuss the overall evolution in Section 7.5.2.1 and then focus on the development of the SWI in Section 7.5.2.2.

7.5.2.1 Overall Evolution

We evolve the planet run for 200 $t_{\rm orb}$. In Figure 7.5, we present the azimuthally averaged surface density distributions at every 40 $t_{\rm orb}$. The planet opens a gap around its orbit and creates a mild density bump at the inner gap edge. In the inner disk ($R \lesssim 0.5$), the disk

looses material through the meridional boundary because of vertical flows induced by the spiral waves.

As inferred from the figure, the depth of the gap does not reach full saturation by the end of the run at 200 $t_{\rm orb}$. Recently, Fung & Chiang (2016) carried out three-dimensional calculations to examine gap opening by planets in a locally isothermal disk. Their results indicate that the saturation of the gap depth requires about 1000 planetary orbits (or even longer depending on the planetary mass) with a disk viscosity of $\alpha = 10^{-3}$. On the other hand, in their 1 M_J case, the density perturbation driven by spiral waves remains roughly constant after 100 planetary orbits (Fung, D., private communication). It is therefore reasonable to assume that the amplitudes of the spiral waves in our simulations have also saturated.

In Figure 7.6, we present the density distribution $\rho/\langle\rho\rangle$ in the midplane at $t = 10\ t_{\rm orb}$, at which time the planetary mass is fully grown to 1 M_J. The planet excites three distinguishable spiral arms. This multi-armed feature can be understood as a consequence of non-linear mode-coupling (e.g., Artymowicz & Lubow, 1992; Lee, 2016) and has been shown to arise in recent numerical simulations (e.g., Fung & Dong, 2015; Juhász et al., 2015; Zhu et al., 2015). Looking in more details at the spiral arms, the first arm is connected to the planet, and the second and third arms start to appear at $R \sim 0.7$ and at $R \sim 0.6$, respectively. The azimuthal separation between the spiral arms, as well as the relative strength of the arms, vary over radius. At $R = 0.4$, for instance, the second arm is $\sim 100^\circ$ ahead of the first arm and the third arm is $\sim 100^\circ$ behind the first arm. The density perturbation by the second arm at this radius is about twice as strong as the perturbation driven by the other two arm. On the other hand, at $R = 0.3$, the second arm is $\sim 75^\circ$ ahead of the first arm and the third arm is $\sim 120^\circ$ behind the first arm. The density perturbation by the second arm is still the strongest, but only $\sim 25\%$ stronger than the perturbation driven by the first arm.

In order to more quantitatively examine the gas response to the spiral waves, in Figure 7.7 we plot the time evolution of the Fourier amplitudes of the density perturbation at different radii. As seen in the figure, spiral waves driven by a planet are not monochromatic, but consist of various azimuthal components that are superimposed on each other. We emphasize that, most importantly for our purpose, the Fourier amplitudes of $m = 1 - 5$ modes remain nearly constant after $t \sim 100\ t_{\rm orb}$ at all radii, despite the fact that the gap

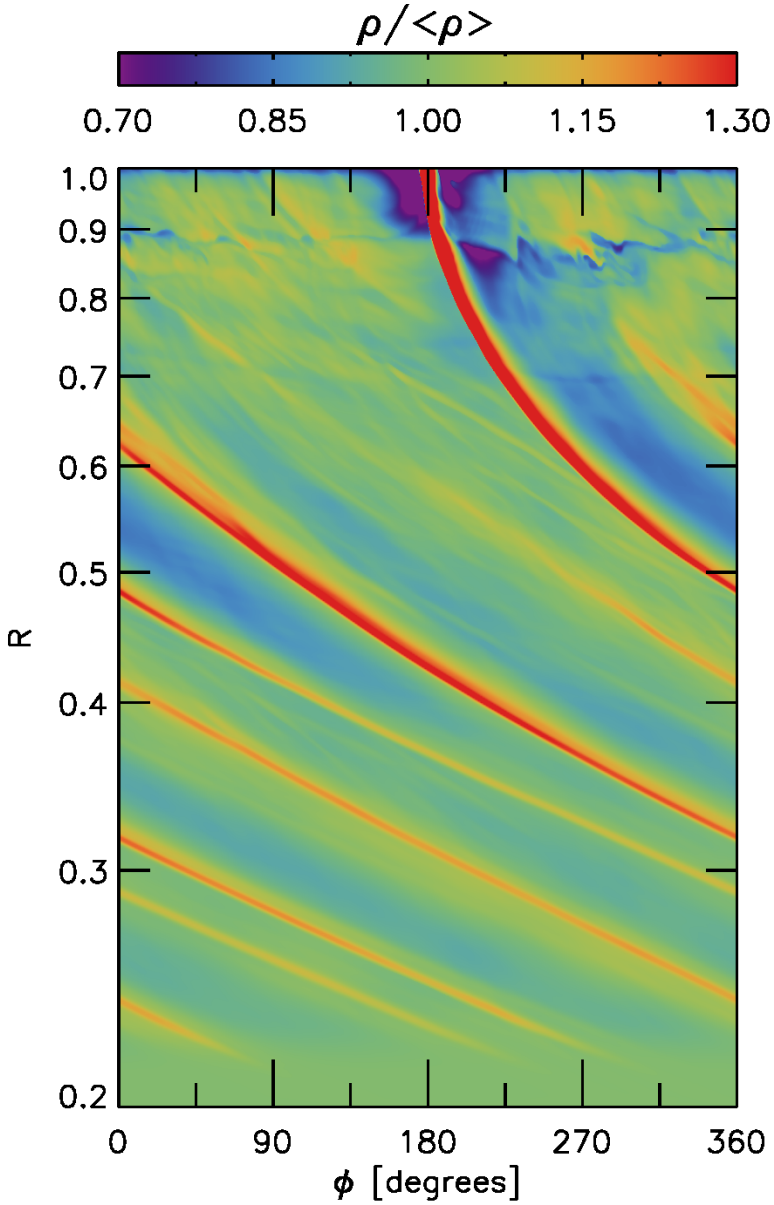

Figure 7.6. Two-dimensional $\phi - R$ distribution of $\rho/\langle\rho\rangle$ in the midplane, taken when the planetary mass is fully grown to 1 M_J at $t = 10t_{\rm orb}$. The planet is located at $(\phi, R) = (180, 1.0)$. The y-axis is plotted using a logarithmic scale to stretch the inner disk.

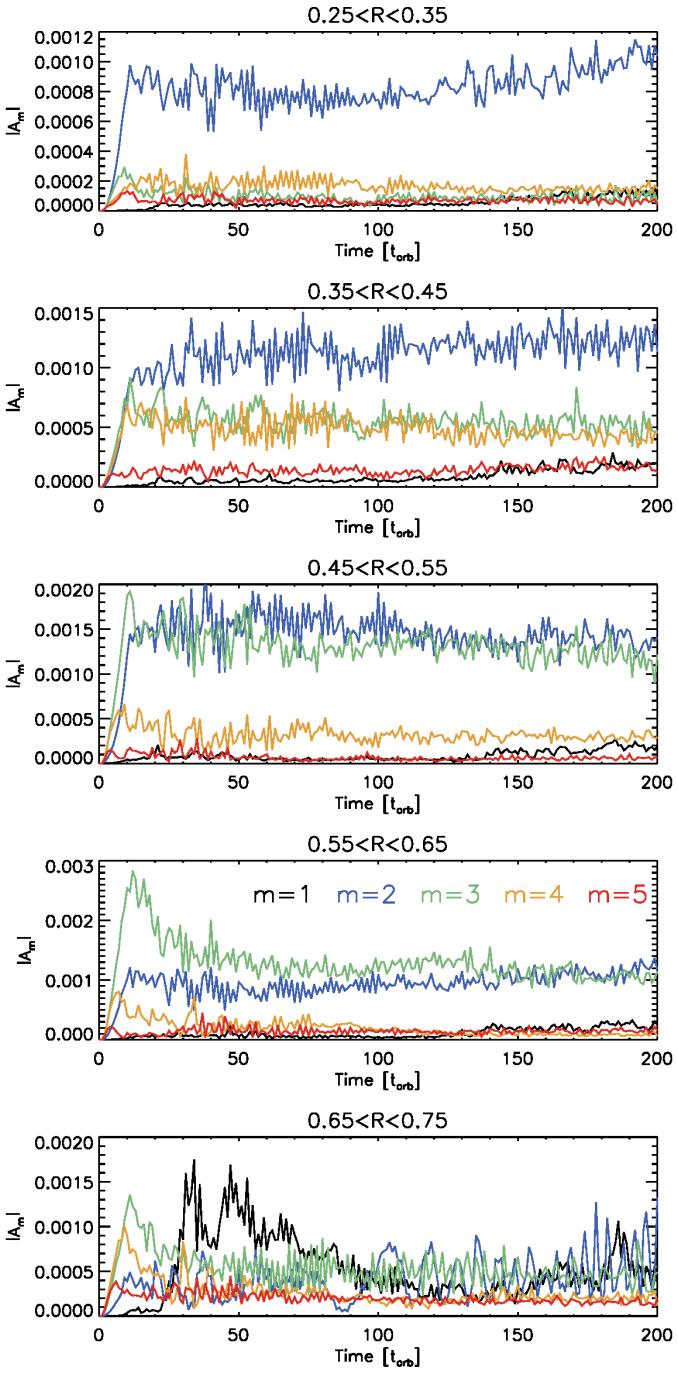

Figure 7.7. Time evolution of the Fourier amplitudes $|A_m|$ for various azimuthal modes ($m = 1 - 5$) in different radius bins. Note that the amplitudes remain nearly constant after $\sim 100\ t_{\rm orb}$.

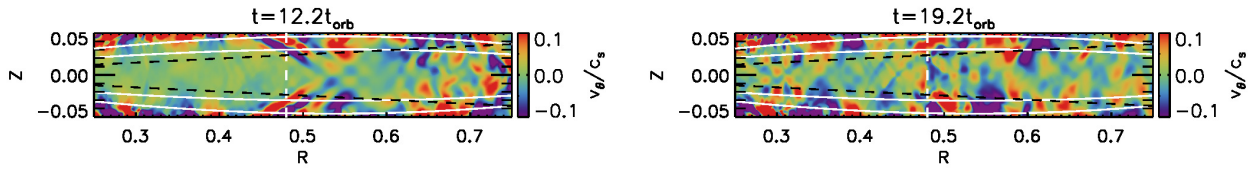

Figure 7.8. Two-dimensional distributions of the meridional velocity in a $R - Z$ plane at (left) $t = 12.2\ t_{\rm orb}$ and (right) $t = 19.2\ t_{\rm orb}$. The two sets of white curves indicate where the local Brunt-Väisälä frequency equals to one half of the Doppler-shifted wave frequency, for monochromatic $m = 2$ waves (the ones close to the midplane) and $m = 3$ waves (the ones close to the surface). The vertical dashed line indicates the radial location inward of which the SWI is forbidden for monochromatic $m = 3$ waves. The black dashed lines denotes where $Z = \pm 1H$. The two axes are drawn isotropically.

depth has increased by about a factor of two in between 100 $t_{\rm orb}$ and 200 $t_{\rm orb}$. Another important feature is that the strongest mode shifts toward smaller azimuthal wave numbers at smaller radii. The $m = 3$ mode has the largest Fourier amplitude at $0.55 < R < 0.65$, the $m = 2$ and $m = 3$ modes have a comparable amplitude at $0.45 < R < 0.55$, and the $m = 2$ dominates at $0.25 < R < 0.45$. For completeness, we note that there are no $m = 1$ spiral modes that propagate interior to the planet because formally the $m = 1$ ILR is not present in the disk. The appearance of a finite amplitude $m = 1$ Fourier component arises presumably because the disk generates an $m = 1$ perturbation due to the appearance of a low amplitude vortex, or because the disk becomes mildly eccentric.

7.5.2.2 Spiral Wave Instability

The SWI starts to grow from very early times even before the planetary mass is fully grown ($t \sim 4 - 5\ t_{\rm orb}$) at $R \gtrsim 0.5$, because the perturbation is strong enough there even with a sub-Jovian mass planet. The weak, wave-like inter-arm structures at $R \gtrsim 0.5$ and the break-up of the second arm at $R \sim 0.6 - 0.7$ seen in Figure 7.6, are some of the indications of the instability.

In Figure 7.8, we display the meridional velocity field in a vertical plane at $t = 12.2\ t_{\rm orb}$ and $t = 19.2\ t_{\rm orb}$. In the snapshot taken at $t = 12.2\ t_{\rm orb}$, one can see the checkerboard pattern suggesting that the SWI is growing there, although the individual unstable modes are not as clearly identifiable as in the monochromatic case due to the complex nature of planet-driven waves (i.e., superposition of various azimuthal modes). However, we note that

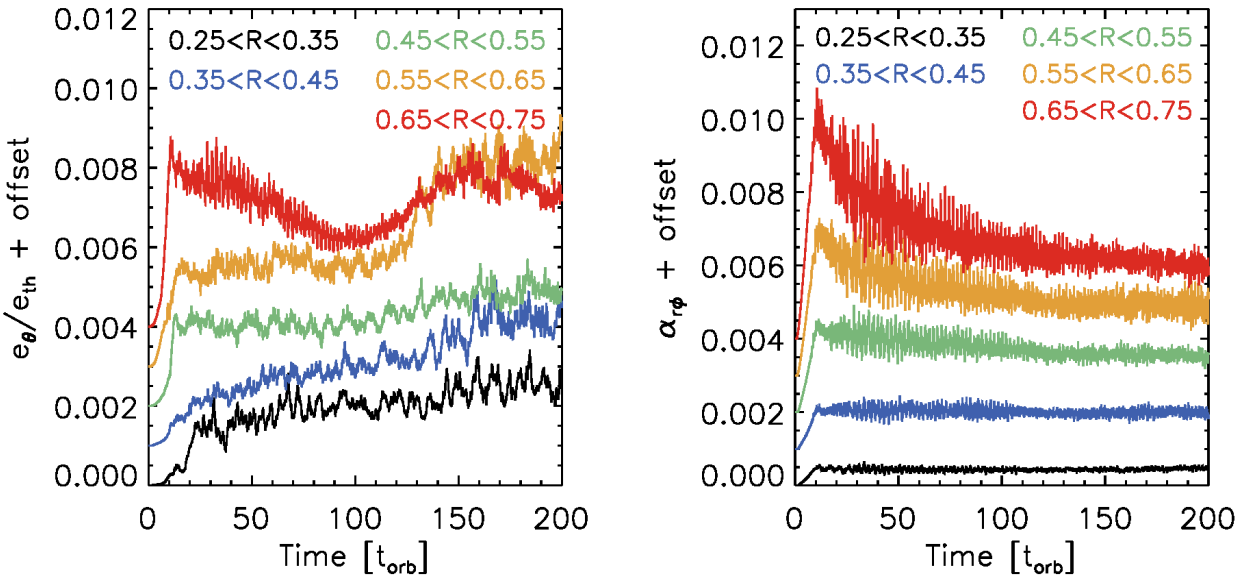

Figure 7.9. (Left) Time evolution of the meridional kinetic energy e_θ at various radius bins, normalized by $e_{\rm th}$ in each bin. (Right) Time evolution of the Reynolds Stress $\alpha_{r\phi}$ at various radius bins. In both panels, we add vertical offsets of 0.001, 0.002, 0.003, and 0.004 to the blue, green, yellow, and red curves for illustration purposes.

there is no signature of the SWI in $R \lesssim 0.5$ at this time epoch. This is probably because (1) the perturbation in the region is small compared with the $R \gtrsim 0.5$ region (Figure 7.6) and/or (2) the $m = 3$ component, with which the SWI is forbidden in this region, has a comparable power to the $m = 2$ mode during the early evolution (e.g., $0.35 < R < 0.45$ region in Figure 7.7) so the growth rate of the instability could be reduced. At $t = 19.2\ t_{\rm orb}$, checkerboard patterns appear in the inner disk region of $R \lesssim 0.5$. The steep increase in the meridional kinetic energy around $t = 20\ t_{\rm orb}$, particularly for the $0.25 < R < 0.35$ region, presented in Figure 7.9 supports the suggestion that the SWI is developing in the region.

As shown in Figure 7.9, the overall perturbed vertical kinetic energy and the stress associated with the combined action of the propagating spiral waves and the SWI (we have not sought to disentangle the contributions from these in this Chapter) reach quasi-steady state after $\sim 100\ t_{\rm orb}$. This adds further evidence that the strength of the SWI is probably not very sensitive to the gap depth after this point as the spiral wave amplitudes have reached steady values. We note that e_θ increases after $\sim 120\ t_{\rm orb}$ for $0.55 < R < 0.75$. However, we do not find any significant changes in the strength of spiral arms or background disk structures to explain this rise. One possible explanation is that some large-scale inertial modes, which

have to have smaller growth rates than small-scale modes (Fromang & Papaloizou, 2007), become unstable at this time, although we were not able to identify any corresponding individual mode growing as the disk has already developed strong vertical flows by this time, which we will discuss now.

In Figure 7.10, we present a three-dimensional global view of the meridional velocity and the density at the end of the simulation ($t = 200\ t_{\rm orb}$). As shown, the checkerboard meridional velocity patterns merge to create radially alternating vertical flows when the SWI saturates. Such vertical flows have been pointed out in the non-stratified, isothermal cylindrical models of Chapter 6, in which other sources capable of inducing vertical motion, such as the vertical shear instability that is known to cause the excitation of corrugation modes (Nelson et al., 2013), are absent. We thus believe that the alternating vertical flow is a generic outcome of the SWI. Visual inspection of the upper panel of figure 7.10 suggests the azimuthal structure of these modes is of low degree, corresponding to perhaps a mixture of $m = 0$ corrugation-type modes and/or $m = 1$ warp or tilt modes, which are inertial modes for which the vertical velocity perturbations have no nodes in the vertical direction. In the case of $m = 0$ corrugation modes, the whole disk column at a given radius, including the midplane, moves up and down in a coherent manner. For $m = 1$ tilt modes the disk acts as a series of narrow rings each of which tilts rigidly. As these disturbances arise in the form of waves, they propagate through the disk as corrugation or warping disturbances. The vertical length scale of the vertical flows is similar to the thickness of the disk region in which the SWI is permitted, suggesting that it is set by the wavelength of the largest unstable inertial modes that are allowed to grow. So these might be modes which are excited directly by the SWI, or they may be the result of nonlinear mode coupling which allows energy to seep into these modes from other modes that are excited by the SWI. Being coherent and quite large scale, once excited these corrugation/tilt modes become a prominent feature of the flow because they do not damp efficiently. We find that the associated vertical flows can have perturbed vertical velocities that are in the range $\sim 30 - 50\%$ of the local sound speed. One caveat, however, which we have already alluded to in Section 7.4.3 and which causes us to be cautious in interpreting our results, is that a resolution of ~ 18 cells per scale height in the vertical and radial directions does not allow for a turbulent cascade to develop efficiently.

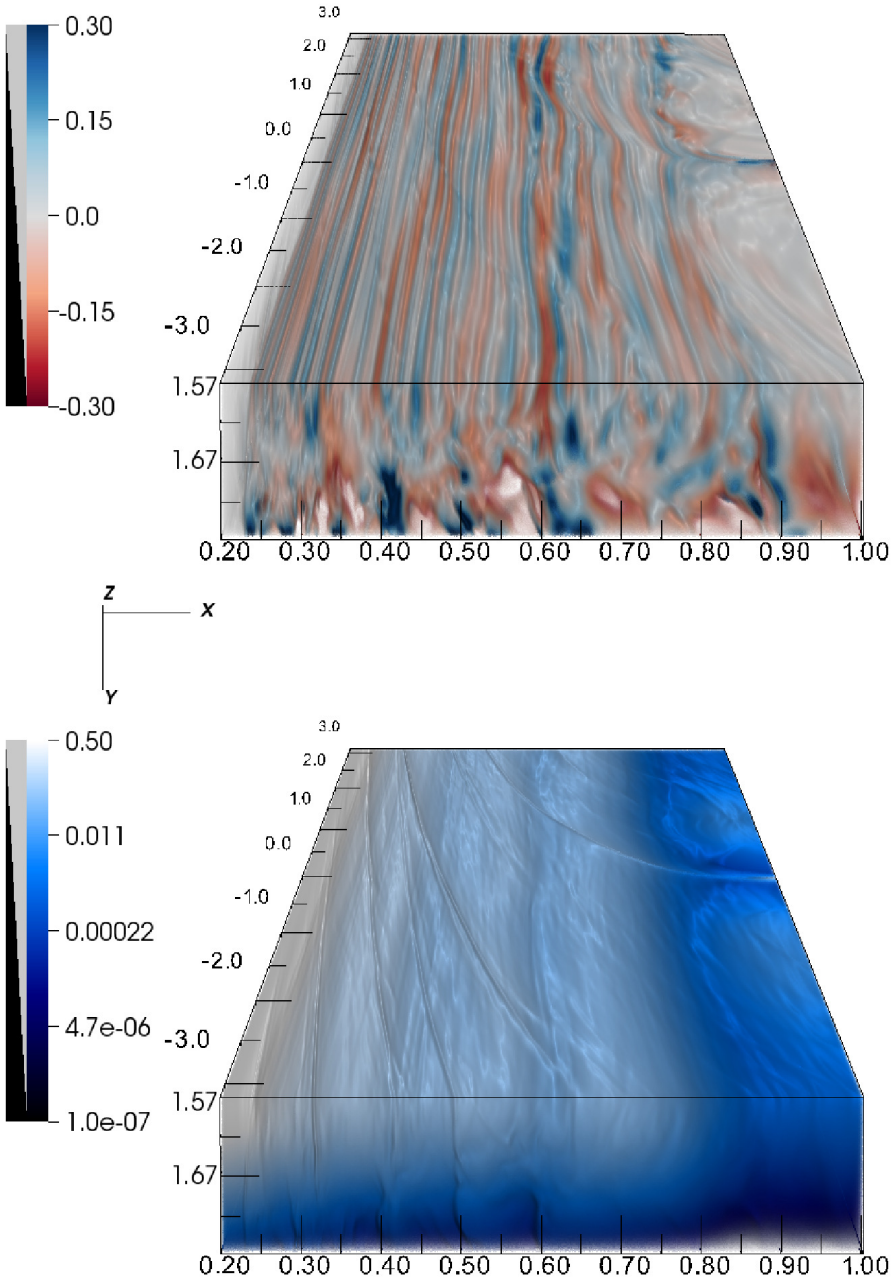

Figure 7.10. (Top) Three-dimensional global view of the meridional velocity field in the bottom half of the simulations domain: the upper surface shows the disk midplane. The quantity is plotted in units of the local sound speed: v_θ/c_s. r on the X-axis, θ on the Y-axis in units of radians, and ϕ on the Z-axis in units of radians. Note that the instability creates radially-alternating vertical flows when saturated. The vertical flows have a magnitude of order of a few tens of percent at the midplane. (Bottom) A volume-rendering view of the density in a logarithmic scale. The snapshots are taken at the end of the simulation ($t = 200\ t_{\rm orb}$). The planet is located at $(X, Y, Z) = (1.0, \pi/2, 0.0)$.

While some transfer of energy to small scales undoubtedly arises in our simulations, leading to dissipation on the grid scale, it may also be the case that the low resolution also favors the development of the SWI in such a manner that the large scale modes are more prominent than they would be in a more highly resolved simulation. Testing the outcome of the SWI as a function of resolution is a task that will be undertaken in the future when available computational resources allow such a study to be conducted.

7.6 Discussion

7.6.1 Particle Stirring Induced by the SWI

We measure the vertical diffusion coefficient to estimate the rate of vertical mixing of dust particles induced by the SWI. In order to do this, we restart the planet run described in Section 7.5.2 from $t = 200 t_{\rm orb}$, with outputs of the meridional velocity in three dimensions every 0.005 $t_{\rm orb}$. We calculate the vertical diffusion coefficient using the approximation $\mathcal{D}_Z = \langle v_Z^2 \rangle t_{\rm corr}$, where $t_{\rm corr}$ is the correlation time of the vertical velocity fluctuations, v_Z (Fromang & Papaloizou, 2006). In practice, we use the meridional velocity v_θ rather than v_Z. The quantity $\langle v_Z^2 \rangle$ represents the ensemble and time average of the mean velocities calculated at all grid cells at the cylindrical radii listed below. Using this definition for the diffusion coefficient implicitly assumes that the turbulence properties are uniform at all heights for each value of R.

In obtaining an estimate for $t_{\rm corr}$, we generate a time series for v_θ at various radii in the disk ($R = 0.3, 0.4, 0.5, 0.6$, and 0.7), within $|Z| < 1H$. We then compute the autocorrelations of the time series and fit the computed autocorrelations with a form of

$$S(t) = [(1 - a) + a \cos(2\pi\omega t)] e^{-t/t_{\rm corr}}, \tag{7.29}$$

following Nelson & Gressel (2010). Here, a indicates the relative strength of the sinusoidal feature in the autocorrelation function, ω is the frequency associated with the sinusoidal component, and $t_{\rm corr}$ is the correlation time. Figure 7.11 shows an example of the fit at $R = 0.6$. For this example, the correlation time is 0.46 $t_{\rm orb}$ or 0.99 Ω^{-1}. While it varies over

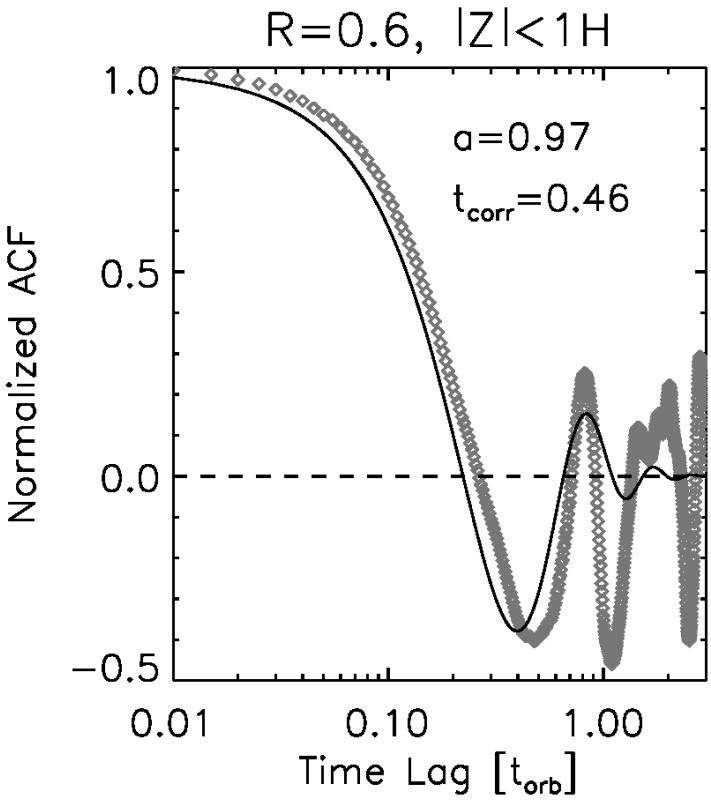

Figure 7.11. The normalized autocorrelation function (ACF) at $R = 0.6$ from the planet run with diamond symbols, and the fit obtained with Equation (7.29) with solid curves.

radius, note that the correlation time is of order of Ω^{-1}, which is longer than the ones obtained for MHD turbulence in protoplanetary disk simulations ($\sim 0.1\Omega^{-1}$; Fromang & Papaloizou, 2006; Yang et al., 2009; Nelson & Gressel, 2010). We suspect that this longer correlation time, combined with the prominent oscillatory component displayed by the autocorrelation function, may arise because of the contribution of the coherent radially-alternating flows that arise in the simulations as described above, such that the resulting flow is a mixture of coherent vertical motion and smaller scale turbulence. The correlation time obtained for various radii is listed in Table 7.1.

With the vertical velocity fluctuation that is $5-11$ % of the local sound speed, the vertical diffusion coefficient is $(0.4-2.3)\times10^{-4}$ in natural units between $R = 0.3$ and $R = 0.7$. Then, the vertical mixing time $t_{\rm mix}$ can be estimated as

$$t_{\rm mix} = H^2/\mathcal{D}_Z. \tag{7.30}$$

Table 7.1. Planet Run Results

R	$\langle v_\theta^2 \rangle$	$\langle v_\theta^2 \rangle^{1/2}/\langle c_s \rangle$	$t_{\rm corr}$ ($t_{\rm orb}$)	$t_{\rm corr}$ (Ω^{-1})	$\mathcal{D}_Z$	$\alpha_{\rm diff}$	$t_{\rm mix}$ ($t_{\rm orb}$)	$\langle \rho_g \rangle$ (g cm^{-3})	$(9/4)\lambda$ (cm)	$s_{\rm mix}$ (cm)
0.3	3.08×10^{-5}	0.050	0.43	2.62	8.32×10^{-5}	0.0065	0.62	8.05×10^{-10}	2.49	4.63
0.4	3.15×10^{-5}	0.059	0.55	2.17	1.09×10^{-4}	0.0075	0.90	4.32×10^{-10}	4.64	3.20
0.5	2.26×10^{-5}	0.055	0.51	1.44	7.24×10^{-5}	0.0043	2.06	3.36×10^{-10}	5.96	1.75
0.6	8.08×10^{-5}	0.112	0.46	0.99	2.34×10^{-4}	0.0124	0.95	2.16×10^{-10}	9.28	3.99
0.7	1.67×10^{-5}	0.054	0.41	0.70	4.30×10^{-5}	0.0020	7.34	2.30×10^{-10}	8.71	0.82

[a]For the quantities in the brackets $\langle\ \rangle$, we average them over azimuth within $|Z| < 1H$.

Using the α prescription

$$\alpha_{\rm diff} = \mathcal{D}_Z/(c_s H), \tag{7.31}$$

the vertical diffusion rate is characterized by values of $\alpha_{\rm diff}$ in the range $\alpha_{\rm diff} = (0.2 - 1.2) \times 10^{-2}$, which is comparable to or greater than the Reynolds stress measured at these radii (see Figure 7.9).

Since we are interested in the maximum size of particle that can be vertically mixed by the SWI-induced turbulence, we calculate the settling time of particles and compare it with the vertical diffusion time. The settling time can be obtained from the terminal velocity by equating the drag force and the vertical component of the stellar gravity. The drag force depends on the size of the particle s, relative to the mean free path of the gas $\lambda \equiv \mu m_{\rm H}/\rho_g \sigma$, where $\mu = 2.4$ is the mean molecular weight of gas, $m_{\rm H}$ is the mass of a Hydrogen atom, ρ_g is the gas mass density, and $\sigma = 2 \times 10^{-15}$ cm^2 (Chapman & Cowling, 1970) is the molecular collisional cross section. When $s \leq (9/4)\lambda$, the Epstein law is applicable and the drag force F_D can be written as

$$F_D = \frac{4}{3}\pi s^2 \rho_g v_g v_{\rm th}, \tag{7.32}$$

where v_g is the gas velocity and $v_{\rm th} = \sqrt{8/\pi} c_s$ is the thermal velocity of gas molecules. When $s \geq (9/4)\lambda$, we can apply the Stokes law and the drag force F_D can be written as

$$F_D = \frac{1}{2}\pi s^2 \rho_g v_g^2 C_D, \tag{7.33}$$

where C_D is the drag coefficient. We use $C_D = 24 Re^{-1}$ (Probstein & Fassio , 1969; Whipple,

1972), since the Reynolds number Re is measured to be always smaller than unity in the region and for the particle sizes of interest. Here, $Re \equiv 2s\rho_g v_g/\eta$ and $\eta \equiv (1/2)\rho_g v_{\rm th}\lambda$ is the gas molecular viscosity.

By setting $F_D = m_s\Omega_K^2 z$, where $m_s = (4/3)\pi s^3\rho_s$ is the mass of a solid particle and $\rho_s = 3$ g cm^{-3} is the internal density of the dust particles, one can obtain the settling time $t_{\rm settle} = z/v_g$. For the Epstein regime, this gives

$$t_{\rm settle} = \frac{1}{s}\frac{\rho_g}{\rho_s}\frac{v_{\rm th}}{\Omega_K^2}, \tag{7.34}$$

whereas for the Stokes regime,

$$t_{\rm settle} = \frac{9}{4}\frac{\lambda}{s^2}\frac{\rho_g}{\rho_s}\frac{v_{\rm th}}{\Omega_K^2}. \tag{7.35}$$

It is immediately obvious from Equations (7.34) and (7.35) that the equations result in the same settling time when $s = (9/4)\lambda$. Also, note that Equations (7.34) can be written as $t_{\rm settle} = 1/(t_{\rm s}\Omega_K^2)$, or $t_{\rm settle}/t_{\rm dyn} = 1/(2\pi t_{\rm s}\Omega_K)$, where the stopping time $t_{\rm s}$ for the Epstein regime is defined by $t_{\rm s} = (\rho_s s)/(\rho_g v_{\rm th})$ (Weidenschilling, 1977) and $t_{\rm dyn} = 2\pi/\Omega_K$.

Then, the maximum particle size $s_{\rm mix}$ that is significantly mixed by the turbulence (i.e., $t_{\rm mix} \sim t_{\rm settle}$) can be computed by setting Equation (7.30) to either Equation (7.34) or (7.35). This leads to

$$s_{\rm mix} = \begin{cases} \sqrt{\dfrac{8}{\pi}}\dfrac{\rho_g}{\rho_s}\dfrac{\mathcal{D}_Z}{c_s H}H & \text{for the Epstein regime,} \\ \left(\dfrac{9}{4}\sqrt{\dfrac{8}{\pi}}\dfrac{\rho_g}{\rho_s}\dfrac{\mathcal{D}_Z}{c_s H}H\lambda\right)^{1/2} & \text{for the Stokes regime.} \end{cases} \tag{7.36}$$

As seen in Table 7.1, in the interval $0.3 \leq R \leq 0.7$, we find that solid particles $s \sim 0.8{-}4.6$ cm in size can be vertically mixed within the first pressure scale height.

We note that the diffusion coefficient $\mathcal{D}_Z$ obtained from our simulation is for gas molecules. For solid particles that are not perfectly coupled to gas, the diffusion coefficient is $\mathcal{D}_{Z,s} \simeq \mathcal{D}_Z/(1{+}St^2)$ (Youdin & Lithwick, 2007), where St is the Stokes number. In the disk assumed here, however, centimeter-sized particles have $St \ll 1$ within the first scale height throughout the entire inner disk so $\mathcal{D}_{Z,s} \simeq \mathcal{D}_Z$. The correlation time, vertical diffusion coefficient, the

mixing time, and the maximum particle size that can be vertically mixed by the turbulence obtained for the planet run are summarized in Table 7.1.

The above calculations relating to particle mixing assume that the SWI generates homogeneous hydrodynamic turbulence at each radius considered, but as discussed already the simulations also show strong evidence for there being coherent large scale vertical motions that might also contribute to lofting particles away from the midplane. Particles can only be advected within the coherent vertical flows if the vertical drag force that they feel due to the moving gas exceeds the vertical force of gravity. The maximum particle size for which this is true can be estimated by equating these forces – $F_D = m_s \Omega_K^2 z$ –, assuming that the vertical gas velocity is equal to its characteristic value measured in the simulations, which is $\sim 10\%$ of the local sound speed. Evaluating this at $R = 0.6$, corresponding to 3 au in physical units, we obtain a maximum particle size of $s_{\max} \sim 1$ cm that can be lofted, consistent with the value obtained from the calculations above within a factor of few.

7.6.2 Implications for the Growth of Large Asteroids and Terrestrial Planet Embryos

Through a combination of the streaming instability producing planetesimals with sizes up to $\sim$ few $\times$100 km (Youdin & Goodman, 2005; Johansen et al., 2007, 2015) and subsequent pebble accretion onto the larger planetesimals (Johansen & Lacerda, 2010; Ormel & Klahr, 2010; Lambrechts & Johansen, 2012; Morbidelli & Nesvorny, 2012), it seems plausible that, at 5 au in a proto-solar nebula-like gaseous disk, planetesimals can grow to become 10 Earth-mass ($M_\oplus$) solid cores within about one million years (Bitsch et al., 2015; Levison et al., 2015a; Morbidelli et al., 2015). This presumably allows sufficient time for such cores to accrete a substantial amount of gas to eventually form gas giants, assuming that another million or so years is required for completion of the gas accretion phase (e.g., Pollack et al., 1996; Movshovitz et al., 2010), and that protoplanetary disks around T Tauri stars dissipate in a few million years (Haisch et al., 2001; Hernández et al., 2007; Mamajek, 2009). While the details of how gas giant planets accrete their gaseous envelopes remain uncertain, it is clear that they must form before protoplanetary disks lose a significant fraction of their gas content (but see Tanigawa & Tanaka 2016).

In the Solar System, Jupiter is generally thought to have been the first planet that finished accretion. By the time Jupiter has formed, it is commonly assumed that terrestrial bodies have grown to become Moon or Mars mass embryos (see review by Dauphas & Chaussidon 2011 and Morbidelli et al. 2012 and references therein). Planetary embryos then complete their growth during the gas-free debris phase through collisions with planetesimals and/or other embryos, which takes several tens to hundreds million years after gas has removed.

More recently, models of the growth of terrestrial planet embryos and large asteroids through the accretion of pebbles and/or chondrules that are continuously generated over multi-Myr time scales have been presented (Johansen et al., 2015; Levison et al., 2015a). In the work of Johansen et al. (2015) it was shown that the formation of planetesimals via high resolution streaming instability simulations leads to the formation of bodies with sizes up to $\sim$ 100 km, and that subsequent chondrule accretion onto these bodies over time scales of $\sim$ 3 Myr is needed to explain the presence of large asteroids such as Ceres and Vesta in the asteroid belt. Similarly, a model of planetary embryo growth that involves only the collisional accretion of planetesimals formed by the streaming instability was shown to be unable to form Mars-size embryos within the required time frame, and that the addition to the model of chondrule accretion over Myr time scales led to a dramatic increase in the efficacy of embryo formation. Levison et al. (2015a) have presented a model in which embryos in the terrestrial planet region grow through pebble accretion over Myr time scales, with the pebbles being continuously generated during this time period, and show that such a model is able to explain certain features of the terrestrial planet system. The model introduces the outer solar system planets at the end of the embryo formation epoch, and subsequent evolution through giant impacts leads to final planetary systems that appear to be a good fit to the basic structure of the inner solar system, including a small mass for Mars.

The results of our present work suggest that a Jupiter-mass planet forming within the first few Myr in a protoplanetary disk can produce turbulence and vertical stirring of solid particles interior to its orbit. The influence seems to be quite significant, such that solid particles with sizes up to several centimeters can be vertically well mixed. While pebble/chondrule accretion takes advantage of the large accretion cross section produced by aerodynamic drag, which can be orders of magnitude larger than the geometric cross section of the target plan-

etesimals, for solid particles having a scale height (H_p) that is larger than the size of the planetesimal Hill radius (r_H) the accretion rate will be reduced by a factor of r_H/H_p (Lambrechts & Johansen, 2012). For example, assuming the planetesimal mass of 10^{24} g with which $r_H/R \sim 5.5 \times 10^{-4}$, the accretion rate for particles that have same scale height as the gas ($H/R = H_p/R = 0.05$) will therefore drop by a factor of ~ 90. This probably results in too long a timescale to form planetary embryos and large asteroids through pebble accretion within the typical lifetime of protoplanetary disks. While this argument considers the decrease in the number density of pebbles near the midplane only, the larger relative velocity between pebbles and planetesimals as well as the non-zero orbital inclination and eccentricity of planetesimals that might arise in the SWI-driven turbulence can make the situation even worse. Thus, *if* pebble accretion is the dominant process by which terrestrial planet embryos and large asteroids gain their mass, the requirement for efficient pebble accretion may put a time and/or space constraint on giant planet formation: planetary embryos have to form before a gas giant forms in the outer disk, otherwise the strong stirring induced by the SWI will significantly drop the chondrule/pebble accretion efficiency. It is interesting to note that isotope measurements of Martian meteorites indicate that Mars, as a stranded planetary embryo (e.g., Chambers & Wetherill, 1998), grew rapidly within about 2 Myr after the birth of the solar system (Dauphas & Pourmand, 2011), and then halted accretion. It is interesting to speculate that the formation of Jupiter at or close to its current location may have occurred at around this time, making pebble accretion onto Mars inefficient and effectively halting its growth and that of the large asteroids.

With our initial density profile the disk is optically thick in the midplane. The main body of the disk therefore behaves fully adiabatically, confining the SWI towards the midplane. As the disk evolves the optical depth of the disk will decrease by accretion of material and/or particle growth and settling, and therefore the disk will behave more isothermally. This will allow the SWI to operate in broader disk regions in height and possibly strengthen the spiral arms with less resistance from gas pressure, although the turbulence level and the significance of vertical mixing have to be further examined with relevant disk models. If the level of turbulence via the SWI remains relatively constant, regardless of the thermal properties of the disk, or decreases over time, this implies that $s_{\rm mix}$ will decrease as the disk

loses its mass over time (see Equation 7.36). In this case, it is possible that planetesimals and/or planetary embryos resume accreting pebbles during the later evolution as far as the disk still has some pebbles that survived rapid migration. On the other hand, when the disk becomes optically thin the vertical shear instability and/or the MRI could operate down to the midplane and provide some turbulence that may limit pebble accretion efficiency.

If a giant planet migrates over a significant distance to reach its final position, as in the "Grand Tack" model proposed for the early Solar System (e.g., Walsh et al., 2011), the SWI could have a significant effect over a broader range of disk radii than otherwise, because the growth timescale of the instability is orders of magnitude shorter than the migration time scale.

It might be possible that gas giants form as early as during the time when their host disks still gain mass from their natal clouds, as recent observation of HL Tau may suggest (ALMA Partnership et al., 2015). Whether or not such an early giant planet formation is common is still an open question. If giant planets form at such an early time, the disk may be left with a very narrow window in time to grow terrestrial bodies in the disk if pebble accretion is the dominant mechanism.

7.6.3 Dependence of SWI on Planetary Mass

We have focused on the SWI arising from the spiral waves excited by a giant planet in the inner regions of a protoplanetary disk in this Chapter. One may wonder if there is a mass requirement for triggering the SWI, and how the strength of the SWI varies with planet mass.

First, given that the instability involves energy from the spiral waves being transferred into inertial modes, it is clear that stronger spiral waves will generate higher amplitudes for unstable inertial modes. In the nonlinear saturated state, we therefore expect that the resulting hydrodynamic turbulence will be more vigorous for larger mass planets.

Second, our general picture of how the instability operates is that a protoplanetary disk hosts the full spectrum of inertial modes that are present at low amplitude. When a source of spiral waves (e.g., a planet) is present, it excites waves with a range of azimuthal mode numbers and Doppler-shifted frequencies. Then, the inertial modes that are resonant with

spiral waves with specific azimuthal mode numbers are able to grow due to the periodic forcing. In the case of a giant, gap forming planet, we have shown that the dominant spiral modes that propagate in the inner disk are the $m = 2$ and $m = 3$ modes, presumably because these are excited at ILRs that lie outside of the low density gap region. As the planet mass is lowered, however, the gap depth reduces and we expect that higher values of m will become prominent, with the amplitudes of waves associated with lower m values decreasing in proportion to the planet mass. The increasing prominence of the higher m spiral modes may then allow the SWI to operate in regions closer to the planet because, at the midplane, the SWI operates in the radial intervals $((m-2)/m)^{2/3}R_p \leq R \leq ((m-1)/m)^{2/3}R_p$ in the inner disk and in $((m+1)/m)^{2/3}R_p \leq R \leq ((m+2)/m)^{2/3}R_p$ in the outer disk. Again, these conditions come from the fact that, as the value of m increases, the synodic period between orbiting fluid elements and the planet needs to increase to match the resonance condition with inertial modes in the disk.

Based on the two points discussed above, we expect that (1) the strength of SWI-driven turbulence will be weaker for lower mass planets; and (2) the region where the instability operates will be narrower and closer to the planet, as the planet mass decreases to the point that the $m = 2$ mode is no longer strong enough to induce the SWI in the inner disk.

In order to support these two points, we have run additional simulations with planetary masses of $q \equiv M_p/M_* = 10^{-3}, 5 \times 10^{-4}, 3 \times 10^{-4}, 10^{-4}, 10^{-5}$. For these runs, we were forced to use a numerical resolution of $(N_r, N_\theta, N_\phi) = (364, 72, 378)$ because of the computational cost. This is a factor of two lower than our reference model and so thus the growth of the SWI is not properly captured, although we can measure spiral wave amplitudes.

The Fourier amplitudes for different planetary masses are plotted in Figure 7.12 as a function of azimuthal mode number. At both $0.55 < R < 0.65$ and $0.25 < R < 0.35$, the Fourier amplitudes are larger for more massive planets in general. It is therefore reasonable to expect that more massive planets will produce larger energy injection rates into the inertial modes, and accordingly stronger turbulence through the SWI. We see that the maximum amplitude shifts towards lower degree azimuthal modes as q increases, presumably due to non-linear mode coupling (e.g., Lee, 2016) and gap formation which suppresses the amplitudes of the high-m modes that are excited close to the planet. This trend is particularly apparent for

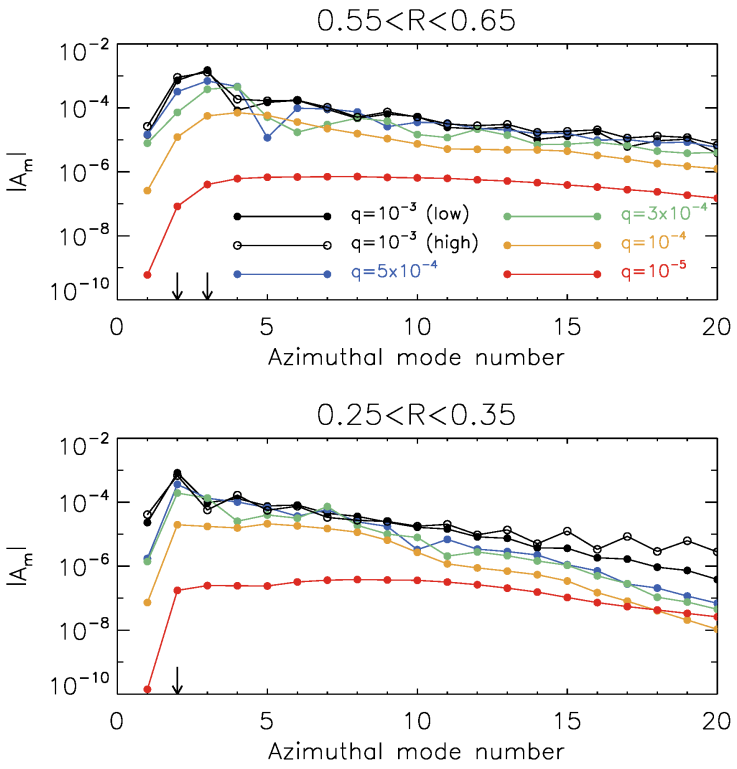

Figure 7.12. The Fourier amplitude $|A_m|$ for various azimuthal modes at (upper) $0.55 < R < 0.65$ and (lower) $0.25 < R < 0.35$, taken at $t = 100\ t_{\rm orb}$ for different planetary masses $q = M_p/M_*$ of (black) 10^{-3}, (blue) 5×10^{-4}, (green) 3×10^{-4}, (yellow) 10^{-4}, and (red) 10^{-5}. Black open circles are for our reference model with the high numerical resolution of $(N_r, N_\theta, N_\phi) = (726, 144, 754)$, whereas all the other models run with low resolution of $(N_r, N_\theta, N_\phi) = (364, 72, 378)$. The arrows indicate the azimuthal mode numbers with which perturbing waves are capable of exciting the SWI at each radius bin.

$q \geq 3 \times 10^{-4}$. As the SWI is expected to operate for $m = 2$ and $m = 3$ perturbations at radii $0.55 < R < 0.65$ (it can also be excited by the $m = 4$ mode between $0.63 \leq R/R_p \leq 0.65$, but this is only just contained in the radial range under consideration), and for $m = 2$ modes only at radii $0.25 < R < 0.35$, we expect that the SWI operates more strongly with larger planetary masses that have most power in $m = 2$ or $m = 3$ in these regions ($q \geq 3 \times 10^{-4}$). When $q = 10^{-5}$, the Fourier amplitudes are relatively flat for $m \simeq 3 - 10$. If the SWI can operate for such a low mass planet, then we might expect that the strength of the outcome will be much weaker than for larger mass planets, and that the regions unstable to the instability will be limited to a narrow radial region around the planetary orbit because of the weakness of the $m = 2$ spiral wave. Global disk calculations performed at high resolution

will be required to confirm or refute these conjectures, and to fully characterize how the SWI operates as a function of planet mass.

7.6.4 Caveats and Future Work

As seen in Figure 7.11, the ACF of the vertical velocity does not converge but oscillates around zero with finite amplitude. This is because the vertical flows developing from the SWI not only contain repeated growth and decay of vertical motions, but also display sustained and coherent oscillations, likely due to the excitation of longer wavelength inertial waves. Due to this apparently complex superposition of turbulence and coherent oscillations, the analysis presented in Section 7.6.1 has to be viewed with some caution by keeping in mind the uncertainty in estimating the correlation time. Nonetheless, a factor of a few uncertainty in the correlation time would not change our conclusions about particle stirring in a qualitative sense.

At this point, it is probably worthwhile pointing out that some previous simulation studies, in which grains and pebbles are implemented as Lagrangian particles, indicate evidence of vertical mixing of solid particles through the SWI. As a potential example, we note that in Figure 13 of Zhu et al. (2014), where the authors placed a 0.65 Jupiter-mass planet around a solar-mass star, particles a and b – that are about a millimeter and a centimeter in size, respectively, when the MMSN disk model and the semi-major axis of 5 au are assumed – are vertically dispersed in the outer disk ($R > 1$ in the figure). In particular, the particle distributions show some wiggling morphology near the midplane, which is tempting to explain with the radially alternating vertical flows arising from the SWI. The vertical dispersal of particles is not seen in the inner disk and we speculate that this is because of the insufficient numerical resolution to properly capture the unstable inertial modes there. They used uniform radial grid cells, with which one scale height is resolved with only about 5 grid cells in both radial and vertical directions at $R = 0.7$, as opposed to with about 15 grid cells at $R = 1.5$.

In the future, more quantitative conclusions will be able to be made from high resolution gas and particle simulations, where one can obtain the vertical distribution of solid particles stirred by the SWI, both interior and exterior to the planet. Furthermore, some of the

questions that we have discussed in this Chapter such as the outcome of the SWI as a function of planet mass, and the influence that this has on pebble accretion, can also be addressed in the context of improved disk models that contain a more sophisticated model of disk thermodynamics. And finally, hydrodynamic simulations combined with radiative transfer calculations can be used to determine the observational appearance of disks with planets, and to determine what influence the SWI has on images formed through scattered light and thermal emission.

7.7 Conclusion

We have presented inviscid three-dimensional global hydrodynamic simulations of protoplanetary disks in which we excite spiral waves either monochromatically using an imposed external potential or using a full planetary potential. Using monochromatic waves, we first show that the region of the SWI operating and the properties of the unstable inertial modes show very good agreement with the predictions made by matching resonance criteria using simple dispersion relations for spiral and inertial waves. When a Jupiter-mass planet is added in the disk, the spiral waves it launches have various azimuthal components superimposed on the dominant $m = 2$ or $m = 3$ modes, depending on the radial position in the disk, and the SWI is found to grow on the order of the planet orbital time. When it is saturated, the SWI generates turbulence and radially alternating vertical flows that have characteristic radial and vertical length scales of about one local pressure scale height and vertical velocities of order of few tens percent of the local sound speed. Using the alpha prescription, the associated vertical diffusion rate of gas is estimated to be characterized by $\alpha_{\rm diff} \sim (0.2-1.2)\times 10^{-2}$ in the range of radii $0.3R_p \leq R \leq 0.7R_p$, where R_p is the semi-major axis of the planet. At this rate, solid particles up to a few centimeters in size can be vertically mixed within the first pressure scale height. Since protoplanetary disks are believed to remain laminar, and thus induce no or very little particle stirring, as suggested by recent magnetized wind models (Bai & Stone, 2013b; Gressel et al., 2015), the SWI can be the mechanism controlling the degree of vertical settling of solid particles in the optically-thick regions of planet-hosting disks where other hydrodynamic instabilities are not thought to operate.

While more quantitative results will be obtained with future high resolution simulations that include particles, we conjecture that significant stirring of solid particles through the instability of the spiral waves excited by giant planets can have an influence on the formation and growth of large asteroids and terrestrial planet embryos in the inner disk, if these bodies are actively growing in the presence of a giant planet (such as Jupiter in the protosolar nebula). In particular, if growth of these bodies proceeds mainly through the accretion of chondrules/pebbles, then they have to form before a gas giant forms in the outer disk as the stirring of solid particles is likely to significantly decrease the chondrule/pebble accretion efficiency. Since the properties of the turbulence driven by the SWI are dependent upon the background thermal structure of the disk as well as the planetary mass, future studies that survey parameter space at high numerical resolution are needed to further examine the significance of the instability for protoplanetary disk evolution and for planet formation.

7.8 Acknowledgments

The authors thank the anonymous referee for a prompt report and helpful comments that improved the initial manuscript. J.B. thanks Edwin Bergin, Jeffrey Fung, Wing-Kit Lee, and Zhaohuan Zhu for helpful conversations. This research was supported in part through computational resources and services provided by Advanced Research Computing at the University of Michigan, Ann Arbor. This work used the Extreme Science and Engineering Discovery Environment (XSEDE), which is supported by National Science Foundation grant number ACI-1053575. The authors acknowledge the San Diego Supercomputer Center at University of California, San Diego for providing HPC resources that have contributed to the research results reported within this Chapter.

CHAPTER VIII

Long-term Evolution of Photoevaporating Protoplanetary Disks

8.1 Abstract

We perform calculations of our one-dimensional, two-zone disk model to study the long-term evolution of the circumstellar disk. In particular, we adopt published photoevaporation prescriptions and examine whether the photoevaporative loss alone, coupled with a range of initial angular momenta of the protostellar cloud, can explain the observed decline of the frequency of optically-thick dusty disks with increasing age. In the parameter space we explore, disks have accreting and/or non-accreting transitional phases lasting of $\lesssim 20$ % of their lifetime, which is in reasonable agreement with observed statistics. Assuming that photoevaporation controls disk clearing, we find that initial angular momentum distribution of clouds needs to be weighted in favor of slowly rotating protostellar cloud cores. Again, assuming inner disk dispersal by photoevaporation, we conjecture that this skewed angular momentum distribution is a result of fragmentation into binary or multiple stellar systems in rapidly-rotating cores. Accreting and non-accreting transitional disks show different evolutionary paths on the $\dot{M} - R_{\rm wall}$ plane, which possibly explains the different observed properties between the two populations. However, we further find that scaling the photoevaporation rates downward by a factor of 10 makes it difficult to clear the disks on the observed timescales, showing that the precise value of the photoevaporative loss is crucial to setting the clearing times. While our results apply only to pure photoevaporative loss (plus disk accretion), there may be implications for models in which planets clear disks preferentially at radii of order 10 AU. This chapter has been published in the Astrophysical Journal, Volume 774, 57 (2013), in collaboration with Lee Hartmann, Zhaohuan Zhu, and

Charles Gammie.

8.2 Introduction

Studies over the last 20 years have shown that optically-thick dusty disks around young stars have a significant range in their lifetimes, with a median value of ~ 3 Myr (Haisch et al., 2001; Hernández et al., 2007; Mamajek, 2009). While the dust emission of these disks may effectively disappear via accretion onto the central star or coagulation into larger bodies including planetesimals and planets, it is difficult to remove disk gas and dust on radial scales larger than a few tens of AU via accretion on short enough timescales (Hollenbach et al., 2000) and there are challenges even forming gap-producing giant planets at a few AU on these lifetimes (see Lissauer & Stevenson, 2007, and references therein).

The currently most popular mechanism for removing outer disk material is photoevaporation by stellar high-energy radiation - either ultraviolet or X-rays, or both - from the central star (Clarke et al., 2001; Alexander et al., 2006; Ercolano et al., 2009; Gorti & Hollenbach, 2009; Gorti et al., 2009; Owen et al., 2010, 2011, 2012).[1] Photoevaporative loss can also produce gaps and inner holes in disks, potentially explaining disks with large optically-thin holes inside of optically thick outer regions - the so-called transitional disks (Calvet et al., 2005) - as well as pre-transitional disks with large gaps but with optically-thick dust in the innermost regions (Espaillat et al., 2007). Alternatively, giant planets can clear disk gaps (Dodson-Robinson & Salyk, 2011), though there may be difficulties in clearing large enough disk regions (Zhu et al., 2011), and Type II migration may also be a problem (Clarke & Owen, 2013).

Observationally, (pre-)transitional disks are usually identified via either detailed modeling of the spectral energy distributions (SEDs) (e.g., Calvet et al., 2002, 2005; Espaillat et al., 2007, 2008; Kim et al., 2013) or high-resolution imaging (e.g., Hughes et al., 2007, 2009; Andrews et al., 2009, 2010, 2011). The gaps and inner holes in (pre-)transitional disks are optically thin but may not be completely evacuated of dust and gas (e.g., Rosenfeld et al., 2012; Kraus et al., 2013), especially as many of these objects exhibit gas accretion onto

[1] We exclude photoevaporation in clusters by massive stars; see e.g. Hollenbach et al. (2000).

the central star (e.g., Calvet et al., 2002, 2005). Dust growth and/or filtration is probably required to explain many of the observations (Dullemond & Dominik, 2005; Rice et al., 2006; Zhu et al., 2012b). It should be emphasized that both SED modeling and current submillimeter interferometric imaging are not able to identify very small disk gaps and inner holes.

As mentioned above, optically-thick pre-main sequence disks exhibit a variety of lifetimes, with the frequency of such disks steadily declining from ages ~ 1 Myr to ~ 10 Myr. Alexander & Armitage (2009) could reproduce the observed disk frequencies by including migrating, gap-opening planets with a range of initial masses at 5 AU while varying the initial disk masses. Owen et al. (2011) were also able to explain the variation of disk lifetimes by assuming that similar stars have very different X-ray fluxes, as seen in observations of, for example, the deep X-ray observations of the Orion Nebula Cluster (Preibisch et al., 2005). However, it is known that X-ray emission from very young low-mass stars is highly time-variable on timescales of days or less due to flares (Montmerle et al., 1983; Feigelson et al., 2002a; Caramazza et al., 2007), as well as on timescales of years, the mechanisms for which are uncertain (Feigelson et al., 2002b, 2003). The level of variability of X-ray emission over relevant timescales for disk evolution of 10^4 to 10^6 yr are of course unknown, but is arguably smaller than the spread observed at a given epoch.

An alternative hypothesis, which we explore here, is that disk lifetimes mostly depend upon the initial angular momentum of the protostellar cloud. As we show, more rapid rotation leads to larger disks which take longer to deplete. Even if X-ray luminosity for individual stars exhibits a wide dispersion over long timescales, substantial differences in initial angular momenta are to be expected and their effects should not be ignored. In addition, much of the previous work on disk photoevaporation has been performed under the assumption of fully-viscous disks; this is questionable for low-temperature protostellar/protoplanetary disks, where ionization states can be far too low for the magnetorotational instability (MRI) to operate - the only mechanism so far known to act in a manner similar to viscous transport (e.g., Balbus & Hawley, 1998, and references therein). The presence of "dead zones" (Gammie, 1996), i.e. regions in which angular momentum transport is very limited or does not occur, can strongly affect disk structure, and by inference the manner in which photoe-

vaporative mass loss changes that structure.

In this Chapter we further develop the two-zone disk model of Zhu et al. (2010a,b), modified as in Chapter 2 to allow for non-zero dead zone residual viscosity, by adding a prescription for photoevaporation taken from the calculations of Owen et al. (2012). We follow the disk evolution from the time of formation during the protostellar phase and analyze the subsequent disk structure during the later, T Tauri phase. As the actual amount of photoevaporative flux (or equivalently, the mass-loss rate it drives) is uncertain, we adopt the fiducial value of Owen et al. (2012) and test 30 and 10 % of that rate. We explore the distribution of initial angular momenta that would be required to explain disk frequencies, and we compare on the predictions of the photoevaporation + accretion model with observations. We find that the lower photoevaporation rate is insufficient to explain the observations, but the fiducial level is adequate, coupled with a frequency distribution of initial cloud angular momenta that is strongly skewed toward low values. We suggest that this skewed distribution is not necessarily representative of protostellar core angular momenta distributions, but rather reflects fragmentation at higher core rotation.

8.3 Methods

We use the one-dimensional, two-zone disk model introduced in Zhu et al. (2010a,b) and modified in Chapter 2 of this thesis, including photoevaporation by energetic photons from the central star (Ercolano et al., 2009; Owen et al., 2010, 2011, 2012). Using their radiation-hydrodynamic models, Owen et al. (2011, 2012) calculate and provide fits to the total mass-loss rate due to X-ray photoevaporation as a function of stellar mass and X-ray luminosity as follows.

$$\dot{M}_{PE} = 6.25 \times 10^{-9} \left(\frac{M_*}{1\ M_\odot} \right)^{-0.068} \left(\frac{L_X}{10^{30}\ \mathrm{erg\ s^{-1}}} \right)^{1.14} M_\odot\ \mathrm{yr}^{-1} \text{ for full disks} \tag{8.1}$$

$$\dot{M}_{PE} = 4.8 \times 10^{-9} \left(\frac{M_*}{1\ M_\odot} \right)^{-0.148} \left(\frac{L_X}{10^{30}\ \mathrm{erg\ s^{-1}}} \right)^{1.14} M_\odot\ \mathrm{yr}^{-1} \text{ for disks with inner holes} \tag{8.2}$$

We note that the photoevaporative mass-loss rate scales nearly linearly with X-ray luminosity and depend weakly on stellar mass.

Preibisch et al. (2005) studied nearly 600 X-ray sources that can be reliably identified with optically well-characterized T Tauri stars in the Orion Nebula Cluster. They found that low-mass ($M_* \leq 2\ M_\odot$) stars show a clear correlation between X-ray luminosity and stellar mass as

$$\log(L_X\ [\mathrm{erg\ s^{-1}}]) = 30.37(\pm 0.06) + 1.44(\pm 0.10)\log(M_*/M_\odot). \tag{8.3}$$

By combining Equations (8.1), (8.2), and (8.3), we obtain the total photoevaporation rate in terms of stellar mass only.

$$\dot{M}_{PE} = 1.65 \times 10^{-8}(M_*/M_\odot)^{1.57}\ M_\odot\ \mathrm{yr}^{-1} \text{ for full disks} \tag{8.4}$$

$$\dot{M}_{PE} = 1.27 \times 10^{-8}(M_*/M_\odot)^{1.49}\ M_\odot\ \mathrm{yr}^{-1} \text{ for disks with inner holes} \tag{8.5}$$

Using the total mass-loss rate and the normalized radial mass-loss profile provided by Owen et al. (2012, see their Appendix B), we calculate a scaled mass-loss profile $\dot{\Sigma}_{PE}$ for a given stellar mass that satisfies $\dot{M}_{PE} = \int 2\pi R\dot{\Sigma}_{PE}\ dR$. The resulting radial mass-loss profiles for 0.3, 0.5, and 0.8 $M_\odot$ stars are presented in Figure 8.1.

The photoevaporation term is added in the mass conservation equation as

$$2\pi R\frac{\partial \Sigma_i}{\partial t} - \frac{\partial \dot{M}_i}{\partial R} = 2\pi g_i(R,t) - 2\pi R\dot{\Sigma}_{PE} \tag{8.6}$$

and this equation is solved together with the angular momentum conservation equation as explained in Chapter 2. In Equation (8.6), Σ_i is the surface density, $\dot{M}_i$ is the radial mass flux, and $2\pi g_i(R,t)$ is the mass flux per unit distance of infall material from an envelope cloud. The subscript i denotes either the active layer ("a") or dead zone ("d"). Since it is unlikely that photons travel through the dusty infalling material, we turn on photoevaporation after infall ends. We thus note that the stellar mass and the corresponding photoevaporation rate do not change dramatically during the photoevaporative period.

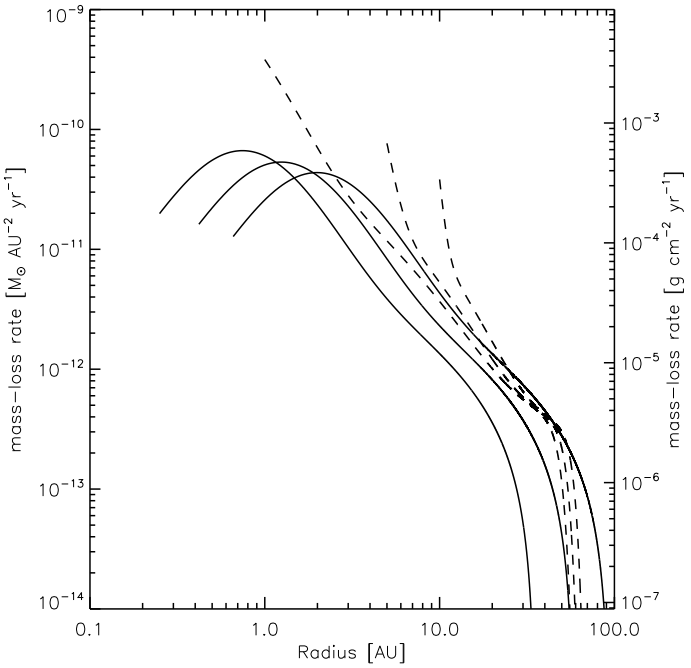

Figure 8.1. Radial mass-loss profiles due to photoevaporation. Solid curves present mass-loss profiles of full disks for three different stellar masses, $M_* = 0.3$, 0.5, and 0.8 $M_\odot$ (from left to right). High energy photons most efficiently evaporate disk material at small radii ($R \lesssim 3$ AU) and the mass-loss becomes negligible beyond ~ 100 AU. Dashed curves show mass-loss profiles of disks with inner holes at $R = 1, 5$, and 10 AU (from left to right), assuming a 0.8 $M_\odot$ central star. Compared to the primordial disk with the same central stellar mass, photoevaporation rate at the inner edge of the disk is enhanced.

As shown in Figure 8.1, the photoevaporative mass-loss rate is enhanced when there is an inner hole, as the inner edge of the optically-thick disk is illuminated normally rather than obliquely. We turned on the photoevaporative rate of Equation (8.5) when the inner disk is essentially totally depleted. In principle, once a large gap is opened and dead zone is absent, there should be an enhancement of the photoevaporative rate which gradually grows as the shadowing by the inner disk decreases over time; but we find that the clearing time of the inner disk is so short compared with the overall disk lifetime that it makes little difference when exactly we turn on inner edge photoevaporation.

As in Zhu et al. (2010b) and in Chapter 2 of this thesis, we follow the disk evolution during and after infall from a protostellar cloud which forms the star as well as the disk.

We assume that the protostellar cloud is spherical with a two-component density profile intended to approximate a Bonnor-Ebert sphere as explained in Zhu et al. (2010b); the flat core inside of r_{ic} has 0.1 $M_\odot$ and the rest of the Bonnor-Ebert sphere ($r > r_{ic}$) has 1 $M_\odot$, with a density profile of r^{-2}. We assume that the inner core material collapses first to form a central star, and then follow the evolution after that event. The outer cloud beyond r_{ic} collapses as in the Terebey et al. (1984) model for an initially-uniformly rotating singular isothermal sphere, with infall landing at progressively large radii as the collapse proceeds. If the cloud core is initially in uniform rotation with angular velocity Ω_c, the material falling in from different directions will have different angular momentum and arrive at the midplane at different radii within the centrifugal radius (Cassen & Moosman, 1981),

$$R_c = r_0^4 \frac{\Omega_c^2}{GM_c}. \tag{8.7}$$

Here, M_c is the central stellar mass and r_0 is the initial radius of material that collapses to the center at time t, defined as $r_0 = (m_0/2)c_s t + r_{ic}$, where $m_0 = 0.975$ (Shu, 1977; Terebey et al., 1984), c_s is the (uniform) sound speed of the cloud, and r_{ic} is the radius of the flat density region in the Bonnor-Ebert sphere. As seen in Equation (8.7), for a fixed cloud temperature the size of protoplanetary disks are mainly determined by the initial angular momentum of their maternal cloud. Infall material is added within the centrifugal radius following the modified infall model explained in Chapter 2.

We parameterize the cloud rotation in terms of $\omega = \Omega_c/\Omega_{\rm b}$, where $\Omega_{\rm b} = 2^{3/2}c_s^3/GM_{\rm c}$ is the breakup angular frequency at the outer cloud edge. We choose ω in a way that the maximum centrifugal radius at the end of infall spans from 1 to 500 AU, which corresponds to $0.007 \leq \omega \leq 0.1$. Our choice of ω and the corresponding maximum centrifugal radii are presented in Table 8.1.

Active layer and dead zone temperatures are determined by the balance between heating and radiative cooling. As explained in Chapter 2, for the heating sources, we consider local heating by the viscosity, the infall, and the gravitational potential energy change, and external heating by stellar and accretion luminosity irradiations. The Rosseland mean opacity was taken from Zhu et al. (2009b) to calculate the optical depths of the layers.

Table 8.1. Model Parameters and Results for Non-photoevaporating Models

$\alpha_{\rm rd}$	ω	$R_{\rm c,max}$ (AU)	$t_{\rm dead}$ (Myr)	M_*[a] ($M_\odot$)	$M_{\rm disk}$[a] ($M_\odot$)	$\dot{M}_{\rm acc}(t = 10$ Myr) ($M_\odot$ yr^{-1})
zero	0.007	1.0	2.59	0.87/0.90/0.90	0.034/0.003/0.001	7.39×10^{-11}
zero	0.012	3.1	3.59	0.81/0.89/0.90	0.091/0.007/0.003	2.61×10^{-10}
zero	0.02	10.0	4.52	0.71/0.89/0.89	0.193/0.013/0.006	6.49×10^{-10}
zero	0.03	25.2	5.19	0.64/0.88/0.89	0.260/0.021/0.012	1.19×10^{-9}
zero	0.04	50.4	5.71	0.57/0.87/0.88	0.328/0.029/0.017	1.78×10^{-9}
zero	0.055	108.2	6.53	0.50/0.86/0.87	0.404/0.040/0.027	2.77×10^{-9}
zero	0.1	529.5	9.06	0.33/0.83/0.84	0.570/0.068/0.061	6.31×10^{-9}
non-zero	0.007	1.0	0.83	0.87/0.89/0.90	0.032/0.005/0.001	7.05×10^{-11}
non-zero	0.012	3.1	1.39	0.81/0.89/0.90	0.089/0.012/0.002	2.49×10^{-10}
non-zero	0.02	9.8	1.94	0.72/0.88/0.89	0.175/0.023/0.006	6.23×10^{-10}
non-zero	0.03	25.1	2.50	0.65/0.87/0.89	0.249/0.035/0.011	1.15×10^{-9}
non-zero	0.04	48.9	3.08	0.59/0.86/0.88	0.313/0.045/0.017	1.74×10^{-9}
non-zero	0.055	105.3	3.92	0.51/0.84/0.87	0.386/0.057/0.026	2.67×10^{-9}
non-zero	0.1	504.1	6.45	0.35/0.81/0.84	0.547/0.087/0.059	5.99×10^{-9}

[a]Masses at the end of infall, at the time deadzone depletes, and at 10 Myr.

Following Chapter 2, we consider a dead zone residual viscosity (DZRV) $\alpha_{\rm rd}$ as well as the MRI viscosity and the GI viscosity; $\alpha_d = \alpha_{M,d} + \alpha_{Q,d} + \alpha_{\rm rd}$. In non-zero DZRV models, $\alpha_{\rm rd}$ is set to

$$\alpha_{\rm rd} = \min\left(10^{-4},\ f_{\rm rd}\alpha_{\rm MRI}\frac{\Sigma_a}{\Sigma_d}\right), \tag{8.8}$$

where $f_{\rm rd}$ is the efficiency of accretion in the dead zone and set to unity. This form is motivated by the conjecture that the accretion driven in the dead zone by the active layer MRI cannot be larger than that of the active zone itself (Chapter 2). The MRI viscosity parameter $\alpha_{\rm MRI}$ is a fixed value of which a region have when it can sustain the MRI. In the dead zone we turn the MRI on and set $\alpha_{M,d} = \alpha_{\rm MRI}$ only if the midplane temperature becomes higher than a critical temperature $T_{\rm MRI}$ to produce sufficient ionization levels, while the active layer is always assumed to be able to sustain the MRI. The GI viscosity parameter is the same as in Zhu et al. (2010b), $\alpha_{Q,i} = e^{-Q^2}$, where Q is the Toomre parameter.

8.4 Results

8.4.1 Initial Conditions

In all cases here we start with a 0.1 $M_\odot$ central protostar surrounded by an 1 $M_\odot$ cloud. Our fiducial models assume a cloud rotation of $\omega = 0.03$ and we vary ω in other models as explained in §8.3. We assume $T_{\rm MRI} = 1500$ K and $\alpha_{\rm MRI} = 0.01$ for all calculations. We adopt a cloud envelope temperature of $T_{\rm env} = 20$ K, which yields a constant infall rate of $\sim 3.4 \times 10^{-6}\ M_\odot\,{\rm yr}^{-1}$. This is 20 % smaller than the infall rate for conventional singular isothermal collapse model (Shu, 1977) because of the modified infall model (see Chapter 2). The infall lasts for ~ 0.24 Myr, adding 0.8 $M_\odot$ to the central star + disk in total.

We use inner and outer disk boundaries of 0.2 AU and 8000 AU, respectively, with 64 logarithmically spaced grid points. These values result in the innermost grid size of 0.036 AU. We tested our results using differing grid cells after implementing photoevaporation prescriptions and found that the results are not sensitive to the resolution. We adopt outflow boundary conditions for both inner and outer boundaries. This assumes that all the material passing the inner boundary to be accreted onto the central star. At the outer boundary, the amount of material leaving is essentially zero so that the disk evolution is independent of the outer boundary conditions.

8.4.2 Evolution of Non-photoevaporating Disks

In Chapter 2 we presented the evolution of non-photoevaporating disks up to ages of 1.5 Myr, focusing on the effects of a non-zero residual viscosity in dead zone. These models showed a variety of patterns of non-steady accretion onto the central star, especially during the phase when matter from the protostellar envelope is still being added to the disk. The reasons for the outburst behavior and their parameter dependence were discussed in Chapter 2. Here we focus on the longer-term evolution of the disks when outbursts are either absent or relatively unimportant.

Figure 8.2 presents the mass accretion rate and the mass of the central star, the disk, and the central star + disk of our fiducial zero DZRV model as a function of time. As seen in

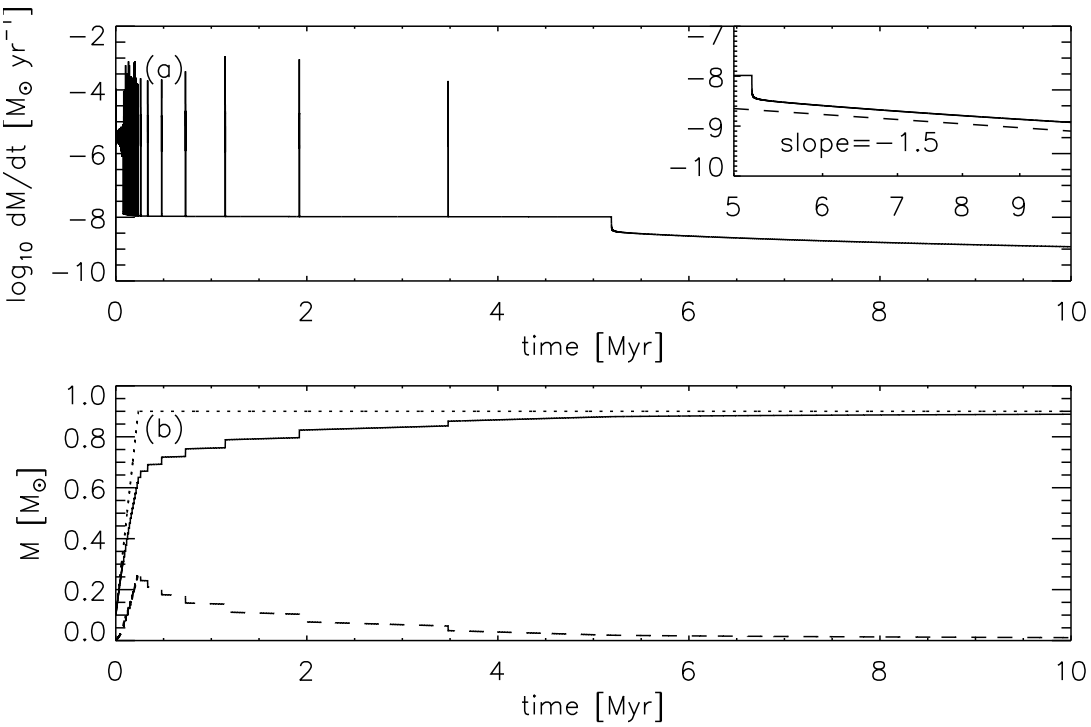

Figure 8.2. (a) Mass accretion rate and (b) mass of the central star + disk (dotted curve), mass of the central star (solid curve), and mass of the disk (dashed curve) with time for our fiducial non-photoevaporating disk with zero DZRV. The upper right panel in (a) shows mass accretion rate vs. log(time) after the dead zone depletes and the disk becomes fully viscous. The dashed line presents the similarity solution for fully viscous disks, $\dot{M} \propto t^{-3/2}$ (Hartmann et al., 2006).

Chapter 2, the system shows a quasi-steady disk accretion at the beginning, an outburst stage during infall, and the T Tauri phase after infall ends. The dead zone depletes at ~ 5.2 Myr and the disk becomes fully viscous, having only the active layer. Mass accretion rate after the dead zone depletes is presented in the upper-right corner of Figure 8.2a, together with the similarity solution for viscous disk evolution, $\dot{M} \propto t^{-3/2}$ (Hartmann et al., 2006). Not surprisingly, mass accretion rate matches the similarity solution well.

In Figure 8.3, we present the mass accretion rate and the mass of the central star, the disk, and the central star + disk of the ficucial non-zero DZRV model. In this case, the disk accretes material more efficiently through small but frequent inside-out bursts (see Chapter 2), resulting in earlier depletion of dead zone than zero DZRV model, at ~ 2.5 Myr. Again, the viscous evolution after dead zone depletes follows the similarity solution well.

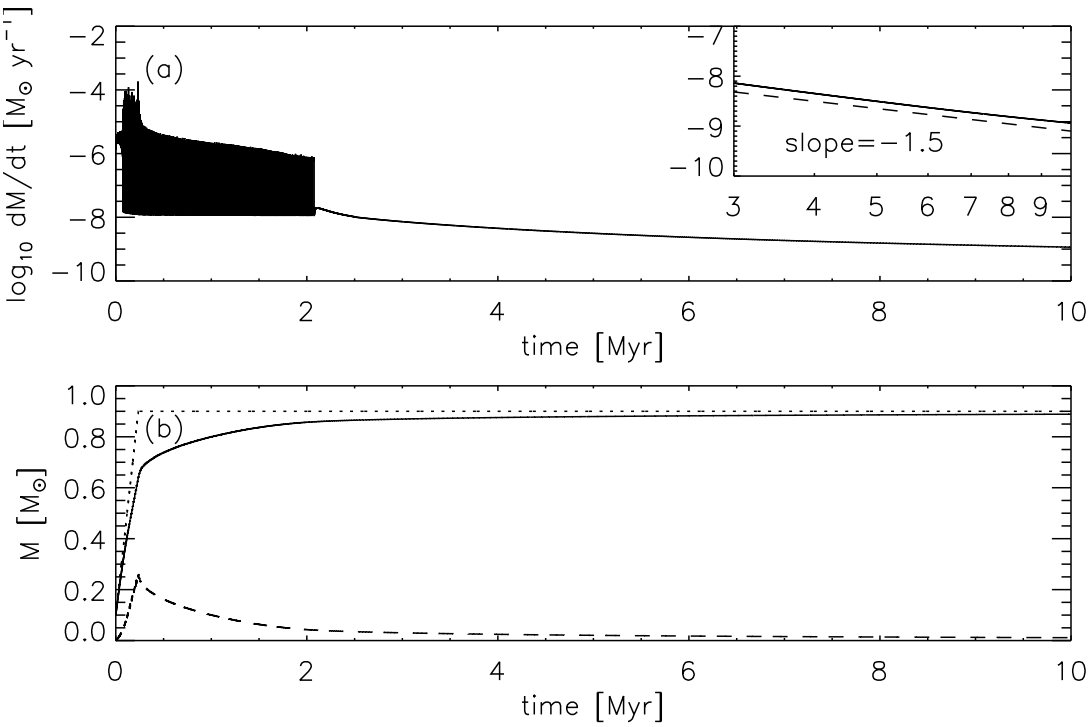

Figure 8.3. Same as Figure 8.2 but results with non-zero DZRV.

Surface density distributions of both zero and non-zero DZRV models at 2, 5, and 10 Myr are presented in Figure 8.4. As seen in the figure, outbursts govern density structures at small radii ($R \lesssim 10$ AU), so the detailed density profiles at such radii depend on the DZRV during outbursting phase. However, the disk properties at large radii ($R \gtrsim 10$ AU) are likely to be controlled more by viscous evolution regardless of the DZRV, and thus the disk properties at such radii appear to be similar in both models.

8.4.3 Evolution of Photoevaporating Disks

Figure 8.5 shows the mass accretion rates of the fiducial photoevaporating models with zero and non-zero DZRV. The overall evolutions resemble those of non-photoevaporating disks. However, accretion stops early at ~ 3.9 and ~ 2.4 Myr, as the inner disk depletes via accretion plus photoevaporation. We note that a gap opens first and then dead zone depletes in the zero DZRV model, while dead zone depletes first and then a gap opens later in the non-zero DZRV model (see below).

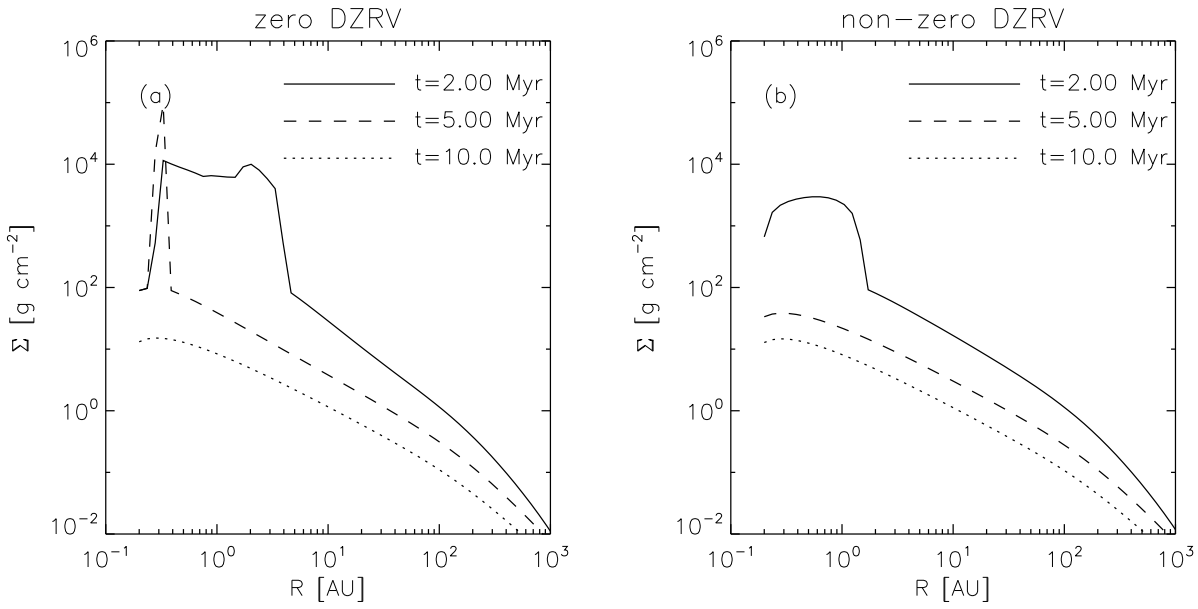

Figure 8.4. Surface density profiles of the fiducial non-photoevaporating models with (a) zero and (b) non-zero DZRV, at 2 Myr (solid curves), 5 Myr (dashed curves), and 10 Myr (dotted curves). While density distribution at small radii ($R \lesssim 10$ AU) is largely affected by outbursts, the disk properties at large radii ($R \gtrsim 10$ AU) is controlled more by viscous evolution, showing similar profiles in both models.

Figure 8.6a presents the surface density distributions of the zero DZRV model at three times; when infall ends, a gap opens, and the wall temperature of outer disk drops below 100 K (see §8.5.1). When infall ends the disk has a maximum centrifugal radius of $R_{c,\max} \sim 25$ AU, which approximately sets the size of the dead zone (Zhu et al., 2010b). Having no infalling material the dead zone loses mass purely through episodic accretion and shrinks in size, but the process is relatively inefficient due to zero DZRV. Meanwhile, photoevaporative winds deplete the outer disk beyond the dead zone and open a gap around $R \sim 9$ AU, at ~ 3.3 Myr. A gap can be opened beyond the dead zone because photoevaporation rate decreases approximately as $\sim R^{-2}$ at $5 \lesssim R \lesssim 50$ AU while disk surface density at the radii drops steeper. The inner disk totally depletes at ~ 3.9 Myr through accretion and photoevaporation.

Figure 8.6b shows the density distributions of the non-zero DZRV model. The disk surface density when infall ends is similar to that of the zero DZRV model. However, the dead zone depletes earlier at ~ 1.9 Myr with the help of frequent inside-out bursts, not

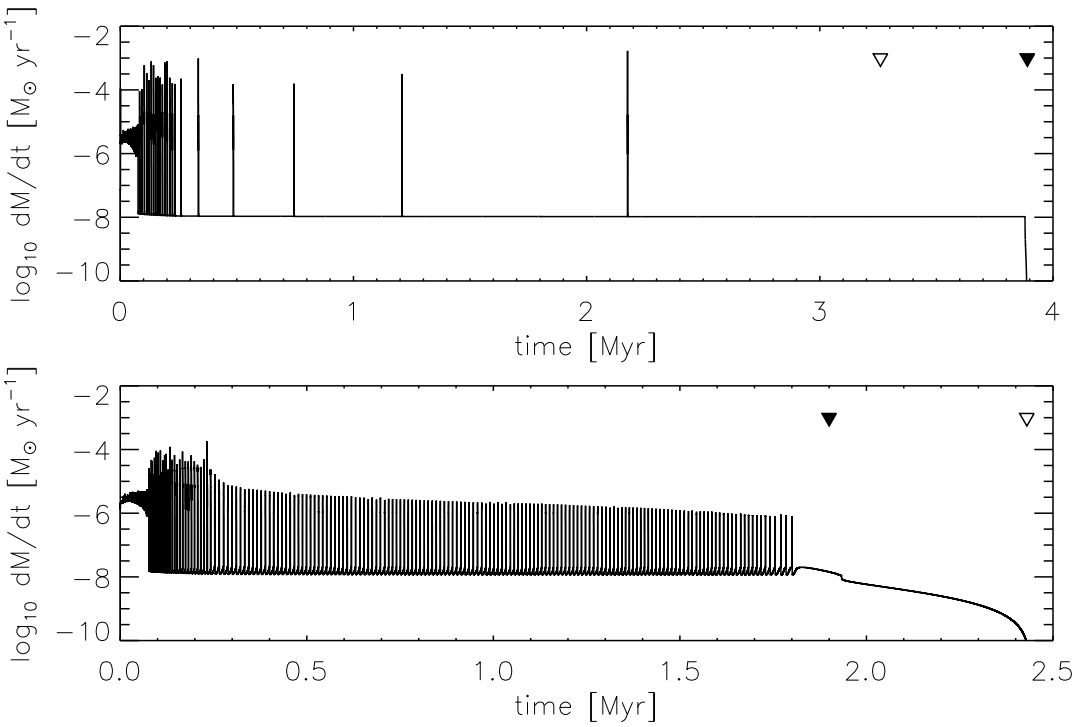

Figure 8.5. Mass accretion rate of photoevaporating models with zero DZRV (upper) and non-zero DZRV (lower) as a function of time. Open triangles indicate the time when a gap is opened, while solid triangles present the time when dead zone is depleted. Note that a gap opens before the dead zone depletes in the zero DZRV case, while the dead zone depletes first and then a gap opens afterward in the non-zero DZRV case.

allowing photoevaporative winds enough time to make a gap beyond the dead zone. As a result, a gap opens after surface density drops significantly through episodic accretion, around $R \sim 1$ AU. Since the gap opens at small radii, the inner disk has little mass within it so depletes immediately after the gap opens. After the inner disk depletes, the outer disk is cleared out rapidly due to the enhanced photoevaporative winds at the inner edge.

8.4.4 Effect of Initial Angular Momentum

As explained in §8.3 the disk size is mainly constrained by the centrifugal radii, or initial angular momentum. Zhu et al. (2010b) showed that if a system has small initial angular momentum it results in a small disk with little mass, having only a few (or no) outbursts. On the other hand, if a system starts with large angular momentum disk becomes larger and more massive, having numerous outbursts. We confirm that the same holds in our

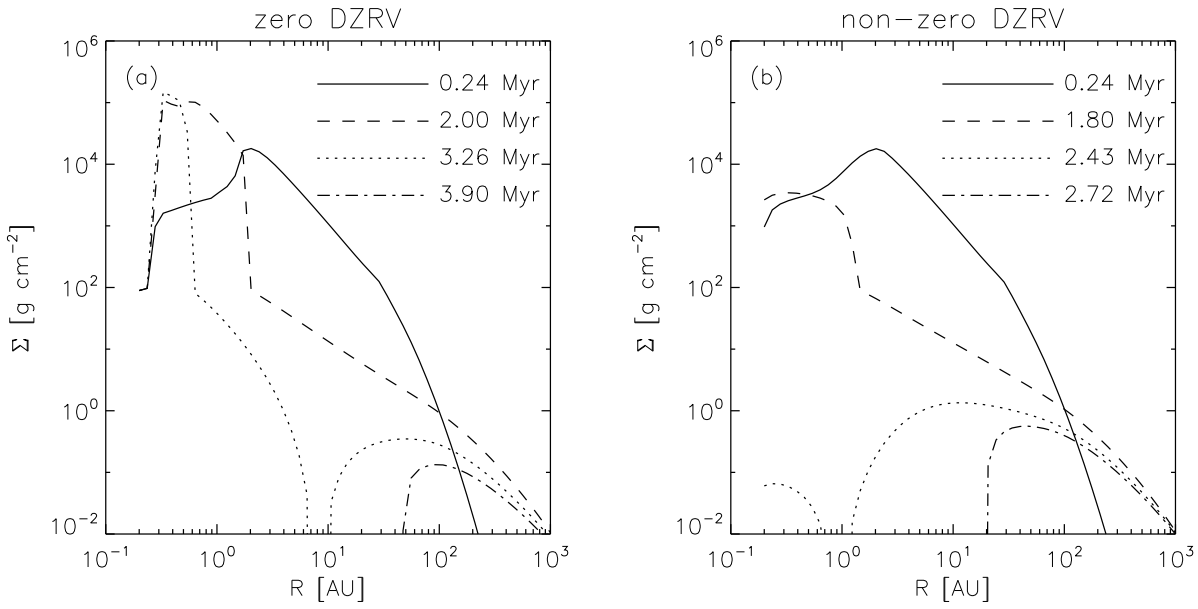

Figure 8.6. Surface density profiles of photoevaporating models with (a) zero and (b) non-zero DZRV models at selected times. We note that dead zone survives long in the zero DZRV model, allowing a gap to be opened beyond it, while a gap opens after dead zone depletes in the non-zero DZRV model.

non-photoevaporating models. The results are summarized in Table 8.1.

By adding photoevaporation and varying initial angular momenta, we find that disks have gaps and inner holes during their evolution. Figure 8.7 shows the evolution of photoevaporating disks with small ($\omega = 0.012$) and large ($\omega = 0.055$) initial angular momenta, assuming zero DZRV. With the small initial angular momentum, plenty of material is accreted onto the central star during infall and only 0.09 $M_\odot$ of material is left in the disk when infall ends. In addition, the maximum centrifugal radius is small enough ($R_{c,\max} = 3.1$ AU) so that high energy photons are able to evaporate disk material and open a gap beyond the dead zone.

With the large initial angular momentum, on the other hand, the disk has a large maximum centrifugal radius of $R_{c,\max} = 108.2$ AU, resulting in a massive disk of 0.40 $M_\odot$ at the end of infall. In this model the dead zone extends out to ~ 50 AU, constrained by the radius where the active layer becomes gravitationally unstable rather than the maximum centrifugal radius (Zhu et al., 2010b). A significant fraction of the disk mass resides in the large radii and therefore photoevaporation cannot open a gap until the disk is sufficiently depleted. A gap finally opens at 4.74 Myr after the dead zone depletes, around 2 AU.

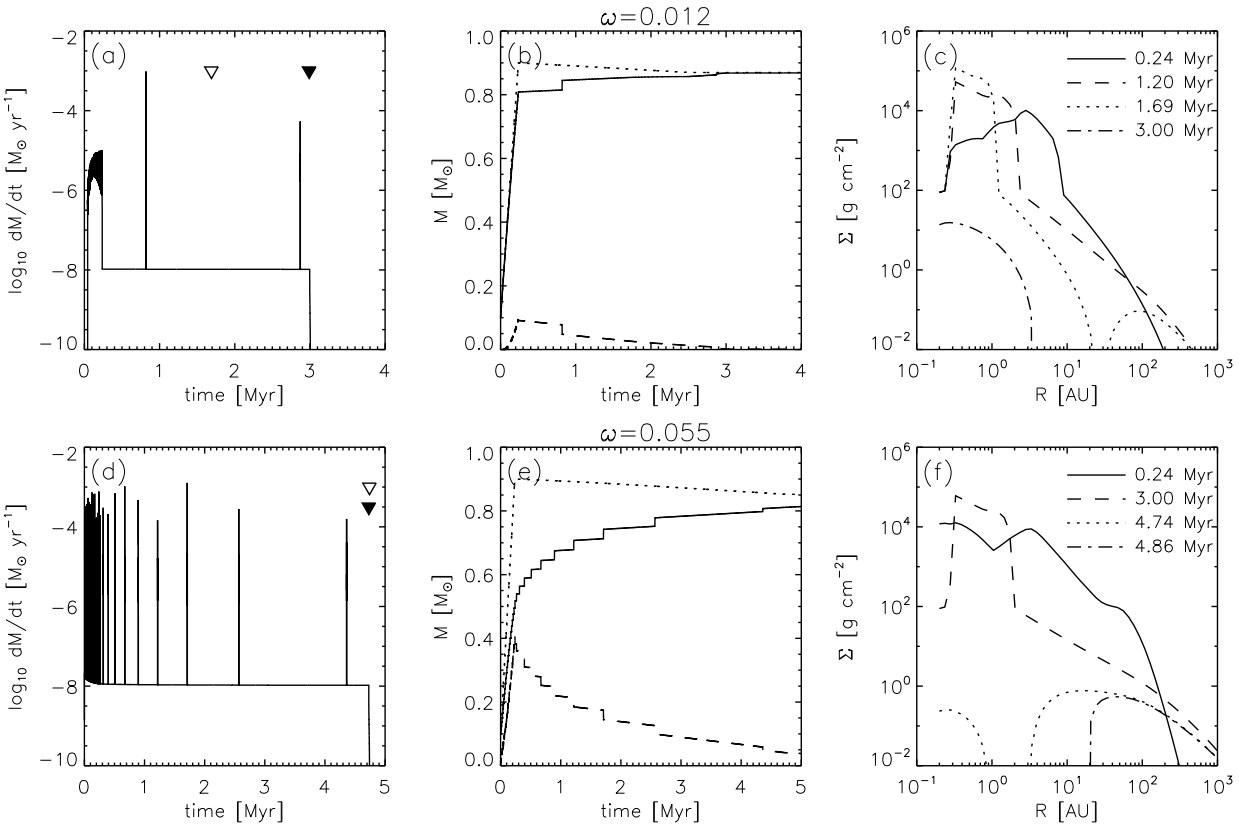

Figure 8.7. Results of photoevaporating models with zero DZRV are presented. (left) Mass accretion rates against time. (middle) Mass of the central star + disk (dotted curve), mass of the central star (solid curves), and mass of the disk (dashed curves). (right) Density distributions at selected times. Upper panels show results of a slowly rotating case ($\omega = 0.012$), while lower panel show results of a rapidly rotating case ($\omega = 0.055$). In (a) and (d), the open triangles indicate the time when a gap is opened, while the solid triangles present the time when dead zone is depleted.

We show the evolution of photoevaporating disks with non-zero DZRV in Figure 8.8. In the small initial angular momentum case dead zone depletes early at 1.17 Myr with the help of frequent inside-out bursts. A gap opens near the inner disk edge and evolves immediately into an inner hole. In the large initial angular momentum case disks have plenty of mass at large radii, so a gap cannot be opened until the disk depletes sufficiently. We note again that once an inner hole is created the inside-out disk clearing occurs in a short timescale compared to the disk lifetime. The results of the photoevaporating models are summarized in Table 8.2.

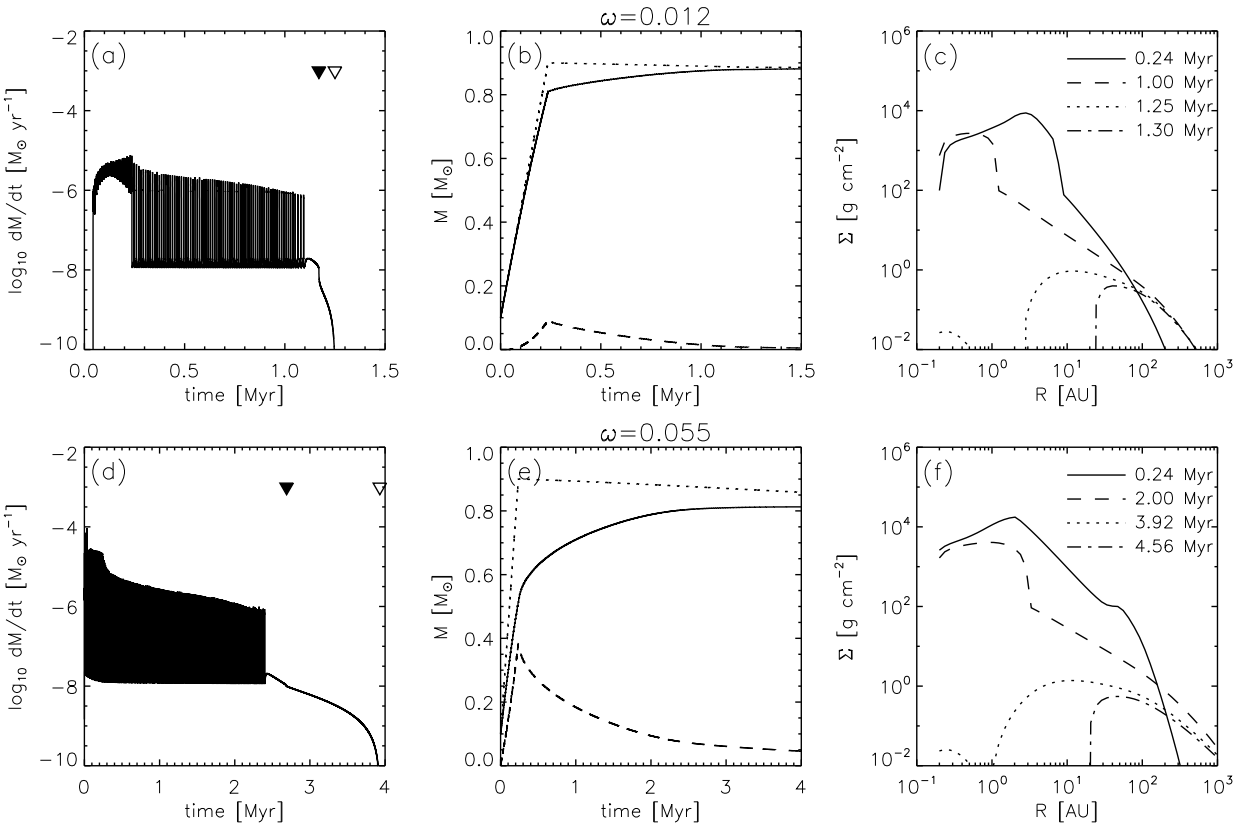

Figure 8.8. Same as Figure 8.7 but results with non-zero DZRV.

8.4.5 Comparison with Other Studies

Our results bear some qualitative similarities to the results of Owen et al. (2011, hereafter OEC11), where the same photoevaporation profile was used, but also some discrepancies. In OEC11, they assumed a 0.7 $M_\odot$ central star with photoevaporation of 7.1×10^{-9} $M_\odot\,\mathrm{yr}^{-1}$, and the zero-time similarity solution of Lynden-Bell & Pringle (1974) with disk mass of 0.07 $M_\odot$, characteristic disk radius of 18 AU, and $\alpha = 2.5 \times 10^{-3}$. In terms of masses of the central star and the disk, their model is close to our model with $\omega = 0.012$; when infall ends the model has a 0.8 $M_\odot$ central star with a 0.09 $M_\odot$ surrounding disk.

Table 8.2. Model Parameters and Results for Photoevaporating Models

$\alpha_{\rm rd}$	PE rate	ω	$t_{\rm dead}$ (Myr)	$t_{\rm gap}$ (Myr)	$t_{\rm acc}$ (Myr)	$t_{\rm evol}$ (Myr)	$R_{\rm gap}$ (AU)	M_*[a] ($M_\odot$)	$M_{\rm disk}$[a] ($M_\odot$)	$\log j$ (cm^2 s^{-1})	Disk phase[b]
zero	1	0.007	2.18	0.73	2.19	2.19	55.7	0.87/0.88	0.034/0.022	17.2	F→AT→NT
zero	1	0.012	3.00	1.69	3.01	3.01	28.7	0.81/0.86	0.091/0.027	17.8	F→AT→NT
zero	1	0.02	3.63	2.56	3.64	3.64	14.8	0.71/0.85	0.193/0.026	18.0	F→AT→NT
zero	1	0.03	3.88	3.26	3.89	3.89	7.6	0.64/0.84	0.260/0.029	18.6	F→AT→NT
zero	1	0.04	4.58	3.89	4.59	4.59	6.5	0.57/0.82	0.328/0.038	19.1	F→AT→NT
zero	1	0.055	4.73	4.74	4.74	4.86	2.8	0.50/0.81	0.404/0.041	19.7	F→NT
zero	1	0.1	6.35	7.15	7.15	8.71	0.6	0.33/0.77	0.570/0.071	20.3	F→NT
non-zero	1	0.007	0.71	0.74	0.74	0.75	3.3	0.87/0.89	0.032/0.001	17.4	F→NT
non-zero	1	0.012	1.17	1.25	1.25	1.30	2.0	0.81/0.88	0.089/0.007	17.9	F→NT
non-zero	1	0.02	1.60	1.83	1.83	1.97	1.5	0.72/0.86	0.175/0.017	18.2	F→NT
non-zero	1	0.03	1.94	2.44	2.44	2.72	1.0	0.65/0.85	0.249/0.027	18.7	F→NT
non-zero	1	0.04	2.23	3.05	3.05	3.47	1.0	0.59/0.83	0.313/0.036	19.2	F→NT
non-zero	1	0.055	2.69	3.92	3.92	4.56	0.9	0.51/0.81	0.386/0.047	19.7	F→NT
non-zero	1	0.1	4.21	6.81	6.81	8.41	0.8	0.35/0.77	0.547/0.071	20.3	F→NT
zero	0.6 (OEC11)	0.012	2.98	2.17	3.00	3.00	24.3	0.81/0.86	0.091/0.025	17.8	F→AT→NT
non-zero	0.6 (OEC11)	0.012	1.24	1.48	1.48	1.60	1.5	0.81/0.88	0.089/0.007	17.9	F→NT
zero	0.3	0.03	4.45	5.06	5.06	5.71	0.9	0.64/0.86	0.260/0.017	18.6	F→NT
non-zero	0.3	0.03	2.22	4.67	4.67	5.41	0.9	0.81/0.87	0.089/0.018	18.7	F→NT
zero	0.1	0.03	4.87	9.57	9.57	13.72	0.8	0.64/0.88	0.260/0.008	18.6	F→NT
non-zero	0.1	0.03	2.39	9.31	9.31	13.49	0.8	0.81/0.88	0.089/0.008	18.7	F→NT

[a]Masses at the end of infall and at the gap opening.

[b]Diks phases indicated as F, AT, and NT denote full disks, accreting transitional disks, and non-accreting transitional disks, respectively.

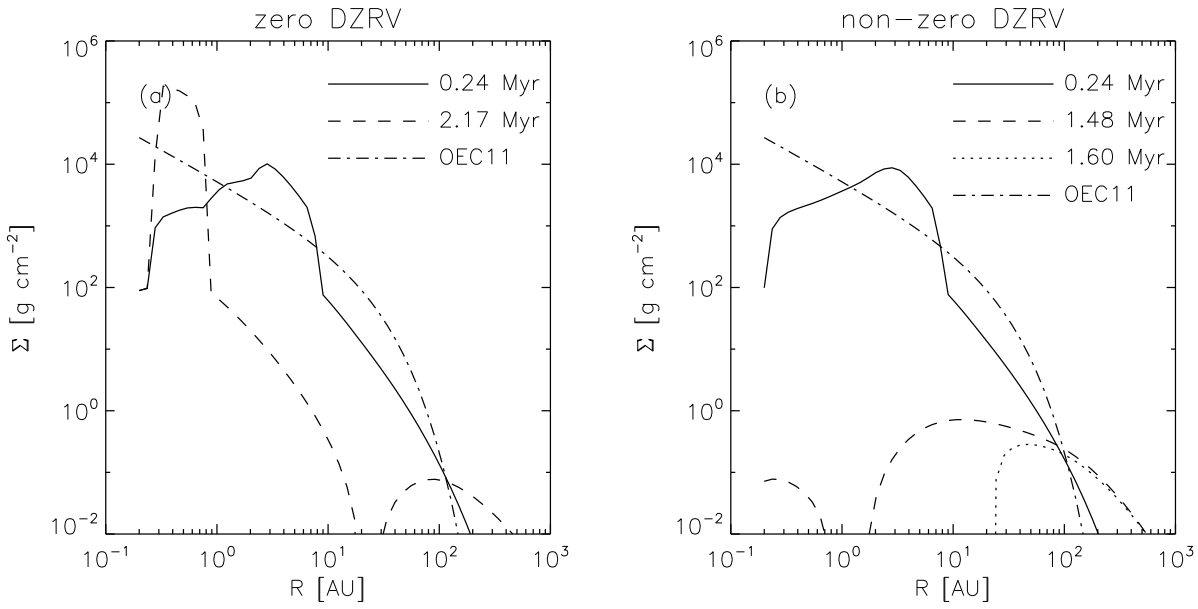

Figure 8.9. Surface density profiles of (a) zero and (b) non-zero DZRV models at the times infall ends (solid curves), a gap opens (dashed curves), and the wall temperature of outer disk drops below 100 K (dotted curve), assuming a comparable photoevaporation rate to OEC11 with $\omega = 0.012$. Dashed-dotted curves present the initial surface density distribution of OEC11.

In order to compare our models to OEC11's, we test the $\omega = 0.012$ model with the same photoevaporation rate as OEC11, which is $\sim$ 60 % of our fiducial rate. As presented in Figure 8.9, with our layered disk model we can have either a gap beyond dead zone or an inner hole depending on the DZRV. The final outcome of OEC11 is similar to our non-zero DZRV model in that a gap opens at similar radii and the outer disk clears out rapidly once an inner hole is created (see their Figure 9). However, in their model the gap opens at $\sim$ 2.7 Myr, during which photoevaporative winds are capable of opening a gap beyond dead zone in our case. In Figure 8.9 we overplot initial surface density distribution of OEC11. While their zero-time similarity solution is close to our density distribution in general, it has about an order of magnitude higher surface density at $10 \lesssim R \lesssim 50$ AU where we open a gap in our zero DZRV model. Due to the high initial surface density at these radii, a gap opens close to the disk inner edge after surface density drops sufficiently through the viscous evolution. To summarize, despite the qualitative resemblance between models, this comparison shows how sensitive the disk evolution is to details of the model one uses.

Morishima (2012) used a layered accretion model (active layer + dead zone) adopting a similar photoevaporation prescription to ours and tested for various parameter sets of X-ray luminosity, active layer surface density, and dead zone viscosity parameter.[2] While details are different, results of Morishima (2012) are in qualitative agreement with ours; for a given X-ray luminosity gaps open beyond the dead zone if the dead zone has small viscosity ($\alpha_d \leq 10^{-5}$ with their standard X-ray luminosity) and thus lives long, while gaps open at a small radius only after the dead zone disappears if dead zone viscosity is large enough ($\alpha_d \geq 10^{-4}$) for the mass accretion in the dead zone to be efficient (see their Figure 4).

8.4.6 Efficiency of Photoevaporation

Since the actual amount of mass-loss due to photoevaporation is uncertain we examined cases with 30 % and 10 % of the standard rate. Figure 8.10 presents the mass accretion rates of the models as a function of time. With 30 % less photoevaporation rate, neither zero DZRV model nor non-zero DZRV model opens a gap beyond dead zone. With 10 % of the standard photoevaporation rate, the mass accretion rates show no significant difference from those of non-photoevaporating disks. The only difference is that photoevaporative winds help to deplete the inner disk and make an inner hole. The inner hole in the models is created at 9.57 and 9.31 Myr, respectively, leaving a 0.01 $M_\odot$ outer disk.

8.5 Comparison with Observations

While an increasing number of (pre-)transitional disks have been observed, the causes of the disk gaps and inner holes are still uncertain. Theories suggested to explain (pre-)transitional disks include photoevaporation (Alexander & Armitage, 2007; Gorti & Hollenbach, 2009; Gorti et al., 2009; Owen et al., 2010, 2011, 2012), planet formation (Dodson-Robinson & Salyk, 2011; Zhu et al., 2011), grain growth (Dullemond & Dominik, 2005), etc. In the following we investigate the implications of the models assuming that photoevaporation is the only mechanism for disk clearing.

[2]Dead zone viscosity in Morishima (2012) is the total viscosity in the dead zone, different from our dead zone "residual" viscosity.

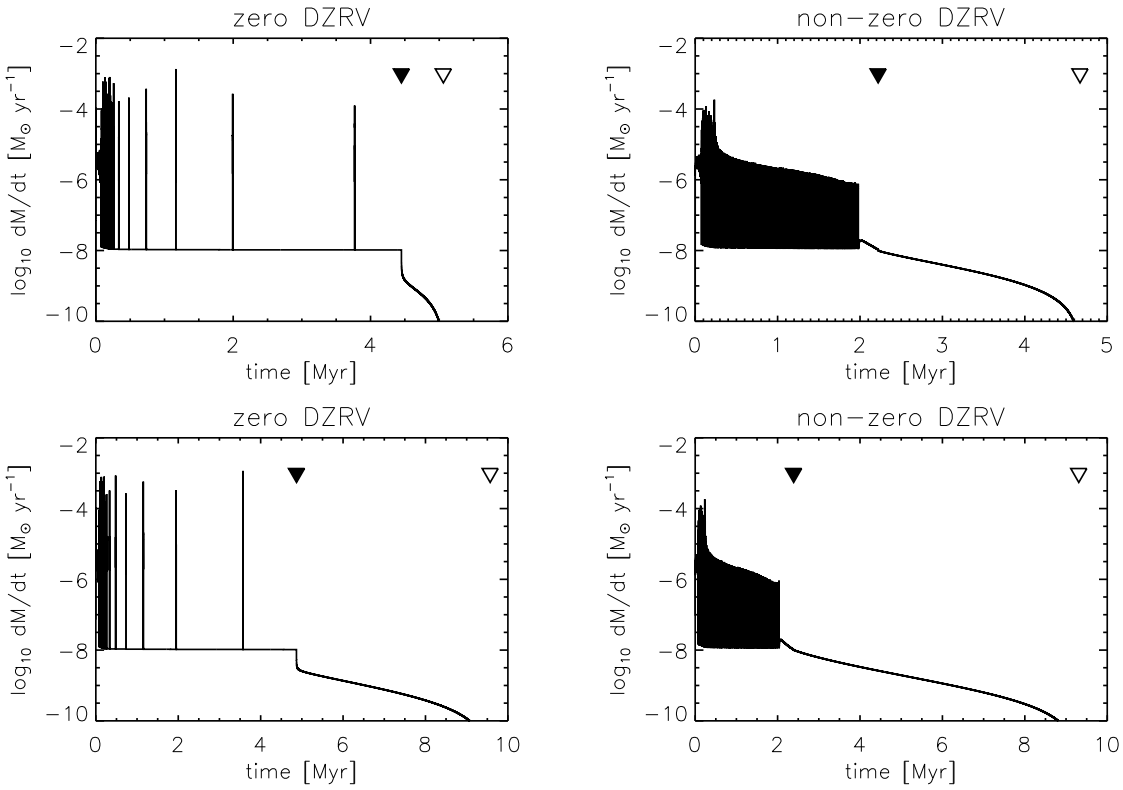

Figure 8.10. Mass accretion rate of photoevaporating models (upper) with 30 % and (lower) with 10 % of the standard photoevaporation rate. The open triangles indicate the time when a gap is opened, while the solid triangles present the time when dead zone is depleted.

8.5.1 Photoevaporation-driven Transitional Disks

We showed in §8.4 that different combinations of parameters result in a variety of evolutionary results, including disks with gaps and inner holes. Those disks obtained in our calculations could be potential analogues of observed (pre-)transitional disks. Observationally, the SED of (pre-)transitional disks are characterized by the near-IR flux close to photospheric emission and the rise of mid-IR flux around ~ 10 μm. We assume that this excess emission can be observed only if gaps and inner holes are large enough; $\Delta R_{\rm gap} > 5$ AU and $R_{\rm hole} > 1$ AU (Strom et al., 1989; Calvet et al., 2005; Espaillat et al., 2007, 2010; Luhman & Mamajek, 2012). In principle we could define pre-transitional disks as disks with gaps that are large enough to satisfy the above criteria and thus distinguishable from transitional disks. However, since our models do not include dust evolution, it is uncertain whether or not there will be observable dust emission from the inner disk. Thus, we do not distinguish

between pre-transitional disks and transitional disks in this work. Instead, we classify the disks into “accreting" and “non-accreting" transitional disks depending on the existence of accretion onto the central star (i.e. existence of an inner disk regardless of the presence of dusts).

With the definitions above and assuming the standard photoevaporation rate, accreting transitional disks can be obtained with zero DZRV plus small initial angular momentum ($\omega \lesssim 0.04$), while non-accreting transitional disks require either non-zero DZRV or zero DZRV with a large initial angular momentum ($\omega > 0.04$). Figure 8.11 shows various disk phases in the disk age vs. ω space. In the zero DZRV cases with initial angular frequency of $\omega \lesssim 0.04$, the maximum centrifugal radius is small enough so that high energy photons are able to evaporate disk material and open a gap beyond dead zone, as explained in §8.4.3. When $\omega > 0.04$, on the other hand, the disk has a large centrifugal radius so gaps cannot be opened until the inner disk is sufficiently depleted and thus disks end up with a non-accreting transitional phase. In the non-zero DZRV cases, all disks in our ω space evolve into non-accreting transitional disks due to a short dead zone depletion time.

We assume that transitional disks become evolved when the outer “wall” – the inner edge of the outer disk – has a temperature less than 100 K (we assume a blackbody temperature for simplicity) with no inner disk left so that we don't expect to see excess emission at 8 μm (the longest wavelength channel of the sensitive IRAC camera on the *Spitzer Space Telescope*). In our models, the wall temperature drops below 100 K at $R_{\rm wall} \sim 20$ AU. The assumption is based on the fact that most of the previous surveys employed the IR excess criteria to study protoplanetary census. With this definition, transitional disks in our models have outer disk clearing time of $\lesssim 20$ % of their lifetime, which reasonably explains the observed statistics (Luhman et al., 2010; Muzerolle et al., 2010).

8.5.2 Disk Frequency

The disk fraction of young stellar objects is known to decrease as a function of their age. Mamajek (2009) compiled results from the literature and showed that the disk frequency can be fitted approximately by an exponential decay with a characteristic time scale of ~ 2.5 Myr. Here we try to explain the observed disk frequency using photoevaporating disks

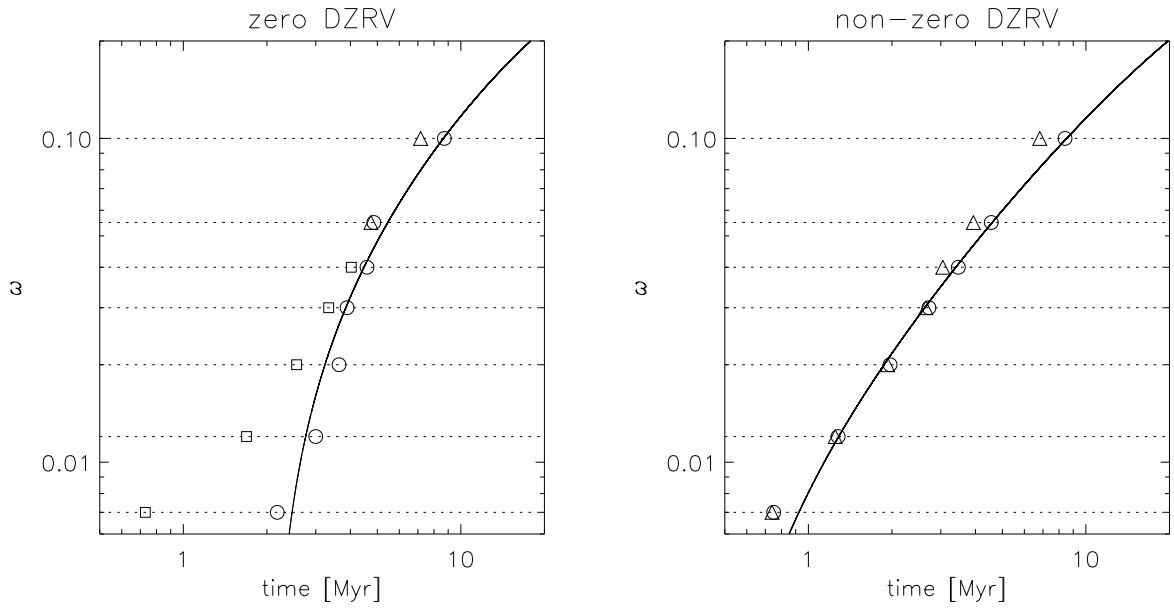

Figure 8.11. A diagram presenting disk phases versus their ages of various disks starting from different initial angular momentum for (a) zero and (b) non-zero DZRV models. Horizontal dotted lines show the path disks evolve on the diagram (from left to right). Circles, triangles, and squares represent evolved disks, accreting transitional disks, and non-accreting transitional disks, respectively. The solid curve is a fit of the evolved disk phase to the initial angular momentum.

with different initial angular momenta.

Since we know more rapid rotation leads to a longer disk depletion time, we can calculate the disk frequency as follows. If we write the distribution of initial angular momentum of systems as $n(\omega)$, the disk frequency at a given time can be written as

$$f(t) = \frac{1}{N_{\rm tot}} \int_{\omega_{\rm evol}}^{\omega_{\rm max}} n(\omega) d\omega, \tag{8.9}$$

where $N_{\rm tot} \equiv \int_{\omega_{\rm min}}^{\omega_{\rm max}} n(\omega) d\omega$ is the total number of systems, $\omega_{\rm min}$ and $\omega_{\rm max}$ are the minimum and the maximum initial angular velocities, and $\omega_{\rm evol}$ is the initial angular velocity of the disks turning into the evolved phase at time t, respectively. Here we set $\omega_{\rm min} = 0.007$ and $\omega_{\rm max} = 0.1$ (see §8.3) because the point is we are trying to derive the initial angular momentum distribution from the disk frequency. Thus, we take $f(t) = \exp(-t/\tau_{\rm disk})$ where $\tau_{\rm disk} = 2.5$ Myr and estimate the initial angular momentum distribution. By taking derivative

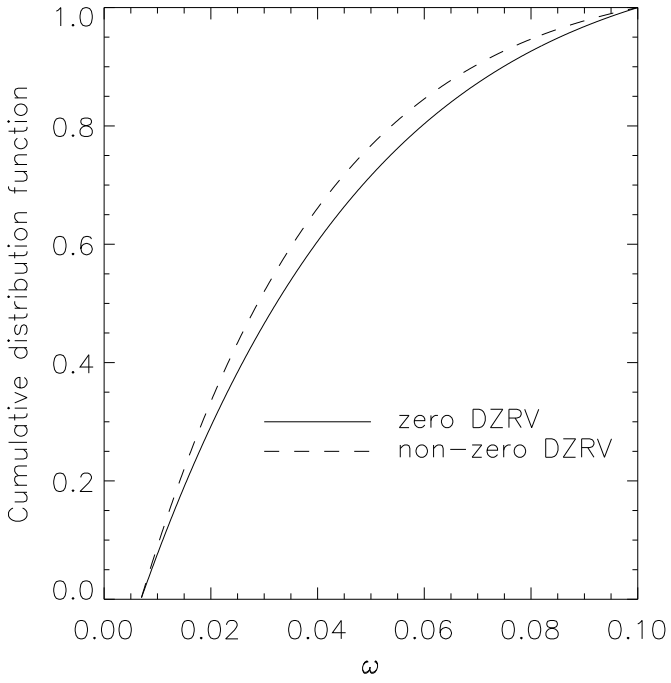

Figure 8.12. Cumulative distribution of initial angular momentum of zero (solid curve) and non-zero (dashed curve) DZRV models.

of Equation (8.9),

$$\frac{df}{dt} = -\frac{1}{N_{\rm tot}} \frac{d\omega_{\rm evol}}{dt} n(\omega). \tag{8.10}$$

Then, since we have $d\omega_{\rm evol}/dt$ from our calculations (a derivative of the fit in Figure 8.11) we can estimate $n(\omega)$.

Figure 8.12 presents the resulting cumulative distribution of initial angular momentum. In both zero and non-zero DZRV cases about a half of the disks have initial angular momentum smaller than our fiducial value 0.03. The distribution steeply decreases toward the populations with large initial angular momentum. In Figure 8.13, we present disk frequency obtained assuming the initial angular momentum distribution we have in Figure 8.12. The lack of initially rapidly-rotating systems might reflect initial conditions; however, a more plausible explanation is that rapidly-rotating protostellar cores end up fragmenting into binaries or multiple stellar systems (Kratter et al., 2008; Vorobyov, 2010; Zhu et al., 2012a). In terms of specific angular momentum in units of cm^2 s^{-1}, our models range from $\log j \sim 17.2$ to 20.3 at the end of infall and have less after infall ends as systems lose angular momen-

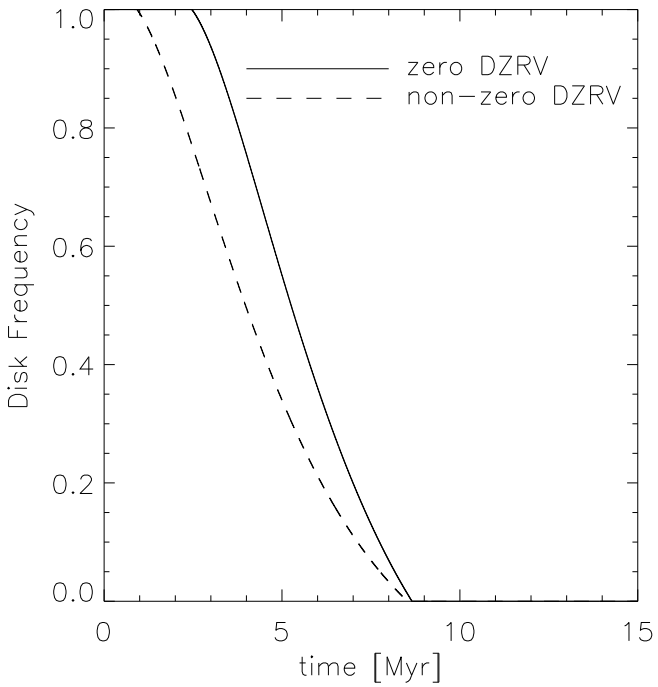

Figure 8.13. Disk frequency of zero (solid curve) and non-zero (dashed curve) DZRV models obtained assuming the initial angular momentum distribution presented in Figure 8.12.

tum through photoevaporative winds. This is about two orders of magnitude smaller than the observed specific angular momenta of molecular clouds, $\log j \sim 19.6 - 22.2$ in units of $\mathrm{cm}^2\ \mathrm{s}^{-1}$ (Goodman et al., 1993; Barranco & Goodman, 1998; Caselli et al., 2002; Andrews et al., 2010). However, since it is questionable to directly compare angular momenta of disk systems to those of molecular clouds given observational difficulties (e.g. Isella et al., 2009), here we limit comparison of our disks to evolved binary systems only. If we take a median orbital period of nearby solar-like binaries $P \sim 180$ yr (Duquennoy & Mayor, 1991), a binary system with two 0.5 $M_\odot$ stars has a specific angular momentum of $\log j \sim 20.4$ which is close to the highest end of the angular momentum distribution obtained in our models. This may support the idea that rapidly rotating molecular cloud cores preferentially fragment into binaries or multiple stellar systems.

8.5.3 Two Populations on the $\dot{M} - R_{\rm wall}$ Plane

Detailed modeling of the broadband SEDs of individual disks enables us to search for gaps or inner holes in their density distribution and to estimate their sizes (e.g. Calvet et al., 2002, 2005; Espaillat et al., 2007, 2008, 2010, 2012; Kim et al., 2013). Combined with mass accretion rate, these information may provide an important clue to the inner disk clearing mechanism.

In Figure 8.14 we show the probability distribution of our transitional disks on the $\dot{M} - R_{\rm wall}$ plane. We calculate the probability based on the time a disk spends at a given grid on the plane. Then, we weight the probability with the initial angular momentum distribution estimated in the previous section. We note that this does not change the overall trend significantly. We additionally assume equal chance to have either zero DZRV or non-zero DZRV for simplicity. The minimum accretion rate is arbitrarily set to $10^{-11}\ M_{\odot}\,{\rm yr}^{-1}$. The gradation in color from the left to right seen in the plot is because of using logarithmic radial grids. In this analysis, we assume that we can verify gaps and inner holes out to large enough radii instead of using the evolved disk criteria described in §4.1 since the studies modeling the SEDs of individual disks we refer here use broadband SEDs out to 40 μm (Kim et al., 2013) or even further out to sub-mm/mm (Espaillat et al., 2010, 2012).

It is evident from Figure 8.14 that there are two distinct populations which occupy different regions and have different evolutionary paths on the $\dot{M} - R_{\rm wall}$ plane as well. Accreting transitional disks open gaps while the dead zone still survives, so can have accretion rates as high as $\sim 10^{-8}\ M_{\odot}\,{\rm yr}^{-1}$ and have gaps at relatively large radii ($R_{\rm wall} \gtrsim 6$ AU). On the other hand, non-accreting transitional disks have lower accretion rate of $\lesssim 10^{-10}\ M_{\odot}\,{\rm yr}^{-1}$ and only produce small inner holes ($R_{\rm wall} \lesssim 3$ AU).

Data taken from the literature (Natta et al., 2006; Najita et al., 2007; Güdel et al., 2007; Brown et al., 2009; Hughes et al., 2009, 2010; Espaillat et al., 2010; Merín et al., 2010; Andrews et al., 2011; Espaillat et al., 2011; Kim et al., 2013) are overplotted on Figure 8.14. While we can see some objects that lie close to the predicted region with high probabilities, a large fraction of the observed disks have moderate accretion rates of $10^{-10} < \dot{M} < 10^{-8}\ M_{\odot}\,{\rm yr}^{-1}$. However, it should be noted that the estimated probability of

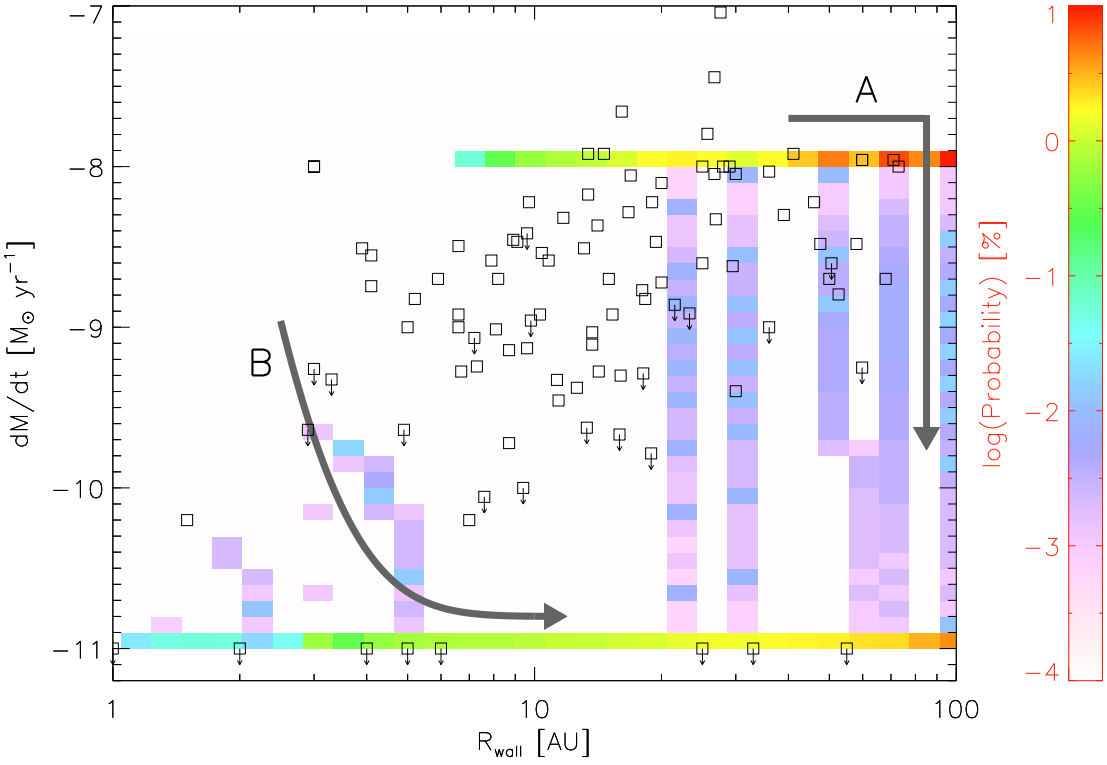

Figure 8.14. The probability distribution of transitional disks on the $\dot{M} - R_{\rm wall}$ plane. The squares present observed transitional disks taken from literatures. The data points with arrows indicate the upper limit of the accretion rate. Objects classified as non-accreting are plotted with an accretion rate of $10^{-11}\ M_\odot\,{\rm yr}^{-1}$. One can see two distinct evolutionary paths; (A) transitional disks with gaps have high accretion rate ($\sim 10^{-8}\ M_\odot\,{\rm yr}^{-1}$) initially and move to right before they stop accreting, while (B) transitional disks with inner holes have lower accretion rate ($\lesssim 10^{-9}\ M_\odot\,{\rm yr}^{-1}$) initially, move downward, and then move to right after stop accreting. It should be noted that the transition to the non-accreting phase in both cases is so fast that one can have only a small chance (< 1 %) to observe moderately accreting transitional disks.

observing such objects with moderate accretion rates is low (< 1 %). This implies that it is unlikely for the observed transitional disks with moderate accretion rate to be transiting from accreting phase to non-accreting phase, as far as its short timescale is considered. Instead, we propose that those disks can be explained by varying Σ_A (e.g., Morishima, 2012), $\alpha_{\rm MRI}$, stellar mass, etc., which are fixed in our calculations. Varying those parameters is, however, beyond the scope of this Chapter.

8.5.4 Millimeter Flux Densities of Transitional Disks

In order to test properties of transitional disks at millimeter wavelengths we calculate flux densities at 1.3 mm. The face-on flux density is calculated as

$$F_\nu = \frac{1}{d^2} \int B_\nu(R) 2\pi R dR, \tag{8.11}$$

assuming a distance of $d = 140$ pc. Here, $B_\nu(R) = B_\nu(T_a(R))(1 - e^{-\tau_a(R)}) + B_\nu(T_d(R))(1 - e^{-\tau_d(R)})e^{-\tau_a(R)}$ where B_ν is the Planck function. We use temperature profiles that are self-consistently calculated in our code as explained in §8.3. Optical depths of the active layer and the dead zone, τ_a and τ_d, are obtained with the general opacity of $\kappa_\nu = 0.1\,(\nu/10^{12}\ \mathrm{Hz})\ \mathrm{cm}^2\ \mathrm{g}^{-1}$ (Beckwith et al., 1990).

Figure 8.15 shows the evolution of transitional disks on the millimeter flux $- R_{\rm wall}$ plane. We see that both accreting and non-accreting transitional disks evolve in a way that the flux density declines and $R_{\rm wall}$ increases, with more massive disks having higher millimeter flux densities in general. In addition, both accreting and non-accreting transitional disks spend most of their time in the large-cavity region ($R_{\rm wall} \gtrsim 15$ AU, Andrews et al. 2011) of the plane; accreting transitional disks open gaps at large radii with an inner dead zone, while in non-accreting transitional disks inner holes open at small radii but grow quickly because of the absence of the dead zone and the enhanced photoevaporation at the inner edge of the disk (see Figure 8.1). We note that transitional disks with large initial angular momenta have a longer disk clearing time (both absolute time and relative time to the total disk lifetime) than those with small initial angular momenta, which possibly explains a high transitional disk fraction in the millimeter-bright disks (Andrews et al., 2011), although the current results may be affected by the observational bias toward detecting larger holes, which favors larger disks with larger masses.

We note that a sudden drop in flux density occurs for accreting transitional disks as the inner disk depletes. This is because the outer disk is already optically thin when a gap opens and thus the inner disk contributes a comparable amount of millimeter emissions (see Figures 8.6, 8.7, and 8.8). The disk mass, however, does not change significantly during the drop since the inner disk has only small mass in it. Due to the emissions from the inner disk, while

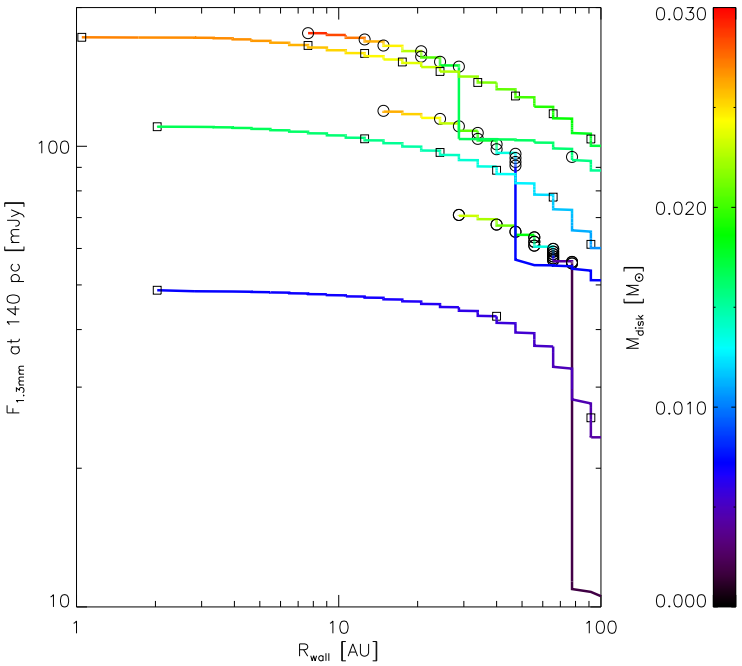

Figure 8.15. Evolution of transitional disks on the millimeter flux$-R_{\rm wall}$ plane with (squares) zero and (circles) non-zero DZRV for three different initial angular momenta; $\omega = 0.012$, 0.02, and 0.03 (from bottom to top). Symbols are overplotted every 0.1 Myr and disk masses are color-coded.

accreting, the accreting transitional disks have systematically higher flux densities than the non-accreting transitional disks with the same initial angular momentum, which presumably explain the observed millimeter-bright transitional disks having considerable higher accretion rates (Owen & Clarke, 2012).

However, we find a number of observed millimeter-faint transitional disks with small cavities as well (see Figure 1 of Clarke & Owen 2013 and references therein). Our models can explain those transitional disks with small initial angular momenta plus non-zero DZRV, but given again that the inner cavity in such models grows rapidly one may need other inner disk clearing mechanisms such as planet formation and/or planet migration.

8.5.5 Viscous Evolution of the Outer Disk

While we have mainly focused on disk properties inside of $\lesssim$ 100 AU so far, sub-mm and mm interferometric observations of CO line emission have shown that some gaseous disks

extend out to several hundred AU or even further (Piétu et al., 2007; Schaefer et al., 2009; Öberg et al., 2010; Andrews et al., 2012). In order to compare our results to observations we use a simple prescription for the viscous evolution of accretion disks (Lynden-Bell & Pringle, 1974; Hartmann et al., 1998). The model assumes a viscosity that is written as a power law in R as $\nu \propto R^{\gamma}$ and has a surface density profile of

$$\Sigma = (2-\gamma)\frac{M_d}{2\pi R_d^2}\left(\frac{R}{R_d}\right)^{-\gamma}\exp\left[-\left(\frac{R}{R_d}\right)^{2-\gamma}\right], \tag{8.12}$$

where R_d is a characteristic scaling radius and M_d is the disk mass. As we show earlier, the evolution of outer disks at $\gtrsim 100$ AU is not affected significantly by outbursts. In addition, the mass-loss due to photoevaporation at such large radii is negligible. Therefore, it seems reasonable to assume that outer disks evolve viscously.

Figure 8.16 shows the best fit characteristic radii of density profiles together with disk masses at given times. Although disk structures at small radii may be complicated, we see that outer disks evolve in the same way that angular momentum is conserved, $M_d \propto R_d^{-1/2}$. Disks with different initial angular momenta spread roughly perpendicular to the evolution path at each given time. The viscous evolution seen in our models is consistent with the observed disk mass – radius relation (e.g. Andrews et al., 2011).

Photoevaporating disks have systematically smaller masses than the non-photoevaporating disks due to mass-loss, but there seems to be no significant difference in the viscous evolution of outer disks between the two populations. However, we see photoevaporation leads depopulation of disks in the lower right corner of the plots, especially in the non-zero DZRV models where disks evolve faster.

8.6 Discussion

Our simulations show that photoevaporative loss alone, coupled with a range of initial angular momenta of the prostellar cloud, can in principle explain the observed disk frequencies, rather than assuming variations in long-term X-ray luminosities as in Owen et al. (2012). However, in both treatments a rather high photoevaporative rate is required which amounts

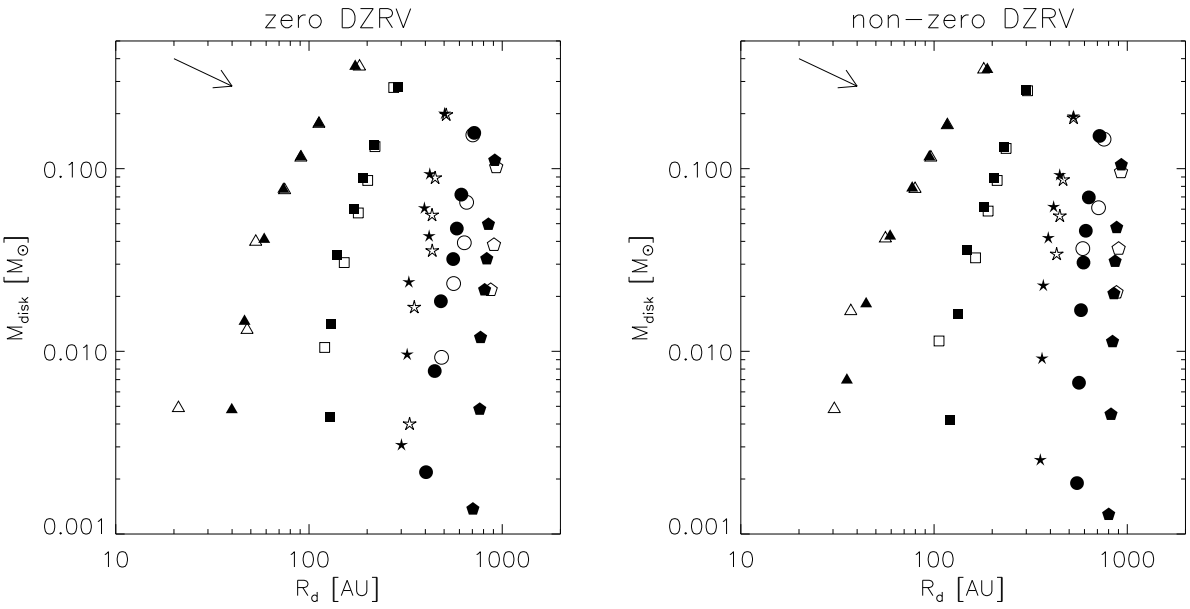

Figure 8.16. The disk masses and characteristic radii of (a) zero and (b) non-zero DZRV models, at 0.5 (triangles), 1 (squares), 2 (stars), 3 (circles), and 5 Myr (pentagons). The filled symbols present non-photoevaporating disks while the opened ones present photoevaporating disks. The arrows indicate the direction of evolution which conserves angular momentum.

to $\sim 10^{-8}\ M_\odot\,\mathrm{yr}^{-1}$, basically the same as the typical disk accretion rate. While direct, quantitative observational estimates of the photoevaporative mass-loss rate are difficult to make, unfortunately, the "low-velocity" wind component seen in forbidden lines of T Tauri stars (Hartigan et al., 1995) may represent the photoevaporative loss from disks. Using the same radiation-hydrodynamic model as in Owen et al. (2010, 2011, 2012), Ercolano & Owen (2010) showed that both the luminosities and profiles of the low-velocity component of the [O I] forbidden lines observed by Hartigan et al. (1995) can be successfully reproduced. Their most successful model assumes a 0.7 $M_\odot$ central star with $L_X = 2 \times 10^{30}$ erg s^{-1}, which corresponds to photoevaporation rate of $\sim 1.4 \times 10^{-8}\ M_\odot\,\mathrm{yr}^{-1}$. However, the predicted line luminosities of the winds depend very sensitively on the assumed X-ray luminosity (see Table 1 of Ercolano & Owen 2010).

The required total photoevaporation rate of $\sim 10^{-8}\ M_\odot\,\mathrm{yr}^{-1}$ also matches well with the expected disk gas dispersal of the solar system. In our model photoevaporation yields mass-loss of ~ 100 g cm^{-2} per million years at Jupiter's orbit. Inferred from the required initial surface density of solids to form Jupiter at its radii and solar chemical compositions,

$\sim$ 700 g cm^{-2} of gas is thought to initially be present at Jupiter's orbit (Pollack et al., 1996, and references therein) but to be depleted over the typical disk lifetime suggested by observations, $\sim$ 3 Myr (Haisch et al., 2001; Hernández et al., 2007; Mamajek, 2009). Thus, within a factor of two our photoevaporative mass-loss rate fits the minimum-mass solar nebula model.

In our models, the dead zone usually has a surface density of $\gtrsim 10^4$ g cm^{-2}. Assuming a 0.8 $M_\odot$ central star, photoevaporation removes maximum $\sim$ 400 g cm^{-2} of material from the circumstellar disk per 1 Myr. This means that without significant accretion it is difficult to deplete the dead zone through photoevaporation only within the typical disk lifetime. In our zero DZRV models, where the outside-in bursts are not efficient and/or not frequent enough to deplete disk material, the dead zone survives long and thus it may act as a potential trap for planets not to migrate inward rapidly (Hasegawa & Pudritz, 2011, 2012). The long-lived dead zone also prevents the outer disk from rapid evaporation through the enhanced photoevaporative and might provide favorable conditions for giant planet formation.

While our photoevaporating disk models can explain observations of the disk frequency vs. age and the transitional disk frequency, it is worthwhile to note that our results are sensitive to the assumed parameters. As we showed in §8.4.5 details of disk evolution, such as when and where a gap opens and whether a disk evolves into an accreting or a non-accreting transitional disk, etc., are significantly dependent upon the density structure of the disk. Also, there should be some regions in which viscous transportation of material is very limited (i.e. a dead zone). In this sense, the assumption of fully-viscous disk assumed in much of protoplanetary disk simulations should be used with caution. Furthermore, our results are sensitive to the photoevaporation rate. As pointed out in §8.4.6, we do not see accreting transitional disks with 30 % less photoevaporation rate, and 10 % of the standard rate turns out to be insufficient to significantly affect disk evolution. Thus, photoevaporation is a crucial factor in long-term disk evolution.

Recently, Kim et al. (2013) claimed that the gaps in transitional disks of their sample are likely due to the gravitational influence of Jovian planets or brown dwarfs orbiting within the gaps, and that X-ray photoevaporation is not the dominant mechanism for creating transitional disks. They draw the latter part of their conclusion by comparing their data

with the theoretical predictions from the X-ray photoevaporation model by Owen et al. (2012). However, one of the main assumptions in Owen et al. (2012) is questionable; profiles of transitional disks are self-similar in a way that if a gap opens at 1 AU around a 1 $M_{\odot}$ it would open at 0.1 AU around a 0.1 $M_{\odot}$ star. This may be true for fully viscous disks obeying the similarity solution (Lynden-Bell & Pringle, 1974). However, as explained in §8.3 disk size is mainly determined by the centrifugal radius R_c, which is proportional to M_c^{-1} if we assume a constant Ω_c and is proportional to M_c^{-3} if we assume a constant ω for different stellar masses. Thus, if this is the case less massive stars will have less massive but more extended surrounding disks, which is not self-similar to more massive stars. Also, the existence of the dead zone will complicate the details of disk structures and their evolution.

In addition, the probability of detecting accreting transitional disks in the predicted region by photoevaporation model of OEC11 (the shaded region of Figure 24 in Kim et al. 2013) is low ($\lesssim$ 1 %, see Figure 13 of OEC11), while Owen et al. (2012) later suggested that there may be a rapid dynamical clearing mechanism of the outer disk of non-accreting transitional disks, so-called thermal sweeping, i.e. X-ray penetrates further in the disk midplane as the bound X-ray heated gas starts to flow predominantly vertically, alleviating the low probability.

We note that there are some limitations in our analysis so caution is needed when interpreting the results. First, our photoevaporation prescription is obtained from the simulations using disks with an approximate power-law radial structure (Owen et al., 2010, 2011, 2012). Thus, it is not obvious that the mass-loss rate and/or profile are applied in the same way to disks with more complicated radial structure, such as the dead zone. The mass-loss rate can be insensitive to disk structure as Owen et al. (2012) stated in their results, but more thorough calculations are needed in order to deal with this issue. Second, we estimate the disk frequency based on the existence of IR excess at 8 μm assuming a simple blackbody wall temperature. This implicitly assumes that gas and dust are well mixed and evolve in the same manner, which is not necessarily the case as several studies have shown observationally (e.g. Ingleby et al., 2011; Andrews et al., 2012) and numerically (e.g. Alexander & Armitage, 2007). Third, close binaries can also disrupt disks, although the analysis of Kraus et al. (2012) suggests that this may not affect the disk frequency vs. age (see their

Figure 3). Fourth, while observations include a wide range of stars in mass, we only consider 0.1 $M_\odot$ core + 1 $M_\odot$ cloud. We expect different initial masses will result in a more diverse evolution. Fifth, note that our definition and classification of transitional disks are limited by the neglect of possible dust migration and evolution, which might increase the ratio of accreting to non-accreting transition disks Alexander & Armitage (2007). Our results also do not rule out giant planet formation as the dominant mechanism for disk clearing; as Rosotti et al. (2013) suggest, a combination of planet gap opening and photoevaporation may be particularly effective in producing large disk gaps.

Finally, we note the importance of using a small inner boundary in simulations. In our photoevaporating models, the non-accreting transitional phase starts with gaps opened at small radii of $0.6 - 3.3$ AU (see Table 8.2). Once an inner hole is created photoevaporative winds clear the outer disk rapidly, within ~ 0.01 Myr in the fastest case for example. Therefore, it is worth emphasizing that simulations need to use a small inner boundary of $R \lesssim 1$ AU to capture the rapid inside-out disk clearing via photoevaporation.

8.7 Summary

In this Chapter, we present long-term evolution of protostellar disks using the one-dimensional, two-zone disk model introduced in Zhu et al. (2010a,b) and modified in Chapter 2 of this thesis. We found that disks accrete material more efficiently when they have non-zero viscosity in the dead zone, and thus have a shorter lifetime.

By adding photoevaporation to our models and varying initial angular momentum, we were able to produce accreting and non-accreting transitional disks with reasonable timescale of $\lesssim 20$ % of the total lifetime which is in reasonable agreement with observations. We found that disks having non-zero DZRV preferentially evolve into non-accreting transitional disks due to a short disk depletion time, while evolution of disks with zero DZRV varies depending on the initial angular momentum. Starting with small initial angular momentum of $\omega \lesssim 0.04$, zero DZRV models evolve into accreting transitional disks with high accretion rate of $\sim 10^8\ M_\odot\,\mathrm{yr}^{-1}$. We note that relatively inefficient accretion in the dead zone help the disks to have the accreting transitional disk phase. On the other hand, for initially rapidly rotating

cases with $\omega > 0.04$, zero DZRV models evolve into non-accreting transitional phase since a significant fraction of the disk mass resides in the large radii and thus photoevaporation cannot open a gap at such radii.

The observed disk frequency could be explained using our photoevaporating disk models by varying initial angular momenta, as an alternative to the adoption of varying long-term stellar X-ray luminosities by Owen et al. (2011). Assuming that photoevaporation controls disk evolution, we found the initial angular momenta need to be distributed in a way that decreasing significantly toward the systems with large initial angular momentum. Comparison of angular momenta of our models to the observed nearby solar-type binaries suggests that rapidly-rotating molecular cloud cores end up fragmenting into multiple systems with smaller disk, while those with slow rotation results in a single star-disk system. Our models also explain the different observed properties between accreting and non-accreting transitional disks, each of which occupies different regions and follows different evolutionary paths on the $\dot{M} - R_{\rm wall}$ plane.

8.8 Acknowledgments

We acknowledge support from NASA grant NNX11AK53G and the use of the University of Michigan Flux cluster. C.G. was supported in part by a Richard and Margaret Romano Professorial Scholarship.

CHAPTER IX

Conclusion

A huge paradigm shift in the studies of circumstellar disks and planet formation has been made during the last decade. On the observational side, state-of-the-art telescopes have revealed fine structures (as well as large gaps and cavities) in circumstellar disks. On the theoretical side, new scenarios have been proposed to ease long-standing problems: MHD winds as a potential dominant disk accretion mechanism, and accreting pebbles as a solution for the excessive timescale needed to assemble solid material into planets/planetary cores. These findings made my PhD years special and exciting moments in studying circumstellar disks and planet formation, and I am very hopeful that there will be more exciting findings in the coming years.

In this Chapter, I first summarize the findings from my thesis. Then, I discuss possible future work that can be built upon the findings to improve our understanding of the evolution of circumstellar disks and the planet formation processes.

9.1 Summary of Findings

9.1.1 Protostellar Accretion Outbursts

In Chapter 2, we have investigated the effects of a finite viscosity in the magnetically inert disk dead-zone on the disk instability-driven protostellar outburst model. We have shown that the presence of a small but finite dead-zone viscosity can significantly alter the properties of accretion outbursts, including the triggering of outbursts, peak accretion rate, outburst duration, and period between outbursts. In particular, we found that the addition of non-

zero dead-zone viscosity can trigger the MRI at or near the inner edge of the disk, resulting in inside-out bursts of accretion, instead of the previously-found outside-in bursts with zero dead-zone viscosity, which originate at a few AU in radius by GI. In terms of outburst behavior, these inside-out bursts of accretion show a slower rise in accretion rate at the beginning of bursts with a lower accretion rate at the peak than the outside-in bursts, bearing a qualitative resemblance to the outburst behavior of one FU Ori object, V1515 Cyg. On the other hand, if accretion in the disk is driven by non-dissipative winds as recently suggested by Bai & Stone (2013a) and Gressel et al. (2015), instead of viscous dissipation, it may be possible that there is not enough heating to thermally trigger the MRI.

GI plays an important role in initiating the outburst cycle, especially when the disk dead-zone has negligible viscosity as we have shown in Chapter 2. However, the works in Chapter 2 used one-dimensional models so the angular momentum transport and disk heating associated with GI (as well as MRI) had to rely on the α parameterization. In Chapter 3, we improved the one-dimensional models presented in Chapter 2, by explicitly solving disk self-gravity in a two dimensional $R-\phi$ computation domain. By investigating the contributions from various heating sources, we found that it is through compressional heating (i.e., $P\mathrm{d}V$ work) that the GI-driven spiral waves heat the inner disk and initiate the outburst cycle. Also, these two-dimensional models showed that the GI-induced spiral waves propagate to sub-AU regions, well inside of gravitationally unstable region, before they thermally trigger the MRI there, which cannot be properly treated with the previously used α parameterization for GI. Regarding the luminosity problem introduced in §1.2.3, our evolutionary models showed that protostellar systems stay roughly two-thirds of the total time during the infall phase in the quiescent accretion phase with $\dot{M} \sim 10^{-8}\ M_{\odot}\ \mathrm{yr}^{-1}$ and spend only about 10 % of the infall phase in the outbursting phase. We suggested that episodic accretion outbursts can thus be a possible solution to the problem. As emphasized in Chapter 3 and above, GI-driven spiral waves are crucial to initiate the outburst cycle. With the SWI, however, GI-driven waves may dissipate and the picture suggested above can change. The implications of the SWI on the disk instability-driven outburst model will be further discussed in §9.2.

9.1.2 Infall-driven Vortex Formation

In Chapter 4, we proposed protostellar infall as a possible new mechanism to form vortices in circumstellar disks. Infall streams generate a steep radial gradient in the azimuthal velocity by locally increasing density around the centrifugal radius – the outer edge of the mass landing on the disk. The RWI can be triggered at the density/pressure bump, forming vortices there. Our two-dimensional, two-fluid calculations showed that the vortices can collect solid particles efficiently, locally enhancing the dust to gas ratio within the vortices. This work demonstrates that vortex formation in circumstellar disks is possible during the infall phase, suggesting planet/planetary core formation can start earlier than previously expected. This scenario potentially explains the emerging observational evidence for early planet formation (e.g., ALMA Partnership et al., 2015).

9.1.3 Planetary Signatures in the SAO 206462 Disk

The disk surrounding SAO 206462, an 8 Myr old Herbig Ae star, is one of the most popular circumstellar disks because of various interesting structures observed. Previous observations have revealed that the disk exhibits two-armed spirals in scattered light images taken at μm bands (Muto et al., 2012; Garufi et al., 2013; Stolker et al., 2016) and a vortex-like asymmetry in sub-millimeter thermal emission (Pérez et al., 2014). In Chapter 5, we have constructed two-dimensional models in which a planetary-mass companion orbits around the central star. The models showed that a planetary-mass companion can create vortex and spiral structure similar to that observed in SAO 206462. We suggested that an interaction between a spiral arm and the vortex can explain the abrupt change in brightness seen in the scattered light observations. We also suggested possible mass range and location of the planetary companion, which can help guide future observations to search for more conclusive evidence of a planetary body in the system.

9.1.4 Spiral Wave Instability

Spiral waves are found in various astrophysical disks, including circumstellar disks. In Chapter 6, we showed that spiral density waves in astrophysical disks, driven for instance by com-

panion bodies or gravitational instability, can undergo a parametric instability by resonantly coupling with and transferring energy into pairs of inertial waves. During the non-linear phase of the instability, growing unstable inertial modes lead to dissipation of the spiral waves, which in turn can enhance the level of turbulence in the disk. We have examined the development of the SWI with a wide range of disk models, including those with/without vertical density stratification, with isothermal/adiabatic equations of state for gas, and with inviscid/viscous disks, as well as with various numerical codes and resolutions, and showed that the instability is robust. The robustness of the SWI suggests that the instability has potential to be applicable to a broad range of astrophysical disk-related phenomena, including protostellar outburst models.

In Chapter 7, we showed that the SWI operates on the spiral waves launched by a Jupiter-mass planet in a circumstellar disk. The instability generates hydrodynamic turbulence, in agreement with the work presented in Chapter 6. Interior to the planetary orbit, the estimated vertical diffusion rate associated with the turbulence is $\alpha \sim (0.2 - 1.2) \times 10^{-2}$, which is sufficient to loft solid particles with sizes up to several centimeters in the disk model considered in the work. In the solar system, the best laboratory to examine the timing and outcome of planet formation in detail, Jupiter is generally thought to be the first planet that finished accretion. By the time Jupiter had formed, terrestrial bodies are generally thought to grow up to about Moon or Mars-mass embryos (see review by Dauphas & Chaussidon 2011 and Morbidelli et al. 2012 and references therein). If gas giant formation generally precedes terrestrial planet formation in circumstellar disks and if accretion of pebbles is the dominant mechanism to grow planetesimals into larger bodies, the results in Chapter 7 can imply that the formation of gas giants in circumstellar disks can put a time constraint on the formation of terrestrial planets.

9.1.5 Photoevaporating Disks

Implementing photoevaporation prescriptions of Owen et al. (2012), which obtain the X-ray-driven photoevaporative mass-loss rate using radiation-hydrodynamic models, onto the one-dimensional evolutionary model in Chapter 2, we examined dispersal of circumstellar disks. In particular, we tested whether the photoevaporative loss, coupled with a range

of initial angular momenta of protostellar clouds, can explain the observed decline of the disk frequency with increasing age. For the parameter space explored in the study, the photoevaporating disk models showed that disks disperse within $\sim$ 1–10 Myr, with the exact timing of dispersal dependent mainly on the initial angular momentum of the natal cloud: disks with larger initial angular momenta disperse at later time because such disks start with more mass to disperse. We also found that, in order to fit the observed frequency of optically thick dusty disks, the initial angular momentum distribution of clouds have to be skewed toward slow initial rotation, with median value of ~ 3 % of the breakup angular rotation for clouds. If disk dispersal is dominated by photoevaporation, the results imply that the skewed angular momentum distribution toward slow rotation can be a result of fragmentation into binary or multiple stellar systems in rapidly rotating cores.

9.2 Future Directions

There are many possible future projects suggested by the results of this thesis work. First of all, it will be interesting to see how the SWI affects the disk instability model of protostellar accretion outbursts. The two-dimensional simulations presented in Chapter 3 have shown that the compressional heating from GI-driven spiral waves is crucial to initiate outburst cycles. However, because those simulations are carried out in two dimensions, the SWI was not able to be properly captured. In three-dimensional disks, the SWI can operate on GI-driven waves, in which case the waves will be (partially or totally) dissipated into turbulence and therefore compressional heating will be much less significant than those found in two-dimensional simulations. On the other hand, the wave energy lost via the SWI has to be converted to some other forms and it is possible that disk gas can still be heated enough to trigger outbursts, through turbulent heating. Another important aspect is that GI-driven waves propagate from the outer disk, where the disk is gravitationally unstable, to sub-AU regions before they trigger outbursts by thermally activating the MRI there. It will be important to study how the propagation of waves changes (or not) and at which radii the wave energy is deposited as waves propagate SWI-turbulent medium. Future three-dimensional simulations with proper treatments for disk thermodynamics will help answer

these questions.

Regarding the SWI itself, it warrants more systematic resolution/parameter studies. The SWI is intrinsically a three-dimensional phenomenon because inertial modes can have arbitrary wave vector in three dimensions. Also, inertial modes have a dense spectrum in their length scales, meaning that they can have any arbitrarily small length scale. As a result, simulations of the SWI have to run for many dynamical timescales in three-dimensions, with sufficiently high resolutions. Using local computation domains thus can help. I am planning on running high-resolution local simulations of the SWI to better investigate the numerical convergence and better characterize the turbulence driven by the SWI – e.g., the level of turbulence; the growth rate of the instability; whether or not the turbulence is isotropic; how the turbulence cascade down; and which length scale of the turbulence contains the largest power. The measured turbulence level can serve as an important – but only poorly constrained by far – input parameter in (1) planet formation models where the thickness of particle layers affects the growth rate of planets/planetary cores (e.g., pebble accretion models); (2) synthetic observations of numerical simulations where the vertical distribution of solid particles determines the radiative properties of the disk; and (3) evolutionary models where one does not have full three dimensions and/or enough numerical resolution to capture the SWI, but can study longer-term evolution of dusty disks. Also, these local simulations will serve as a solid standing point for future studies of circumstellar disks with more realistic disk properties (e.g., thermodynamics), but also other disks with spiral arms, such as circumplanetary disks, circumbinary disks, and the accretion disks around cataclysmic variables, X-ray binaries.

Searching for observational evidence of the SWI at work will also be of great interest. The best testbed for this purpose would be the circumstellar disks that are known to have spiral arms (e.g., SAO 206462, MWC 758). As suggested by recent magnetocentrifugal wind models (Bai & Stone, 2013a; Gressel et al., 2015), circumstellar disks are believed to remain laminar – no or very little turbulence – near the midplane. ALMA observations of optically thin emission lines, which trace near the midplane, will help constrain the level of turbulence that can be driven by the SWI.

BIBLIOGRAPHY

Adams, F. C., & Watkins, R. 1995, ApJ, 451, 314

Alexander, R. D., & Armitage, P. J. 2007, MNRAS, 375, 500

Alexander, R. D., & Armitage, P. J. 2009, ApJ, 704, 989

Alexander, R. D., Clarke, C. J., & Pringle, J. E. 2006, MNRAS, 369, 216

Alexander, R., Pascucci, I., Andrews, S., Armitage, P., & Cieza, L. 2014, in Protostars and Planets VI, ed. H. Beuther, R. Klessen, C. Dullemond, & T. Henning (Tucson, AZ: Univ. Arizona Press), 475

Allen, A., Li, Z.-Y., & Shu, F. H. 2003, ApJ, 599, 363

ALMA Partnership, Brogan, C.L., Pérez, L. M., et al. 2015, ApJL, 808, L3

Andrews, S. M., Wilner, D. J., Hughes, A. M., Qi, C., & Dullemond, C. P. 2009, ApJ, 700, 1502

Andrews, S. M., Wilner, D. J., Hughes, A. M., Qi, C., & Dullemond, C. P. 2010, ApJ, 723, 1241

Andrews, S. M., Wilner, D. J., Espaillat, C., et al. 2011, ApJ, 732, 42

Andrews, S. M., Wilner, D. J., Hughes, A. M., et al. 2012, ApJ, 744, 162

Andrews, S. M., Rosenfeld, K. A., Kraus, A. L., & Wilner, D. J. 2013, ApJ, 771, 129

André, P., Ward-Thompson, D., & Barsony, M. 1993, ApJ, 406, 122

André, P., Ward-Thompson, D., & Barsony, M. 2000, in Protostars and Planets IV, ed. V. Mannings, A. P. Boss, & S. S. Russell (Tucson, AZ: Univ. Arizona Press), 59

Armitage, P. J., Livio, M., & Pringle, J. E. 2001, MNRAS, 324, 705

Artymowicz, P., & Lubow, S. H. 1992, ApJ, 389, 129

Artymowicz, P., & Lubow, S. H. 1994, ApJ, 421, 651

Aspin, C., Reipurth, B., Herczeg, G. J., & Capak, P. 2010, ApJL, 719, L50

Bai, X.-N. 2013, ApJ, 772, 96

Bai, X.-N. 2014, ApJ, 791, 137

Bai, X.-N. 2015, ApJ, 798, 84

Bai, X.-N., & Goodman, J. 2009, ApJ, 701, 737

Bai, X.-N., & Stone, J. M. 2011, ApJ, 736, 144

Bai, X.-N., & Stone, J. M. 2013a, ApJ, 767, 30

Bai, X.-N., & Stone, J. M. 2013b, ApJ, 769, 76

Balbus, S. A., & Hawley, J. F. 1998, Reviews of Modern Physics, 70, 1

Balbus, S. A., & Hawley, J. F. 1991, ApJ, 376, 214

Balbus, S. A., & Papaloizou, J. C. B. 1999, ApJ, 521, 650

Barge, P., & Sommeria, J. 1995, A&A, 295, L1

Barker, A. J., & Latter, H. N. 2015, MNRAS, 450, 21

Barker, A. J., & Ogilvie, G. I. 2014, MNRAS, 445, 2637

Barranco, J. A., & Goodman, A. A. 1998, ApJ, 504, 207

Baruteau, C., & Masset, F. 2008, ApJ, 678, 483

Baruteau, C., & Masset, F. 2008, ApJ, 672, 1054

Baruteau, C., Meru, F., & Paardekooper, S.-J. 2011, MNRAS, 416, 1971

Basu, S. 1997, ApJ, 485, 240

Beckwith, S. V. W., Sargent, A. I., Koresko, C. D., & Weintraub, D. A. 1989, ApJ, 343, 393

Beckwith, S. V. W., Sargent, A. I., Chini, R. S., & Gusten, R. 1990, AJ, 99, 924

Bell, K. R. 1999, ApJ, 526, 411

Bell, K. R., & Lin, D. N. C. 1994, ApJ, 427, 987

Benisty, M., Juhasz, A., Boccaletti, A., et al. 2015, A&A, 578, L6

Benson, P. J., & Myers, P. C. 1989, ApJS, 71, 89

Benítez-Llambay, P., & Masset, F. 2016, ApJS, 223, 11

Béthune, W., Lesur, G., & Johathan, F. 2016, arXiv:1612.00883

Birnstiel, T., Dullemond, C. P., & Pinilla, P. 2013, A&A, 550, L8

Bitsch, B., Lambrechts, M., & Johansen, A. 2015, A&A, 582, A112

Boley, A. C., Mejía, A. C., Durisen, R. H., et al. 2006, ApJ, 651, 517

Boley, A. C., Hayfield, T., Mayer, L., & Durisen, R. H. 2010, Icarus, 207, 509

Bonnell, I., & Bastien, P. 1992, ApJL, 401, L31

Boss, A. P. 1997, Sci, 276, 1836

Boss, A. P. 1998, ApJ, 503, 923

Bracco, A., Chavinis, P. H., Provenzale, A., & Spiegel, E. A. 1999, PhFl, 11, 2280

Brown, J. M., Blake, G. A., Qi, C., Dullemond, C. P., Wilner, D. J., & Williams, J. P. 2009, ApJ, 704, 496

Bryden, G., Chen, X., Lin, D. N. C., Nelson, R. P., & Papaloizou, J. C. B. 1999, ApJ, 514, 344

Calvet, N., D'Alessio, P., Hartmann, L., Wilner, D., Walsh, A., & Sitko, M. 2002, ApJ, 568, 1008

Calvet, N., D'Alessio, P., Watson, D. M., et al. 2005, ApJL, 630, L185

Caramazza, M., Flaccomio, E., Micela, G., et al. 2007, A&A, 471, 645

Carmona, A., Pinte, C., Thi, W. F., et al. 2014, A&A, 567, A51

Carpenter, J. M., Mamajek, E. E., Hillenbrand, L. A., & Meyer, M. R. 2006, ApJL, 651, L49

Casassus, S., van der Plas, G., Perez M., S., et al. 2013, Natur, 493, 191

Caselli, P., Benson, P. J., Myers, P. C., & Tafalla, M. 2002, ApJ, 572, 238

Cassen, A., & Moosman, A. 1981, Icarus, 48, 353

Cha, S.-H., & Nayakshin, S. 2011, MNRAS, 415, 3319

Chambers, J. E., & Wetherill, G. W. 1998, Icarus, 136, 304

Chapman, S., & Cowling, T. G. 1970, The Mathematical Theory of Non-uniform Gases. An account of the Kinetic Theory of Viscosity, Thermal Conduction and Diffusion in Gases (3rd ed.; Cambridge: Cambridge Univ. Press)

Chavanis, P. H. 2000, A&A, 356, 1089

Cheng, A. F. 1978, ApJ, 221, 320

Clarke, C. J., & Owen, J. E. 2013, MNRAS, 433, 69

Clarke, C. J., & Pringle, J. E. 1988, MNRAS, 235, 365

Clarke, C. J., Lin, D. N. C., & Pringle, J. E. 1990, MNRAS, 242, 439

Clarke, C. J., Gendrin, A., & Sotomayor, M. 2001, MNRAS, 328, 485

Cossins, P., Lodato, G., & Clarke, C. J. 2009, MNRAS, 393, 1157

Covey, K. R., Hillenbrand, L. A., Miller, A. A., et al. 2011, AJ, 141, 40

Currie, T., Muto, T., Kudo, T., et al. 2014, ApJL, 796, L30

Dauphas, N., & Chaussidon, M. 2011, AREPS, 39, 351

Dauphas, N., & Pourmand, A. 2011, Natur, 473, 489

D'Alessio, P., Calvet, N., & Hartmann, L. 1997, ApJ, 474, 397

D'Angelo, G., Henning, T., & Kley, W. 2003, ApJ, 599, 548

de Val-Borro, M., Edgar, R. G., M., Artymowicz, P., et al. 2006, MNRAS, 370, 529

de Val-Borro, M., Artymowicz, P., D'Angelo, G., & Peplinski, A. 2007, A&A, 471, 1043

Dodson-Robinson, S. E., & Salyk, C. 2011, ApJ, 738, 131

Dominik, C., & Tielens, A. G. G. M. 1997, ApJ, 480, 647

Dong, R. 2015, ApJ, 810, 6

Dong, R., & Fung, J. 2017, ApJ, 835, 38

Dong, R., Zhu, Z., Rafikov, R. R., & Stone, J. M. 2015, ApJL, 809, L5

Dong, R., Fung, J., & Chiang, E. 2016, 826, 75

Dullemond, C. P., & Dominik, C. 2005, A&A, 434, 971

Dunham, M. M., Arce, H. G., Allen, L. E., et al. 2013, AJ, 145, 94

Dunham, M. M., Stutz, A. M., Allen, L. E., et al. 2014, in Protostars and Planets VI, ed. H. Beuther, R. Klessen, C. Dullemond, & T. Henning (Tucson, AZ: Univ. Arizona Press), 195

Dunham, M. M., & Vorobyov, E. I. 2012, ApJ, 747, 52

Duquennoy, A., & Mayor, M. 1991, A&A, 248, 485

Durisen, R. H., Boss, A. P., Mayer, L., et al. 2007, in Protostars and Planets V, ed. B. Reipurth, D. Jewitt, & K. Keil (Tucson, AZ: Univ. Arizona Press), 607

Eisner, J. A. 2012, ApJ, 755, 23

Enoch, M. L., Evans, N. J., II, Sargent, A. I., & Glenn, J., 2009, ApJ, 692, 973

Ercolano, B., Clarke, C. J., & Drake, J. J. 2009, ApJ, 699, 1639

Ercolano, B., & Owen, J. E. 2010, MNRAS, 406, 1553

Espaillat, C., Calvet, N., D'Alessio, P., et al. 2007, ApJ, 670, L135

Espaillat, C., Muzerolle, J., Hernández, J., et al. 2008, ApJ, 689, L145

Espaillat, C., D'Alessio, P., Hernández, J., et al. 2010, ApJ, 717, 441

Espaillat, C., Furlan, E., D'Alessio, P., et al. 2011, ApJ, 728, 49

Espaillat, C., Ingleby, L., Hernández, J., et al. 2012, ApJ, 747, 103

Evans, N. J., II 1999, ARA&A, 37, 311

Evans, N. J., II, Dunham, M. M., Jørgensen, J. K., et al. 2009, ApJS, 181, 321

Fatuzzo, M.F., Adams, F. C., & Myers, P. C. 2004, ApJ, 615, 813

Faure, J., Fromang, S., Latter, H., & Meheut, H. 2015, A&A, 573, A132

Feigelson, E. D., Broos, P., Gaffney, J. A., III, et al. 2002a, ApJ, 574, 258

Feigelson, E. D., Garmire, G. P., & Pravdo, S. H. 2002b, ApJ, 572, 335

Feigelson, E. D., Gaffney, J. A., III, Garmire, G., Hillenbrand, L. A., & Townsley, L. 2003, ApJ, 584, 911

Fleming, T., & Stone, J. M. 2003, ApJ, 585, 908

Forgan, D., & Rice, K. 2010, MNRAS, 402, 1349

Fressin, F., Torres, G., Charbonneau, D., et al. 2013, ApJ, 766, 81

Fromang, S., & Nelson, R. P. 2006, MNRAS, 364, L81

Fromang, S., & Papaloizou, J. 2006, A&A, 452, 751

Fromang, S., & Papaloizou, J. 2007, A&A, 468, 1

Fu, W., Li, H., Lubow, S., & Li, S. 2014a, ApJL, 788, L41

Fu, W., Li, H., Lubow, S., Li, S., & Liang, E. 2014b, ApJL, 795, L39

Fukagawa, M., Tsukagoshi, T., Momose, M., et al. 2013, PASJ, 65, L14

Fung, J., & Dong, R. 2015, ApJL, 815, L21

Fung, J., & Chiang, E. 2016, ApJ, 832, 105

Galli, D., & Shu, F. H. 1993, ApJ, 417, 220

Galli, D., Lizano, S., Shu, F. H., & Allen, A. 2006, ApJ, 647, 374

Gammie, C. F. 1996, ApJ, 457, 355

Gammie, C. F. 1999, Astrophysical Discs - an EC Summer School, 160, 122

Gammie, C. F., Goodman, J., & Ogilvie, G. I. 2000, MNRAS, 318, 1005

Gammie, C. F. 2001, ApJ, 553, 174

Garufi, A., Quanz, S. P., Avenhaus, H., et al. 2013, A&A, 560, A105

Garufi, A., Quanz, S.P., & Schmid, H. M. 2016, A&A, 588, A8

Godon, P., & Livio, M. 1999, ApJ, 523, 350

Goldreich, P., & Tremaine, S. 1978, ApJ, 222, 850

Goldreich, P., & Tremaine, S. 1979, ApJ, 233, 857

Goldreich, P., & Tremaine, S. 1980, ApJ, 241, 425

Goodman, J. 1993, ApJ, 406, 596

Goodman, A. A., Benson, P., Fuller, G., & Myers, P. 1993, ApJ, 406, 528

Gorti, U., & Hollenbach, D. 2009, ApJ, 690, 1539

Gorti, U., Dullemond, C. P., & Hollenbach, D. 2009, ApJ, 705, 1237

Gómez, M., & Kenyon, S. J. 2001, AJ, 121, 974

Grady, C. A., Muto, T., Hashimoto, J., et al. 2013, ApJ, 762, 48

Gressel, O., Nelson, R. P., & Turner, N. J. 2012, MNRAS, 422, 1140

Gressel, O., Nelson, R. P., Turner, N. J., & Ziegler, U. 2013, ApJ, 779, 59

Gressel, O., Turner, N. J., Nelson, R. P., & McNally, C. P. 2015, ApJ, 801, 84

Gutermuth, R. A., Megeath, S. T., Muzerolle, J., et al. 2004, ApJS, 154, 374

Güdel, M., Briggs, K. R., Arzner, K., et al. 2007, A&A, 468, 353

Güttler, C., Blum, J., Zsom, A., Ormel, C.W., & Dullemond, C. P. 2010, A&A, 513, A56

Haisch, K. E., Lada, E. A., & Lada, C. J. 2001, ApJ, 553, L153

Hameury, J.-M., Menou, K., Dubus, G., Lasota, J.-P., & Huré, J.-M. 1998, MNRAS, 298, 1048

Harsono, D., Jørgensen, J. K., van Dishoeck, E. F., et al. 2014, A&A, 562, A77

Hartigan, P., Edwards, S., & Ghandour, L. 1995, ApJ, 452, 736

Hartmann, L. 2009, Accretion Processes in Star Formation (2nd ed.; Cambridge: Cambridge Univ. Press)

Hartmann, L., & Kenyon, S. J. 1996, ARA&A, 34, 207

Hartmann, L., Calvet, N., Gullbring, E., & D'Alessio, P. 1998, ApJ, 495, 385

Hartmann, L., Megeath, S. T., Luhman, K., et al. 2005, ApJ, 629, 881

Hartmann, L., D'Alessio, P., Calvet, N., & Muzerolle, J. 2006, ApJ, 648, 484

Hartmann, L., Herczeg, G., & P., Calvet, N., 2016, ARA&A, 54, 135

Hasegawa, Y., & Pudritz, R. E. 2011, MNRAS, 417, 1236

Hasegawa, Y., & Pudritz, R. E. 2012, ApJ, 760, 117

Hashimoto, J., Tsukagoshi, T., Brown, J. M., et al. 2015, ApJ, 799, 43

Hatzes, A. P., Cochran, W. D., Endl, M., et al. 2003, ApJ, 599, 1383

Hayashi, C. 1981, Progress of Theoretical Physics Supplement, 70, 35

Hayashi, M., Ohashi, N., & Miyama, S. M. 1993, ApJL, 418, L71

Hawley, J. F. 1987, MNRAS, 225, 677

Heng, K., & Kenyon, S. J. 2010, MNRAS, 408, 1476

Hennebelle, P., & Fromang, S. 2008, A&A, 477, 9

Hennebelle, P., & Ciardi, A. 2009, A&A, 506, L29

Herbig, G. H. 1977, ApJ, 217, 693

Herbig, G. H. 2008, AJ, 135, 637

Hernández, J., Calvet, N., Hartmann, L., Briceño, C., Sicilia-Aguilar, A., & Berlind, P. 2005, AJ, 129, 856

Hernández, J., Hartmann, L., Megeath, T., et al. 2007, ApJ, 662, 1067

Hirose, S., & Turner, N. J. 2011, ApJL, 732, L30

Hollenbach, D., Johnstone, D., Lizano, S., & Shu, F. 1994, ApJ, 428, 654

Hollenbach, D. J., Yorke, H. W., & Johnstone, D. 2000, in Protostars and Planets IV, ed. V. Mannings, A. P. Boss, & S. S. Russell (Tucson, AZ: Univ. Arizona Press), 401

Horn, B., Lyra, W., Mac Low, M.-M., & Sándor, Z. 2012, ApJ, 750, 34

Hubeny, I. 1990, ApJ, 351, 632

Hughes, A. M., Wilner, D. J., Calvet, N., D'Alessio, P., Claussen, M. J., & Hogerheijde, M. R. 2007, ApJ, 664, 536

Hughes, A. M., Andrews, S. M., Espaillat, C., et al. 2009, ApJ, 698, 131

Hughes, A. M., Andrews, S. M., Wilner, D. J., et al. 2010, AJ, 140, 887

Ilgner, M., & Nelson, R. P. 2006, A&A, 455, 731

Ilgner, M., & Nelson, R. P. 2008, A&A, 483, 815

Inaba, S., Barge, P., Daniel, E., & Guillard, H. 2005, A&A, 431, 365

Inaba, S., & Barge, P. 2006, ApJ, 649, 415

Ingleby, L., Calvet, N., Hernández, J., et al. 2011, AJ, 141, 127

Isella, A., Carpenter, J. M., & Sargent, A. I. 2009, ApJ, 701, 260

Jin, S, Li, S., Isella, A., Li, H., & Ji, J. 2016, ApJ, 818, 76

Johansen, A., Oishi, J. S., Mac Low, M.-M., et al. 2007, Nature, 448, 1022

Johansen, A., Mac Low, M.-M., Lacerda, P., & Bizzarro, M. 2015, SciA, 1, 1500109

Johnson, B. M., & Gammie, C. F. 2003, ApJ, 597, 131

Johansen, A., & Lacerda, P. 2010, MNRAS, 404, 475

Ju, W., Stone, J. M., & Zhu, Z. 2016, ApJ, 823, 81

Juhász, A., Benisty, M., Pohl, A., et al. 2015, MNRAS, 451, 1147

Kenyon, S. J., & Hartmann, L. 1995, ApJS, 101, 117

Kenyon, S. J., Hartmann, L. W., Strom, K. M., & Strom, S. E. 1990, AJ, 99, 869

Kerswell, R. R. 2002, AnRFM, 34, 83

Kim, K. H., Watson, D. M., Manoj, P., et al. 2013, ApJ, 769, 149

Klahr, H., & Bodenheimer, P. 2006, ApJ, 639, 432

Klahr, H., & Kley, W. 2006, A&A, 445, 747

Kley, W. 1999, MNRAS, 303, 696

Kley, W., D'Angelo, G., & Henning, T. 2001, ApJ, 547, 457

Kley, W., & Nelson, R. P. 2008, A&A, 486, 617

Koller, J., Li, H., & Lin, D. N. C. 2003, ApJL, 596, L91

Kratter, K. M., Matzner, C. D., & Krumholz, M. R. 2008, ApJ, 681, 375

Kratter, K. M., Murray-Clay, R. A., & Youdin, A. N. 2010, ApJ, 710, 1375

Kratter, K. M., & Lodato, G. 2016, ARA&A, 54, 271

Kraus, A. L., Ireland, M. J., Hillenbrand, L. A., & Martinache, F. 2012, ApJ, 745, 19

Kraus, S., Ireland, M. J., Sitko, M. L., et al. 2013, ApJ, 768, 80

Kryukova, E., Megeath, S. T., Gutermuth, R. A., et al. 2012, AJ, 144, 31

Lada, C. J. 1987, in IAU Symposium, Vol. 115, Star Forming Regions, ed. M. Peimbert & J. Jugaku (Dordrecht: Reidel), 1

Lada, C. J., Muech, A. A., Luhman, K. L., et al. 2006, AJ, 131, 1574

Lambrechts, M., & Johansen, A. 2012, A&A, 544, A32

Laughlin, G., & Bodenheimer, P. 1994, ApJ, 436, 335

Lee, W.-K. 2016, ApJ, 832, 166

Lee, C. W., & Myers, P. C. 1999, ApJS, 123, 233

Lesur, G., Kunz, M. W., & Fromang, S. 2014, A&A, 566, A56

Lesur, G., Hennebelle, P., & Fromang, S. 2015, A&A, 582, L9

Lesur, G., & Papaloizou, J. C. B. 2009, A&A, 498, 1

Lesur, G., & Papaloizou, J. C. B. 2010, A&A, 513, A60

Levison, H. F., Kretke, K. A., & Duncan, M. J. 2015a, Natur, 524, 322

Levison, H. F., Kretke, K. A., Walsh, K. J., & Bottke, W. F. 2015b, Proceedings of the National Academy of Science, 112, 14180

Li, H., Finn, J. M., Lovelace, R. V. E., & Colgate, S. A. 2000, ApJ, 533, 1023

Li, H., Colgate, S. A., Wendroff, B., & Liska, R. 2001, ApJ, 551, 874

Li, H., Li, S., Koller, J., et al. 2005, ApJ, 624, 1003

Li, Z.-Y., Banerjee, R., Pudritz, R. E., et al. 2014, in Protostars and Planets VI, ed. H. Beuther et al. (Tucson, AZ: Univ. of Arizona Press), 173

Lin, M.-K. 2012, MNRAS, 426, 3211

Lin, M.-K. 2014, MNRAS, 437, 575

Lin, D. N. C., & Papaloizou, J. 1979, MNRAS, 186, 799

Lin, M.-K., & Papaloizou, J. C. B. 2010, MNRAS, 405, 1473

Lin, M.-K., & Papaloizou, J. C. B. 2011, MNRAS, 415, 1426

Lin, D. N. C., & Pringle, J. E. 1987, MNRAS, 225, 607

Lin, D. N. C., & Pringle, J. E. 1990, ApJ, 358, 515

Lin, C. C., & Shu, F. H. 1964, ApJ, 140, 646

Lin, D. N. C., Papaloizou, J. C. B., & Savonije, G. J. 1990, ApJ, 364, 326

Lissauer, J. J., & Stevenson, D. J. 2007, in Protostars and Planets V, ed. B. Reipurth, D. Jewitt, & K. Keil (Tucson, AZ: Univ. Arizona Press), 591

Lodato, G., & Rice, W. K. M. 2004, MNRAS, 351, 630

Lorenzetti, D., Antoniucci, S., Giannini, T., et al. 2012, ApJ, 749, 188

Lovelace, R. V. E., Li, H., Colgate, S. A. & Nelson, A. F. 1999, ApJ, 513, 805

Lubow, S. H., & Pringle, J. E. 1993, ApJ, 409, 360

Luhman, K. L., Allen, P. R., Espaillat, C., Hartmann, L., & Calvet, N. 2010, ApJS, 186, 111

Luhman, K. L., & Mamajek, E. E. 2012, ApJ, 758, 31

Lynden-Bell, D., & Kalnajs, A. J. 1972, MNRAS, 157, 1

Lynden-Bell, D., & Pringle, J. E. 1974, MNRAS, 168, 603

Lyo, A-R., Ohashi, N., Qi, C., et al. 2011, AJ, 142, 151

Lyra, W., Johansen, A., Zsom, A., Klahr, H., & Piskunov, N. 2008, A&A, 491, L41

Lyra, W., Johansen, A., Zsom, A., Klahr, H., & Piskunov, N. 2009, A&A, 497, 869

Lyra, W., Paardekooper, S.-J., & Mac Low, M.-M. 2010, ApJL, 715, L68

Lyra, W., & Lin, M.-K. 2013, ApJ, 775, 17

Lyra, W., & Mac Low, M.-M. 2012, ApJ, 756, 62

Lyra, W., Richert, A. J. W., Boley, A., et al. 2016, ApJ, 817, 102

Mac Low, M.-M., & Klessen, R. S. 2004, RvMP, 76, 125

Mamajek, E. E. 2009, in AIP Conf. Proc. 1158, Exoplanets and Disks: Their Formation and Diversity, ed. T. Usuda, M. Tamura, & M. Ishii (Melville, NY: AIP), 3

Martin, R. G., & Lubow, S. H. 2011, ApJL, 740, L6

Martin, R. G., Lubow, S. H., Livio, M., & Pringle, J. E. 2012a, MNRAS, 420, 3139

Martin, R. G., Lubow, S. H., Livio, M., & Pringle, J. E. 2012b, MNRAS, 423, 2718

Masset, F. 2000, A&AS, 141, 165

Masset, F., D'Angelo, G., & Kley, W. 2006, ApJ, 652, 730

Megeath, S. T., Hartmann, L., Luhman, K. L., & Fazio, G. G. 2005, ApJL, 634, L113

Meheut, H., Casse, F., Varniere, P., & Tagger, M. 2010, A&A, 516, A31

Meheut, H., Keppens, R., Casse, F., & Benz, W. 2012a, A&A, 542, A9

Meheut, H., Meliani, Z., Varniere, P., & Benz, W. 2012b, A&A, 545, A134

Meheut, H., Yu, C., & Lai, D. 2012c, MNRAS, 422, 2399

Mellon, R. R., & Li, Z.-Y. 2008, ApJ, 681, 1356

Menou, K., Hameury, J.-M., & Stehle, R. 1999, MNRAS, 305, 79

Meru, F., & Bate, M. R. 2011a, MNRAS, 410, 559

Meru, F., & Bate, M. R. 2011b, MNRAS, 411, 1

Meru, F., & Bate, M. R. 2012, MNRAS, 427, 2022

Merín, B., Brown, J. M., Oliveira, I., et al. 2010, ApJ, 718, 1200

Mignone, A., Bodo, G., Massaglia, S., et al. 2007, ApJS, 170, 228

Miller, A. A., Hillenbrand, L. A., Covey, K. R., et al. 2011, ApJ, 730, 80

Miotello, A., Testi, L., Lodato, G., et al. 2014, A&A, 567, A32

Montmerle, T., Koch-Miramond, L., Falgarone, E., & Grindlay, J. E. 1983, ApJ, 269, 182

Morbidelli, A., & Nesvorny, D. 2012, A&A, 546, A18

Morbidelli, A., Lunine, J. I., O'Brian, D. P., Raymond, S. N., & Walsh, K. J. 2012, AREPS, 40, 251

Morbidelli, A., Lambrechts, M., Jacobson, S., & Bitsch, B. 2015, Icarus, 258, 418

Morishima, R. 2012, MNRAS, 420, 2851

Movshovitz, N., Bodenheimer, P., Podolak, M., & Lissauer, J. J. 2010, Icarus, 209, 616

Murillo, N. M., Lai, S.-P., Bruderer, S., Harsono, D., & van Dishoeck, E. F. 2013, A&A, 560, A103

Muto, T., Grady, C. A., Hashimoto, J. 2012, ApJL, 748, L22

Muzerolle, J., Megeath, S. T., Flaherty, K. M., et al. 2005, ApJL, 620, L107

Muzerolle, J., Allen, L. E., Megeath, S. T., Hernández, J. & Gutermuth, R. A. 2010, ApJ, 708, 1107

Myers, P. C., Linke, R. A., & Benson, P. J. 1983, ApJ, 264, 517

Müller, A., van den Ancker, M. E., Launhardt, R., et al. 2011, A&A, 530, A85

Najita, J. R., Strom, S. E., & Muzerolle, J. 2007, MNRAS, 378, 369

Natta, A. 1993, ApJ, 412, 761

Natta, A., Testi, L., & Randich, S. 2006, A&A, 452, 245

Nayakshin, S. 2010, MNRAS, 408, 36

Nayakshin, S. 2011, MNRAS, 413, 1462

Nelson, R. P., & Gressel, O. 2010, MNRAS, 409, 639

Nelson, R. P., Papaloizou, J. C. B., Masset, F., & Kley, W. 2000, MNRAS, 318, 18

Nelson, R. P., Gressel, O., & Umurhan, O. M. 2013, MNRAS, 435, 2610

Nelson, R. P., & Papaloizou, J. C. B. 2004, MNRAS, 350, 849

Nelson, R. P. 2005, A&A, 443, 1067

Offner, S. S. R., & McKee, C. F. 2011, ApJ, 763, 53

Ogilvie, G. I., & Latter, H. N. 2013, MNRAS, 433, 2420

Ogilvie, G. I., & Lubow, S. H. 1999, ApJ, 515, 767

Okuzumi, S., & Hirose, S. 2011, ApJ, 742, 65

Ormel, C. W., & Klahr, H. H. 2010, A&A, 520, A43

Ormel, C. W., Spaans, M., & Tielens, A. G. G. M. 2007, A&A, 461, 215

Owen, J. E., & Clarke, C. J. 2012, MNRAS, 426, L96

Owen, J. E., Ercolano, B., Clarke, C. J., & Alexander, R. D. 2010, MNRAS, 401, 1415

Owen, J. E., Ercolano, B., & Clarke, C. J. 2011, MNRAS, 412, 13

Owen, J. E., Clarke, C. J., & Ercolano, B. 2012, MNRAS, 422, 1880

Öberg, K. I., Qi, C., Fogel, J. K. J., et al. 2010, ApJ, 720, 480

Paardekooper, S.-J., & Papaloizou, J. C. N. 2008, A&A, 485, 877

Paardekooper, S.-J., Thébault, P., & Mellema, G. 2008, MNRAS, 386, 973

Paardekooper, S.-J., Lesur, G., & Papaloizou, J. C. N. 2010, ApJ, 725, 146

Papaloizou, J. C. B. 2005a, A&A, 432, 743

Papaloizou, J. C. B. 2005b, A&A, 432, 757

Papaloizou, J. C. B., & Pringle, J. E. 1984, MNRAS, 208, 721

Papaloizou, J. C. B., & Pringle, J. E. 1985, MNRAS, 217, 387

Papaloizou, J. C., & Savonije, G. J. 1991, MNRAS, 248, 353

Perez-Becker, D., & Chiang, E. 2011, ApJ, 735, 8

Petersen, M. R., Julien, K., & Stewart, G. R. 2007, ApJ, 658, 1236

Petigura, E. A., Howard, A. W., & Marcy, G. W. 2013, PNAS, 110, 19273

Pérez, L. M., Isella, A., Carpenter, J. M., & Chandler, C. J. 2014, ApJL, 783, L13

Pfalzner, S., Tackenberg, J., & Steinhausen, M. 2008, A&A, 487, L45

Pierens, A., & Nelson, R. P. 2008, A&A, 482, 333

Piétu, V., Dutrey, A., & Guilloteau, S. 2007, A&A, 467, 163

Pinilla, P., van der Marel, N., van Dishoeck, E. F., et al. 2015, A&A, 584, A16

Pollack, J. B., Hubickyj, O., Bodenheimer, P., et al. 1996, Icarus, 124, 62

Preibisch, T., Kim, Y.-C., Favata, F., et al. 2005, ApJS, 160, 401

Probstein, R. F., & Fassio, F. 1969, AIAA, 8, 4

Rafikov, R. R. 2005, ApJ, 621, L69

Regály, Zs., Juhász, A., Sándor, Zs., & Dullemond, C. P. 2012, MNRAS, 419, 1701

Reipurth, B., & Aspin, C. 2010, Evolution of Cosmic Objects through Their Physical Activity, ed. H. A. Harutyunian, A. M. Michaelian, & Y. Terzian (Yerevan: Gitutyun Publishing House),19

Reipurth, B., & Bally, J. 2001, ARA&A, 39, 403

Reipurth, B., Aspin, C., Beck, T. 2007, AJ, 133, 1000

Rice, W. K. M., Armitage, P. J., Bate, M. R., & Bonnell, I. A. 2003, MNRAS, 339, 1025

Rice, W. K. M., Armitage, P. J., Wood, K., & Lodato, G. 2006, MNRAS, 373, 1619

Richard, S., Barge, P., & Le Dizès, S. 2013, A&A, 559, A30

Rosenfeld, K. A., Qi, C., Andrews, S. M., et al. 2012, ApJ, 757, 129

Rosotti, G. P., Ercolano, B., Owen, J. E., & Armitage, P. J. 2013, MNRAS, 430, 1392

Ryu, D., & Goodman, J. 1994, ApJ, 422, 269

Sano, T., Miyama, S. M., Umebayashi, T., & Nakano, T. 2000, ApJ, 543, 486

Sawada, K., Matsuda, T., & Hachisu, I. 1986, MNRAS, 219, 75

Schaefer, G. H., Dutrey, A., Guilloteau, S., Simon, M., & White, R. J. 2009, ApJ, 701, 698

Seifried, D., Banerjee, R., Pudritz, R. E., & Klessen, R. S. 2015, MNRAS, 446, 2776

Shakura, N. I., & Sunyaev, R. A. 1973, A&A, 24, 337

Shu, F. H. 1977, ApJ, 214, 488

Sicilia-Aguilar, A., Hartmann, L. W., Hernández, J., Briceño, C., & Calvet, N. 2005, AJ, 130, 188

Siess, L., Dufour, E., & Forestini, M. 2000, A&A, 358, 593

Simon, J. B., Lesur, G., Kunz, M. W., & Armitage, P. J. 2015, MNRAS, 454, 1117

Smak, J. 1984, AcA, 34, 161

Stolker, T., Dominik, C., Avenhaus, H., et al. 2016, A&A, 595, 113

Stone, J. M., & Norman, M. L. 1992, ApJS, 80, 753

Stone, J. M., Hawley, J. F., Gammie, C. F., & Balbus, S. A. 1996, ApJ, 463, 656

Strom, K. M., Strom, S. E., Edwards, S., Cabrit, S., & Skrutskie, M. F. 1989, AJ, 97, 1451

Stutz, A. M., Tobin, J. J., Stanke, T., et al. 2013, ApJ, 767, 36

Szulágyi, J., Morbidelli, A., Crida, A., & Masset, F. 2014, ApJ, 782, 65

Tanga, P., Babiano, A., Dubrulle, B., & Provenzale, A. 1996, Icarus, 121, 158

Tanigawa, T., & Tanaka, H. 2016, ApJ, 823, 48

Takeuchi, T., & Lin, D. N. C. 2002, ApJ, 581, 1334

Terebey, S., Shu, F. H., & Cassen, P. 1984, ApJ, 286, 529

Testi, L., Birnstiel, T., Ricci, L., et al. 2014, in Protostars and Planets VI, ed. H. Beuther et al. (Tucson, AZ: Univ. of Arizona Press), 339

Tobin, J., Hartmann, L., Looney, L. W., & Chiang, H.-F. 2010, ApJ, 712, 1010

Tobin, J., Hartmann, L., Chiang, H.-F., et al. 2011, ApJ, 740, 45

Tobin, J., Hartmann, L., Bergin, E., et al. 2012, ApJ, 748, 16

Tobin, J. J., Hartmann, L., Chiang, H.-F., et al. 2012, Natur, 492, 83

Tobin, J. J., Kratter, K. M., Persson, M. V., et al. 2016, Natur, 538, 483

Toomre, A. 1964, ApJ, 139, 1217

Ulrich, R. K. 1976, ApJ, 210, 377

Urpin, V., & Brandenburg, A. 1998, MNRAS, 294, 399

van der Marel, N., van Dishoeck, E. F., Bruderer, S., et al. 2013, Sci, 340, 1199

van der Marel, N., van Dishoeck, E. F., Bruderer, S., et al. 2015, A&A, 579, A106

van der Marel, N., van Dishoeck, E. F., Bruderer, S., et al. 2016, A&A, 585, 58

van Leer, B. 1977, Journal of Computational Physics, 23, 276

Varnière, P., & Tagger, M. 2006, A&A, 446, L13

Vicente, S., Mer'in, B., Hartung, M., et al. 2011, A&A, 533, A135

VonNeumann, J., & Richtmyer, R. D. 1950, JAP, 21, 232

Vorobyov, E. I. 2010, NewA, 15, 24

Vorobyov, E. I., & Basu, S. 2005, ApJL, 633, L137

Vorobyov, E. I., & Basu, S. 2006, ApJ, 650, 956

Vorobyov, E. I., & Basu, S. 2007, MNRAS, 381, 1009

Vorobyov, E. I., & Basu, S. 2009, MNRAS, 393, 822

Vorobyov, E. I., & Basu, S. 2010, ApJ, 719, 1896

Walsh, K. J., Morbidelli, A., Raymond, S. N., O'Brien, D. P., & Mandell, A. M. 2011, Nature, 475, 206

Whipple, F. L. 1972, in From Plasma to Planet, ed. A. Evlius (New York: Wiley), 211

Weidenschilling, S. J. 1977, MNRAS, 180, 57

Weidenschilling, S. J., & Cuzzi, J. N. 1993, in Protostars and Planets III, ed. E. H. Levy & J. I. Lunine (Tucson: Univ. Arizona Press), 1031

Wilking, B. A., Lada, C. J., & Young, E. T. 1989, AJ, 340, 823

Williams, J. P., & Cieza, L. A. 2011, ARA&A, 49, 67

Williams, J. P., Blitz, L., & McKee, C. F. 2000, in Protostars and Planets IV, ed. V. Mannings, A. P. Boss, & S. S. Russell (Tucson, AZ: Univ. Arizona Press), 97

Winn, J. N., & Fabrycky, D. C. 2015, ARA&A, 53, 409

Yang, C.-C., Mac Low, M.-M., & Menou, K. 2009, ApJ, 707, 1233

Yen, H.-W., Takakuwa, S., Ohashi, N., et al. 2014, ApJ, 793, 1

Youdin, A. N., & Goodman, J. 2005, ApJ, 620, 459

Youdin, A. N., & Lithwick, Y. 2007, Icar, 192, 588

Zhu, Z., Hartmann, L., Calvet, N., Hernandez, J., Muzerolle, J., & Tannirkulam, A.-K. 2007, ApJ, 669, 483

Zhu, Z., Hartmann, L., Calvet, N., Hernandez, J., Tannirkulam, A.-K., & D'Alessio, P. 2008, ApJ, 684, 1281

Zhu, Z., Espaillat, C., Hinkle, K., Hernandez, J., Hartmann, L., & Calvet, N. 2009a, ApJL, 694, L64

Zhu, Z., Hartmann, L., & Gammie, C. 2009b, ApJ, 694, 1045

Zhu, Z., Hartmann, L., Gammie, C., & McKinney, J. C. 2009c, ApJ, 701, 620

Zhu, Z., Hartmann, L., Gammie, C. F., Book, L. G., Simon, J. B., & Engelhard, E. 2010a, ApJ, 713, 1134

Zhu, Z., Hartmann, L., & Gammie, C. F. 2010b, ApJ, 713, 1143

Zhu, Z., Nelson, R. P., Hartmann, L., Espaillat, C., & Calvet, N. 2011, ApJ, 729, 47

Zhu, Z., Hartmann, L., Nelson, R. P., & Gammie, C. F. 2012a, ApJ, 746, 110

Zhu, Z., Nelson, R. P., Dong, R., Espaillat, C. & Hartmann, L. 2012b, ApJ, 755, 6

Zhu, Z., & Stone, J. M. 2014, ApJ, 795, 53

Zhu, Z., Stone, J. M., Rafikov, R. R., & Bai, X. 2014, ApJ, 785, 122

Zhu, Z., Dong, R., Stone, J. M., & Rafikov, R. R. 2015, ApJ, 813, 88

Ziegler, U., & Yorke, H. W. 1997, Computer Physics Communications, 101, 54

Zsom, A., Ormel, C. W., Güttler, C., Blum, J., & Dullemond, C. P. 2010, A&A, 513, A57